Studies of Charge Transport and Phase Transition Equilibria in Blends of Ionic Liquids for Dye-Sensitised Solar Cells

A Dissertation Presented for the Degree of
Doctor of Natural Sciences
(Dr. rer. nat.)

At the Natural Sciences Faculty IV
Chemistry and Pharmacy
Universität Regensburg

Philipp Wachter

Regensburg 2008

Official Registration:	19.03.2008
Defence:	18.04.2008
Ph.D. Supervisor:	Prof. Dr. H. J. Gores
Adjudicators:	Prof. Dr. W. Kunz, Chair
	Prof. Dr. H. J. Gores
	Prof. Dr. G. Schmeer
	Prof. Dr. J. Daub

For Stefanie

and

My Parents

Acknowledgments

The presented work took place between October 2005 and March 2008 at the Chair of Physical Chemistry (Solution Chemistry) at the Faculty for Natural Sciences IV at the Universität Regensburg.

First of all, I would like to express my gratitude to my doctoral advisor Prof. Dr. H. J. Gores for the interesting subject. His excellent mentoring and support in all theoretical and practical questions contributed substantially to the success of this work. Prof. Gores deserves great respect for his commitment towards his undergraduate and PhD students and his ability to secure the necessary funds.

I would also like to thank the head of the Chair of Physical Chemistry (Solution Chemistry) Prof. Dr. W. Kunz and all members of the Chair for the constructive collaboration.

I thank my research-group colleagues Mr. R. Hartl, Dr. T. Herzig, Dr. J. Lodermeyer, Dr. M. Multerer, Mr. F. Wudy Dipl.-Chem. und Ms. S. Zugmann Dipl.-Chem. for their moral and technical support. A very special thanks goes out to Mr. C. Schreiner Dipl.-Chem. and Dr. M. Zistler, members of the notorious “coffee-lab”, for their everlasting support and the three entertaining years we spent together.

I would also like to thank the Federal Ministry of Education and Research (BMBF) for the funding of this work within the scope of the network-project "Development of system components for long-term stable dye-sensitised solar cells with high efficiency” (Nr. 01SF0304).

Appreciation also goes out to Prof. Dr. P. Wasserscheid (Universität Erlangen-Nürnberg) and his co-workers Dr. D. Gerhard and Dr. S. Himmler for the close collaboration.

I would also like to thank Mr. W. Simon and Mr. G. Berger for their technical support.

A special thanks goes to Dr. R. E. Panzer for his assistance in editing this dissertation.

I would also like to thank my family for the support they provided through my entire life and in particular, my wife and best friend, Stefanie, without whose love, encouragement and editing assistance, I would not have finished this dissertation.

Danksagung

Die vorliegende Arbeit entstand in der Zeit von Oktober 2005 bis März 2008 am Lehrstuhl für Chemie VI – Physikalische Chemie (Solution Chemistry) – an der naturwissenschaftlichen Fakultät IV – Chemie und Pharmazie – der Universität Regensburg.

Mein ganz besonderer Dank gilt meinem Doktorvater Herrn Prof. Dr. H. J. Gores für die Bereitstellung des interessanten Themas. Seine ausgezeichnete Betreuung und seine Unterstützung in allen theoretischen und praktischen Fragen trugen wesentlich zum Erfolg dieser Arbeit bei. Für seinen unermüdlichen Einsatz für die Belange seiner Diplomanden und Doktoranden sowie bei der Mittelbeschaffung gebührt ihm Respekt und mein größter Dank.

Herrn Prof. Dr. W. Kunz und allen Mitarbeitern des Lehrstuhls danke ich für die angenehme und konstruktive Zusammenarbeit.

Meinen Laborkollegen Herrn R. Hartl, Herrn Dr. T. Herzig, Herrn Dr. J. Lodermeyer, Herrn Dr. M. Multerer, Herrn Dipl.-Chem. F. Wudy und Frau Dipl.-Chem. S. Zugmann danke ich für die gute und freundschaftliche Arbeitsatmosphäre und die stete Hilfsbereitschaft. Mein besonderer Dank gilt meinen beiden „Kaffee“-Laborkollegen Herrn Dipl.-Chem. C. Schreiner und Herrn Dr. M. Zistler für ihre Unterstützung bei Problemen jeglicher Art und die drei unterhaltsamen Jahre am Lehrstuhl.

Dem Bundesministerium für Bildung und Forschung (BMBF) danke ich für die Finanzierung dieser Arbeit im Rahmen des Netzwerk-Projekts „Entwicklung von Systemkomponenten für langzeitstabile Farbstoffsolarzellen mit hohem Wirkungsgrad“ (Nr. 01SF0304).

Mein weiterer Dank gilt Herrn Prof. Dr. P. Wasserscheid (Universität Erlangen-Nürnberg) und seinen Mitarbeitern Herrn Dr. D. Gerhard und Frau Dr. S. Himmler für die konstruktive Zusammenarbeit.

Weiterhin möchte ich mich bei unserem Lageristen Herrn W. Simon und unserem EDV-Systemadministrator Herrn G. Berger für die stete Hilfsbereitschaft bedanken, sowie bei Dr. R. E. Panzer für die Unterstützung beim Korrekturlesen.

Meinen Eltern und meiner Frau möchte ich für die Unterstützung während des Studiums danken.

Abstract

In this work a comprehensive characterisation of four ionic liquid (IL) based electrolyte systems for dye-sensitised solar cells (DSSCs) was performed by determination of triiodide diffusion coefficients, conductivities and liquid ranges. The electrolytes, consisting of iodine, 1-methyl-3-propylimidazolium iodide (MPII), and a low viscosity solvent IL, were examined at varying IL molar ratios and fixed iodine concentration, as well as at fixed IL molar ratio and varying iodine concentrations. Diffusion and conductivity measurements were conducted over a broad temperature range to analyse the electrolyte properties in regards to thermal stress of the DSSC for later practical application. The triiodide diffusion coefficient and the electrolyte conductivity typically increase with decreasing MPII concentration or increasing temperature, caused by decreasing electrolyte viscosity. Generally, strong non-Stokesian diffusion behaviour was found for all electrolytes, decreasing at higher temperatures. In contrast to MPII concentration and temperature, the triiodide concentration had no distinct effect on the triiodide diffusion. Determination of the electrolyte's liquid ranges by thermal analysis with simultaneous recording of conductivity yielded unexpected narrow liquid ranges for the electrolytes based on 1-ethyl-3-methylimidazolium bis(trifluoromethylsulfonyl)imide and 1-ethyl-3-methylimidazolium tetrafluoroborate. For the electrolyte systems based on 1-ethyl-3-methylimidazolium dicyanamide and 1-ethyl-3-methylimidazolium trifluoromethanesulfonate, in principle, wider liquid ranges were obtained. However, for most of their blends no phase transitions were obtained. Investigation of conductivity and phase transition points of eleven pure ILs yielded in several cases conductivity data and melting points that were not previously reported. Consideration of fragility, based on the temperature dependence of conductivity, yielded that all examined ILs are fragile glass formers and show strong non-Arrhenius behaviour.

Zusammenfassung

Im Rahmen dieser Arbeit wurden vier auf ionischen Fluiden (ILs) basierende Elektrolyt-Systeme hinsichtlich ihrer Eignung als Elektrolyte für farbstoffsensibilisierte Solarzellen (DSSCs) untersucht. Dazu wurden in den Elektrolyten, die sich aus Iod, 1-Methyl-3-propylimidazoliumiodid (MPII) und einem zweiten, niedriger viskosen ionischem Fluid zusammensetzen, die Triiodid-Diffusionskoeffizienten, Leitfähigkeiten und Fest-Flüssig-Phasenübergänge über den kompletten Mischungsbereich der ILs untersucht. Der Temperaturbereich von Diffusions- und Leitfähigkeitsmessungen wurde dem voraussichtlichen Bereich der Arbeitstemperatur von DSSCs angepasst. Sowohl Triiodid-Diffusionskoeffizienten als auch Leitfähigkeiten steigen bei sinkender MPII-Konzentration oder steigender Temperatur aufgrund der sinkenden Viskosität stark an. Für alle Elektrolyt-Systeme wurde ein ausgeprägter nicht-Stokes'scher Anteil an der Diffusion festgestellt, der mit steigender Temperatur abnimmt. Eine zusätzliche Variierung der Iodkonzentration hatte keinen nennenswerten Einfluss auf den Triiodid-Diffusionskoeffizienten. Durch Thermische Analyse bei gleichzeitiger Aufzeichnung der Leitfähigkeit konnte gezeigt werden, dass die zwei Elektrolyt-Systeme mit 1-Ethyl-3-methylimidazoliumbis(trifluoromethylsulfonyl)-imid bzw. 1-Ethyl-3-methylimidazoliumtetrafluoroborat als niedrig viskosem IL erst bei relativ hohen Temperaturen vollständig in die flüssige Phase übergehen. Für die Mischungen auf der Basis von 1-Ethyl-3-methylimidazoliumdicyanamid bzw. 1-Ethyl-3-methylimidazoliumtrifluoromethansulfonat ist die flüssige Phase prinzipiell bis zu sehr viel niedrigeren Temperaturen stabil. Allerdings konnten für einen großen Teil der Mischungen dieser beiden Systeme keine Phasenübergänge beobachtet werden. Zusätzlich zu den Elektrolyt-Mischungen wurden Leitfähigkeiten sowie Fest- und Schmelzpunkte von elf reinen ILs untersucht. Die dabei erhaltenen Werte für Fest- und Schmelzpunkte waren größtenteils noch nicht publiziert; auch einige Leitfähigkeiten wurden erstmalig gemessen. Die Untersuchung der Fragilität ergab für alle untersuchten ILs sehr niedrige Stärke-Indizes und somit hohe Fragilitäten. Die Temperaturabhängigkeit von Transporteigenschaften in diesen ILs kann somit nicht nach Arrhenius beschrieben werden.

1 Motivation

1.1 Introduction

Since 1960 the world-wide energy consumption almost triplicated. [1] According to a study performed by the energy company Shell [2] the energy needs of the planet are likely to double until 2050 because of the increasing world population and economy. The rapid growth of the economy in developing and newly industrialised countries such as India, China, and Brazil and the increasing desire for prosperity of their population especially push the world-wide energy consumption to continuously rising levels. As energy needs increase, resources of fossil fuels such as crude oil and natural gas are estimated to be exhausted in about 60 years at present level of energy consumption. [3] Development and exploitation of these deposits becomes continuously more expensive and has already caused armed conflicts. The peaceful use of nuclear energy is linked to finite recoverable resources of uranium minerals. It additionally involves the problem of final storage of radioactive waste and the risk of a nuclear crisis. Therefore, it is mandatory to increasingly cover the surge for energy by renewable energy.

The concept of renewable energy comprises various aspects such as wind energy, geothermic energy, energy from biomass, and tidal power stations. The most promising aspect however is the use of solar energy by photovoltaic cells or solar thermal collectors as it is usable world-wide and will not be exhausted until the end of our planet. In this context it should also be taken into consideration that the energy supply from the sun to the earth is about 10000 times larger than the current energy consumption on earth [4].

Another reason for a change towards renewable energies is the need to reduce the world-wide CO_2-emission. Nowadays, it is common knowledge that CO_2 and methane are the major greenhouse gases but the influence of anthropogenic CO_2 on global warming is still controversial.

However, a more intensified extension of renewable energies and the replacement of fossil fuels is the only way to soften the climate change and its negative consequences due to the anticipated increasing energy need in the future. Despite world-wide effects of the climate change only very few and comparably wealthy countries seriously try to replace fossil fuels with renewable energies due to the much higher costs involved.

To the present time the high production costs of silicon based solar cells are the major obstacle for their large scale application. The large quantities of high purity silicon and the

resulting energy-intensive and technologic sophisticated production steps are especially responsible for the high production costs. Several attempts were made to reduce the production costs of silicon based solar cells:

- Decreasing the level of processing of the applied silicon from monocrystalline towards amorphous silicon;
- Reducing the thickness of the applied silicon layer;
- Alternative solar cell concepts;

After first successful laboratory tests in 1988 [5], O'Regan and Grätzel presented a possible alternative to conventional silicon based solar cells in 1992 [6]: dye-sensitised solar cells (DSSCs). Efficiencies and energy payback periods of several types of solar cells are listed in Table 1-1.

Table 1-1: Efficiencies and energy payback periods of different types of solar cells.

Type of cell	Max. efficiency [%] laboratory	Max. efficiency [%] large scale	Energy payback period
Crystalline silicon	24 [7]	14 to 17 [7]	48 to 75 months [8]
Multicrystalline silicon	18 [7]	13 to 15 [7]	25 to 57 months [8]
Amorphous silicon	13 [7]	5 to 7 [7]	17 to 41 months [8]
Dye-sensitised nanostructured materials	10-11 [4]	7 [4]	-

Despite lower efficiencies of DSSCs when compared to silicon based solar cells (Table 1-1), DSSCs show some advantageous features that are of special interest for commercial application:

- Lower production costs [7]:
  a) Application of comparably low-cost materials such as glass, glass solder, polymer foils, TiO_2, iodine, and smallest amounts of cost-intensive materials such as Pt, dye, and ionic liquid based electrolyte.

b) Less energy-intensive and complex production steps.

- Increasing efficiencies with increasing temperatures in contrast to silicon based solar cells that show a 20% efficiency loss in the temperature range from 20 °C to 60 °C. [4,9]
- Good performance under diffused light due to a bifacial configuration. [4]
- Transparent and semi-transparent versions of different colours can be made, enabling costumer-specific design and application as electric power-producing windows. [4]

These properties are the base for an increasing interest in DSSCs (Figure 1-1) and the associated technology over the last decade and should enable their large scale application in the future.

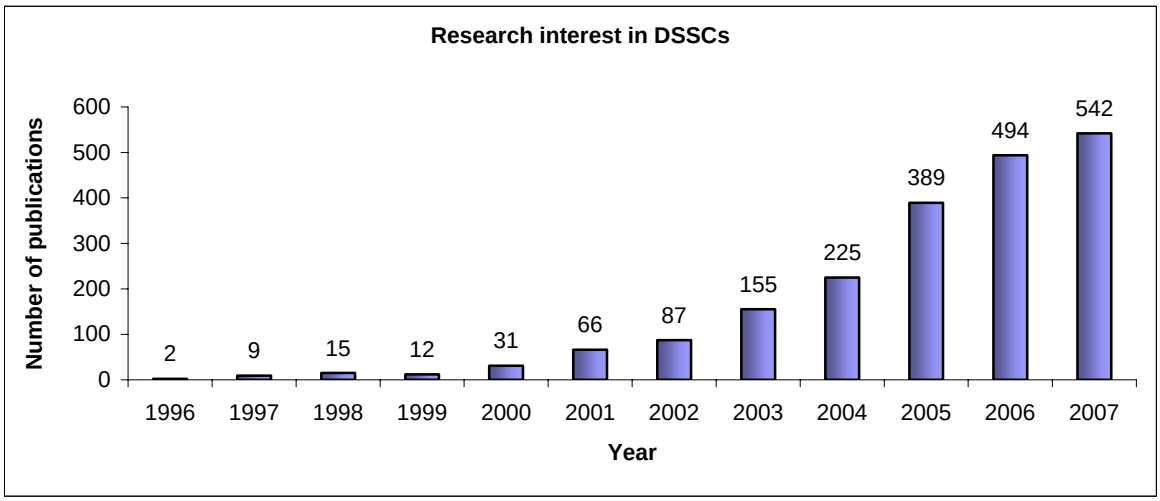

Figure 1-1: Number of publications for the research topic dye-sensitised solar cells in the period from 1996 to 2007. [10] Our research group contributed one publication in 2006, two in 2007, and so far four in 2008, i.e. our share of publications lies between 0.5 and 1%.

1.2 Aims and Objectives

The primary objective of this dissertation was to characterise and optimise ionic liquid (IL) based electrolytes for application in DSSCs. For this purpose two electrolyte parameters were systematically examined. One parameter is the charge transport in the electrolyte that has a major impact on the efficiency of the DSSC. The other one is the liquid range of the electrolyte that generally limits the operating range of the DSSC. The predominant and for DSSCs most important mode of charge transport is the I_3^--diffusion that was examined by steady-state cyclic voltammetry at ultramicroelectrodes. To complete the characterisation of the electrolytes with respect to charge transport, their conductivities were also determined. The liquid range of the electrolytes was examined by thermal analysis with simultaneous recording of conductivity.
Testing single components in assembled DSSCs is an expensive and elaborate task. Thus, it is of major importance to characterise and optimise single components with fast and reliable techniques. This dissertation focuses exclusively on electrolytes and their later application in DSSCs.

For a better orientation a brief overview of the structure of the dissertation is given below. It complements the more detailed index of contents.

Chap. 2 provides an overview of the theoretical background. DSSCs and the physico-chemical concept of charge transport are introduced and the preferences of thermal analysis in contrast to other and more common methods are discussed.

Chap. 3 introduces the most important measurement techniques that were applied in this dissertation. The examined materials are described as well.

In **Chap. 4** the results from diffusion measurements are summarised and discussed. In contrast to the common approach in this field of research a detailed study of the influence of iodine and iodide concentration on the I_3^--diffusion coefficient was performed over a broad temperature range. The occurring non-Stokesian charge transport was also analysed with respect to iodide concentration and temperature.

Chap. 5 deals with conductivity measurements in pure ILs and their binary mixtures. Analysis of the temperature dependence of conductivity of pure ILs also enabled their classification according to their glass forming behaviour.

In **Chap. 6** the results from thermal analysis with simultaneously recorded conductivity are presented including different melting points of pure ionic liquids and phase diagrams of IL-based electrolyte systems, which were determined for the first time.

In **Chap. 7** the results of the specific measurement techniques are briefly discussed to provide a short overview of the dissertation and to enable a final appraisal of the examined electrolyte systems. In addition, a short report is given on already accepted and still intended publications along with lectures given in meetings and plenary sessions.

2 Theory

2.1 Dye-Sensitised Solar Cells

2.1.1 General Parameters of Solar Cells

This chapter presents a short overview summarising the most important solar cell parameters and their meanings. The most used parameter in connection with solar cells is the efficiency of the solar cell η_{sol}, which is defined as ratio of the maximum extractable electric power P_m and incident optical power Φ_i [11]:

$$\eta_{sol} = \frac{P_m}{\Phi_i} \tag{2.1}$$

Further important parameters are the open-circuit voltage U_{OC}, the short-circuit current I_{SC} or current density j_{SC}, and the fill factor FF. (see Figure 2-1)
The operating point of the solar cell is defined by the intersection of the IU-curve with the straight line $I = UR_L^{-1}$, where R_L is the resistance of the external load. The optimum value for R_L is given, if the area of the dark-grey rectangle in Figure 2-1 is maximal, with [11]:

$$P_m = I_m U_m \tag{2.2}$$

The corresponding operating point is the so called maximum power point (MPP).
The fill factor is the ratio of the areas of the dark-grey rectangle and of the light grey rectangle, which is defined by U_{OC} and I_{SC} [11]:

$$FF = \frac{I_m U_m}{I_{SC} U_{OC}} = \frac{P_m}{I_{SC} U_{OC}} \tag{2.3}$$

The fill factor is a measure for the performance of a solar cell and is typically in the range between 0.70 and 0.85.

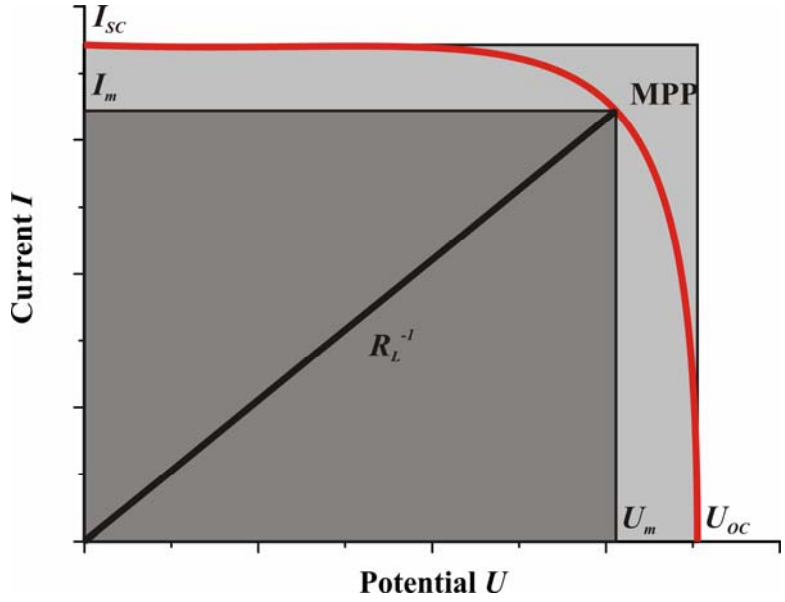

Figure 2-1: Current-voltage characteristic of a solar cell; I_m current, U_m voltage at the maximum power point (MPP); U_{OC} open circuit voltage, I_{SC} short circuit current, R_L external load; according to Ref. [11].

The *IU*-characteristic of a solar cell varies with the incident solar radiation or with temperature. To operate the solar cell at the MPP, one must be able to adjust the value of the external load by an electronic circuit. A first approximation of the optimum external load is given by [11]:

$$R_{L,opt} \approx \frac{U_{OC}}{I_{SC}} \tag{2.4}$$

The spectrum of the solar radiation depends on the angle and the path length through the atmosphere. A relative measure for both is the so called Air Mass (*AM*), which is given by the ratio of the path length *l* and standard value l_0: $AM = l/l_0$. l_0 is the shortest possible path length, the case of perpendicular incident solar radiation. A standard value for characterisation of solar cells is $AM = 1.5$. [11]

2.1.2 Design and Operation Principle of a Dye-Sensitised Solar Cell

The general design and operation principle of a DSSC are schematically shown in Figure 2-2. The body of the DSSC consists of two glass plates coated on the insides with a transparent conducting oxide (TCO, typically fluorine-doped SnO_2) and held at a distance of about 40 µm by a glass frit which acts simultaneously as sealant. The heart of the cell is a wide band gap semiconductor which is applied as an 8-15 µm thick layer of mesoporous or nanocrystalline morphology on the front TCO-glass plate, the photoanode. Attached to the surface of the semiconductor particles is a monolayer of the charge transfer dye. The counter electrode consists of platinum which is sputtered onto the second TCO-glass. Charge transfer dye and counter electrode are in contact with a redox electrolyte or an organic hole conductor which is located in the space between the two electrodes. [6,9,12]

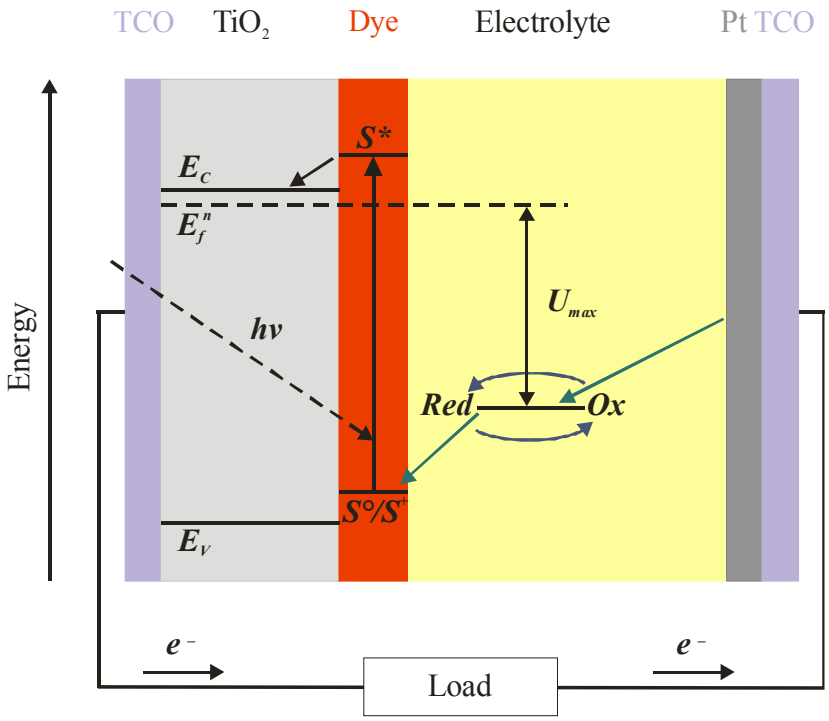

Figure 2-2: Schematic illustration of the general design and operating mode of a DSSC.

An alternative cell setup is the monolithic cell, where the counter electrode is made up of graphite/carbon-black instead of platinised TCO-glass. [13]

Application of a wide band gap semiconductor is based on the fact that semiconductors with narrower band gap, small enough for efficient absorption of visible sunlight, are unstable against photocorrosion. The preferred semiconductor is TiO_2 in its anatase

modification although other wide band gap oxides such as ZnO [14], and Nb_2O_5 [15] were also investigated. [9,4,12]

Since a direct absorption of sunlight with application of these materials is no longer possible a mono-molecular layer of an electron transfer sensitizer, typically a Ru- or Os-dye, is attached to the oxide surface. The applied dyes are metal-complexes with the general formula $ML_2(X)_2$ where M stands for Ru or Os, L is 2,2'-bipyridyl-4,4'-dicarboxylic acid and X is, e.g. halide, cyanide, or thiocyanate. This kind of dye features a sufficient light absorption, even in the infrared region, convenient located energy levels, and a sufficient long-term stability. Phthalocyanine and porphyrin dyes show a lack of these properties what hinders a breakthrough of these classes of dyes. As example for a sensitizer the often used N3-dye ($Ru(dcbpyH_2)_2(NCS)_2$) is shown in Figure 2-3. [4,9]

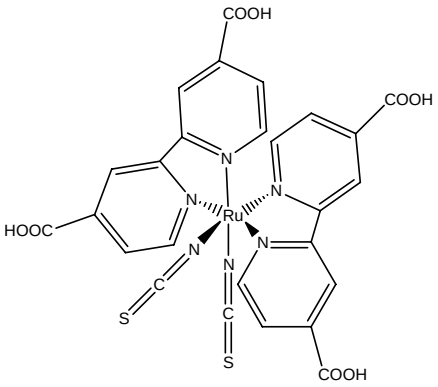

Figure 2-3: Structure of $Ru(dcbpyH_2)_2(NCS)_2$.

Incident light excites the dye which passes into an excited state and subsequently injects an electron into the conduction band of the semiconductor, what represents the actual charge separation. [16-19] Afterwards the dye falls into its cationic ground state and is regenerated by reduction from the redox couple dissolved in the electrolyte. The injected electrons diffuse through the conduction band of the TiO_2 until they reach the back contact of the film with the TCO-glass. [19,20]

The morphology of the applied nanocrystalline TiO_2 allows efficient light harvesting by the adsorbed dye due to the enlarged surface which is about 1000 times larger than for a compact TiO_2 layer of similar measures. In addition, it introduces fundamental changes in the photoelectrochemical properties of TiO_2 because it is no longer necessary to dope the oxide film since this is already sufficiently ensured by injection of one electron from the sensitizer to a TiO_2 nanoparticle. No space-charge limitation of the photocurrent is

observed since the injected majority carriers are efficiently screened by the electrolyte. [4,9]

Except for hole conductors, the reduction of the dye-cation and simultaneously regeneration of the dye is performed by electron donation from the reduced species of a redox couple. This so called redox mediator is typically the I^-/I_3^--redox couple whose redox potential matches the energy levels of the sensitizer. Regeneration of the dye yields I_3^- that diffuses to the counter electrode where it is again reduced to I^- by the electrons which migrate through the external circuit. The reduction of I_3^- is catalysed by the applied Pt-electrode. The charge transport in the electrolyte consequently occurs by diffusion of I^- to the photoanode and of I_3^- to the counter electrode respectively. [16,21,22]

The most important chemical and electrochemical reactions which occur in the cell under working conditions can be summarised as follows [23]:

$$S^0 \xrightarrow{h\nu} S^* \qquad \text{[I]}$$

$$S^* \longrightarrow S^+ + e^- \qquad \text{[II]}$$

$$S^+ + \frac{3}{2} I^- \longrightarrow S^0 + \frac{1}{2} I_3^- \qquad \text{[III]}$$

$$I_3^- + 2e^- \longrightarrow 3I^- \qquad \text{[IV]}$$

Since the overall concentrations of all participating components stay constant and no permanent chemical transformation occurs, this kind of device is a regenerative photo-electrochemical cell. The obtained photovoltage corresponds to the difference between the Fermi level of the electrons in the solid and the redox potential of the electrolyte. [4,9]

Additional to the above mentioned reactions ([I]-[IV]), some side reactions occur which reduce the overall conversion efficiency of the cell [23-25]:

$$S^* \xrightarrow[-h\nu]{} S^0 \qquad \text{[V]}$$

$$e^-_{TiO_2} + S^+ \longrightarrow S^0 \qquad \text{[VI]}$$

$$2e^-_{TiO_2} + I_3^- \longrightarrow 3I^- \qquad \text{[VII]}$$

$$2e^-_{SnO_2} + I_3^- \longrightarrow 3I^- \qquad \text{[VIII]}$$

The backslide of the excited dye into its ground state enabled by energy release by fluorescence [V] can be disregarded since the electron injection (ps time scale) is about 10^5

times faster. [9,25] Recapture of a previously injected electron by a dye-cation [VI] (µs time scale) has also only minor influence on the efficiency loss because reduction of the dye-cation by I^- [III] (ns time scale) is much faster. [9,25] If the TCO-surface of the photoanode is not completely coated with TiO_2 and the I_3^- is able to diffuse to this back contact of the TiO_2-layer, reaction [VIII] can occur. Because there is no catalysis by Pt, the I_3^--reduction at the TCO-surface is much slower than at the counter electrode and has therefore only minor influence on the cell efficiency. [9,12,16,23-25]

Since the TiO_2-surface is not completely coated with the dye, reaction [VII] can not be completely inhibited. This reaction, the recapture of a previously injected electron by an I_3^--anion, causes most of the efficiency loss of the cell which is therefore strongly correlated to the applied electrolyte. [24] That means that there is a correlation to the diffusion coefficient of the I_3^- which is a measure for the rate of the I_3^--transport in the DSSC and therefore also for the exposure time of the I_3^- at the photoanode [22] and also a correlation to the I_3^--concentration which has an influence on the quantity of I_3^--anions near the photoanode. [26,27]

2.1.3 Electrolyte of a Dye-Sensitised Solar Cell

The most important component of the electrolyte is the dissolved redox couple or so called redox mediator because it is responsible for both dye regeneration and charge transport in the DSSC. The typically applied redox mediator is the I^-/I_3^--redox couple although alternative redox couples such as $SeCN^-/Se(CN)_3^-$ [28] or Co(II)/Co(III)-complexes [29] were investigated. A further alternative is the application of organic or inorganic hole conductors which regenerate the dye under hole formation. Some investigated examples for inorganic hole conductors are Cu(I)-compounds such as CuSCN [30] or CuI [31].

To the present time, electrolytes for DSSCs were most frequently made up of iodide salts, iodine, and optional additional organic and inorganic compounds, dissolved in an organic solvent. DSSCs with this kind of electrolyte achieve the highest efficiencies but also suffer from various drawbacks. Due to the volatility of these solvents the cell must be completely sealed, a complex and cost-intensive process. A further disadvantage is the often poor solubility of inorganic salts in most organic solvents at lower temperatures. These disadvantages combined with the risk of a poor long-term stability of the cells, in the case of insufficient sealing, limit a large scale implementation of this technology. [32-34]

Therefore, the search for potential alternatives to the organic solvent based electrolytes was highly intensified during the last years. To completely avoid the problem of leak tightness application of liquid-crystal electrolytes [35,36], gel or polymer electrolytes [37-46], and the above mentioned hole conductors [30,31] were investigated. Application of this kind of electrolytes opens up interesting possibilities, but so far the achieved DSSCs efficiencies are typically still in the range of 2-3% and therefore much lower than for liquid electrolytes.

A second promising alternative to organic solvents is the application of ionic liquid (IL)-based electrolytes in DSSCs. ILs feature several interesting properties so that they often replace organic solvents in various electrochemical devices and applications [47,48]:

- Negligible vapour pressure and therefore also reduced toxicity;
- Usually non-flammable;
- Broad liquid range, from partly far below 0 °C up to 400 °C;
- High thermal, chemical and electrochemical stability;
- High conductivity and ionic strength;
- Typically high solubility of organic and inorganic materials over a broad concentration and temperature range;
- Adjustable solvent properties by choice of anion and cation;

Due to the sum of these properties ILs are also of interest for application in DSSCs. The negligible vapour pressure which enhances not only the long term stability of the DSSC [49], also facilitates the production and sealing process. The application of liquid iodide salts enables high iodide concentrations in the electrolyte thus enhancing the regeneration of the dye. [50]

The major disadvantage of ILs is their comparatively high viscosity that renders physical transport processes in ILs much slower than in conventional electrolytes. The resultant low I_3^--diffusion coefficients lead therefore to charge transport limitations of the DSSCs and hence also reduced efficiencies. This is one of the major problems for application of IL-based electrolytes for DSSC.

There are few electrolyte parameters which have major impact on the efficiency of a DSSC and its applicability, two of them were studied during this work. One is the above mentioned I_3^--diffusion coefficient that reflects the efficiency of the charge transport in the DSSC. [23,51,52] The requirements on the I_3^--diffusion coefficient vary with the cell

design (monolithic or conventional), the electrode distance, the porosity of the TiO_2-layer, the I_3^--concentration, and so on. This amount of variation possibilities also leads to varying critical values for the I_3^--diffusion coefficient. According to the work of Papageorgiou et al. [51] and Asano et al. [52] a critical value of about $3 \cdot 10^{-6}$ cm^2 s^{-1} can be derived. The estimation of a critical value performed by Rau [53] yields a limiting I_3^--diffusion coefficient of 10^{-6} cm^2 s^{-1}. The last value is already in the magnitude of diffusion coefficients of solutes in common solvents and is therefore assumed to be sufficient large to avoid diffusion limitation of the DSSC. Thus, the value of 10^{-6} cm^2 s^{-1} is chosen as base for the appraisal of I_3^--diffusion coefficients determined in this work.

The second important electrolyte parameter which was studied during this work is the liquid range of the applied electrolyte. It is obvious that crystallisation or evaporation of the electrolyte lead to a breakdown of the cell, at least temporarily, and more serious damage may occur. Since evaporation of the electrolyte can be disregarded in the case of ILs, the main study was done on the liquid to solid phase transition. Crystallisation of the electrolyte leads to a sudden and strong decrease of all occurring transport processes. The lower limit of the liquid range of potential electrolytes for DSSCs should be of major interest for all groups which refer to DSSCs in their studies, but up to now no publication is addressing this problem in the case of IL-based electrolytes. The same holds for liquid electrolytes for high energy batteries. During this work also some preliminary studies concerning electrolytes for high energy batteries were performed. A publication is in preparation, addressing a phase diagram study of a common electrolyte for lithium-ion-cells.

A third important electrolyte property is the charge transfer resistance at the counter electrode which determines the I_3^--reduction. This property was not studied during this work but in close cooperation to it (see Ref. [54]).

The most basic IL-based electrolyte for DSSCs consists of a liquid iodide salt (e.g. 1-methyl-3-propylimidazolium iodide or 1-hexyl-3-propylimidazolium iodide) and iodine. Even for ILs, these iodides have rather high viscosities. To optimise the electrolyte with respect to the above discussed properties, a second comparatively low-viscosity and low-melting IL was added which acts as so called “solvent IL”. This also enables the utilization of solid iodide salts. Additionally, various additives may be added which enhance, for instance, the UV-stability or the open circuit voltage. Despite the fact that the electrolyte properties are strongly based on the electrolyte composition and also vary with

temperature, very few publications concerning DSSCs deal with these parameters. [13,27,55-59]

For this work electrolytes consisting of 1-methyl-3-propylimidazolium iodide, iodine and one solvent IL, either 1-ethyl-3-methylimidazolium bis(trifluoromethylsulfonyl)imide, 1-ethyl-3-methylimidazolium dicyanamide, 1-ethyl-3-methylimidazolium tetrafluoroborate, or 1-ethyl-3-methylimidazolium trifluoromethanesulfonate, were examined with regard to electrolyte composition and temperature as well.

2.2 Transport Properties

2.2.1 Ionic Conductivity

Presently, there are no theoretical equations available for the conductivity of ionic liquids. This section shows some general approaches that were used to interpret the data of this work. More detailed information on conductivity in aqueous and non-aqueous solutions, including the state of art of conductivity equations for these electrolytes, can be found in Refs. [60-64] and on the theory of ion-ion interactions and ion-solvent interactions in Refs. [63,65].

The ionic conductivity is a characteristic electrolyte parameter that is based on migration of ions in an electric field. From a macroscopic point of view, the conductivity (G) of an electrolyte is the reciprocal value of the electrolyte resistance (R) between two electrodes at a specific applied voltage (U) and resulting current (i). As can be seen from the Ohm's Law (Eq. (2.5)) the conductivity depends on electrolyte properties (here the specific resistance ρ), and on the dimensions of the applied measuring cell (length l, cross sectional area A). [66]

$$i = \frac{U}{R} = \frac{1}{\rho}\frac{A}{l}U = GU \tag{2.5}$$

A more characteristic value for the electronic behaviour of electrolytes is the specific conductivity κ which can be calculated from recorded conductivity values according to Eq. (2.6), where B is the cell constant of the measuring cell. [66]

$$\kappa = \frac{l}{A}G = BG \tag{2.6}$$

The relation between the specific conductivity of an electrolyte solution and the properties of the dissolved ions is cleared in the following sections. For the case of a binary electrolyte, the specific conductivity can also be described according to Eq. (2.7) [61,66]:

$$\kappa = n_e c \Lambda \tag{2.7}$$

where

$$n_e = \nu_+ z_+ = \nu_- \left| z_- \right| \tag{2.8}$$

and c is the molar concentration of the salt, Λ the equivalent conductivity, n_e the electrochemical valency, z_+ and z_- are cationic and anionic charges, and ν_+ and ν_- stoichiometric coefficients.

The equivalent conductivity Λ is the sum of the equivalent conductivities of the individual ions λ_+ and λ_- which are proportional to the single ion mobilities u_+ and u_-, with the Faraday constant F as proportional factor [61,66]:

$$\Lambda = \lambda_+ + \lambda_- = F\left(u_+ + u_-\right) \tag{2.9}$$

Single ion mobilities can be described as the ratio of the velocity $\vec{v}$ of ions in an electric field $\vec{E}$ leading to the following expression for the equivalent conductivity [61,66]:

$$\Lambda = F\left(\nu_+ z_+ \frac{\left|\vec{v}_+\right|}{\left|\vec{E}\right|} + \nu_- z_- \frac{\left|\vec{v}_-\right|}{\left|\vec{E}\right|}\right) \tag{2.10}$$

with:
$$u_+ = \frac{\left|\vec{v}_+\right|}{\left|\vec{E}\right|}; u_- = \frac{\left|\vec{v}_-\right|}{\left|\vec{E}\right|} \tag{2.11}$$

Very large spherical ions in a viscous medium are accelerated under the influence of an electric field by the electric force F_E until the occurring Stokesian frictional force F_R and F_E are equal (Eq. (2.12)) leading to a steady state. A constant ion velocity results (Eq. (2.13)) [61,66]:

$$F_E = z_i e_0 \vec{E} = 6\pi\eta R_i \vec{v}_i = F_R \tag{2.12}$$

$$\vec{v}_i = \frac{z_i e_0 \vec{E}}{6\pi\eta R_i} \tag{2.13}$$

where e_0 is the elementary charge, η the viscosity of the solution, and R_i the radius of the ion. In general, very large spherical ions are very unusual. Eq. (2.13) is therefore only an approximation that however is valid for real ions that are only weakly solvated, such as rather large organic ions. In cases of very small ions, such as Li-ions, R_i in Eq. (2.13) is not the radius of the ion, but that of the solvated ion. [61-63,66]

With Eqs. (2.10) and (2.13) the equivalent conductivity of an individual ion can be described as [61,66]:

$$\lambda_i = F\frac{|z_i|e_0}{6\pi\eta R_i} = N_A\frac{|z_i|e_0^2}{6\pi\eta R_i} \tag{2.14}$$

According to Eq. (2.14) the equivalent conductivity of an individual ion is solely dependent on the charge of the ion and the viscosity of the solution, since all remaining parameters are constant. This assumption leads to the empirical Walden rule (Eq. (2.15)) which states that the product of equivalent conductivity and viscosity is constant for a specific temperature. [61,63,66]

$$\lambda_i\eta = N_A\frac{|z_i|e_0^2}{6\pi R_i} \equiv const. \tag{2.15}$$

However, it was found that Eqs. (2.14) and (2.15) are only valid without restrictions for infinite diluted solutions, with Λ^0 and λ_i^0 as limiting values of the equivalent conductivities [61,63,66]:

$$\lim_{c\to 0}\Lambda = \Lambda^0; \lim_{c\to 0}\lambda_i = \lambda_i^0 \tag{2.16}$$

In fact, several parameters have major impact on the equivalent conductivity. One of them is the strongly temperature dependent viscosity of the solution, mentioned above. Another is the radius of the solvated ion, because typically, except for rather large inert organic ions, no naked ions exist in solutions. The quantity of the solvent molecules in the solvation sheath and therefore its radius depends on the kind, radius, and charge of the ion and the kind of solvent as well. In the case of non-infinite diluted solutions, interactions with varying ranges between dissolved ions play an important role. The resulting ion cloud reduces the equivalent conductivity due to relaxation and electrophoretic effects.

Another result of these ionic interactions is the association of ions into neutral ion-pairs or larger aggregates with increasing salt concentration. This leads to a decreasing quantity of charged species in the solution and reduces the equivalent conductivity of the electrolyte.

This effect is heightened in the case of weak electrolytes and solvents with low dielectric permittivities respectively and the resulting incomplete dissociation.

Due to these restrictions of Eq. (2.14) particular conductivity equations for diluted and concentrated solutions of weak and strong electrolytes have been derived in the past decades. More detailed information about conductivity in solutions can be found in Refs. [60-63,65].

Conductivity in ILs and its dependence on the properties of specific anions and cations is by far not as well understood as the conductivity of diluted electrolyte solutions. As for conventional electrolyte solutions the conductivity of ILs is based on the mobility of the ions and on the quantity of charge carriers. [67]

The mobility itself depends on several parameters. One of them is the size of the ions; another is the viscosity of the IL. To minimise the frictional force (Eq. (2.12)) and therefore enhance the ion velocity a small ion radius and low viscosity would be best. Since the viscosity of ILs is also based on the size and shape of the ions [68,69], a simple reduction of cation and anion radii does not yield the expected results. In general, viscosity increases with increasing attractive ionic interactions, in particular Coulombic and van der Waals interactions and hydrogen bridge bonds as well. Coulombic interactions typically increase with decreasing ion radii whereas the van der Waals interactions increase with increasing ion size, especially for cations with large hydrocarbon side chains. Increasing side chains also lead to a decreased rotational freedom. [69,70] Additionally, Coulombic interactions also correlate with the rate of charge delocalisation of the ions. The formation of hydrogen bridge bonds also correlates with the rate of charge delocalisation and therefore basicity of the anion. Beside the above discussed ionic interactions there are additional molecular parameters that may affect the viscosity, such as the planarity of the cation or the molecular weight of the ions. [68-70] The mobility of an ion can also be directly affected by ionic interactions since these may cause correlated ion motions of ions with opposed charges. [69]

The quantity of charge carriers in an IL is reduced by association of ions under formation of neutral ion pairs and larger aggregates. Responsible for ionic association are again the ionic interactions, mentioned above. The predominance of the various cation/anion interactions on the conductivity of ILs is a special feature of ILs and is caused by extraordinary high ion concentrations in ILs and the resulting physical proximity of cations and anions. [69]

According to the Nernst-Einstein equation (Eq. (2.17)) the conductivity of a charge carrier

is direct proportional to its diffusion coefficient D_i [48,68,69]:

$$\lambda_i = \frac{z_i^2 e_0 F D_i}{k_B T} = \frac{z_i^2 N_A e_0^2 D_i}{k_B T} \tag{2.17}$$

where N_A represents the Avogadro number and k_B the Boltzmann constant. The equivalent conductivity of an IL can therefore be calculated from the diffusion coefficients of the cation (D_+) and anion (D_-). [48,68,69]

$$\Lambda = \frac{z_i^2 N_A e_0^2}{k_B T}\left(D_+ + D_-\right) \tag{2.18}$$

Self-diffusion coefficients obtained by NMR-measurements contain portions of uncharged species, e.g. ion-pairs and larger aggregates, which also diffuse through the electrolyte. Equivalent conductivities calculated from these diffusion coefficients according to Eq. (2.18) also contain portions of these uncharged species. Therefore the level of ionic association can be estimated by comparison of these calculated conductivities and measured conductivities that are only based on contributions of charged species. [68,69,71]
During the previous considerations of conductivity of electrolyte solutions and ILs the influence of the temperature on the conductivity was disregarded. As discussed above the conductivity of electrolyte solutions and ILs is based on various parameters whose summarised temperature dependencies result in the temperature dependence of the conductivity. That means in detail the temperature dependence of the viscosity, of the radius of the solvated ion, and generally of ionic interactions and ionic association in particular. Similar to concentration dependence of the conductivity in electrolyte solutions the temperature dependence of conductivity was intensively studied. [61-63]
The developed theories and relations for the temperature dependence of conductivity in electrolyte solutions are also used for its behaviour in ILs.
For ILs, the temperature dependence of the radius of the solvated ion can be disregarded since no solvent molecules are present. In addition, the temperature dependence of viscosity is typically assumed to be most pronounced and therefore with the largest impact on conductivity. It is most frequently described according to two competing approaches. The first and older approach is the assumption of Arrhenius-type behaviour according to Eq. (2.19) [70,72] that was originally derived for the rate constant of a chemical reaction:

$$\eta(T) = A\exp\left(\frac{E_A}{RT}\right) \tag{2.19}$$

where A is a fitting parameter, E_A the activation energy, R the molar gas constant, and T the temperature. This approach is based on the presence of holes in the electrolyte and transport processes that need to be activated by activation energies. Overall it is a valid and useful concept for solid materials only. Alder and Einwohner [73] showed that liquids have neither holes nor transport activation energies. Assumption of Arrhenius-type behaviour for the conductivity according to Eq. (2.20) in the case of strongly temperature dependent ionic association can even result in negative $d\kappa/dT$ values and therefore negative activation energies for conductive transport which is physically impossible. [74]

$$\kappa(T) = A\exp\left(\frac{-E_A}{RT}\right) \tag{2.20}$$

It has been shown that the second approach and analysis of the temperature dependence according to the Vogel-Fulcher-Tamann (VFT)-equation (Eq. (2.21)) [75-77] is more suitable for liquids. The VFT-equation was empirically obtained by combination of the theory of cooperatively rearranging regions according to Adam and Gibbs [78] and the percolation theory according to Grest and Cohen [79,80]. The VFT-equations for viscosity and the specific conductivity are given in the following form:

$$\eta(T) = \eta_0\exp\left[\frac{B}{T-T_0}\right] \tag{2.21}$$

$$\kappa(T) = \kappa_0\exp\left[\frac{-B}{T-T_0}\right] \tag{2.22}$$

where η_0, κ_0 and B are fitting parameters, T is the measurement temperature and T_0 the ideal glass transition temperature. In addition to the above shown versions of the VFT-equation (Eqs. (2.21) and (2.22)) also some modified forms are in use. The most frequent modifications are based on the assumption that the pre-exponential factors η_0 and κ_0 are also temperature dependent, usually expressed as $\eta_0, \kappa_0 = AT^{1/2}$ or $\eta_0, \kappa_0 = AT^{1}$. Since this temperature dependence is very weak, when compared with that of the exponential term, Eqs. (2.21) and (2.22)) are generally used in the given form.

In general, the validity of the chosen working equation, i.e. Arrhenius or VFT, is determined by the behaviour of the liquid sample at its liquid-to-glass transition. Angell introduced the concept of fragility to characterise the different types of glass forming liquids [81-83], with two extreme limits: strong and fragile liquids. The fragility m and strength D of a liquid define the temperature dependence of viscosity in reduced plots of $log(\eta) = f(T_g/T)$ [81], where T_g is defined as the temperature where $\eta = 10^{12}$ Pa s (Figure 2-4). A more universal approach for analysis of the type of liquid is a reduced plot of the average relaxation times $log\langle\tau\rangle = f(T_g/T)$ [84], with $\langle\tau(T_g)\rangle = 100$ s.

Strong liquids with nonhydrogen bonded networks, such as SiO_2 or GeO_2, show a strong resistance against structural degradation upon heating. Fragile glass formers, typically substances with nondirectional interatomic/intermolecular bonds, such as o-terphenyl, show only little resistance against temperature induced structural degradation. [84] This behaviour also correlates with the magnitude of the c_p jump at T_g (small for strong liquids, large for fragile liquids [83]). Alcohols (hydrogen bonds) and molten salts (Coulombic interactions and hydrogen bonds of varying strength) lie between these two extremes. [85] The fragility m that corresponds to the characteristical slope of the function at T_g (Figure 2-4) is a convenient measure for this classification. Low values of m (high values of D) correspond to a low fragility and hence almost Arrhenius-type behaviour, high values of m (low values of D) correspond to large fragility and consequently VFT behaviour.

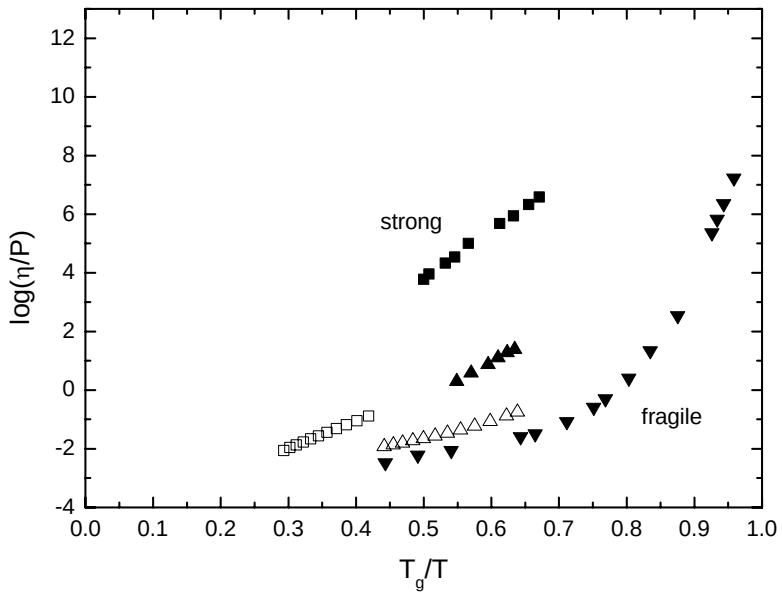

Figure 2-4: Arrhenius plot of IL viscosities with reduced temperature according to Angell [81], the inverse temperature is scaled by $T_g := T(\eta = 10^{13}$ P). The viscosities of SiO_2 (■), $ZnCl_2$ (□), and o-terphenyl (▼) are obtained from Ref. [86], the viscosities of 1-propanol (▲) and propylene carbonate (△) are obtained from Ref. [87].

The fragility *m* is also related to the strength *D* (Eq. (2.23) [84]) that can be obtained from a slightly modified version of the VFT-equation (Eq. (2.24) [84,88]):

$$m = \left(\frac{D}{\ln 10}\right)\left(\frac{T_0}{T_g}\right)\left(\frac{1-T_0}{T_g}\right)^{-2} = 16 + \frac{590}{D} \tag{2.23}$$

$$\eta(T) = \eta_0 \exp\left[\frac{B}{T-T_0}\right] = \eta_0 \exp\left[\frac{DT_0}{T-T_0}\right] \tag{2.24}$$

This image of the fragility also meets its characterisation by Vilgis [88] who correlates *D* with the mean coordination number z_0 of a molecule and its fluctuation Δz:

$$D = \frac{1}{4}\left(\frac{z_0}{\Delta z}\right) \tag{2.25}$$

Strong liquids have, due to their strong interactions, typically small coordination numbers (SiO_2, $z_0 = 4$) with little deviations at increased temperatures and consequently large *D* values (≈ 100) [85]. For fragile liquids and a random closed packing where $z_0 \approx 14$ and $\Delta z \approx 4$ the calculated value for D = 3.1 [88] is in very good agreement with the lowest experimental obtained value D = 3.2 [82] for common liquids. Polymers, such as polycarbonates and polyvinyl chloride, were found to be even more fragile with $D \approx 2$ [83].

2.2.2 Diffusion

In general, the charge- and mass-transport in an electrolyte solution is performed by diffusion, migration and convection and can be described according to the Nernst-Planck equation:

$$\vec{J} = -D\nabla c - \frac{zF}{RT} Dc\nabla\Phi + c\vec{v} \tag{2.26}$$

where $\vec{J}$ represents the flux of particles, *D* the diffusion coefficient, *c* the electrolyte concentration, *z* the charge of the particle being examined, *F* the Faraday constant, *R* the

molar gas constant, Φ the electric potential, and $\vec{v}$ the velocity that is externally impressed by convection. [89]

The case of migration of charged species, described by the electrolyte conductivity, has already been discussed in Chap. 2.2.1. In the following sections the main focus is on diffusion which is the predominant transport mode in the DSSC. For this application migration can be disregarded due to high electrolyte concentrations and consequently high ionic strength. Convection is absent due to the very low electrode distances.

Diffusion results from a gradient in (electro)chemical potential that is caused by concentration (or activity) difference of a specific species. A flux of matter occurs to compensate this concentration difference.

For the case of DSSCs charge- and mass-transport is assumed to be one-dimensional due to the cell geometry. Thus, in the following sections only the one-dimensional diffusion is discussed. Considered at microscopic level the diffusion is performed by a random walk process. The mean square of displacement $\overline{\Delta}^2$ can be calculated according to Eq. (2.27) [89]:

$$\overline{\Delta}^2 = ml^2 = \frac{t}{\tau} l^2 = 2Dt \tag{2.27}$$

where l represents the step length, m the number of time units τ, t the measurement time, and D the diffusion coefficient. For a sufficient large volume, the mean direction of motion of matter is towards areas of lower concentration. [89]

From the microscopic model a relation between the flux and concentration gradient, which is known as Fick's first law (Eq. (2.28)), can be derived. The flux $J_O(x,t)$ represents the number of moles of the species O that pass a given location per second per cm^2 of area normal to the axis of diffusion. The minus sign in Eq. (2.28) results from the negative concentration gradient. [89]

$$J_O(x,t) = -D_O \frac{\partial c_O(x,t)}{\partial x} \tag{2.28}$$

The time dependence of the concentration of O can be described according to Fick's second law that can be derived from Eq. (2.28) as follows. The change in concentration at a location x is given by the difference in flux into and flux out of an element of width dx

(Eq. (2.29)) and the flux at $x+dx$ can be described in terms of the flux at x (Eq. (2.30)) [89]:

$$\frac{\partial c_O(x,t)}{\partial t} = \frac{J_O(x,t) - J_O(x+dx,t)}{dx} \tag{2.29}$$

$$J_O(x+dx,t) = J_O(x,t) + \frac{\partial J_O(x,t)}{\partial x} dx \tag{2.30}$$

From Eq. (2.28) the second part of Eq. (2.30) can be obtained [89]:

$$\frac{\partial J_O(x,t)}{\partial x} = -\frac{\partial}{\partial x} D_O \frac{\partial c_O(x,t)}{\partial x} \tag{2.31}$$

Combination of Eq. (2.29) and (2.31) yields [89]:

$$\frac{\partial c_O(x,t)}{\partial t} = \frac{\partial}{\partial x}\left[D_O \frac{\partial c_O(x,t)}{\partial x} \right] \tag{2.32}$$

When D_O is not a function of x, Fick's second law (Eq. (2.33)) results. This is the case if the changes in solution composition are sufficiently small and no significant changes in solution properties occur. [89]

$$\frac{\partial c_O(x,t)}{\partial t} = D_O \frac{\partial^2 c_O(x,t)}{\partial x^2} \tag{2.33}$$

The general formulation of Fick's first law (Eq. (2.34)) and second law (Eq. (2.35)) for any geometry is given as following [89]:

$$J_O = -D_O \nabla c_O \tag{2.34}$$

$$\frac{\partial c_O}{\partial t} = D_O \nabla^2 c_O \tag{2.35}$$

Similar to conductivity (Chap. 2.2.1, Eq. (2.14)), the relation between electrolyte viscosity and the diffusion coefficient of the dissolved species can typically be described according to the Stokes-Einstein equation [90,91]:

$$D = \frac{k_B T}{6\pi\eta R_i} \tag{2.36}$$

The temperature dependence of the diffusion coefficient is also based on the temperature dependence of viscosity and ionic interactions. If the ionic interactions and their temperature dependence are only weakly pronounced and no non-Stokesian charge transport (see Chap. 2.2.3) occurs, the temperature dependence of the diffusion coefficient can be described according to the VFT-equation [48,68]:

$$D(T) = A \exp\left[\frac{-B}{T - T_0}\right] \tag{2.37}$$

2.2.3 Non-Stokesian Charge Transport

According to Eq. (2.15) in Chap. 2.2.1 the product of conductivity and viscosity is assumed to be constant (Walden rule) which is in fact only valid without restrictions for infinite diluted solutions. Based on Eq. (2.36) a similar relation can be derived for the diffusion coefficient. This so called Einstein-Stokes ratio (Eq. (2.38)) should be also constant at constant temperatures. If this requirement is observed a Stokesian behaviour exists. [90,92,93]

$$\frac{D\eta}{T} = const. \tag{2.38}$$

The first deviation from this Stokesian behaviour reported in literature was the high mobility of protons in water, for which an alternative transport mechanism was proposed by Grotthus. [94]

Another deviation from the strict Stokesian behaviour was found for the I_3^- transport in ILs and their binary blends that are often applied as electrolytes in DSSCs. The I_3^--diffusion coefficients in these electrolytes are much higher than expected according to recorded viscosity data and calculated Einstein-Stokes ratios. As reason for this enhanced I_3^- transport a mechanism has already been suggested that depends on the assumption that the I_3^- transport is created by a combination of an ordinary diffusion process and a Grotthus-

type charge-transfer mechanism. [34,95] A similar behaviour was observed for the I_3^- transport along laminar phases in liquid crystals. [35,96]

The suggested charge-transfer process for the case of I_3^- is illustrated in Figure 2-5. The length of the actually participating poly-iodide chains is not definitely determined up to now, but chain lengths up to five atoms are know from literature. [42,96]

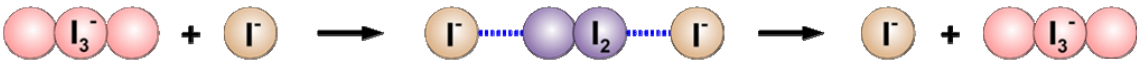

Figure 2-5: Schematic drawing of the non-Stokesian I_3^- transport or exchange mechanism; (the scheme was created by C. Schreiner)[a].

According to the above mentioned I_3^- transport mechanism the apparent or overall diffusion coefficient D_{app} can be split in a physical diffusion coefficient D_{phys} based on diffusion and on a diffusion coefficient D_{ex} based on charge transfer [95,97-99]:

$$D_{app} = D_{phys} + D_{ex} \tag{2.39}$$

For the transfer of I_2 from I_3^- to I^- both ions have to be in close physical proximity to one another. This leads to a kinetic constraint of this transfer, due to the negative charge of both reactants and the resulting energetic disadvantageous transition state. The constraint would be reduced by larger poly-iodide chain lengths and the resulting distribution of the negative charge over the whole chain.

The enhanced I_3^- transport is typically observed in ILs. As already discussed in Chap. 2.2.1 a special feature of ILs is the extremely high ion concentration and therefore also high ionic strength. Due to the high ionic strength, the negative charges of the reacting ions are better insulated from one another and the necessary activation energy is reduced. The result of this kinetic salt effect is the facilitated I_2 transfer compared to other media. [95]

[a] Thanks to C. Schreiner for providing this scheme.

2.3 Thermal Analysis

Several measurement techniques are available for determination of phase transition points of pure substances, blends, and solutions which can be selected according to experimental conditions and other specific requirements. The main issue of all below discussed techniques is that they try to determine an equilibrium property (a freezing/melting point) during heating or cooling a sample, where the system is not in an equilibrium state.

Determination of invariant points (degree of freedom $f = 0$) in single-component systems (triple points), can be performed comparably easy and with high accuracy (better than 1 mK). Therefore, several reference values of the international temperature scale are based on these points, such as the triple point of water at 273.160 K. In single-component systems the determination of univariant points ($f = 1$) is much more complex but often possible with high accuracy because they are reduced to invariant points when the determination is performed at constant pressure. This was shown for acetonitrile [100-102], a single-component system with very little tendency to supercooling. [103] Even at constant pressure x(T)-lines of binary solid-liquid phase diagrams are generally not easily determined as - for eutectic systems - the composition of the phases changes during heating or cooling ($f = 1$).

Examination of melting and freezing points for preparation of such phase diagrams is relatively often performed by application of differential thermal analysis (DTA) and differential scanning calorimetry (DSC) [104-106]. The advantages of both methods are their fast and comparatively easy practicability and the very small sample volumes that are required; the latter is of major interest when examining very expensive substances. The main disadvantages are however a lower accuracy [100] and higher sensitivity to systematic errors. The reduced accuracy is mainly caused by the small sample volumes because in this special case already smallest impurities can strongly falsify the phase transition temperature by means of a lowered melting point and raised boiling point as well. Additional effects that are caused by the wall of the sample vessel become strongly apparent by examination of such small sample volumes. [103] Another factor that is responsible for the reduced accuracy of these methods is generally the lack of a stirring device. Hence, mass transport and heat transfer are exclusively performed by comparatively slow diffusion and weakly pronounced convection that leads to anisotropic temperature distribution and, in the case of mixtures, to an inhomogeneous sample composition. [103] The latter is a major disadvantage for determination of phase transition

points in multicomponent systems, where a homogeneous sample constitution is a crucial point. The anisotropic temperature distribution, combined with generally applied high cooling rates, enhances the supercooling of studied samples. [107,108] Supercooling is an important error source during investigations of liquid to solid phase transitions. For common organic solvents supercooling can reach a level of about 15 K, but for ILs the supercooling effect is even worse and can reach up to 200 K [109] which strongly falsifies the determined crystallisation points. The large supercooling, in combination with the generally applied high cooling and heating rates, made a determination of crystallisation and melting points for some ILs impossible because the samples do not crystallise within the working range of common DSC and DTA devices.

An alternative to the above discussed methods is the investigation of cooling curves proposed by Andrew, Kohman and Johnston [110]. Additional examples of this method are shown in Refs. [100,111]. This method requires observation of the temperature of a sample which is slowly cooled down or heated up. Using this procedure, greater accuracy is achieved, because much larger probe volumes are used. Small cooling and heating rates can be applied to reduce supercooling, because they have no negative influence on the sensitivity of this method. [103] As shown by Rossini et al. [100] the melting point of pure substances, not tending to supercooling, can be measured with an uncertainty of ± 10 mK. A disadvantage of this method, when compared to DSC and DTA, is the lower sensitivity, which makes determination of phase transitions, where only little energy quantities are transferred, nearly impossible.

Another method is described by Schrödle et al [112]. This method is similar to the cooling curve method but the phase transition is determined with a photo detector instead of a temperature sensor and the temperature of the thermostat bath at this point is assumed to be the phase transition temperature. [103] The disadvantages of this method are its restriction to transparent samples, the assumption of identical temperatures of the sample and the thermostat bath and it gives no information if supercooling has occurred.

All of the above discussed techniques require exposing the sample to a temperature gradient with simultaneously recording of its temperature as a function of time. If a phase transition occurs in a single component system a halt is observed due to the released phase transition enthalpy that counterbalances the cooling process of the sample. In multi component systems the phase transition enthalpy results in a breaking point because only one component crystallises and the composition of the remaining phase changes with time.

Ideal examples of temperature-time curves of single-component and multicomponent systems respectively are shown in Figure 2-6.

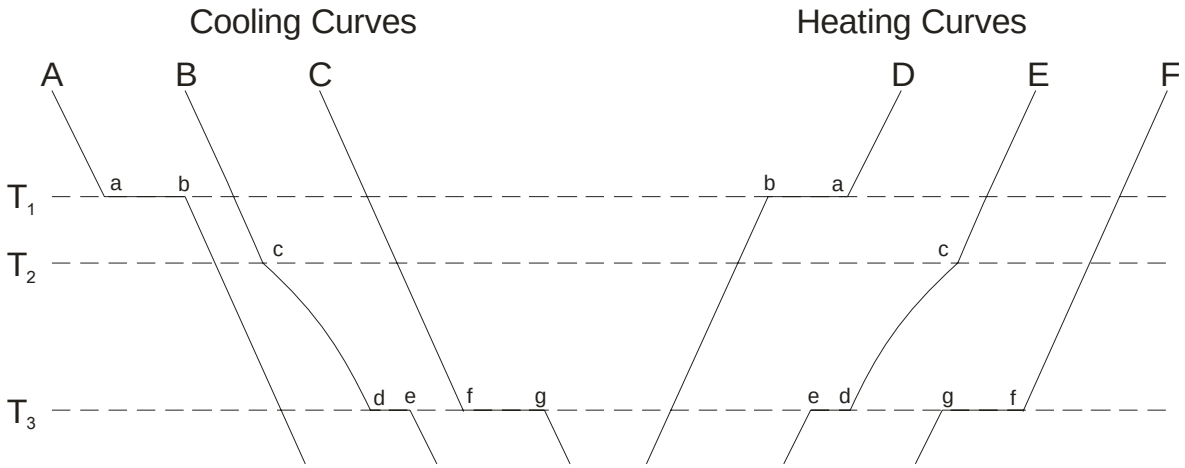

Figure 2-6: Examples of idealised cooling and heating curves of a pure substance and a binary mixture; according to Ref. [100].

In general, there are three types of cooling and heating curves which can be observed.

1) Crystallisation of a pure substance (curve A of Figure 2-6)
   The temperature of the sample varies with the applied temperature gradient until the freezing point T_1 is reached. This temperature is kept constant (*a*-*b*) by the phase transition enthalpy compensating the thermal loss to the surrounding. After the substance is completely crystallised, the temperature of the sample decreases continuously again according to the applied temperature gradient, following Newton's equation.
2) Cooling of a binary mixture (curve B of Figure 2-6)
   The temperature of the sample varies with the applied temperature gradient until point *c* at temperature T_2 is reached. At this point, one substance starts to precipitate from the liquid. The released phase transition enthalpy compensates only part of the heat loss of the sample to the surroundings, resulting in a reduced slope of the cooling curve (breaking point). If the eutectic composition at T_3 is reached, the liquid crystallizes completely without further variation of its composition, resulting in a eutectic halt (*d*-*e*).
3) Cooling of a eutectic mixture (curve C of Figure 2-6)
   If the eutectic temperature T_3 is reached, the system crystallizes completely forming a solid with eutectic composition.

The curves D, E, and F (Figure 2-6) show heating curves which are complementary to the cooling curves A, B, and C (Figure 2-6).

During a real cooling experiment delayed crystallisation or supercooling can occur, which leads to a curve like the one shown in Figure 2-7. Therefore, it can be necessary to determine the melting point by extrapolation of the horizontal or quasi-horizontal parts of the curves. The intersection point of the two curves determines the crystallisation point. [103,107,108]

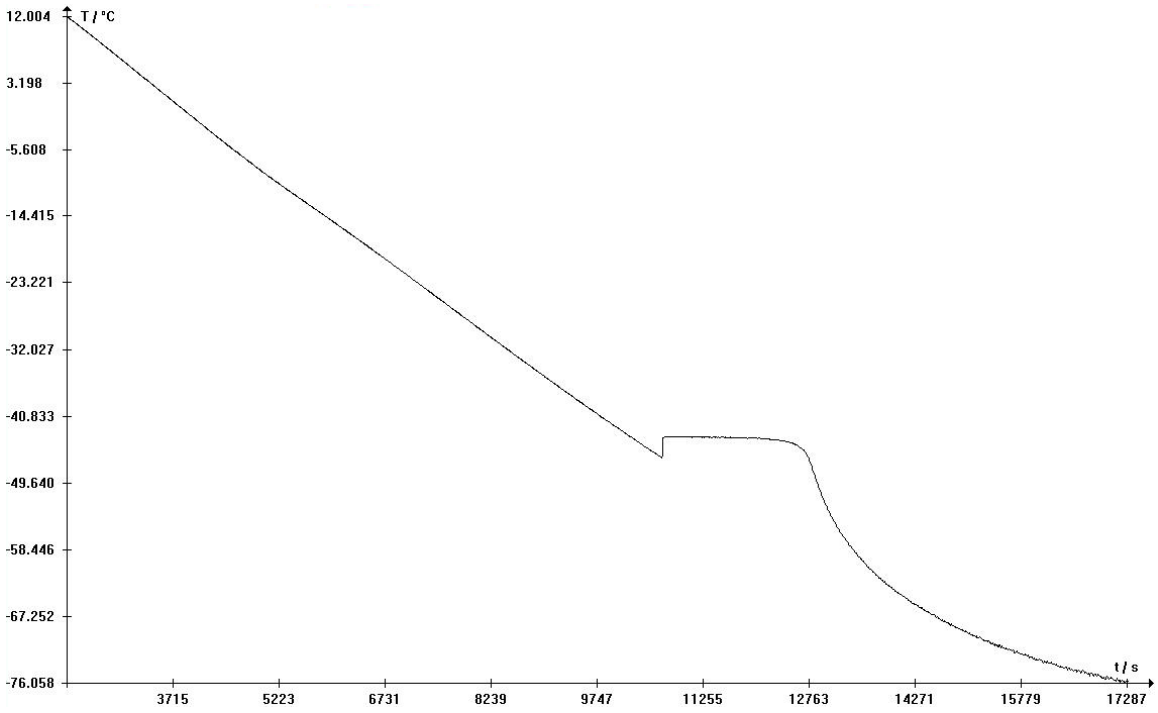

Figure 2-7: Nearly ideal cooling curve of a common organic solvent (γ-butyrolactone) determined at a cooling rate of -30 K h^{-1}.

Unfortunately, supercooling in the case of pure ILs and their mixtures is too large to get viable freezing points, even with the extrapolation procedure mentioned above. Therefore, in the case of ILs, melting points were investigated instead of freezing points. The observation of melting processes with this method suffers some drawbacks just as their determination with DTA/DSC, because it is very complicated to sufficiently mix a sample which contains a large amount of solid. Additionally, a solid, which is in the sample container, melts from the edge of the sample container to the centre, where the temperature sensor is usually placed. This sensor is then still surrounded by the solid, despite an already started melting process. But despite these theoretically based drawbacks, melting points of organic solvents determined with this method are in good agreement with the

corresponding freezing points and values from literature as well, along with a high reproducibility [107,108]. Therefore, in this work melting points of ILs were determined, because they are assumed to be less affected with errors than the corresponding freezing points.

To support the determination of phase transition points and to verify the results obtained from cooling and heating curves, the conductivity of the sample was simultaneously recorded with its temperature. Realization and evaluation of the determination of phase transition points is explained in Chap. 3.4.

3 Procedures and Methods

3.1 Materials

The ILs that were examined during this study were obtained from different sources. 1-Butyl-3-methylimidazolium tetrafluoroborate ($BMIBF_4$), 1-ethyl-3-methylimidazolium bis(trifluoromethylsulfonyl)imide ($EMINTf_2$), 1-ethyl-3-methylimidazolium dicyanamide (EMIDCA), 1-ethyl-3-methylimidazolium tetrafluoroborate ($EMIBF_4$), 1-methyl-3-propyl¬imidazolium iodide (MPII), and trimethylsulfonium dicyanamide (Me_3SDCA) were obtained from the research group of Prof. Wasserscheid[a] at the University of Erlangen-Nürnberg, a project partner within the DSSC-network-project, and synthesised by Schreiner[b] [57,113] respectively. 1-Ethyl-3-methylimidazolium trifluoromethanesulfonate (EMIOTf) was purchased from *Solvent Innovation*. 1-Butyl-1-methylpyrrolidinium tris-(pentafluoroethyl)trifluorophosphate (BMPlFAP), 1-butyl-1-methylpyrrolidinium bis-(trifluoromethylsulfonyl)imide ($BMPlNTf_2$), 1-butyl-1-methylpyrrolidinium trifluoro-methanesulfonate (BMPlOTf,), and 1-hexyl-3-methylimidazolium bis(trifluoromethyl-sulfonyl)imide ($HMINTf_2$) were obtained from *Merck*. Iodine was obtained from *Riedel-de Haën* with a purity of ≥ 99.8%.

NMR data (^1H, ^{13}C, ^{11}B, ^{19}F) of all used ILs do not show any impurities. Water contents of all ILs were determined via Karl-Fischer titration (KFT). If necessary the ILs were dried for several days at high vacuum (10^{-6} Pa) and elevated temperatures (app. 60 °C) to get water contents below 100 ppm.

[a] Thanks to Prof. Wasserscheid and co-workers;
[b] Thanks to C. Schreiner;

3.2 Diffusion Measurements

3.2.1 Measurement Setup

3.2.1.1 Measuring Cell

The cross section of the measuring cell (*G. Glass, Greensborough*) used for diffusion measurements is shown in Figure 3-1a, a horizontal projection of the measuring cell is shown in Figure 3-1b. The cell features a glass jacket, which is connected to a thermostat (RK 8 KP, *Lauda*, constancy of temperature: ± 0.05 °C) for temperature control, four NS-7 female ground joints, and one NS-10 female ground joint. Counter electrode (CE) and reference electrode (RE) are fed through two of the NS-7 female ground joints. One NS-7 female ground joint is supplied with a cock for working under inert gas and a temperature sensor is adapted to the last NS-7 female ground joint. The working electrode (WE) is fed through the NS-10 female ground joint, which is situated in the centre of the cell. The measuring cells were assembled, filled and sealed gas tight in a glove-box under Ar-atmosphere. For the measurement the cell was placed within a Faraday cage to prevent electrical interference which can strongly affect the measurement accuracy, due to very low measured currents. The height of the specific cells and the length of the specific working electrodes respectively vary slightly. Therefore, dedicated WE/cell combinations were introduced to minimize the necessary sample volume. Thus, the necessary sample volume could be reduced to < 3 mL.

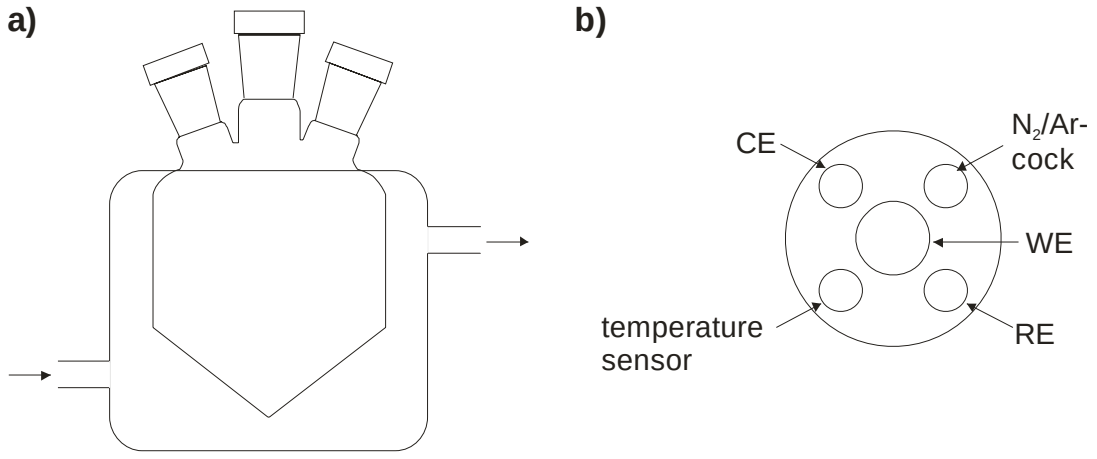

Figure 3-1: a) Cross section of the measuring cell, b) horizontal projection of the measuring cell; CE = counter electrode, RE = reference electrode, WE = working electrode.

The operating mode of the applied high precision temperature sensors (BetaTHERM Betacurve 30K6A1) is described more explicitly in Chap. 3.4.1.3. The temperature sensor is embedded in the tip of a short glass tube which is flexible connected with a NS-7 male ground joint. The feedthrough of the cables within the ground joint is sealed gas tight with epoxy resin. The completely assembled temperature sensor is shown in Figure 3-2. The four-channel thermometer used was constructed by Schweiger [103]. The temperature sensors were calibrated at the five different measurement temperatures vs. an ASL F-250 MkII thermometer (*Automatic Systems Laboratories, Milton Keynes*) to an accuracy of 0.01 °C vs. the ASL-thermometer. The constancy of temperature in the cells was better than ± 0.05 °C.

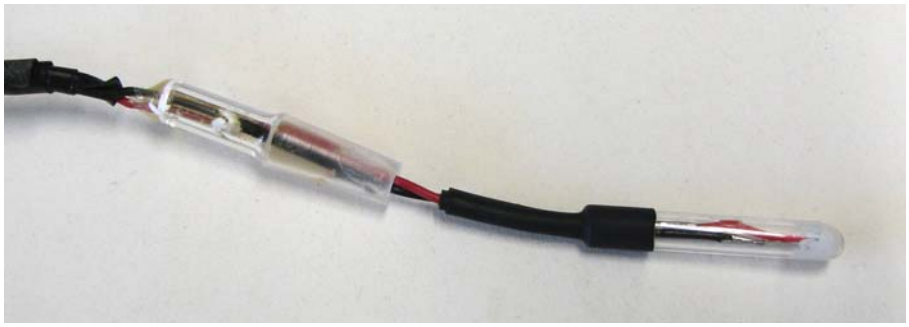

Figure 3-2: Assembled temperature sensor for diffusion measurements.

3.2.1.2 Working Electrodes

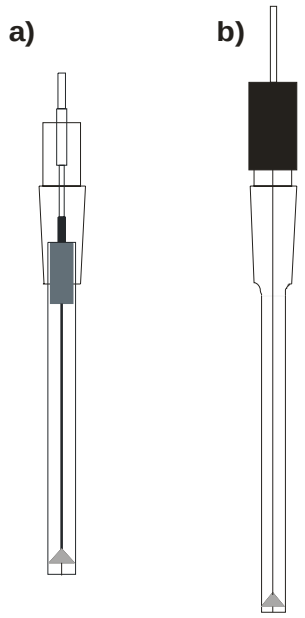

Figure 3-3: a) Pt disk UME (*BAS*), b) Pt disk UME (*G. Glass*).

Several Pt disk ultramicroelectrodes with varying electrode radii, purchased from different suppliers, were tested for application as working electrodes. The term ultramicroelectrode (UME) is generally used for electrodes having at least one dimension smaller than 25 µm. [89,114] There are several different types of UMEs, but the disk UME is by far the most often used type because fabrication of a disk embedded in an infinite insulating plane can be readily accomplished and the electrode surface can be easily renewed by polishing. Three Pt disk UMEs with nominal electrode radii of 0.3 µm, 0.5 µm, and 1.0 µm were purchased at *G. Glass, Greensborough*. A schematic drawing of these electrodes is shown in

Figure 3-3b. Three other Pt disk UMEs with nominal electrode radii of 5 µm were obtained from *Bioanalytical Systems, Inc., West Lafayette (BAS)*. Each of these three electrodes was fixed with epoxy resin into a NS-10 male ground joint (Figure 3-3a) to get a gas tight measurement setup and, due to a varying electrode length, a minimised sample volume as well.

Directly after receiving the UMEs from the supplier, the electrode radius and the quality of each UME was determined via scanning electrode microscopy (SEM). The determined electrode radii are slightly different from the radii given by the manufacturer. The electrode shapes are nearly perfect circular for the *BAS*-UMEs, the smaller UMEs from *G. Glass* show larger deviations from this ideal circular shape. A SEM micrograph of a brand-new 5 µm *BAS*-UME is shown in Figure 3-4a. To ensure high accuracy of diffusion measurements, the electrode radii and shapes of the applied UMEs were controlled several times during this work showing only little variation over the whole time period (Figure 3-4b).

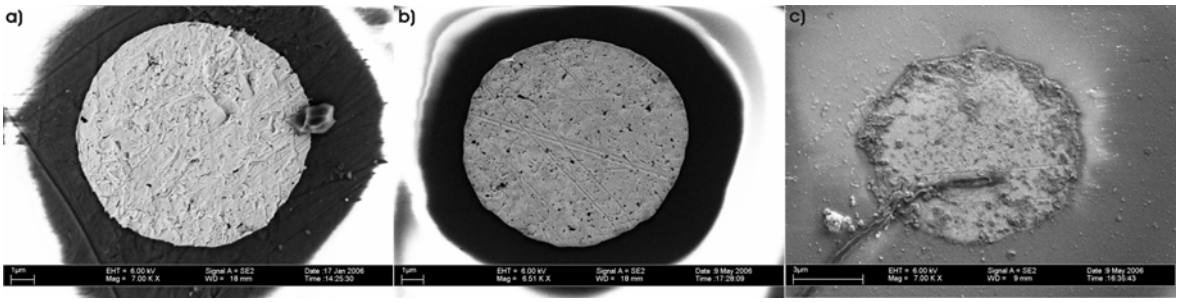

Figure 3-4: SEM micrographs of a a) brand-new 5 µm UME obtained from *BAS*, b) same electrode after over 200 steady-state measurements and about 20 polishing procedures, c) unpolished 5 µm UME after one measurement series in a binary mixture of ionic liquids.[a]

Prior to each new series of measurements (in general 6 to 9 individual measurements) the electrode surface was renewed by polishing with 0.05 µm alumina-water slurry (*Buehler Ltd., Lake Bluff)* on a polishing cloth (*Microcloth, Buehler Ltd., Lake Bluff*). To prevent variation of the electrode radius and shape, a 90° angle should be kept between polishing cloth and electrode surface. To remove adherent Al_2O_3 particles, the electrode surface was rinsed thoroughly with deionised water (Millipore), acetone p.a. and finally immersed for 1 min. in an ultrasonic bath. The polishing procedure alters the electrode surface and its

[a] Thanks to Dr. J. Stahl from the research group for semiconducting nanostructures of the University of Regensburg for SEM-measurements.

radius only slightly as it can be seen in Figure 3-4b, but this treatment is necessary due to residues and reaction products which adhere on the electrode surface (Figure 3-4c).

3.2.1.3 Counter and Reference Electrodes

Generally, diffusion measurements were performed with a three electrode arrangement. Schematic drawings of the applied counter and reference electrodes are shown in Figure 3-5. The individual components used to assemble the counter electrodes are shown in detail in Figure 3-5a. The counter electrode consists of a copper pin (A in Figure 3-5a) that is connected within the Teflon® screw (B) to a Pt-wire (C) with a diameter of 0.3 mm. A and C are glued in B with epoxy resin. The NS-7 male ground joint (F) is also glued with epoxy resin in the Teflon® ferrule (E) which features in its upper half a screw thread compatible to the screw thread of B. C is fed through a Teflon® tube (D) which is fed through F. The upper end of D is beaded and therefore pressed on to a ledge in E by screwing B in E which yields gas tight counter electrodes.

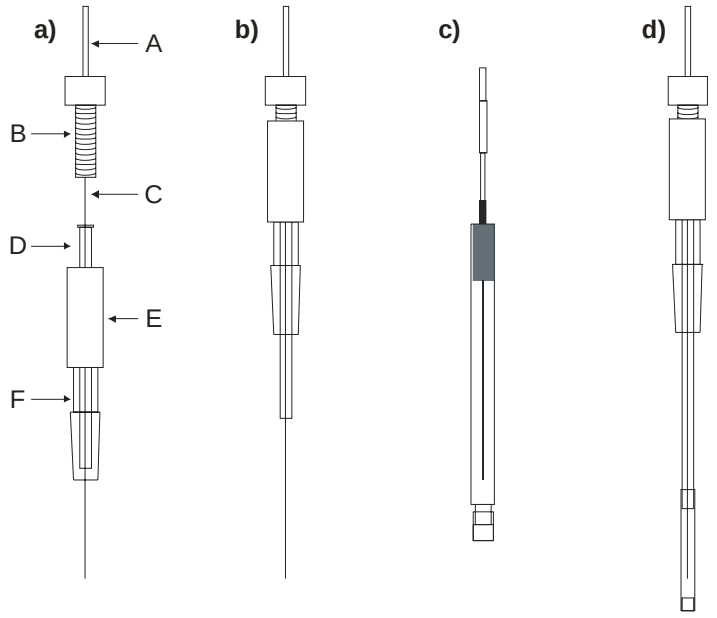

Figure 3-5: a) Fragmented counter electrode, b) assembled counter electrode, c) Ag/AgCl-reference electrode *BAS*, d) home-built reference electrode for non-aqueous electrolytes.

Three different reference or pseudo-reference electrodes were applied for diffusion measurements. An aqueous Ag/AgCl reference electrode from *BAS* (Figure 3-5c) was used for fast test measurements in aqueous solutions of $K_3Fe(CN)_6$. The Ag/AgCl reference electrode consists of a glass tube, tapering at the lower end where a Vycor® glass frit is

attached with a Teflon® heat shrink tube. The cell body is filled with a 3 M aqueous solution of NaCl in which an AgCl-coated Ag-wire is immersed. The electrode is stored in a 3 M NaCl solution between the measurements to prevent crystallisation of NaCl within the Vycor® glass frit and variation of the reference solution respectively. For measurements in non-aqueous electrolytes a modified version of an Ag/Ag^+-cryptate reference electrode (Figure 3-5d), originally proposed by Izutsu [64,115], was used. The solution within the reference electrode was prepared accordingly [116] by adding 25 µL of a solution containing 0.205 mol L^{-1} $AgNO_3$ and 0.410 mol L^{-1} Kryptofix 22 (*Merck*, for synthesis) in acetonitrile to 1 mL of the electrolyte which shall later be examined. The chosen design of this reference electrode (Figure 3-5d) resembles the design of the counter electrodes (Figure 3-5a and b) except for two important differences. Instead of a Pt-wire a 1 mm strong Ag-wire is connected to the copper pin within the Teflon® screw and a 2 cm long piece of a Teflon® heat shrink tube with a Vycor® tip is attached to the bottom of the Teflon® tube. For measurements in mixtures of ILs a Pt-wire was applied as pseudo-reference electrode, whose design is identical to the used counter electrodes (Figure 3-5a and b).

3.2.1.4 Potentiostat

For diffusion measurements the electrochemical workstation IM6 (*Zahner-Elektrik, Kronach*) was applied. The *Zahner* IM6 is equipped with a digitally controlled potentiostat and an impedance measuring unit. The potentiostat enables measurements in a voltage range of ± 4 V or ± 10 V with booster. The measuring range for the current stretches from ± 1 nA to ± 3 A. The measuring instrument is connected to a PC via a Flink-card and controlled by the Thales-software (*Zahner-Elektrik*).

3.2.2 Mass Transport and Current Response during Electrochemical Experiments at UMEs

Despite similar procedures of electrochemical experiments at UMEs and conventional electrodes, the electrochemical responses recorded during these experiments can differ greatly. Applying a potential to an electrode immersed in a quiescent solution which contains an electroactive species initiates a heterogeneous charge transfer at the electrode/electrolyte phase boundary. The beginning electrolysis generates a concentration

gradient between the electrode surface and the solution, which causes a mass transport to the electrode and away from the electrode respectively. If kinetic inhibition of the heterogeneous charge transfer reaction and chemical side reactions can be excluded, the current measured at all voltammetric electrodes depends on the modes of mass transport that are operant. In general, three different types of mass transport may occur during such electrochemical experiment:

- migration
- convection
- diffusion

As explained below, the predominant transport mode at UMEs is diffusion. Type and magnitude of the occurring diffusion processes are determined by the geometry and dimensions of the applied electrode.

In the following paragraphs the mass transport at a disk UME is considered for the case of chronoamperometry because analytical solutions for the case of cyclic voltammetry are more complicated due to the additional voltage dependence of the measured current. In the simplest form of a chronoamperometric experiment the potential at the electrode is stepped from a value where no electrolysis occurs to a value where a dissolved electroactive substance is completely oxidised or reduced at the electrode surface, resulting in a diffusion limited current.

The theoretical approach below follows more detailed explanations given in Refs. [89,114,117].

For an assumed reduction of the species O, of bulk concentration c_O^* at a conventional electrode, the boundary conditions are listed below:

$$c_O(x,0) = c_O^* \tag{3.1}$$

$$\lim_{x\to\infty} c_O(x,t) = c_O^* \tag{3.2}$$

$$c_O(0,t) = 0 \text{ for } (t > 0) \tag{3.3}$$

Eq. (3.1) is the initial condition: Previous to the beginning of the reaction the concentration c_O of O is identical to the bulk concentration c_O^* in the whole solution. Eq. (3.2) is a semi-infinite boundary condition which states that for infinite distance *x* to the electrode surface the concentration of O is identical to the bulk concentration during the measurement. The last boundary condition (Eq. (3.3)) is valid for application of a potential where the

concentration of O on the electrode surface is reduced to zero, resulting in diffusion limited currents. For conventional electrodes and the resulting planar diffusion, the diffusion limited faradaic current at the electrode surface is directly proportional to the concentration gradient:

$$-J_O(0,t) = \frac{i}{nFA} = D_O \frac{\partial c_O(x_0,t)}{\partial x} \tag{3.4}$$

where D_O is the diffusion coefficient of the species being electrolysed, A the area of the electrode, F the Faraday constant, and n the number of electrons per molecule oxidised or reduced. This concentration gradient causes the formation of a diffusion layer in front of the electrode, which gradually spreads into the solution (Figure 3-7a). To obtain a solution for the concentration gradient, Fick's second law for planar diffusion (Eq. (3.5)) must be utilized.

$$\frac{\partial c_O(x,t)}{\partial t} = D_O\left(\frac{\partial^2 c_O(x,t)}{\partial x^2}\right) \tag{3.5}$$

Solution of Eq. (3.5) with the appropriate boundary conditions and combination of the result with Eq. (3.4) yields a well known relation for the time dependent current, the Cottrell-equation (Eq. (3.6)):

$$i(t) = \frac{nFAD_O^{\frac{1}{2}} c_O^*}{\pi^{\frac{1}{2}} t^{\frac{1}{2}}} \tag{3.6}$$

The conditions for planar diffusion are only properly fulfilled if the electrode surface is large enough. In case of a disk UME, diffusion occurs in two dimensions, parallel to the electrode and perpendicular to the electrode. An overview of the geometry of the diffusion for a disk UME is given in Figure 3-6.

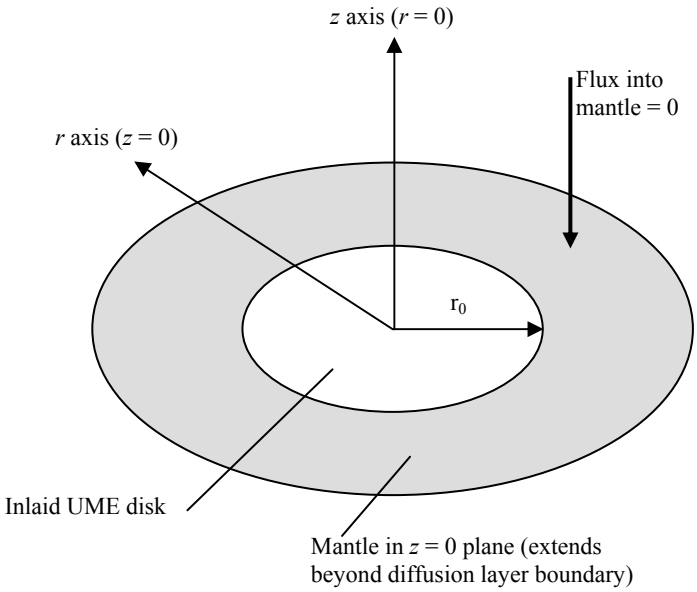

Figure 3-6: Geometry of diffusion at a disk UME; according to Ref. [89].

Therefore, the current density is not uniform across the electrode surface, but greater at the edge. Electroactive species in the region around the electrode may easily reach that area. The extent of these edge effects varies with the duration of the measurement and the electrode radius. Heinze [114] computed concentration profiles at disk electrodes with varying radii recorded after 1 s measuring time which are shown in Figure 3-7c-e. These concentration profiles clearly show that the semi-infinite planar diffusion at conventional disk electrodes is gradually transformed with decreasing electrode radius into a semi-infinite hemispherical diffusion at disk UMEs. A similar effect is caused by longer measurement times. The transformation to a semi-infinite hemispherical diffusion leads to a larger solvent volume from were electroreactants have access to the electrode surface. This enhances the number of electroreactants reaching the electrode and therefore the mass transport as well. The growing volume means that at finite times the particle flux into and out of the volume becomes stationary and the diffusion layer stops growing (Figure 3-7b). [89,114,117]

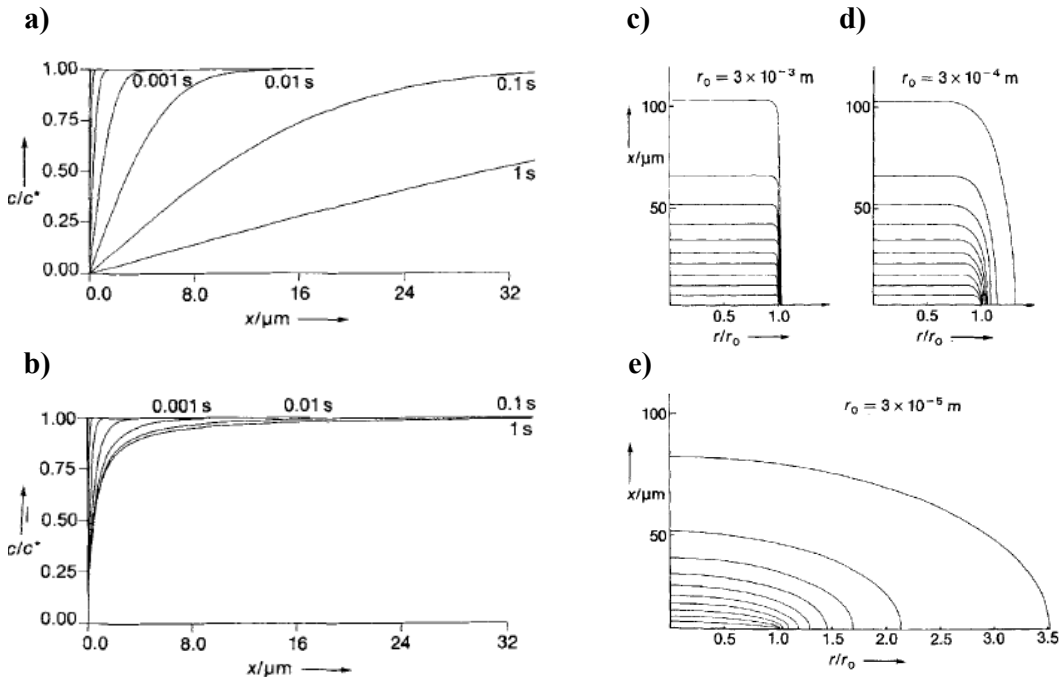

Figure 3-7: Concentration profiles of diffusion layers ($D = 10^{-6}$ cm^2 s^{-1}) in a chronoamperometric experiment for different times *t* after application of a potential step; a) semi-infinite planar diffusion; b) spherical diffusion for a spherical UME with $r_0 = 0.5$ µm.; c/c^* = normalised concentration, x = distance from electrode. c-d) Normalized calculated concentration profiles c/c^* calculated for disk electrodes with different radii ($r_0 = 3{\cdot}10^{-3}$, $3{\cdot}10^{-4}$, $3{\cdot}10^{-5}$ m; $D = 10^{-6}$ cm^2 s^{-1}) 1 s after start of a chronoamperometric experiment; Concentration curves are separated by 0.1 of a concentration unit, x = distance perpendicular to the electrode. From Ref. [114].

The concentration gradient for this semi-infinite hemispherical diffusion cannot be described with Eq. (3.5), which was valid for the case of a planar diffusion. Due to the diffusion geometry shown in Figure 3-6, the diffusion equation for a species O and the case of semi-infinite hemispherical diffusion is written as follows [89]:

$$\frac{\partial c_O(r,z,t)}{\partial t} = D_O\left[\frac{\partial^2 c_O(r,z,t)}{\partial r^2} + \frac{1}{r}\frac{\partial c_O(r,z,t)}{\partial r} + \frac{\partial^2 c_O(r,z,t)}{\partial z^2}\right] \tag{3.7}$$

where r is the position normal to the axis of symmetry at $z = 0$, and z is the distance normal to the electrode surface at $r = 0$. For solution of Eq. (3.7) five boundary conditions are needed, where Eq. (3.8), (3.9), (3.10), and (3.12) all have the same meaning as the corresponding boundary conditions for the planar diffusion which are listed above, except the additional respect to the radial direction of the diffusion. The fourth condition

(Eq. (3.11)) comes from the recognition that there can be no flux of O into or out of the glass mantle. [89]

$$c_O(r,z,0) = c_O^* \tag{3.8}$$

$$\lim_{r\to\infty} c_O(r,z,t) = c_O^* \tag{3.9}$$

$$\lim_{z\to\infty} c_O(r,z,t) = c_O^* \tag{3.10}$$

$$\left(\frac{\partial c_O(r,z,t)}{\partial z}\right)_{z=0} = 0 \text{ for } (r > r_0) \tag{3.11}$$

$$c_O(r,0,t) = 0 \text{ for } (r \le r_0, t > 0) \tag{3.12}$$

The derivation of the diffusion limited current at a disk UME is extensive and very mathematically demanding. Therefore, only the results of this derivation are presented and discussed in the following paragraph. The first rigorous solution for the chronoamperometric current response at a disk UME was given by Aoki and Osteryoung [118,119]. They expressed the current *i* as a function of the dimensionless parameter τ.

$$i = \frac{4nFAD_O c_O^*}{\pi r_0} f(\tau) \tag{3.13}$$

with:
$$\tau = \frac{4D_O t}{r_0^2} \tag{3.14}$$

where *n* is the number of electrons per molecule oxidised or reduced, *F* the Faraday constant, *A* the area of the electrode, D_O the diffusion coefficient and c_O^* the bulk concentration of the species being electrolysed, r_0 the electrode radius, and *t* the measuring time.

The function $f(\tau)$ was determined as two series applicable in different domains of τ. At short times ($\tau < 1$):

$$f(\tau) = 0.88623\tau^{-\frac{1}{2}} + 0.78540 + 0.094\tau^{\frac{1}{2}} \tag{3.15}$$

whereas at long times ($\tau > 1$):

$$f(\tau) = 1 + 0.71835\tau^{-\frac{1}{2}} + 0.005626\tau^{-\frac{3}{2}} - 0.00646\tau^{-\frac{5}{2}} \tag{3.16}$$

The two versions of $f(\tau)$ overlap for intermediate values of τ, i.e. in the range $0.82 < \tau < 1.44$. [119]

For sufficiently long times the exact solution given by Aoki and Osteryoung (Eq. (3.16)) can be reduced to Eq. (3.17) [120,121] which is much easier to handle. For $\tau > 3.2$ the deviation from the exact solution is less than 1 %. [120]

$$i = \left(\frac{8}{\pi^2}\right)\frac{nFAD_O^{\frac{1}{2}}c_O^*}{\pi^{\frac{1}{2}}t^{\frac{1}{2}}} + 4nFD_O c_O^* r_0 \tag{3.17}$$

Shoup and Szabo [122] were able to derive a relation for the current which is valid for all τ with deviations < 0.6% [119].

$$f(\tau) = 0.7854 + 0.8862\tau^{-\frac{1}{2}} + 0.2146e^{-0.7823\tau^{-\frac{1}{2}}} \tag{3.18}$$

The current-time relationship for a disk UME (Eq. (3.13)) can be separated into three time regimes. If the time scale of the measurement remains short, so that the diffusion layer remains thin compared to r_0, the radial diffusion stays negligible and the diffusion has exclusive semi-infinite planar character. Therefore, the initial current after a large amplitude potential step is given by the Cottrell equation [89,114,117]:

$$i(t) = \frac{nFAD_O^{\frac{1}{2}}c_O^*}{\pi^{\frac{1}{2}}t^{\frac{1}{2}}} = \lim_{\tau \to 0}\frac{4nFAD_O c_O^*}{\pi r_0} f(\tau) \tag{3.19}$$

As measurement proceeds, an intermediate regime is reached where the diffusion layer thickness is comparable to r_0 and the radial diffusion becomes increasingly important. The current is higher than for a continuously proceeding pure planar diffusion. At still longer times, when the diffusion field is much larger than r_0, the diffusion is pure hemispherical and the current approaches a constant steady state i_{ss} [89,114,117]:

$$i_{ss} = \frac{4nFAD_O c_O^*}{\pi r_0} = 4nFD_O c_O^* r_0 = \lim_{\tau \to \infty} \frac{4nFAD_O c_O^*}{\pi r_0} f(\tau) \qquad (3.20)$$

In contrast to chronoamperometry where a potential step from an initial to a final value is applied to the working electrode, in voltammetry the potential changes linearly with time. Starting from an initial value the potential is varied linearly until a reverse potential is reached where the direction of the sweep is changed and the potential is led back to its initial value. During the experiment the current is recorded as function of the applied potential or with known sweep rate as function of time. The experimental time scale is defined by the potential sweep or scan rate *v*.

Application of UMEs in cyclic voltammetry generates, in principle, the same phenomena as for the chronoamperometric experiment. The transition to the stationary state is achieved by reducing the scan rate and is accelerated by smaller electrode radii. That means for high *v* values the shape of the recorded cyclic voltammograms resembles the shape of cyclic voltammograms recorded at conventional electrodes. With reducing *v* the shape becomes sigmoid such as for polarograms or cyclic voltammograms recorded at a rotating disk electrode.

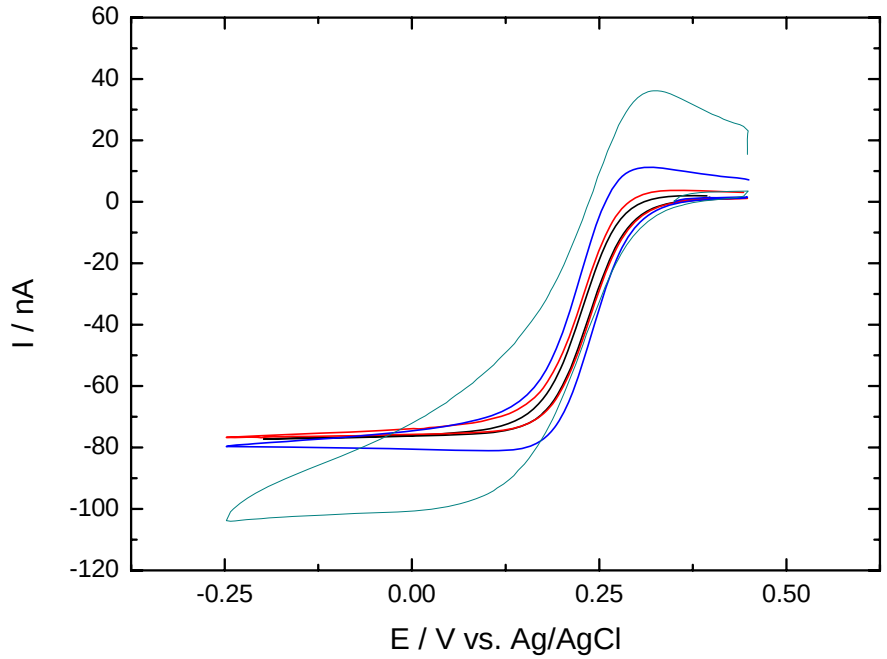

Figure 3-8: Cyclic voltammograms of 0.005 mol L^{-1} $K_3Fe(CN)_6$, 0.5 mol L^{-1} KCl in H_2O at varying scan rates; *v*: (—) 1 mV s^{-1}, (—) 2 mV s^{-1}, (—) 10 mV s^{-1}, (—) 100 mV s^{-1}. Measurements recorded at a Pt disk UME (r_0 = 50 µm, *BAS*).

Under steady-state conditions, the current is time independent and the scan rate no longer influences the shape and size of the recorded voltammogram. For these conditions and for the simple case of a reversible electrode reaction, the current of the forward scan is given by [117]:

$$i = \frac{4nFAD_O c_O^* r_0}{1 + \exp[(-nF/RT)(E^{0'} - E_{app})]} \tag{3.21}$$

The reverse wave is not observed under these conditions because the products formed at the electrode leave the vicinity of the electrode at enhanced rate for the same reasons as the inward flux to the electrode is so large. Therefore, the current on the reverse scan is identical to the current of the forward scan. The diffusion limited steady-state current corresponds to the values obtained for the stationary current in chronoamperometry and is given by Eq. (3.22). [89,114,117]

$$i_{ss} = 4nFD_O c_O^* r_0 \tag{3.22}$$

As stated above, the predominant mode of mass transport at UMEs is diffusion and is based on the transition to semi-infinite hemispherical diffusion. In the case of disk UMEs, and the enhanced diffusive mass transport, the flowing current is very small, on the order of nano-amperes. The measurement times are comparatively short resulting in only very small concentration differences and thus density differences. Therefore, with adequate temperature regulation of the measurement cell the impact of convection on the mass transport is negligible. The third potential mode of mass transport is migration, which preferably occurs in highly resistive media. In the case of conventional electrodes a large excess of supporting electrolyte is used to inhibit migration. Oldham [123] showed that for UMEs the quantitative ratio of supporting electrolyte to electroreactant can be reduced to 1:1 without any significant distortion of the steady-state voltammogram. Therefore, the impact of migration on mass transport is also negligible for the systems examined during this work.

UMEs feature two additional advantages which are relevant for their application during this work. The first advantage is an almost negligible capacitive current i_c, providing a good i_F / i_c ratio for both chronoamperometry and cyclic voltammetry. For chronoamperometry i_c is given by Eq. (3.23) [114,117]:

$$i_c = \frac{\Delta E}{R} \exp\left(-\frac{t}{RC_d} \right) \tag{3.23}$$

where ΔE is the applied potential step, R the resistance of the electrolyte solution and C_d the double layer capacity. According to Eq. (3.23) i_c falls exponentially over time because $RC_\mathrm{d} \sim r_0$ the process is accelerated for decreasing electrode radii. For cyclic voltammetry i_c is given by Eq. (3.24), where E_i is the initial potential. Eq. (3.24) can be simplified to Eq. (3.25) at low and medium scan rates v [114,117].

$$i_c = \left[\left(\frac{E_i}{R} - vC_d \right) \exp\left(-\frac{t}{RC_d} \right) \right] + vC_d \tag{3.24}$$

$$i_c = vC_d \tag{3.25}$$

The second advantage is the low impact of the ohmic resistance of the electrolyte on the electrochemical experiment. According to experimental [124] and theoretical [125] studies the ohmic potential drop is exclusively dependent on the properties of the electrolyte for the case of steady-state conditions (Eq. (3.26) [114]).

$$iR = nFDc^* \kappa^{-1} \tag{3.26}$$

The iR drop in the case of IL based electrolytes ($D = 10^{-7}$ cm^2 s^{-1}, $c^* = 0.05$ mol L^{-1}, specific conductivity $\kappa \geq 0.6$ mS cm^{-1}) which were examined in Chap. 4 is according to Eq. (3.26) 0.8 mV and therefore almost negligible.

3.2.3 Testing of Different Electrode Radii, Electrode Setups and Measuring Methods

To find an optimised measurement setup for determination of diffusion coefficients in ILs and their binary mixtures, Pt disk UMEs with four different electrode radii, as described in Chap. 3.2.1.2, were tested in a solution of 0.00604 mol L^{-1} ferrocene (*ABCR*, purity of 100%) and 0.199 mol L^{-1} tetraethylammonium tetrafluoroborate ($TEABF_4$, *Merck*, selectipur®) in acetonitrile (AN, *Merck*, selectipur®). The results obtained from the two different measurement methods explained in Chap. 3.2.2, steady-state cyclic voltammetry

and chronoamperometry, were compared as well as the application of three different measurement setups; two three electrode measurement setups, with an Ag/Ag^+-cryptate reference electrode and a Pt wire as pseudo-reference electrode respectively, and a two electrode measurement setup.

Reference electrodes are necessary to control the applied potential during voltammetric and chronoamperometric measurements for which they have to fulfil several requirements [126]. To inhibit appearance of liquid junction potentials and to prevent contamination of the measuring solution with traces of solvent or salt, the solution within the reference electrode has to be as similar as possible to the measuring solution. That is why an Ag/Ag^+-cryptate reference electrode [64,115] was used for measurements in organic electrolytes. Due to difficult and time consuming handling of an iodine/iodide reference electrode for measurements in ILs [127-130], and the above mentioned problem of contamination of the investigated ILs with traces of organic solvent or water by application of the Ag/Ag^+-cryptate or a common aqueous reference electrode, the application of a Pt wire as pseudo-reference electrode was examined as well as the application of a two electrode measurement setup. Utilisation of a two electrode measurement setup and a Pt wire pseudo-reference electrode respectively are common and adequate procedures for steady state measurements at UMEs in ILs [131,132] due to the almost negligible IR-drop (see Chap. 3.2.2 or Refs. [89,114,117]).

To exemplify the relation between limiting current and electrode radius, four steady-state cyclic voltammograms recorded at Pt disk UMEs with four different electrode radii are shown in Figure 3-9.

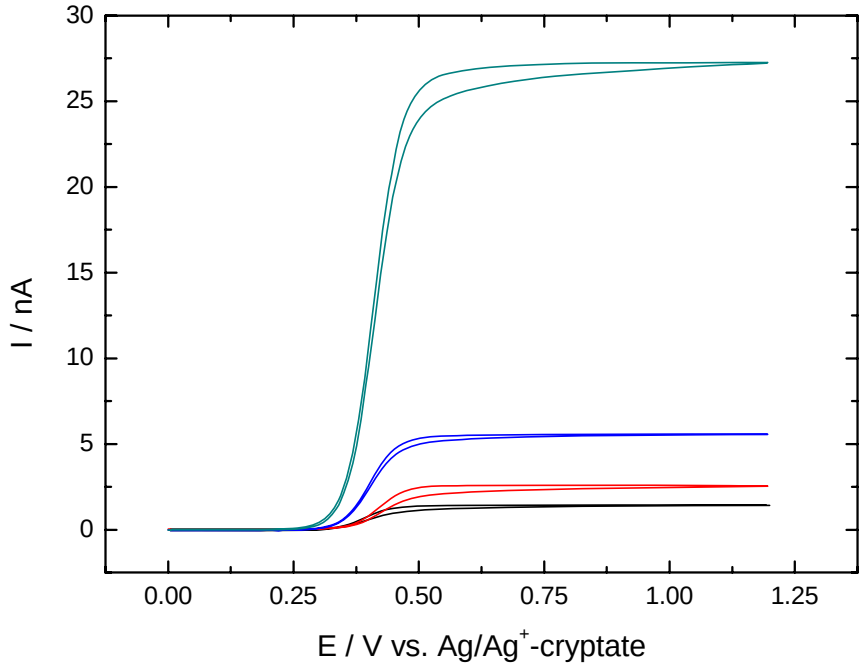

Figure 3-9: Comparison of steady-state cyclic voltammograms recorded at Pt disk UMEs with four different radii in a solution of 0.00604 mol L^{-1} ferrocene and 0.199 mol L^{-1} $TEABF_4$ in AN using an Ag/Ag^+-cryptate reference electrode; r_0: (—) 0.3 µm, (—) 0.5 µm, (—) 1 µm, (—) 5 µm.

The diffusion coefficients of ferrocene in AN show, within the measurement accuracy, a very good agreement for the four different electrode radii and with the values from literature (Table 3-1). Reproducibility of diffusion coefficients within one measurement series was typically over 98% for all electrodes, but for several consecutive measurement series, including polishing after each series, it stayed only for the 5 µm electrodes at a comparably high value (> 97%).

Table 3-1: Diffusion coefficients of ferrocene in a solution of 0.00604 mol L^{-1} ferrocene and 0.199 mol L^{-1} $TEABF_4$ in AN determined at electrodes with different radii and compared with values from literature.

$r_0 \cdot 10^4$ [cm]	$D \cdot 10^5$ [$cm^2\ s^{-1}$]	$D_{lit} \cdot 10^7$ [$cm^2\ s^{-1}$]
0.3	2.06	2.4 [124] 2.17 [120]
0.5	2.34	
1	2.40	
5[a]	2.31	
5[b]	2.45	
5[c]	2.44	

[a] Two electrode setup.
[b] Three electrode setup with a Pt wire as pseudo-reference electrode.
[c] Three electrode setup with an Ag/Ag^+-cryptate reference electrode.

As mentioned above, steady-state cyclic voltammograms were recorded with a three electrode measurement setup with an Ag/Ag^+-cryptate reference electrode or a Pt wire as pseudo-reference electrode and with a two electrode measurement setup respectively. The determined diffusion coefficients showed, within the measurement accuracy, a very good agreement for the three different measurement setups (Table 3-1) but their reproducibility and the reproducibility of the shapes of the recorded cyclic voltammograms were best for the three electrode measurement setup with an Ag/Ag^+-cryptate reference electrode, followed by the three electrode measurement setup with a Pt wire as pseudo-reference electrode.

Chronoamperometric measurements were also performed with electrodes of different radii and with different measuring setups. But here the main focus was set on application of three different methods for evaluating the recorded current-time curves. Method one is similar to evaluation of steady-state cyclic voltammograms. After a sufficiently long time, the limiting current of the chronoamperometric measurements shown in Figure 3-10, is assumed to be strictly faradaic and diffusion controlled and therefore Eq. (3.20) is valid.

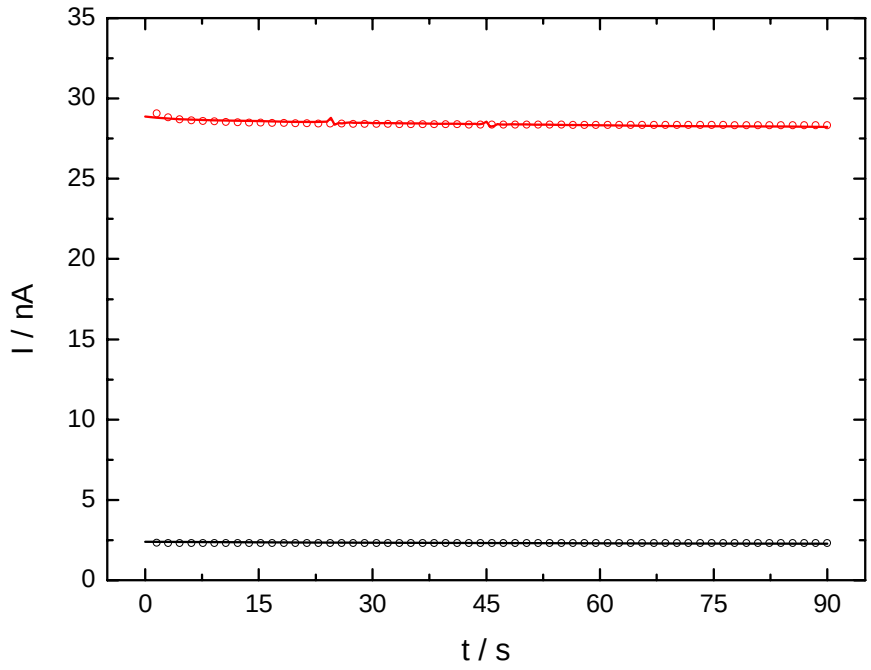

Figure 3-10: Current-time curves recorded during chronoamperometric measurements in a solution of 0.00604 mol L^{-1} ferrocene and 0.199 mol L^{-1} $TEABF_4$ in AN at a 0.5 µm (─) and a 5 µm (─) Pt disk UME using an Ag/Ag^+-cryptate reference electrode; (○) and (○) corresponding fits of the current according Eq. (3.18).

A second approach is also shown in Figure 3-10, where diffusion coefficients were determined by non-linear-regression of the data according to Eq. (3.18). The third method is shown in Figure 3-11, where according to Eq. (3.17) the diffusion coefficient *D* can be determined from the y-axis intercept of a plot of *i* vs. $t^{-1/2}$.

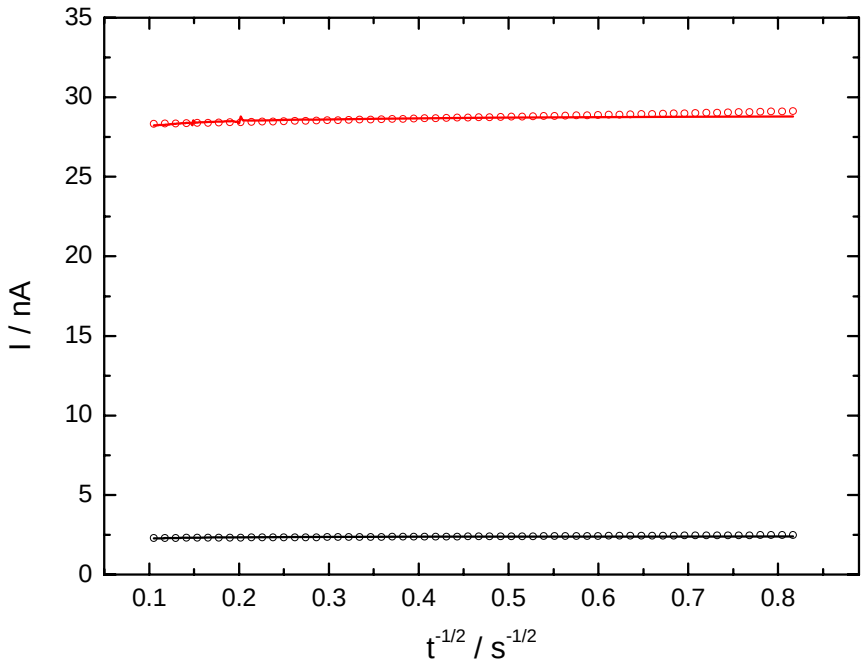

Figure 3-11: Plot of the current recorded during chronoamperometric measurements in a solution of 0.00604 mol L^{-1} ferrocene and 0.199 mol L^{-1} $TEABF_4$ in AN at a 0.5 µm (─) and a 5 µm (─) Pt disk UME using an Ag/Ag^+-cryptate reference electrode vs. $t^{-1/2}$; (○) and (○) corresponding fits of the current according Eq. (3.17) vs. $t^{-1/2}$.

In general, the diffusion coefficients of ferrocene in acetonitrile determined with chrono-amperometry showed, within the measurement accuracy, a very good agreement with the diffusion coefficients determined with steady-state cyclic voltammetry (typically > 95%) and therefore with the values from literature too (Table 3-2). The results of three different evaluation methods showed also very good agreement (> 99%) among each other. Similar to steady-state cyclic voltammetry, reproducibility of the limiting currents was best for the three electrode measurement setup with an Ag/Ag^+-cryptate reference electrode and a 5 µm electrode as working electrode.

Table 3-2: Diffusion coefficients of ferrocene in a solution of 0.00604 mol L^{-1} ferrocene and 0.199 mol L^{-1} $TEABF_4$ in AN determined with chronoamperometry at electrodes with 5 µm nominal radius and compared with values from literature.

Reference electrode	$D \cdot 10^5$ [$cm^2\ s^{-1}$]	$D_{lit} \cdot 10^7$ [$cm^2\ s^{-1}$]
Ag/Ag^+-cryptate	2.41 [a]	2.4 [124] 2.17 [120]
Ag/Ag^+-cryptate	2.42 [b]	
Ag/Ag^+-cryptate	2.42 [c]	
Ag/Ag^+-cryptate	2.42 [c]	
Pt-wire	2.53 [c]	
-	2.42 [c]	

[a] Evaluation according Shoup and Szabo (Eq. (3.18)).
[b] Evaluation according Baur and Wightman (Eq. (3.17)).
[c] Assumption of a time independent diffusion controlled current and evaluation according Eq. (3.20).

To sum it up, the best results for both, steady-state cyclic voltammetry and chrono-amperometry were achieved with an Ag/Ag^+-cryptate reference electrode and a 5 µm electrode as working electrode. As mentioned above, application of a reference electrode in ILs causes some problems, hence for further measurements a Pt wire was used as pseudo-reference electrode instead the Ag/Ag^+-cryptate reference electrode. Generally, chrono-amperometry is a faster method than steady-state cyclic voltammetry, but the shape of the cyclic voltammograms gives some additional and useful information, e.g. the location of the reaction on the potential scale, the occurrence of additional electrode processes and electrode passivation, which can provide additional direction on reliability and reproducibility of the determined values.

Due to that, for determination of diffusion coefficients in ionic liquids, steady-state cyclic voltammetry was conducted at a three electrode setup with a Pt wire as pseudo-reference electrode and a 5 µm Pt disk UME.

3.2.4 Error Estimation

The following error calculation was performed for cyclic voltammetry and the three electrode arrangement with Pt wire as pseudo-reference electrode according to the maximum error technique. If there are multiplicative variables, their relative errors add up. This is for example the case for the working equation for cyclic voltammetry (Eq. (3.22)).

Eq. (3.22) contains three parameters, the concentration, electrode radius, and limiting current, which are potentially afflicted with errors. The error of the concentration is

negligible due to highly accurate weighing and density determination. The radii of the electrodes were determined via SEM-measurements, with an estimated error of 2%. The error for the measured limiting current was estimated to 3%, which is the average maximum error for the limiting current of several consecutive measurements including polishing procedures.

The maximum error of the diffusion coefficient is therefore:

$$\frac{\Delta D}{D} = \frac{\Delta r}{r} + \frac{\Delta i_{SS}}{i_{SS}} = 5\% \tag{3.27}$$

3.3 Conductivity Measurements

3.3.1 Measurement Setup

3.3.1.1 Thermostat Assembly

Temperature control was ensured by using the thermostat assembly which is described in detail in Refs. [60,61]. The thermostat consists of a thermal insulated bath of about 60 L silicone oil (Baysilon M5®, *Bayer*) in which a mechanical stirrer, a heat exchanger, a source of heat, a platinum resistance thermometer, and the measuring cell are immersed. Via the heat exchanger a cryostat (HM 90W, *Holzwarth & Co.*), which acts as cold bath, is coupled to the thermostat. A thorough mixing of the bath is ensured by a mechanical stirrer. The temperature is controlled by a PID controller joined to an a.c. bridge which is connected to the platinum resistance thermometer. The error voltage of the bridge is used for temperature measurement and, via the PID controller, for controlling heating power of the heating source as well. [61] With this assembly a temperature stability of ± 2 mK was achieved. The temperature of the thermostat bath and simultaneous measurement temperature was determined by an ASL F-250 MkII thermometer (*Automatic Systems Laboratories, Milton Keynes*). The lower limit of the working range at about -60 °C is set by the insufficient cooling power of the cryostat, the upper limit at about 50 °C by the flammability of ethanol, which is used a cooling liquid.

3.3.1.2 Conductivity Cells

The used conductivity cells are already described in Ref. [134]. The conductivity cells consist of a two-electrode arrangement and feature a small sample volume of only 2-3 mL, which is very important for investigation of expensive electrolytes such as ILs. Due to the cell geometry the cell constants are independent of the fill level and due to the small temperature coefficient of the used Pyrex®-glass, they are assumed to be temperature independent [61,133]. The cell constants are listed in Table 3-3, an example of the conductivity cells is shown in Figure 3-12. The cells were filled and sealed gas tight in a glove-box under Ar-atmosphere. For fast and easy measurements, a mounting was used that fits in the top cover of the thermostat bath and can hold up to 10 conductivity cells.

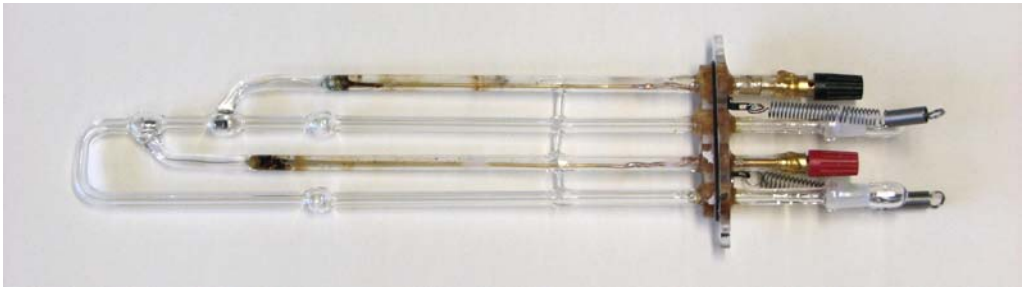

Figure 3-12: Conductivity cell for conductivity measurements.

3.3.1.3 Conductivity Bridge

The exact design of the used conductivity bridge is described by Wachter et al. [60]. The conductivity bridge is made up of a symmetrical *Wheatstone*-bridge with a Wagner earth, a resistance decade and a sine generator, which feds the measuring bridge with alternating voltage and enables measurements in a frequency range from 30 Hz to 10 kHz. The measuring cell represents a branch of the *Wheatstone*-bridge. The electrical equivalent circuit of the measuring cell consists of a series connection of the ohmic resistance of the electrolyte R_E and the double-layer capacity at the phase boundary C_d. Opposed to it is the reference impedance which is, due to practical reasons, made up of parallel connection of the resistance decade and a capacitor. The balancing conditions are fulfilled, if:

$$R_E = \frac{R}{1+\left(\omega R_E C_d\right)^{-2}} \tag{3.28}$$

$$C = \frac{C_d}{1+\left(\omega R_E C_d\right)^{-2}} \tag{3.29}$$

where R is the resistance and C the capacity of the balanced measuring bridge. $(\omega R_E C_d)^{-2}$ becomes negligibly small and therefore R to R_E, by platinisation of the electrodes due to the enlarged electrode surface and C_d respectively. Actually a slight frequency dependence of R_E in ω^{-1} was found.

3.3.2 Calibration of Conductivity Cells

Since some measuring cells needed extensive repairs, a calibration of these measuring cells was necessary. Instead of using internal references, a direct calibration via aqueous KCl-solutions was performed as no reliable reference cell with a cell constant of similar magnitude was available.

The diluted aqueous KCl-solutions of known concentrations were made by adding weighed KCl (*Merck*, supra pure) under nitrogen into tri-distilled, gas-free weighed water. The used scale (AE240 range I d = 0.01 mg, II d = 0.1 mg, *Mettler*) has an accuracy of ± 0.01 mg. The equivalent conductivity $\Lambda_{KCl}^{25\,°C}$ of KCl can be calculated according to a conductivity equation given by Barthel et al. [133]:

$$\Lambda = 149.873 - 95.01c^{1/2} + 38.48c\log c + 183.1c - 176.4c^{3/2} \tag{3.30}$$

where c is the concentration in mol L^{-1}. The electrolyte resistance R_E is obtained by extrapolation of the frequency dependent resistance values R_v to infinite frequencies, as explained in Chap. 3.3.3. To get the exact electrolyte resistance R_{KCl}, R_E is corrected by subtraction of the supply line resistance, which was determined to be 0.3 Ω for all measuring cells. The cell constants B were calculated with the determined resistance R_{H_2O} of the applied water according to Eq. (3.31).

$$B = \Lambda c\left(\frac{1}{R_{KCl}} - \frac{1}{R_{H_2O}}\right)^{-1} \tag{3.31}$$

Every cell was calibrated with three 0.01 M KCl-solutions at 25 °C. The cell constants for each measuring cell show maximum errors which are based on errors of KCl concentration and temperature regulation and inaccuracies during extrapolation of the frequency dependent R_v values as well. The extent of these specific errors can only be estimated; therefore a rigorous calculation of errors is not feasible. The calculated mean values of the cell constants are listed in Table 3-3 along with the corresponding maximum errors and relative errors which were obtained by deviations of the results of the three measurements.

Table 3-3: Cell constants of the conductivity cells and the corresponding maximum and relative errors.

Cell	B [cm^{-1}]	ΔB [cm^{-1}]	$\frac{\Delta B}{B}100$ [%]
2	38.45	0.13	0.3
3	48.13	0.15	0.3
4	57.9	0.2	0.4
5	62.63	0.14	0.2
6	91.0	0.2	0.2
7	47.33	0.14	0.3
8	52.5	0.2	0.4

The determined errors are much larger than the errors that were originally determined for these cells by Carl [134]. These may be due to inappropriate storing and handling of the cells in the past and insufficient platinisation of the electrodes which resulted in stronger frequency dependence as well. The cell constants are assumed to be temperature independent according to results of previous studies [61,133].

3.3.3 Data Editing and Evaluation

As explained in Chap. 3.3.1.3, due to the applied parallel connection of the reference impedance, a dependency of R_v in ω^{-2} was expected. Instead of that, a dependency of R_v in ω^{-1} was found. Therefore the frequency dependent R_v values were analysed according to Eq. (3.32) and extrapolated to infinite frequencies to get the real electrolyte resistance R_E from the interception with the y-axis.

$$R_v = R_E + b\nu^{-1} \tag{3.32}$$

The obtained value for R_E was corrected by the sum of the supply line resistances. From the determined R_E values the specific conductivities κ were calculated with the previously determined cell constants B according to the following equation:

$$\kappa = \frac{B}{R_E} \tag{3.33}$$

Due to their magnitude and their impact on the determined specific conductivities, the relative errors of the cell constants are also assumed to be the relative errors of the specific conductivities. Other specific errors, such as inaccuracies during extrapolation of the frequency dependent R_v values and errors of temperature regulation, can only be estimated and are assumed to be negligible. In general, purities of the examined ILs are much lower compared to organic solvents and inorganic salts which can be obtained with very high purities. Therefore the required measuring accuracies for examination of ILs are also lower. The applied measurement setup is consequently appropriate.

3.4 Conductivity-Temperature Measurements

3.4.1 Measurement Setup

3.4.1.1 Thermostat Assembly

The thermostat used for conductivity-temperature measurements is similar to the one used for stationary conductivity measurements, which is described in Chap. 3.3.1.1. The major difference is the applied cryostat (unistat 390w, *Huber*, *Offenburg*) which is able to carry out heating- and cooling-experiments with variably adjustable heating- and cooling-rates as well as with adjustable heating power and cooling efficiency. A further advantage of this cryostat is that it can be used to set up measurement programs, consisting of several cooling- and heating-experiments, enabling, along with the integrated safety installations [103], automated operating for several days. Application of temperature gradients on samples is necessary to determine the phase transition points. Therefore the control device with the PID controller is only used for calibration of the temperature sensors, which is performed at constant temperature. Due to the applied cooling liquid (Thermofluid DW-Therm M90.200.02, -90 °C to +200 °C, *Huber*), the lower limit of the working range at about -80 °C is set by the cooling power of the cryostat, the upper limit at 65 °C was set by the author. Higher measurement temperatures up to 120 °C would be possible, but then the thermal expansion of the silicone oil within the measurement thermostat would have to be considered.

3.4.1.2 G(t)-T(t)-Measuring Cells

The G(t)-T(t)-measuring cells were constructed to obtain another indication besides T(t)-curves for phase transitions, see Chap. 2.3, especially for electrolyte solutions and blends of ILs. With some precautions they also yield conductivities, however at a reduced precision.

The G(t)-T(t)-measuring cell which is shown in Figure 3-13 is already described in detail in [103]. It is very similar to the T(t)-measuring cells described in [103,107,108], except for the electrodes (A in Figure 3-13) and the connection to the conductometer (G). The sample volume is approx. 6 mL because the temperature sensor (B) can not reach as far into the cell as is the case for T(t)-measuring cells, due to the electrodes. The inner glass tube (D) is weakened by the Pt-wire feedthrough. To avoid serious damage of the cell, an

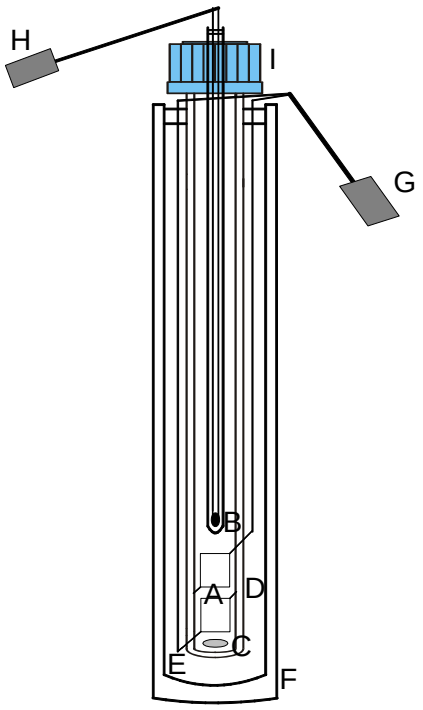

Figure 3-13: G(t)-T(t)-measuring cell; Electrodes (A), glass tube with thermistor (B), magnetic stirrer bar (C), inner Pyrex tube (D), thermal insulation (E), outer Pyrex tube (F), SQ 18 closure with Teflon coated rubber seal (I), connector for the thermistor (H) and electrodes (G). [103]

o-ring, which is usually used to centre the inner glass tube inside the outer glass tube (F), was not placed in the top of the electrode feedthrough because it also transfers pressure from the outer glass tube onto the inner glass tube at very low temperatures. In contrast to the conductivity cells described in Chap. 3.3.1.2 the cell constants of the G(t)-T(t)-measuring cells are fill level dependent due to their cell geometry and dependent on the electrode arrangement. As the cell diameter - electrode distance ratio is much larger for G(t)-T(t)-measuring cells the electric field reaches further into the electrolyte. In the case of expensive electrolytes where minimized sample volumes are used the electric field reaches as far as the liquid/gas boundary which leads to varying cell constants at varying temperatures and therefore varying sample volumes. The electrode arrangement may be altered by crystallising samples or during the cleaning process which may lead to varying cell constants between two measurements.

The measuring cells were filled and sealed gas tight in a glove box under inert gas atmosphere. For measurements the cells were placed in a stirring device that is immersed into the thermostat bath. Mixing of the substances during cooling- or heating-experiments is necessary to avoid errors caused by temperature variations. For this work two different stirring devices were used: the “planetary stirring device” with a capacity of 21 measuring cells and the “alternating field stirring device” with a capacity of 30 measuring cells. Both stirring devices are also described in Refs. [103,107,108]. The advantage of the “planetary stirring device” is a better magnetic coupling between the stirring device and the magnetic stirring bar in the cell. The magnetic stirring bar is driven by a cobalt samarium magnet whose holder is connected with a gear wheel. The 21 gear wheels are arranged in two concentrically circles. The gear wheels in the inner circle drive the gears in the outer circle. The inner wheels are driven by an auxiliary wheel, which is driven by the centre drive wheel. An electrical motor drives this wheel via a drive shaft. The advantage of the

“alternating field stirring device” is the larger measuring cell capacity and the lack of mobile mechanical parts which are more vulnerable to malfunctions than the 4 magnetic coils which generate the alternating magnetic field.

3.4.1.3 30-Channel-Conductometer and -Thermometer

The temperature of the samples was measured with a home build fast multi-channel precision thermometer [103,135]. The thermometer measures the resistances of 30 high precision temperature sensors (BetaTHERM Betacurve 30K6A1), so called thermistors, which are resistances with large temperature coefficients. The resistance values are transformed into digital signals, then transferred to a personal computer, where they are transformed into temperatures and recorded by the applied software [103]. In the temperature range from -50 °C to +10 °C the thermistor provides a measuring accuracy better than 30 mK with regular calibration. Temperatures are recorded with a constant sampling rate of 1 s. [103]

The applied 30-channel-conductometer was also constructed by Schweiger and is described in detail in Ref. [103]. In principle it is a further development of the above described 30-channel-thermometer that uses conductivity cells instead of thermistors as applied sensors. The major difference between temperature and conductivity measurement is the applied voltage, because for conductivity measurements alternating voltage is necessary. Therefore the conductometer is equipped with sine generators. The output voltage of the potentiometer circuit is rectified into direct voltage by a precision rectifier. The further transformation and recording of measurement data is carried out in analogy to the thermometer. The application of the home built software provides long term automatic data recording of both temperature and conductivity measurements. [103]

3.4.2 Data Editing and Evaluation

Evaluation of the recorded T(t)-curves was performed with the home developed software as described in Refs. [103,107]. An example for a cooling curve with subsequent heating curve is shown as a screen shot of the applied software in Figure 3-14, the examined substance was $EMIBF_4$, the applied cooling and heating rates were -5 and +5 $K\,h^{-1}$ respectively. Due to the distinct supercooling of ILs [108,109] evaluation of crystallisation points (Figure 3-14, between 71267 s and 95023 s) is affected with large errors. Therefore, phase transition points of pure ILs and mixtures of ILs were only gained from heating

curves. Evaluation of the heating curves is shown in Figure 3-15 with respect to melting points of pure ILs and eutectic points of mixtures for the melting point of $EMIBF_4$. Both phase transition points are assumed as intersection point of two straight lines which are fitted by linear regression to the horizontal or quasi-horizontal part of the curve and the nearly linearly increasing part of the curve below the melting point respectively.

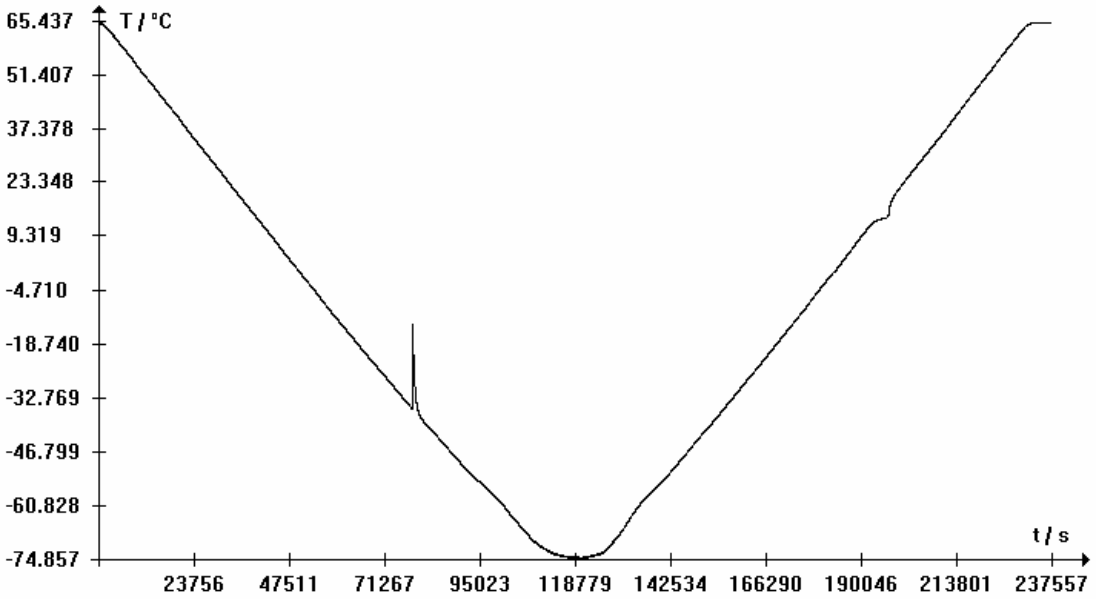

Figure 3-14: T(t)-curves of $EMIBF_4$ with cooling and heating rates *v* of -5 and +5 K h^{-1} respectively.

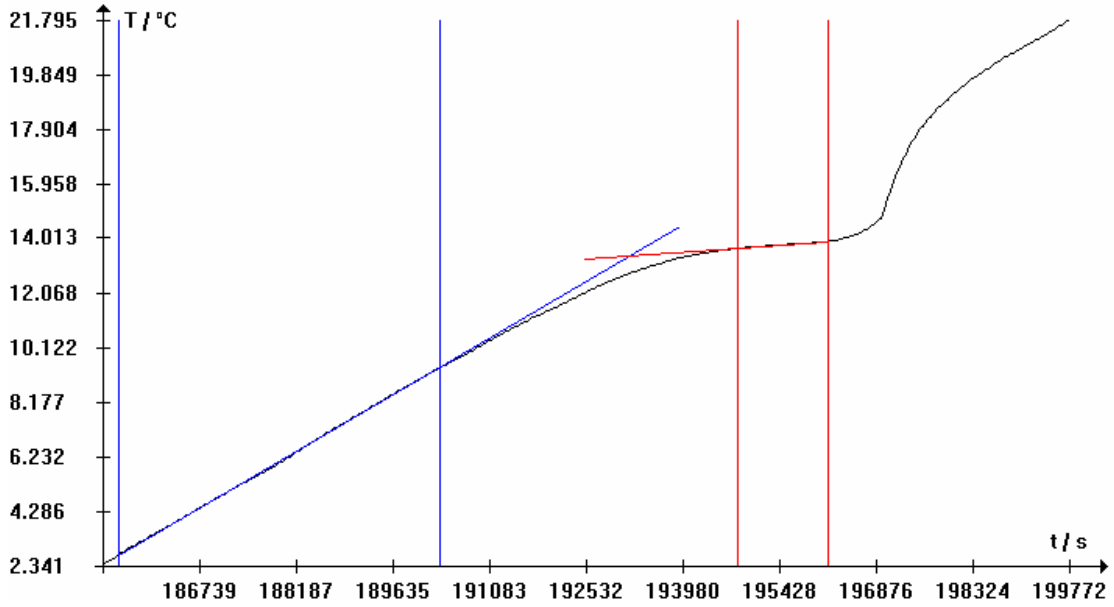

Figure 3-15: Enlargement of the melting region of $EMIBF_4$ shown in Figure 3-14 (—), extrapolation of the linearly increasing part (—) and quasi-horizontal part (—) of the curve for determination of the corresponding melting point.

The determination of breaking points from T(t)-curves is demonstrated in Figure 3-16 for the breaking point of ≈ 0.05 mol L^{-1} I_2 in EMIDCA/MPII with 10.9 mol% MPII. Here, only the enlarged breaking point region of the heating branch of a T(t)-curve recorded at a heating rate v of + 5 K h^{-1} is shown, since the breaking point is not distinct enough to be detected if the whole cooling and heating cycle would be shown as in Figure 3-14. The breaking point is assumed as intersection of two straight lines which are fitted by linear regression to the curve parts previous and after the breaking point respectively.

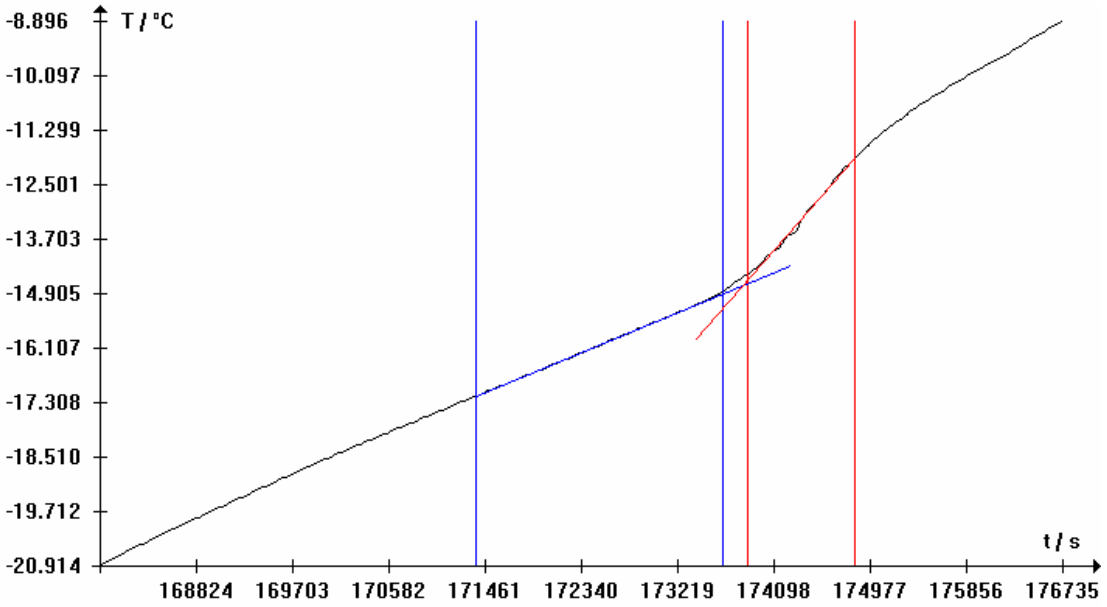

Figure 3-16: Enlarged breaking point region of the heating branch of a T(t)-curve of ≈ 0.05 mol L^{-1} I_2 in EMIDCA/MPII with 10.9 mol% MPII recorded at a heating rate v of + 5 K h^{-1} (—), extrapolation of the part of the curve with smaller slope (—) and the part with larger slope (—) for determination of the corresponding breaking point.

In general, evaluation of G(t)-curves was performed in a similar manner as for T(t)-curves. An example for the time dependent behaviour of conductivity during a cooling curve with subsequent heating curve is shown in Figure 3-17 for the same substance and measurement parameters as for the T(t)-curve in Figure 3-14. Since conductivity strongly correlates with the mobility of the charge carriers, it drops to a value of zero by crystallisation of the sample. But due to the already mentioned distinct supercooling of ILs and a too low sensitivity of the measuring cell the conductivity often tends to zero at low temperatures prior to an occurring crystallisation of the sample. Therefore, similar to evaluation of T(t)-curves, the focus is on the heating part of the experiment.

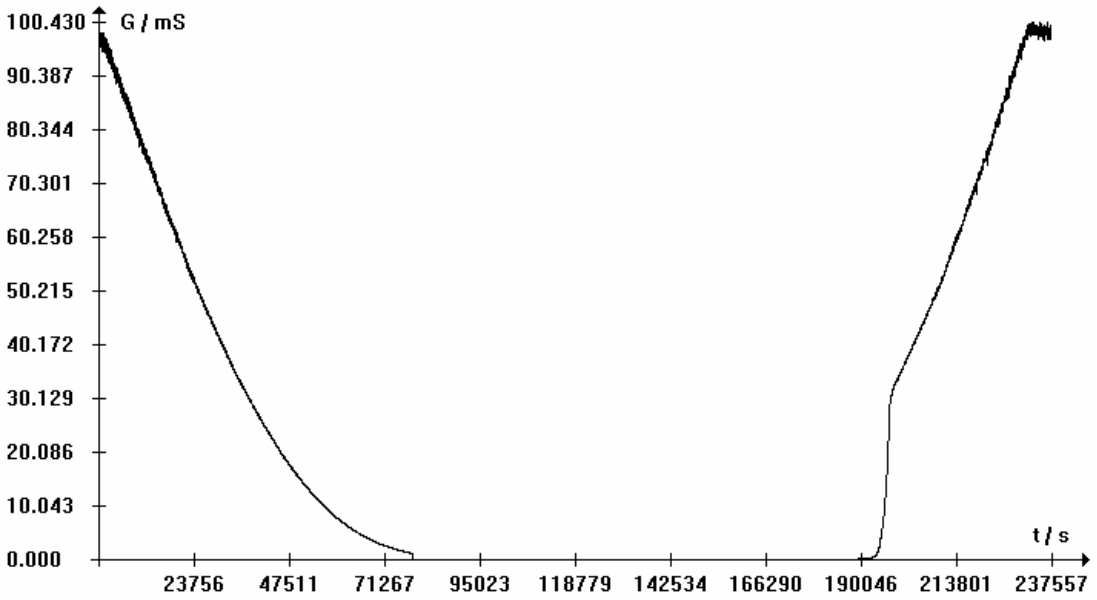

Figure 3-17: G(t)-curves of $EMIBF_4$ with cooling and heating rates of -5 and +5 K h^{-1} respectively.

At the melting point the behaviour of the conductivity is exactly reversed to its behaviour at the crystallisation point of the sample. Here, the conductivity shows a nearly steplike increase until the melting process is finished, again based on the varying mobility of charge carriers, and followed by its usual increase with increasing temperature. The trend of the G(t)-curve shown in Figure 3-17 is enlarged illustrated in Figure 3-18 for the region around the melting point, along with the evaluation of the melting point. The melting point for this kind of measurement is assumed as intersection point of two straight lines which are fitted by linear regression to the horizontal or quasi-horizontal part at the beginning of the curve and the nearly vertical part of the curve after the actual melting point respectively. (Figure 3-18) Since this method only yields a time for the melting, the actual temperature for the melting point must be obtained from the original text-file, where time, temperature, and conductivity values are listed together.

The determination of breaking points from G(t)-curves is performed in a similar manner as for melting points and eutectic points. The G(t)-curve of a mixture with a eutectic temperature below the lower limit of conductivity detection is very similar to the G(t)-curve of pure ILs (Figure 3-17). The major difference is a more weakly pronounced and less steep conductivity increase at the breaking point (Figure 3-19) compared to the nearly steplike conductivity increase at the melting point (Figure 3-18). Evaluation of a G(t)-curve with regard to the breaking point is illustrated in Figure 3-19 for the same EMIDCA blend as in Figure 3-16. The breaking point is assumed as intersection of two straight lines which are

fitted by linear regression to the steeply increasing part of the curve before and the slowly and uniformly increasing part of the curve after the actual breaking point respectively.

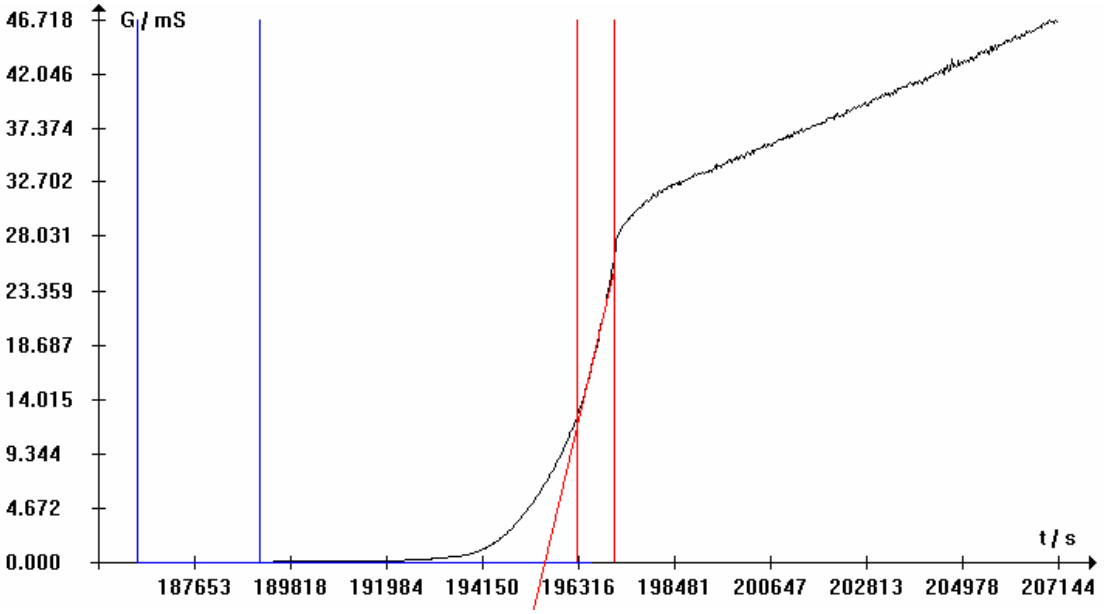

Figure 3-18: Enlargement of the melting region of $EMIBF_4$ shown in Figure 3-17 (—), extrapolation of the quasi-horizontal part (—) and nearly vertical part (—) of the curve for determination of the corresponding melting point.

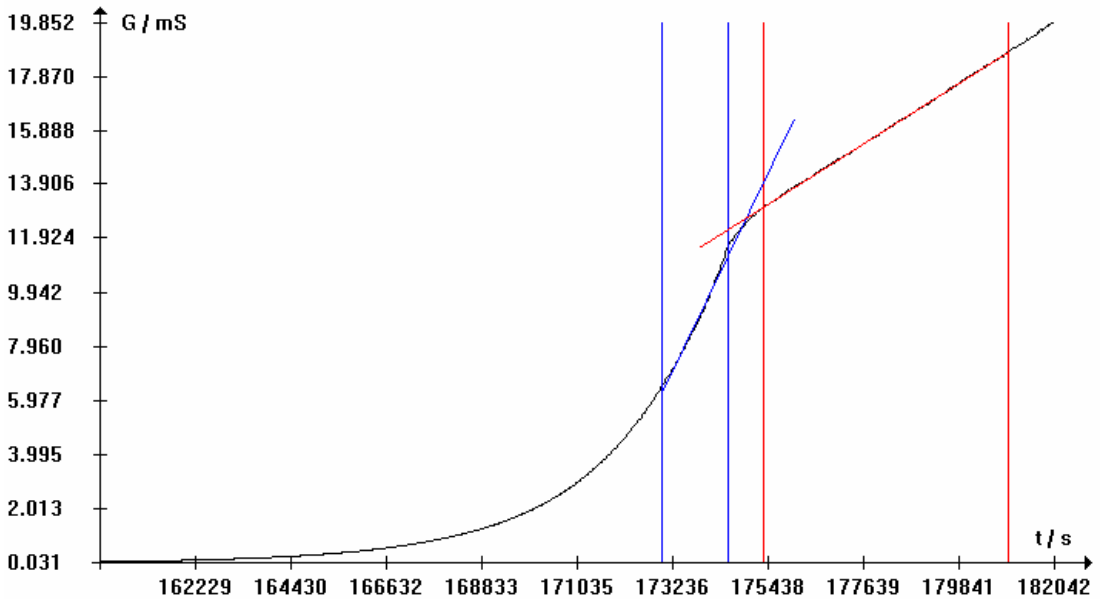

Figure 3-19: Enlarged breaking point region of the heating branch of a G(t)-curve of ≈ 0.05 mol L^{-1} I_2 in EMIDCA/MPII with 10.9 mol% MPII recorded at a heating rate *v* of + 5 K h^{-1} (—), extrapolation of the steeply increasing part of the curve (—) and the part with smaller and uniform slope (—) for determination of the corresponding breaking point.

A third option for evaluation of phase transitions is a plot of *lnG* vs. T^{-1}*1000 shown in Figure 3-20 and Figure 3-22. The absolute values for phase transition points provided by this Arrhenius-type plot are typically less accurate than for the T(t)- and G(t)-curves, but it offers a higher sensitivity for only weakly pronounced alterations in the sample. The conductivity of a sample is, within certain conditions and boundaries, equal for a specific temperature prior cooling and after heating. With the *lnG*-plot the conductivity at a specific temperature can be compared for the cooling and heating curve, as shown in Figure 3-20 for a blend which is liquid beyond the limit of detection of conductivity and then crystallises. The melting process can be determined again and evaluated for both melting points and breaking points as shown in Figure 3-21. Both are assumed as intersection of two straight lines which are fitted by linear regression to the steeply increasing part of the plot (in case of a melting point nearly vertically increasing) and the Arrhenius-like slowly increasing part of the curve.

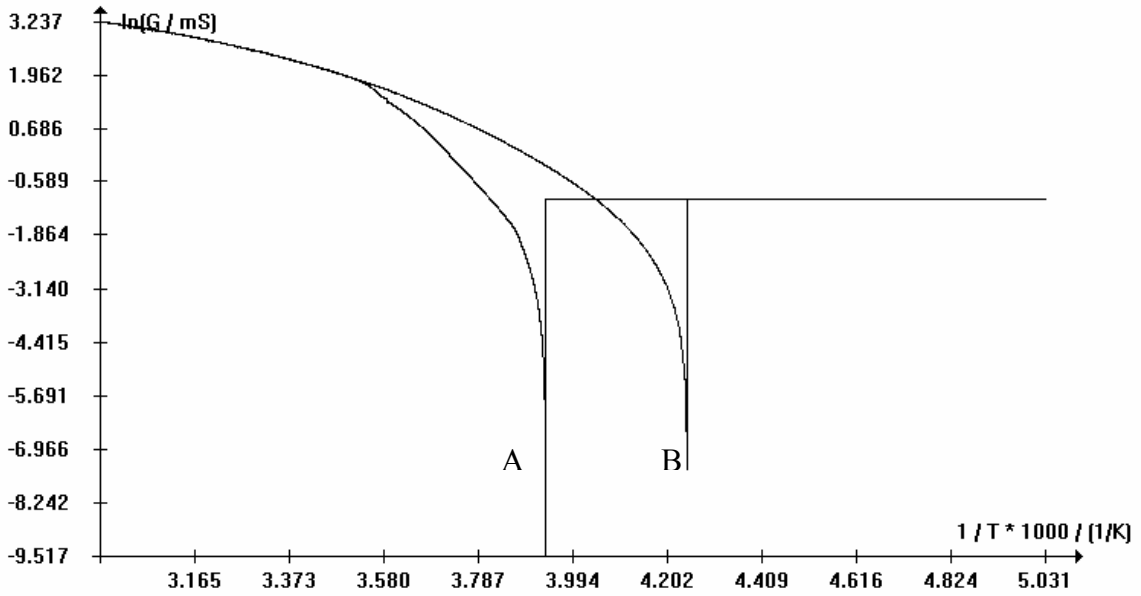

Figure 3-20: Plot of *lnG* vs. T^{-1}*1000 of ≈ 0.05 mol L^{-1} I_2 in $EMIBF_4$/MPII with 30.0 mol% MPII recorded with cooling (B) and heating (A) rates of -5 and +5 K h^{-1} respectively.

Evaluation of *lnG*-plots is of particular significance for samples which show no change of state during cooling or heating according to T(t)- and G(t)-curves but deviations of the conductivity values for cooling and heating curves (Figure 3-22). These deviations are either based on a phase separation or, more likely, on a fractional solidification of the sample within this specific temperature range. Starting and ending temperature of these processes can be determined from the *lnG*-plots.

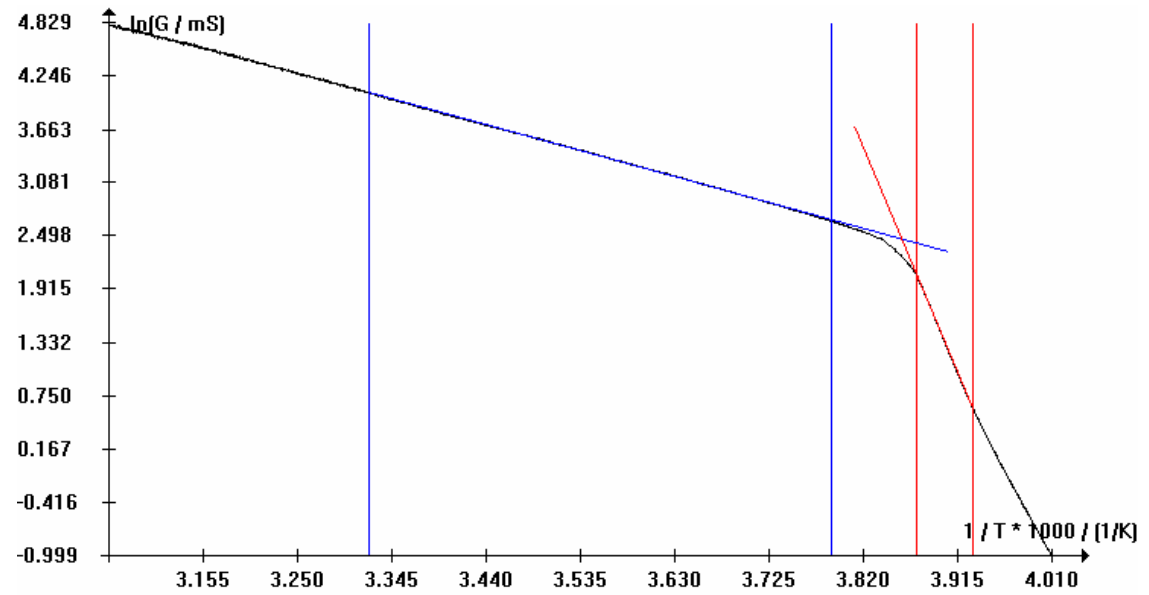

Figure 3-21: Enlarged breaking point region of the heating branch of a *lnG*-plot of ≈ 0.05 mol L^{-1} I_2 in EMIDCA/MPII with 10.9 mol% MPII recorded at a heating rate *v* of + 5 K h^{-1} (—), extrapolation of the steeply increasing part of the curve (—) and the part with smaller and uniform slope (—) for determination of the corresponding breaking point.

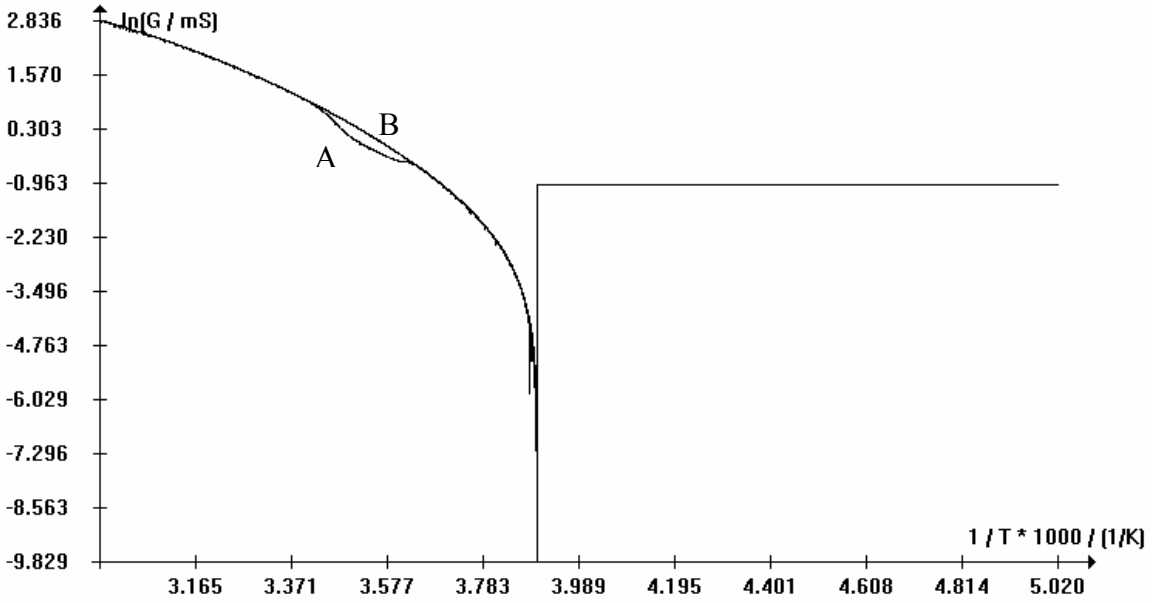

Figure 3-22: Plot of *lnG* vs. T^{-1}*1000 of ≈ 0.05 mol L^{-1} I_2 in EMINTf$_2$/MPII with 80.0 mol% MPII recorded with cooling (B) and heating (A) rates of -5 and +5 K h^{-1} respectively.

Additionally to facilitate detection of phase transition points, especially for mixtures of ILs, G(t)-measurements also yield conductivity data over a broad temperature range, that are however less accurate than for the method explained in Chap. 3.3, for reasons given above.

To sum it up conductivity data obtained by G(t)-measurements are used as additional indicator for phase transitions during cooling and heating experiments. Simultaneous recording of G(t) and T(t) also enables evaluation of the recorded measurement data in various ways.

The basic method, evaluation of T(t)-curves according to Figure 3-15 (melting points and eutectic points) and Figure 3-16 (breaking points), is the method of choice in the case of pure substances and blends of non-conducting materials, e.g. binary mixtures of organic carbonates [103,107]. If possible it is also used in the case of the examined electrolyte mixtures for DSSCs. These blends are made up of just three components, two ILs and iodine, but due to various present cations and anions and the resulting various combination options they do not behave like three component systems. This differing behaviour makes evaluation of T(t)-curves often impossible, since occurring phase transitions are not distinct enough for evaluation. In this case evaluation of G(t)-curves (Figure 3-18 and Figure 3-19) can often produce relief because conductivity is more sensitive to phase transitions. Comparison of the conductivities recorded during the cooling and heating experiment (shown in Figure 3-20 and Figure 3-22 for *lnG*) is the most sensitive method for determination of weakly pronounced alterations in the sample. This method is of particular importance if evaluation of T(t)- and G(t)-curves yields no result. The disadvantage of this method is that for weakly pronounced alterations (Figure 3-22) only starting and ending temperature of the region with varying conductivity can be determined from the *lnG*-plots and no exact crystallisation or melting point.

4 Diffusion Measurements

In the following chapters the results from steady-state cyclic voltammetric measurements at UMEs (Chap. 3.2) are summarised and discussed. The obtained I_3^--diffusion coefficients are an important measure for evaluation of potential DSSC-electrolytes. (Chap. 2.1)
The electrolyte densities that are necessary for calculation of I_3^--concentrations and consequently evaluation of the diffusion measurements were determined by Zistler[a] and are listed, along with measurement parameters and further details to the measurement method, in Ref. [54]. Viscosity measurements, which are essential for a better insight in the occurring transport-processes, were performed by Gerhard and Himmler[b] at the group of Prof. Wasserscheid with a MCR 100 rheometer from *Paar* (*Graz*).
Unless otherwise stated, I_3^--concentrations are always given for 25 °C.

4.1 EMIDCA/MPII

1-Ethyl-3-methylimidazolium dicyanamide (EMIDCA) was the first choice as solvent IL due to its remarkably low viscosity of 21 mPa s at 25 °C [136]. Additionally, compared to other very low viscosity ILs, it features a high electrochemical stability [137], a broad liquid range according to literature [136,138], and sufficient availability, especially compared to the recently tested ILs like 1-ethyl-3-methylimidazolium tricyanomethanide [139] and 1-ethyl-3-methylimidazolium tetracyanoborate [55] which are very expensive due to their complex syntheses [140]. The application of EMIDCA as solvent IL should reduce the overall viscosity of the complete electrolyte, enhance the I_3^--transport and enlarge the liquid range of the complete electrolyte.
The system EMIDCA/MPII was studied with regard to two parameters and their influence on I_3^--diffusion including the variation of iodide concentration at constant iodine concentration followed by the variation of iodine concentration at constant iodide concentration.

[a] Thanks to Dr. M. Zistler;
[b] Thanks to Dr. D. Gerhard and Dr. S. Himmler;

4.1.1 Variation of Iodide Concentration

To study the influence of the MPII concentration on the I_3^--diffusion, the system EMIDCA/MPII was examined over a broad IL mixing range, varying from 9 mol% MPII to 100 mol% MPII, at a constant I_2 concentration of ≈ 0.05 mol L^{-1}. For each MPII concentration, the I_3^--diffusion coefficient was determined at five different temperatures, ranging from 25 °C to 60 °C, and at least three times for each temperature. The determined diffusion coefficients and their calculated and exact mean values with standard deviations are shown in Chap. 8.1.1 along with the corresponding measurement parameters and examples of the recorded steady-state CVs. The resulting standard deviations for this electrolyte system are typically < 2% and therefore lower than the estimated relative maximum error of 5% (Chap. 3.2.4). The reason for the relatively high standard deviations and outliers of the diffusion coefficients of this system seems due to some kind of deactivation of the electrode surface by EMIDCA. This required more numerous measurements as for the other systems in order to achieve reliable results. The mean values of the I_3^--diffusion coefficients at each temperature and MPII concentration are also listed in Table 4-1.

Table 4-1: I_3^--diffusion coefficients of ≈ 0.05 mol L^{-1} I_2 in mixtures of EMIDCA/MPII at varying MPII concentrations.

$D \cdot 10^7$ [cm^2 s^{-1}]					
ϑ [°C] / Mol% MPII	**25**	**30**	**40**	**50**	**60**
9.1	8.3	9.8	13.4	16.9	20.8
20.1	7.7	9.2	12.3	15.9	20.3
29.9	6.8	8.2	11.6	15.3	19.7
41.3	5.7	7.0	9.9	13.4	17.7
49.6	4.7	6.0	8.7	12.2	16.5
60.0	3.9	5.1	8.0	11.6	15.8
80.1	2.6	3.5	5.7	8.6	12.6
100.0	1.2	1.7	3.0	4.9	7.4

4.1.1.1 Temperature Dependence of the I_3^--Diffusion Coefficient

The temperature dependence of the detected I_3^--diffusion coefficients was analysed by fitting the measurement data according to the VFT-equation (Eq. (4.1)) introduced in Chap. 2.2.2:

$$D(T) = A \exp\left[\frac{-B}{T - T_0}\right] \tag{4.1}$$

The significance of this analysis is not as high as for viscosity or conductivity data due to less accurate data points yielded by diffusion measurements, the comparatively small temperature range and small number of data points.

The determined I_3^--diffusion coefficients and the resulting VFT-plots are shown in Figure 4-1; the fitting parameters of these plots are summarised in Table 8-13. The I_3^--diffusion coefficients for all blends show a strong increase with increasing temperature. The magnitude of the relative increase varies strongly within the mixing range, increasing from 150% for 9 mol% MPII to 509% for 100 mol% MPII. But, note, the absolute value stays nearly constant (12-13·10^{-7} cm^2 s^{-1}) in the region between 9 and 60 mol% MPII, decreasing with higher MPII concentrations.

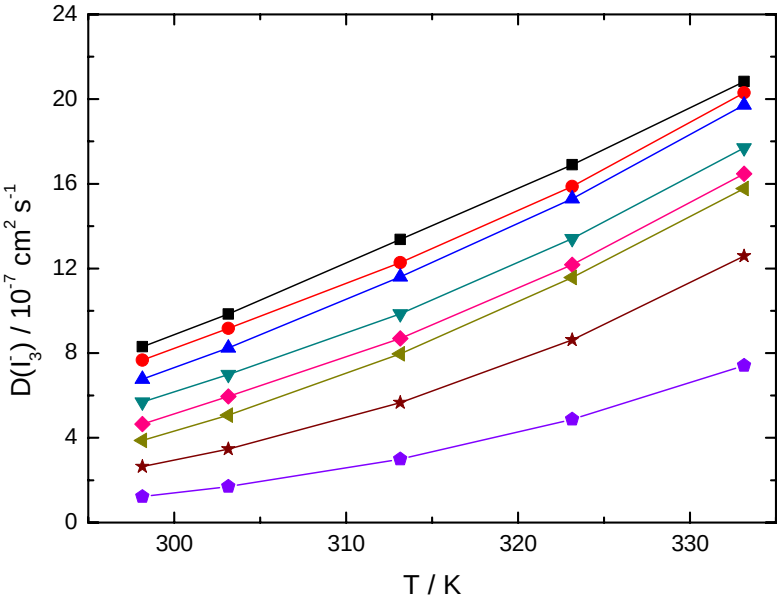

Figure 4-1: Temperature dependence of I_3^--diffusion coefficients of ≈ 0.05 mol L^{-1} I_2 in mixtures of EMIDCA/MPII at varying MPII concentrations; (—■—) 9 mol% MPII, (—●—) 20 mol% MPII, (—▲—) 30 mol% MPII, (—▼—) 41 mol% MPII, (—◆—) 50 mol% MPII, (—◀—) 60 mol% MPII, (—★—) 80 mol% MPII, (—⬟—) 100 mol% MPII.

According to Rau et al. [53] the limiting value for the diffusion limitation of the DSSC is an I_3^--diffusion coefficient > $1 \cdot 10^{-6}$ cm^2 s^{-1} because this is the magnitude of I_3^--diffusion coefficients in electrolytes containing organic solvents.
For EMIDCA rich blends, the critical value of $1 \cdot 10^{-6}$ cm^2 s^{-1} is already exceeded at 40 °C, for the blends with lower EMIDCA concentrations at 60 °C. Therefore, for the application of electrolytes based on binary mixtures of EMIDCA and MPII the diffusion limitation shifts to lower temperatures with increasing EMIDCA concentration.

4.1.1.2 Iodide Concentration Dependence of the I_3^--Diffusion Coefficient

Both the temperature dependence of the I_3^--diffusion coefficients and their dependence on the MPII concentration are of interest. To clarify the influence of the MPII concentration, the I_3^--diffusion coefficients are shown in Figure 4-2 as a function of the MPII concentration at different temperatures. As expected, the increase of the MPII concentration leads to a strong decrease of the I_3^--diffusion coefficients. The relative difference between I_3^--diffusion coefficients of blends with low MPII concentration and high MPII concentration becomes smaller for increasing temperature. In detail, the I_3^--diffusion coefficient of the blend with 9 mol% MPII at 25 °C is about 8 times larger than the one of the blend with 100 mol% MPII at the same temperature. At 60 °C the difference between the two blends is much smaller; the I_3^--diffusion coefficient of the blend with 9 mol% MPII is just 3 times larger than the one of the blend with 100 mol% MPII at this temperature.
Within the measurement range the maximum values of the I_3^--diffusion coefficients are at 9 mol% MPII for each temperature. Thus, with the assumption of the I_3^--diffusion as exclusive limiting process in the DSSC, this would be the best EMIDCA/MPII-based electrolyte blend for a later application in DSSCs.

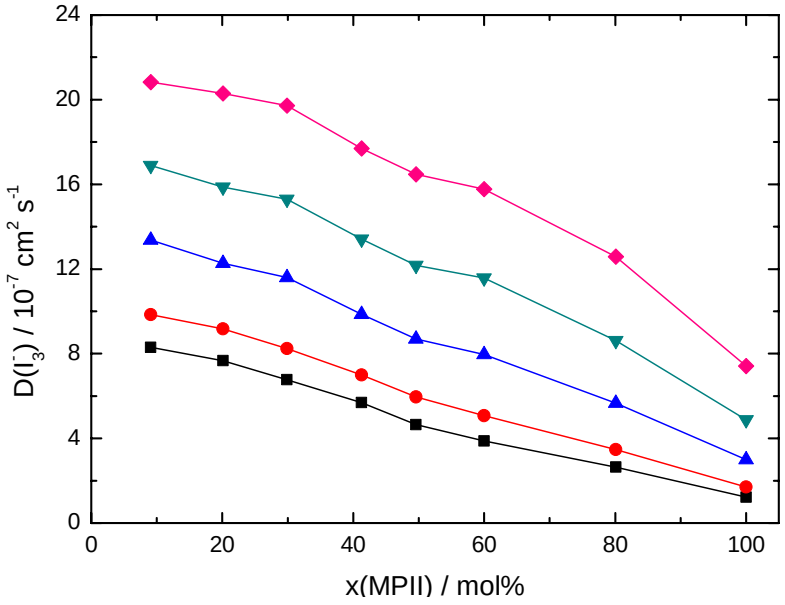

Figure 4-2: I_3^--diffusion coefficients of ≈ 0.05 mol L^{-1} I_2 in mixtures of EMIDCA/MPII as a function of the MPII concentration at different temperatures; *θ*: (—■—) 25 °C, (—●—) 30 °C, (—▲—) 40 °C, (—▼—) 50 °C, (—◆—) 60 °C.

As explained in Chap. 2.1.2, the recombination of the dye-cation and reduction of I_3^- with previously injected electrons at the TiO_2 electrode are also crucial factors for the efficiency of the DSSC. To enhance the regeneration of the oxidized dye, a preferably high iodide concentration is necessary [50]. Therefore, the blends with 20 mol% MPII to 30 mol% MPII are of interest for an application in DSSCs, because they exceed the critical value of $1 \cdot 10^{-6}$ cm^2 s^{-1} at temperatures > 40 °C. Additionally there is little difference for the I_3^--diffusion coefficients in the range between 9 mol% MPII and 30 mol% MPII, compared to a duplication or triplication of the iodide concentration.

The I_3^--diffusion coefficients of the blends with higher iodide concentration are sufficiently large for 50 °C and 60 °C, but too low for the other temperatures, as is the case for the blend with 100 mol% MPII over the whole temperature range.

In Figure 4-3 the Einstein-Stokes ratios (see Chap. 2.2.3) for the system EMIDCA/MPII are shown as function of the MPII concentration at three exemplary temperatures. Instead of staying constant over the whole mixing range, as expected according to the Einstein-Stokes-law, they increase with increasing MPII concentration and increasing viscosity. Thus, the I_3^--diffusion in this electrolyte system does not obey the Einstein-Stokes-equation. The magnitude of the growth decreases with rising temperature from 720% at 25 °C passing 550% at 40 °C to 420% at 60 °C.

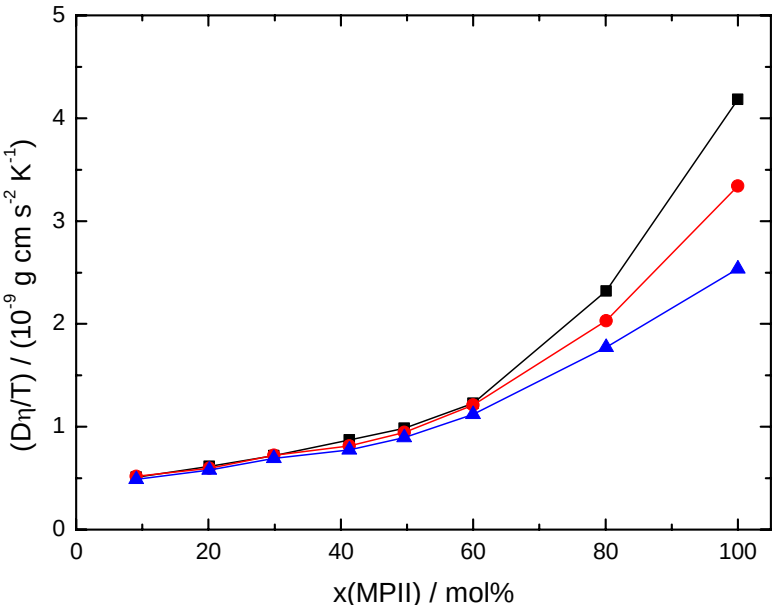

Figure 4-3: Einstein-Stokes ratios of ≈ 0.05 mol L^{-1} I_2 in mixtures of EMIDCA/MPII as a function of the MPII concentration at different temperatures; θ: (—■—) 25 °C, (—●—) 40 °C, (—▲—) 60 °C.

A possible explanation for this behaviour may be a change in the mechanism of mass- or charge-transport, from a pure physical diffusion process to a chemical or electronic exchange mechanism, similar to the Grotthus-mechanism:

$$I_3^- + I^- \rightarrow I^- \cdots I_2 \cdots I^- \rightarrow I^- + I_3^- \qquad (4.2)$$

This exchange mechanism was primarily suggested by Kawano et al. [95] and by Grätzel and co-workers [23] and occurs in addition to the diffusive transport. The length of the poly-iodide chain can vary; chain lengths up to five atoms are known from literature. [96,42]

The increase of the Einstein-Stokes ratios with increasing MPII concentration corresponds to the suggested mechanism because an exchange between I_3^- and I^- is necessary for this kind of charge transport. Larger iodide concentrations raise the chance of a collision between I_3^- and I^- and therefore enhance this kind of transport mechanism.

For the transfer of I_2 from I_3^- to I^- both ions should be in close proximity to one another. This leads to a kinetic constraint of this transfer, due to the negative charge of both reactants and the necessary energetic disadvantageous transition state. The constraint would be reduced by larger poly-iodide chain lengths and the resulting distribution of the negative charge over the whole chain.

The investigated electrolyte system EMIDCA/MPII is based on a binary mixture of ILs and consists only of ions, therefore the ionic strength in this kind of electrolytes is very high. Due to the high ionic strength, the negative charges of the reactants are better insulated from one another, thus the I_2 transfer is facilitated by the kinetic salt effect. Rising temperature leads to decreasing viscosity of the electrolyte and should therefore lead to an increasing portion of the physical diffusion on the overall I_3^- transport. That matches the behaviour of the Einstein-Stokes ratios shown in Figure 4-3, where the increase of the Einstein-Stokes ratios decreases with rising temperature.

4.1.2 Variation of Iodine Concentration

To study the influence of the I_2 concentration on the I_3^--diffusion, a fixed EMIDCA/MPII composition with 80 mol% MPII was examined at varying I_2 concentrations. This IL composition was chosen due to the already large viscosity drop for this MPII concentration and the resulting comparatively high I_3^--diffusion coefficient, as well as the large iodide concentration, both important parameters for application in DSSCs.

The object of this study of I_2 concentration dependence was to determine if the I_3^--diffusion coefficient in this system shows a similar concentration dependent behaviour, as does the diffusion coefficient of ferrocene in 1-butyl-3-methylimidazolium bis(trifluoromethylsulfonyl)imide. In that system, a clearly increasing ferrocene diffusion coefficient with increasing ferrocene concentration was observed, and nearly constant viscosity was obtained. [131,141,142]

The diffusion measurements were conducted at I_2 concentrations between 0.05 mol L^{-1} and 0.49 mol L^{-1} I_2, in a temperature range from 25 °C to 60 °C. At least three values were determined at each temperature. The determined diffusion coefficients and their calculated and exact mean values with standard deviations are shown in Chap. 8.1.1 along with the corresponding measurement parameters and examples of the recorded steady-state CVs. The resulting standard deviations for this electrolyte system are typically < 1% and therefore lower than the estimated relative maximum error of 5% (Chap. 3.2.4). The mean values of the I_3^--diffusion coefficients at each temperature and I_2 concentration are listed in Table 4-2.

Table 4-2: I_3^--diffusion coefficients of I_2 in mixtures of EMIDCA/MPII with 80 mol% MPII at varying I_2 concentrations.

$D \cdot 10^7$ [cm^2 s^{-1}]					
θ [°C] / $c(I_2)$ [mol L^{-1}]	**25**	**30**	**40**	**50**	**60**
0.05	2.5	3.3	5.5	8.8	12.7
0.10	2.5	3.3	5.5	8.8	13.0
0.20	2.3	3.2	5.7	8.7	13.0
0.30	2.6	3.3	5.8	9.0	13.1
0.40	2.8	3.7	6.1	8.6	12.4
0.49	2.7	3.6	6.0	9.4	13.8

4.1.2.1 Temperature Dependence of the I_3^--Diffusion Coefficient

The determined I_3^--diffusion coefficients and the resulting VFT-plots are shown in Figure 4-4; the fitting parameters for these plots are summarised in Table 8-14. The I_3^--diffusion coefficients for all blends show a strong increase with increasing temperature. There are only small differences between the I_3^--diffusion coefficients of specific blends as well as for the magnitude of the relative or absolute growth.

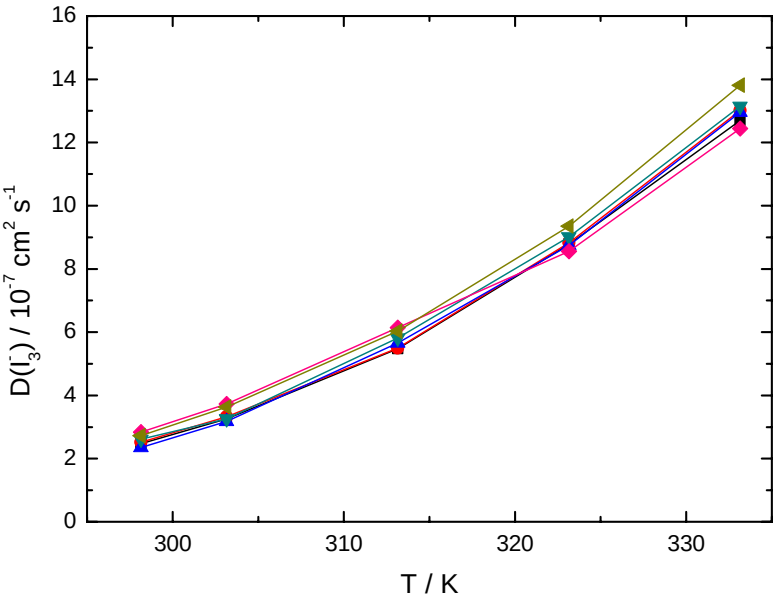

Figure 4-4: Temperature dependence of I_3^--diffusion coefficients of I_2 in mixtures of EMIDCA/MPII with 80 mol% MPII at I_2 concentrations of: (—■—) 0.05 mol L^{-1}, (—●—) 0.10 mol L^{-1}, (—▲—) 0.20 mol L^{-1}, (—▼—) 0.30 mol L^{-1}, (—◆—) 0.40 mol L^{-1}, (—◀—) 0.49 mol L^{-1}.

4.1.2.2 Iodine Concentration Dependence of the I_3^--Diffusion Coefficient

The I_2 concentration dependence of the I_3^--diffusion coefficients is shown in Figure 4-5. There is only a small increase of the I_3^--diffusion with increasing I_2 concentration, most distinct at lower temperatures, which can be explained with regard to the viscosity data for these blends [27,54,57]. The reason for this small increase of the I_3^--diffusion is a small decrease of the viscosity, when adding iodine, which is again most distinct for lower temperatures and therefore higher viscosities [27,54,57].

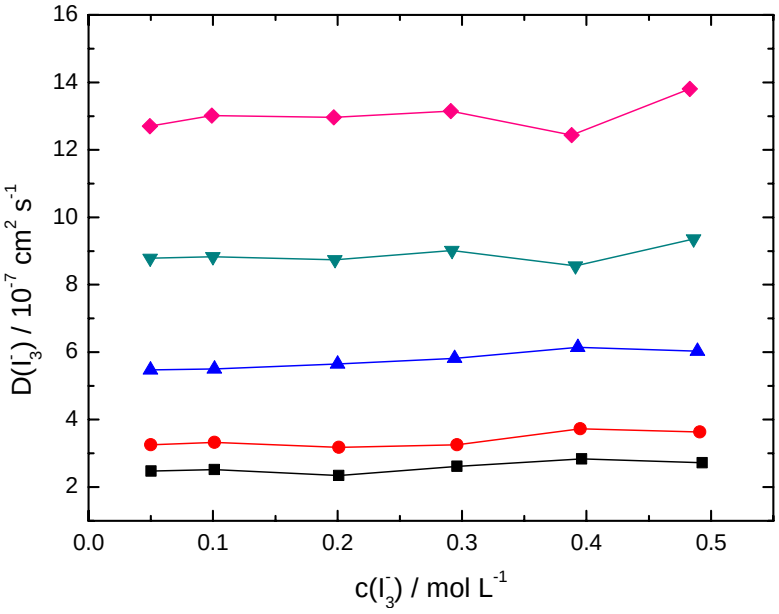

Figure 4-5: I_3^--diffusion coefficients of I_2 in mixtures of EMIDCA/MPII with 80 mol% MPII as a function of the I_3^- concentration at different temperatures; θ: (—■—) 25 °C, (—●—) 30 °C, (—▲—) 40 °C, (—▼—) 50 °C, (—◆—) 60 °C.

4.2 $EMIBF_4$/MPII

In spite of its higher viscosity (37 mPa s at 25 °C [143]) when compared to EMIDCA, 1-ethyl-3-methylimidazolium tetrafluoroborate ($EMIBF_4$) was examined as solvent IL due to its well known electrochemical behaviour and its extraordinary electrochemical and chemical stability. [137,143] Additionally, it is a comparatively cheap IL and therefore often used and investigated in electrochemical devices.

The system $EMIBF_4$/MPII was also studied with regard to two parameters; a) variation of iodide concentration at constant iodine concentration and b) variation of iodine concentration at constant iodide concentration, respectively.

4.2.1 Variation of Iodide Concentration

As for the system EMIDCA/MPII, the system $EMIBF_4$/MPII was examined over a broad IL mixing range, varying from 10 mol% MPII to 100 mol% MPII, at a constant I_2 concentration of 0.05 mol L^{-1}. The blends with 10, 20, and 30 mol% MPII were examined by Fleischmann during a research placement.[a] For each MPII concentration, the I_3^--diffusion coefficient was determined at five different temperatures, ranging from 25 °C to 60 °C, and at least three times for each temperature. The determined diffusion coefficients and their calculated and exact mean values with standard deviations are shown in Chap. 8.1.2 along with the corresponding measurement parameters and examples of the recorded steady-state CVs. The resulting standard deviations for this electrolyte system are typically < 1% and therefore lower than the estimated relative maximum error of 5% (Chap. 3.2.4). The mean values of the I_3^--diffusion coefficients at each temperature and MPII concentration are also listed in Table 4-3.

[a] This research placement was instructed by Gores, Zistler, and by the author of this work. Thanks to M. Fleischmann for realisation and evaluation of the measurements.

Table 4-3: I_3^--diffusion coefficients of 0.05 mol L^{-1} I_2 in mixtures of EMIBF$_4$/MPII at varying MPII concentrations.

$D \cdot 10^7$ [cm^2 s^{-1}]					
θ [°C] / Mol% MPII	**25**	**30**	**40**	**50**	**60**
10.1	3.6	4.4	6.5	8.9	11.6
20.1	3.2	3.9	5.7	8.6	11.6
30.1	3.1	4.0	5.6	8.4	11.9
40.0	2.9	3.8	5.8	8.9	11.7
50.1	2.9	3.7	5.8	8.5	11.8
60.1	2.5	3.3	4.6	7.2	10.6
79.9	1.8	2.5	4.2	7.1	10.4
100.0	1.2	1.7	3.0	4.9	7.4

4.2.1.1 Temperature Dependence of the I_3^--Diffusion Coefficient

The determined I_3^--diffusion coefficients and the resulting VFT-plots are shown in Figure 4-6, the fitting parameters of these plots are summarised in Table 8-27. The I_3^--diffusion coefficients for all blends show a strong increase with increasing temperature. For some blends, little deviations from the behaviour according to the VFT-equation occurred, caused by few inaccurate data points. The magnitude of the relative growth varies strongly within the mixing range, increasing from 220% for 10 mol% MPII to 509% for 100 mol% MPII, whereas the absolute value of the growth stays nearly constant (8-9·10^{-7} cm^2 s^{-1}) in the region between 10 and 80 mol% MPII, with a slight maximum in the middle of the mixing range.

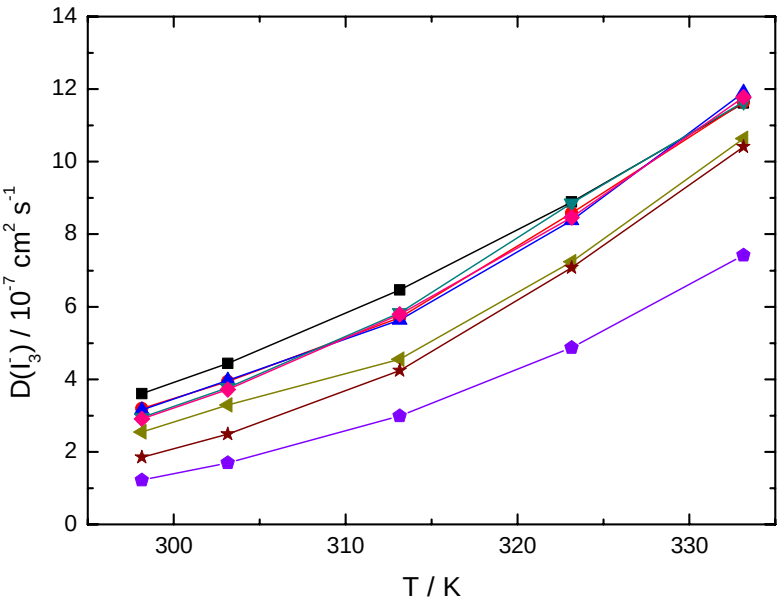

Figure 4-6: Temperature dependence of I_3^--diffusion coefficients of 0.05 mol L^{-1} I_2 in mixtures of $EMIBF_4$/MPII at varying MPII concentrations; (—■—) 10 mol% MPII, (—●—) 20 mol% MPII, (—▲—) 30 mol% MPII, (—▼—) 40 mol% MPII, (—◆—) 50 mol% MPII, (—◀—) 60 mol% MPII, (—★—) 80 mol% MPII, (—⬟—) 100 mol% MPII.

For this electrolyte system the critical value of 1·10^{-6} cm^2 s^{-1} for the diffusion limitation in DSSCs is only exceeded at 60 °C, except the much lower values of the blend with 100 mol% MPII. Therefore, application of electrolytes based on binary mixtures of $EMIBF_4$ and MPII in DSSCs always leads to diffusion limited DSSC-efficiencies with one exception for operating temperatures of > 60 °C.

4.2.1.2 Iodide Concentration Dependence of the I_3^--Diffusion Coefficient

Figure 4-7 shows the iodide concentration dependence of the I_3^--diffusion coefficients of the system EMIBF$_4$/MPII at varying temperatures. Compared to the previously examined system EMIDCA/MPII, this system shows a completely unexpected and different behaviour with regard to viscosity data. The I_3^--diffusion coefficients at lower temperatures decrease only slightly in the region between 10 mol% MPII and 50 mol% MPII, with a maximum I_3^--diffusion coefficients at 10 mol% MPII, and the major decrease at iodide concentrations > 50 mol% MPII. With increasing temperature, the tendency in the region between 10 mol% MPII and 50 mol% MPII changes from a slight decrease to a slight increase despite increasing viscosity, with the maximum I_3^--diffusion coefficients between 30 mol% MPII and 50 mol% MPII. This is again a first hint for the existence of a non-Stokesian charge transport.

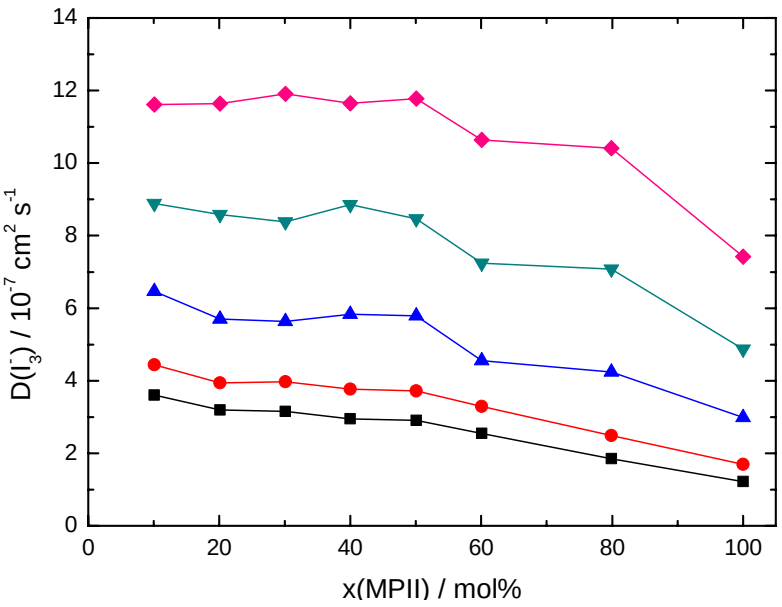

Figure 4-7: I_3^--diffusion coefficients of 0.05 mol L^{-1} I_2 in mixtures of EMIBF$_4$/MPII as a function of the MPII concentration at different temperatures; θ: (—■—) 25 °C, (—●—) 30 °C, (—▲—) 40 °C, (—▼—) 50 °C, (—◆—) 60 °C.

The limiting value of $1 \cdot 10^{-6}$ cm^2 s^{-1} is only exceeded at 60 °C, but then for all EMIBF$_4$ containing blends of this system. Since for application in DSSCs high iodide concentrations are beneficial and due to the fact that there is only little difference between the I_3^--diffusion coefficients in the region from 10 mol% MPII to 50 mol% MPII for all examined temperatures, the blends with 40-50 mol% MPII would be the most recommendable electrolyte compositions for application in DSSCs.

As mentioned above, the behaviour of the I_3^--diffusion coefficients with increasing MPII concentration (Figure 4-7) indicates a non-Stokesian transport mechanism, which is confirmed by the behaviour of the Einstein-Stokes ratios with increasing MPII concentration, shown in Figure 4-8.

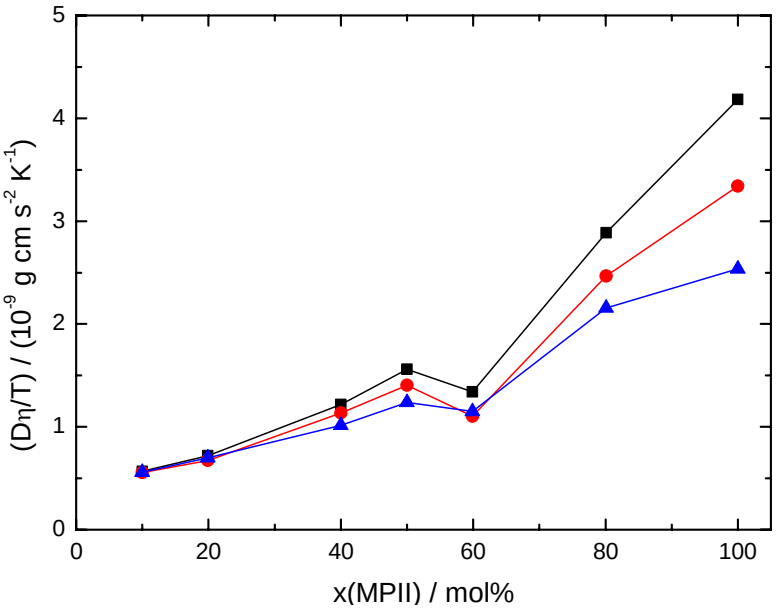

Figure 4-8: Einstein-Stokes ratios of 0.05 mol L^{-1} I_2 in mixtures of $EMIBF_4$/MPII as a function of the MPII concentration at different temperatures; θ: (—■—) 25 °C, (—●—) 40 °C, (—▲—) 60 °C.

The outlier at 60 mol% MPII is probably caused by insertion of moisture during the viscosity measurement, since a rising water content leads to a decreasing viscosity. Apart from that, the Einstein-Stokes ratios for this system strongly and continuously increase with increasing MPII concentration. The magnitude of the growth decreases with rising temperature from 640% at 25 °C passing 500% at 40 °C to 360% at 60 °C.

The explanation for this behaviour is again, as for the system EMIDCA/MPII, the enhancement of the overall I_3^--diffusion by a non-Stokesian charge transport. The impact of this charge transfer mechanism on the overall I_3^--transport decreases with increasing temperature, decreasing viscosity and simultaneously increasing physical I_3^--diffusion. But its impact is large enough to counterbalance the increasing viscosity up to a MPII concentration of 50 mol% for which reason the I_3^--diffusion stays at a nearly constant level at all temperatures.

4.2.2 Variation of Iodine Concentration

As for EMIDCA/MPII in Chap. 4.1.2, the influence of the I_2 concentration on the I_3^--diffusion in EMIBF$_4$/MPII was examined in blends with 80 mol% MPII at varying I_2 concentrations. The I_2 concentrations ranged from 0.05 mol L^{-1} to 0.49 mol L^{-1} I_2 and were investigated at five different temperatures from 25 °C to 60 °C. At least three values were determined at each temperature. The determined diffusion coefficients and their calculated mean values with standard deviations are shown in Chap. 8.1.2 along with the corresponding measurement parameters and examples of the recorded steady-state CVs. The resulting standard deviations for this electrolyte system are typically < 0.8% and therefore lower than the estimated relative maximum error of 5% (Chap. 3.2.4). The mean values of the I_3^--diffusion coefficients at each temperature and I_2 concentration are also listed in Table 4-4.

Table 4-4: I_3^--diffusion coefficients of I_2 in mixtures of EMIBF$_4$/MPII with 80 mol% MPII at varying I_2 concentrations.

$D \cdot 10^7$ [cm^2 s^{-1}]					
θ [°C] / $c(I_2)$ [mol L^{-1}]	**25**	**30**	**40**	**50**	**60**
0.05	1.8	2.5	4.2	7.1	10.4
0.10	2.1	2.8	4.5	7.2	11.0
0.20	2.2	2.9	4.8	7.6	11.1
0.30	2.1	2.9	5.0	8.0	11.9
0.39	2.3	3.1	5.1	7.9	11.6
0.49	2.4	3.2	5.3	8.5	12.5

4.2.2.1 Temperature Dependence of the I_3^--Diffusion Coefficient

The determined I_3^--diffusion coefficients and the resulting VFT-plots are shown in Figure 4-9, the fitting parameters for these plots are summarised in Table 8-28. The I_3^--diffusion coefficients for all blends show a strong increase with increasing temperature. The differences between the I_3^--diffusion coefficients of specific blends at the same temperature are relatively small; tendencies are not very distinct.

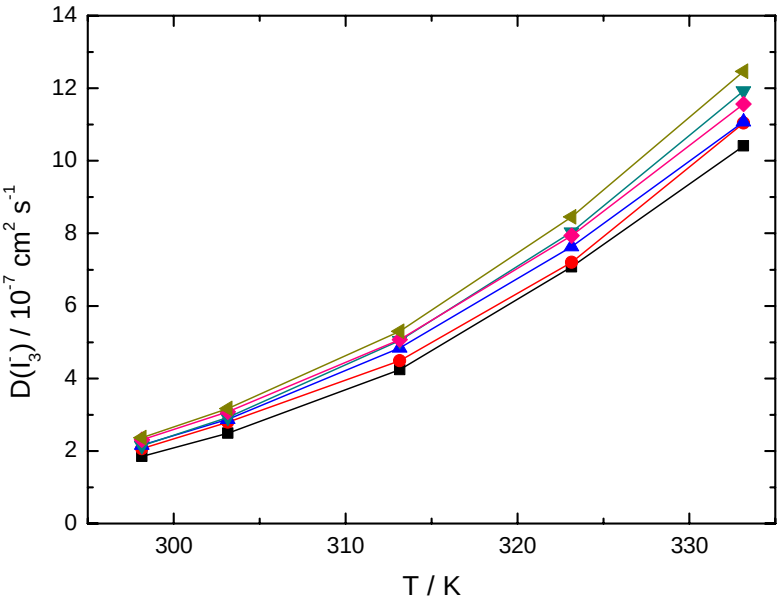

Figure 4-9: Temperature dependence of I_3^--diffusion coefficients of I_2 in mixtures of $EMIBF_4$/MPII with 80 mol% MPII at I_2 concentrations of: (—■—) 0.05 mol L^{-1}, (—●—) 0.10 mol L^{-1}, (—▲—) 0.20 mol L^{-1}, (—▼—) 0.30 mol L^{-1}, (—◆—) 0.39 mol L^{-1}, (—◀—) 0.49 mol L^{-1}.

4.2.2.2 Iodine Concentration Dependence of the I_3^--Diffusion Coefficient

The I_2 concentration dependence of the I_3^--diffusion coefficients is shown in Figure 4-10. The increase of the I_3^--diffusion with increasing I_2 concentration is relatively small but much more distinct than for EMICDA/MPII (Chap. 4.1.2). The reason for this increase is the same for both cases a decreasing viscosity at increasing iodine concentration. [54]

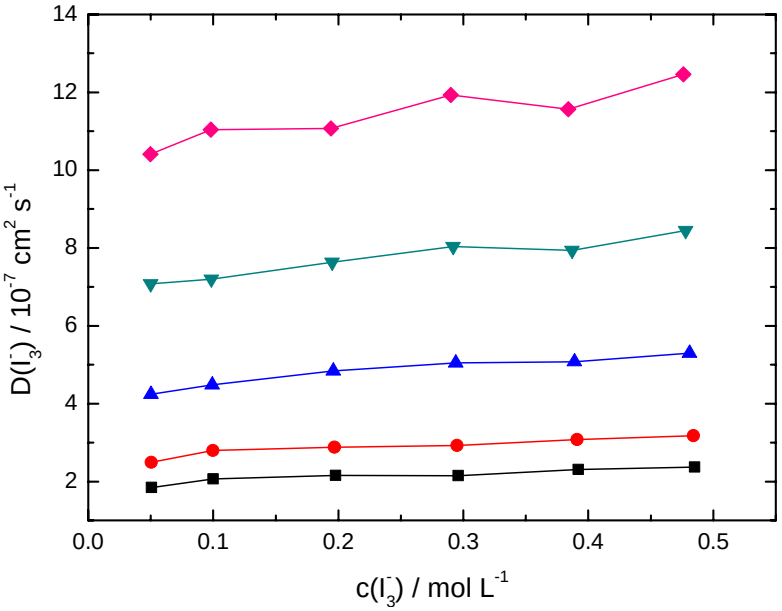

Figure 4-10: I_3^--diffusion coefficients of I_2 in mixtures of EMIBF$_4$/MPII with 80 mol% MPII as a function of the I_3^- concentration at different temperatures; θ: (—■—) 25 °C, (—●—) 30 °C, (—▲—) 40 °C, (—▼—) 50 °C, (—◆—) 60 °C.

Due to the higher viscosity for the EMIBF$_4$/MPII blends, compared to the EMIDCA/MPII blends, addition of I_2 has a stronger influence resulting in a larger viscosity loss than for the previously examined system. Therefore, the increase of the I_3^--diffusion coefficients with increasing I_2 concentration is also larger at 25 °C, 28% for EMIBF$_4$/MPII compared to 10% for EMIDCA/MPII but decreasing with increasing temperature (20% at 60 °C) again caused by a decreasing viscosity.

Since for both systems, EMIDCA/MPII and EMIBF$_4$/MPII, no significant improvement of the I_3^--diffusion was achieved by increasing I_2 concentration, all following systems were only studied with a variation of iodide concentration at constant I_2 concentration of 0.05 mol L^{-1}.

4.3 EMIOTf/MPII

1-Ethyl-3-methylimidazolium trifluoromethanesulfonate (EMIOTf) was studied as solvent IL due to its sufficient electrochemical and chemical stability. [137] The viscosity of EMIOTf (42.7 mPa s at 25 °C [144]) is only slightly higher than for $EMIBF_4$ and hence sufficiently low to reduce the viscosity of the resulting electrolyte if mixed with MPII.

Due to the small effect of increasing I_2 concentration on the I_3^--diffusion for the systems EMIDCA/MPII and $EMIBF_4$/MPII, the system EMIOTf/MPII was only examined with varying MPII concentration at constant I_2 concentration.

As for the previous systems, the system EMIOTf/MPII was examined over a broad IL mixing range, varying from 10 mol% MPII to 100 mol% MPII, at a constant I_2 concentration of 0.05 mol L^{-1}. For each MPII concentration the I_3^--diffusion coefficient was determined at five different temperatures, ranging from 25 °C to 60 °C, and at least three times for each temperature. The determined diffusion coefficients and their calculated and exact mean values with standard deviations are shown in Chap. 8.1.3, along with the corresponding measurement parameters and examples of the recorded steady-state CVs. The resulting standard deviations for this electrolyte system are typically < 1% and therefore lower than the estimated relative maximum error of 5% (Chap. 3.2.4). The mean values of the I_3^--diffusion coefficients at each temperature and MPII concentration are also listed in Table 4-5.

Table 4-5: I_3^--diffusion coefficients of 0.05 mol L^{-1} I_2 in mixtures of EMIOTf/MPII at varying MPII concentrations.

$D \cdot 10^7$ [cm^2 s^{-1}]					
ϑ [°C] / Mol% MPII	**25**	**30**	**40**	**50**	**60**
10.1	3.0	3.7	5.4	7.4	9.8
20.1	3.1	3.8	5.5	7.8	10.3
30.1	3.0	3.7	5.5	7.6	10.4
40.0	2.9	3.7	5.5	7.8	10.6
50.1	2.8	3.6	5.5	8.0	11.1
60.1	2.6	3.3	5.2	7.6	10.7
70.0	2.3	3.0	4.9	7.6	10.9
79.9	2.0	2.7	4.5	7.0	10.1
100	1.2	1.7	3.0	4.9	7.4

4.3.1 Temperature Dependence of the I_3^--Diffusion Coefficient

The temperature dependence of the I_3^--diffusion coefficients is made clear in Figure 4-11 where the determined I_3^--diffusion coefficients and the resulting VFT-plots are shown. The fitting parameters of these VFT-plots which are summarised in Table 8-37 were achieved with the smallest errors of all investigated systems due to a slightly modified measurement procedure.

The I_3^--diffusion coefficients for all blends show a strong increase with increasing temperature. The magnitude of the relative growth varies strongly within the mixing range, increasing from 225% for 10 mol% MPII to 509% for 100 mol% MPII. The absolute value of the growth varies between $6.2 \cdot 10^{-7}$ cm^2 s^{-1} and $8.6 \cdot 10^{-7}$ cm^2 s^{-1} with slight minima at both ends of the mixing range and the maximum in the region from 50 mol% MPII to 70 mol% MPII.

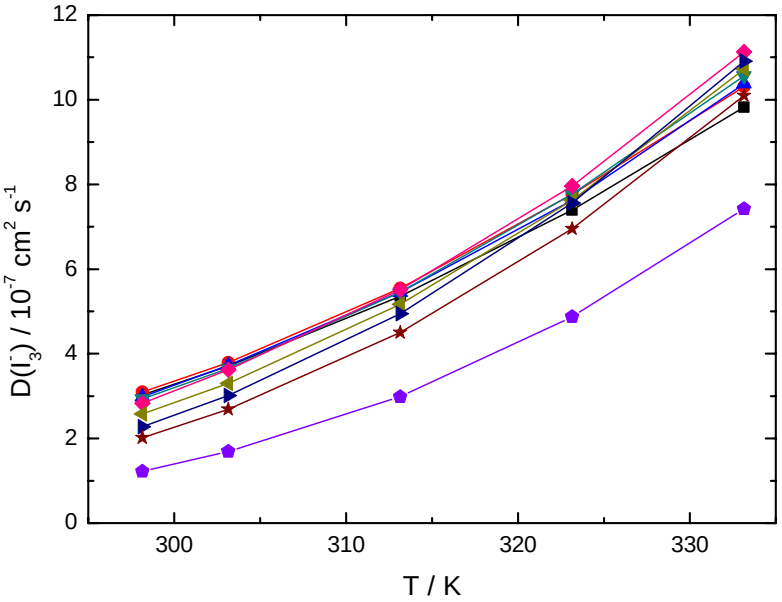

Figure 4-11: Temperature dependence of I_3^--diffusion coefficients of 0.05 mol L^{-1} I_2 in mixtures of EMIOTf/MPII at varying MPII concentrations; (—■—) 10 mol% MPII, (—●—) 20 mol% MPII, (—▲—) 30 mol% MPII, (—▼—) 40 mol% MPII, (—◆—) 50 mol% MPII, (—◀—) 60 mol% MPII, (—▶—) 70 mol% MPII, (—★—) 80 mol% MPII, (—⬟—) 100 mol% MPII.

For this electrolyte system, the critical value of $1 \cdot 10^{-6}$ cm^2 s^{-1} for the diffusion limitation in DSSCs is only reached at 60 °C, except in the much lower values of the blend with 100 mol% MPII. Therefore, application of electrolytes based on binary mixtures of EMIOTf and MPII in DSSCs always leads to diffusion limited DSSC-efficiencies with one exception for operating temperatures of > 60 °C.

4.3.2 Iodide Concentration Dependence of the I_3^--Diffusion Coefficient

In Figure 4-12 the I_3^--diffusion coefficients of the system EMIOTf/MPII are shown as a function of MPII concentration at varying temperatures. The I_3^- diffusion coefficients at lower temperatures stay nearly constant in the region between 10 mol% MPII and 50 mol% MPII and do not decrease until a further increase of the MPII concentration. The behaviour at 40 °C and 50 °C is similar but the beginning of the decrease shifts to higher MPII concentrations and a slight maximum is formed at 50 mol% MPII. The I_3^--diffusion coefficients at 60 °C increase with increasing MPII concentration until the maximum between 50 mol% MPII and 70 mol% MPII is reached.

All in all, the iodide concentration dependence of the I_3^--diffusion coefficients stays in strong contrast to the iodide concentration dependence of the viscosity of this system which shows an approximate exponential increase with increasing MPII concentration. This is again a hint of the existence of a non-Stokesian charge transport mechanism.

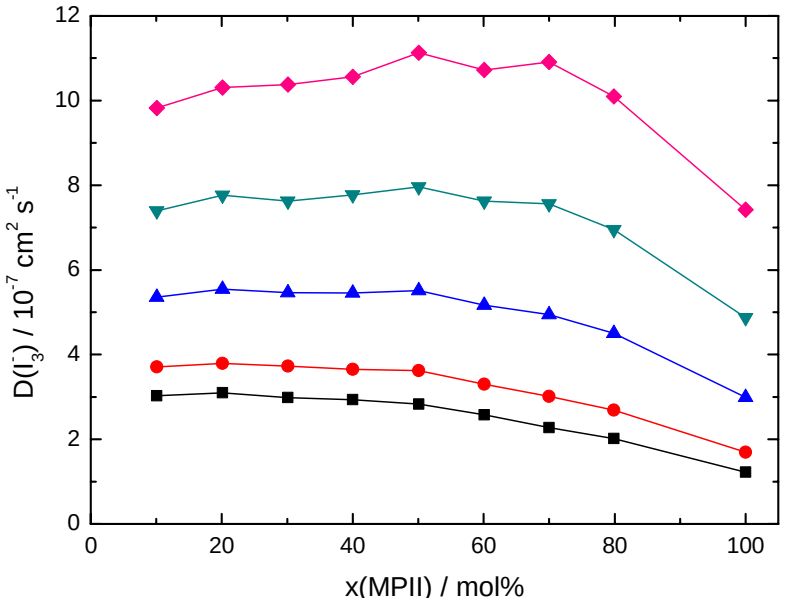

Figure 4-12: I_3^--diffusion coefficients of 0.05 mol L^{-1} I_2 in mixtures of EMIOTf/MPII as a function of the MPII concentration at different temperatures; θ: (—■—) 25 °C, (—●—) 30 °C, (—▲—) 40 °C, (—▼—) 50 °C, (—◆—) 60 °C.

Similar to the system $EMIBF_4$/MPII the limiting value of $1 \cdot 10^{-6}$ cm^2 s^{-1} is only reached or exceeded at 60 °C but then for all EMIOTf containing blends. With reference to a preferably high I_3^--diffusion coefficient and iodide concentration the blends with

50-70 mol% MPII are the most recommendable electrolyte compositions based on EMIOTf and MPII for application in DSSCs.

Figure 4-13 shows the behaviour of the Einstein-Stokes ratios as a function of the MPII concentration at varying temperatures. In line with the previously examined electrolyte systems the Einstein-Stokes ratios for the system EMIOTf/MPII increase strongly with rising MPII concentration. The magnitude of the growth is smaller than for the other systems and decreases with rising temperature from 580% at 25 °C passing 440% at 40 °C to 330% at 60 °C.

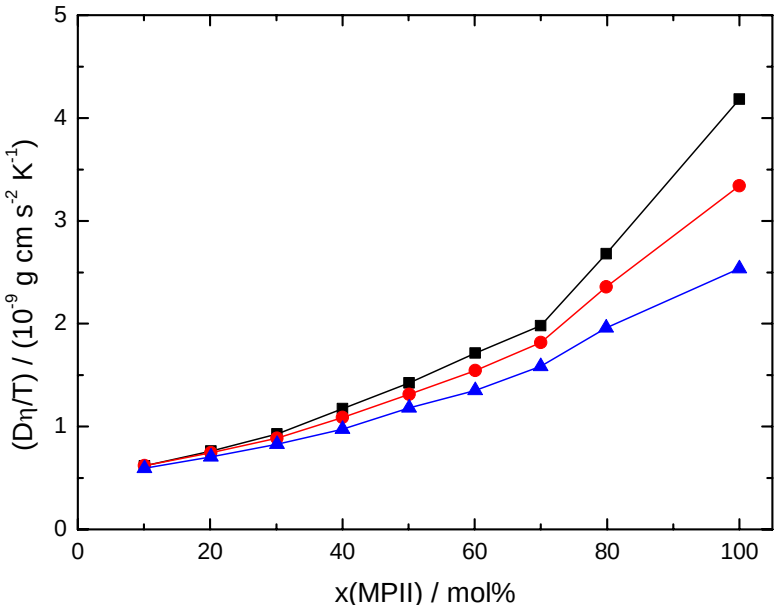

Figure 4-13: Einstein-Stokes ratios of 0.05 mol L^{-1} I_2 in mixtures of EMIOTf/MPII as a function of the MPII concentration at different temperatures; *θ*: (—■—) 25 °C, (—●—) 40 °C, (—▲—) 60 °C.

This behaviour is based again on the enhancement of the overall I_3^--diffusion by a non-Stokesian charge transport. The impact of this charge transfer mechanism on the overall I_3^--transport decreases with rising temperature, decreasing viscosity and simultaneously increasing physical I_3^--diffusion. In spite of that, its impact is not only large enough to counterbalance the increasing viscosity at lower temperatures (nearly constant I_3^--diffusion coefficients over broad mixing range) but also to exceed its influence at higher temperatures, leading to a maximum of the I_3^--diffusion coefficients in the region between 50 mol% MPII and 70 mol% MPII.

4.4 $EMINTf_2$/MPII

1-Ethyl-3-methylimidazolium bis(trifluoromethylsulfonyl)imide ($EMINTf_2$) has several features which are of interest for a possible application in DSSCs. For example, a comparatively low viscosity (34 mPa s at 25 °C [145]), a high liquid range [69,146] as well as a high chemical and electrochemical stability [137]. The most interesting feature and the most important reason for its examination during this study is its hydrophobic behaviour [70,147], which is based on the bis(trifluoromethylsulfonyl)imide-anion. This is especially important because all previously tested solvent ILs were hydrophilic and a inert-gas atmosphere was needed for all work steps to inhibit changes of physical properties by adsorption of water as well as decomposition reactions induced by water. Since working under inert-gas atmosphere is one of the most expensive parts of the DSSCs production, application of hydrophobic electrolytes would bring a big advantage.

Like the system EMIOTf/MPII the system $EMINTf_2$/MPII was only examined with varying MPII concentration at constant I_2 concentration.

Like the previous systems, the system $EMINTf_2$/MPII was examined over a broad IL mixing range, varying from 10 mol% MPII to 100 mol% MPII, at a constant I_2 concentration of 0.05 mol L^{-1}. For each MPII concentration, the I_3^--diffusion coefficient was determined at five different temperatures, ranging from 25 °C to 60 °C and at least three times for each temperature. The determined diffusion coefficients and their calculated and exact mean values with standard deviations are shown in Chap. 8.1.4 along with the corresponding measurement parameters and examples of the recorded steady-state CVs. The resulting standard deviations for this electrolyte system are typically < 2% and therefore lower than the estimated relative maximum error of 5% (Chap. 3.2.4). The mean values of the I_3^--diffusion coefficients at each temperature and MPII concentration are also listed in Table 4-6.

Table 4-6: I_3^--diffusion coefficients of 0.05 mol L^{-1} I_2 in mixtures of EMINTf$_2$/MPII at varying MPII concentrations.

$D \cdot 10^7$ [cm^2 s^{-1}]					
θ [°C] / Mol% MPII	**25**	**30**	**40**	**50**	**60**
10.1	4.1	4.9	6.8	9.2	12.1
19.9	3.7	4.4	6.3	8.8	11.7
30.0	3.5	4.4	6.4	9.0	12.1
40.0	3.1	3.8	5.7	8.3	11.2
50.1	3.1	3.8	5.7	8.0	11.0
60.0	2.7	3.4	5.3	8.2	11.6
70.0	2.4	3.2	5.0	7.2	10.2
80.0	2.2	2.9	4.7	7.2	10.5
100.0	1.2	1.7	3.0	4.9	7.4

4.4.1 Temperature Dependence of the I_3^--Diffusion Coefficient

The temperature dependence of the I_3^--diffusion coefficients is made clear in Figure 4-14, where the determined I_3^--diffusion coefficients and the resulting VFT-plots are shown. The fitting parameters of these VFT-plots are summarised in Table 8-47. The I_3^--diffusion coefficients for all blends of this system show again a strong increase with increasing temperature. The magnitude of the relative growth varies strongly within the mixing range, increasing from 200% for 10 mol% MPII to 509% for 100 mol% MPII, whereas the absolute value of the growth oscillates between $7.8 \cdot 10^{-7}$ cm^2 s^{-1} and $8.9 \cdot 10^{-7}$ cm^2 s^{-1} in the region from 10 mol% MPII to 80 mol% MPII.

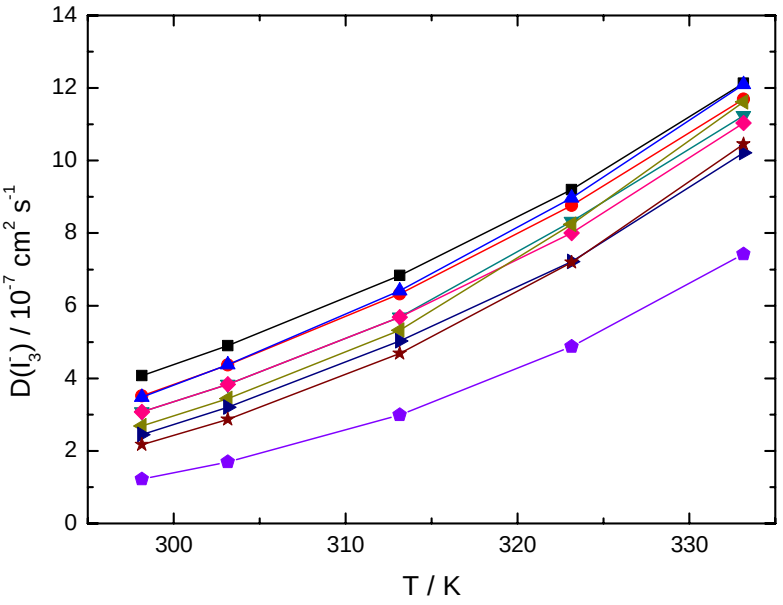

Figure 4-14: Temperature dependence of I_3^--diffusion coefficients of 0.05 mol L^{-1} I_2 in mixtures of EMINTf$_2$/MPII at varying MPII concentrations; (—■—) 10 mol% MPII, (—●—) 20 mol% MPII, (—▲—) 30 mol% MPII, (—▼—) 40 mol% MPII, (—◆—) 50 mol% MPII, (—◀—) 60 mol% MPII, (—▶—) 70 mol% MPII, (—★—) 80 mol% MPII, (—⬟—) 100 mol% MPII.

As for the systems EMIBF$_4$/MPII and EMIOTf/MPII, the I_3^--diffusion coefficients of the system EMINTf$_2$/MPII exceed the critical value of $1 \cdot 10^{-6}$ cm^2 s^{-1} at 60 °C, except the much lower values of the blend with 100 mol% MPII. Therefore, application of electrolytes based on binary mixtures of EMINTf$_2$ and MPII in DSSCs always leads to diffusion limited DSSC-efficiencies with one exception for operating temperatures of > 60 °C.

4.4.2 Iodide Concentration Dependence of the I_3^--Diffusion Coefficient

In Figure 4-15 the I_3^--diffusion coefficients of the system EMINTf$_2$/MPII are shown as a function of MPII concentration at varying temperatures. The behaviour of the I_3^--diffusion coefficients with increasing MPII concentration for this system is situated between their behaviour for the systems EMIDCA/MPII and EMIBF$_4$/MPII. The I_3^--diffusion coefficients decrease with increasing MPII concentration but the decrease flattens at rising temperatures.

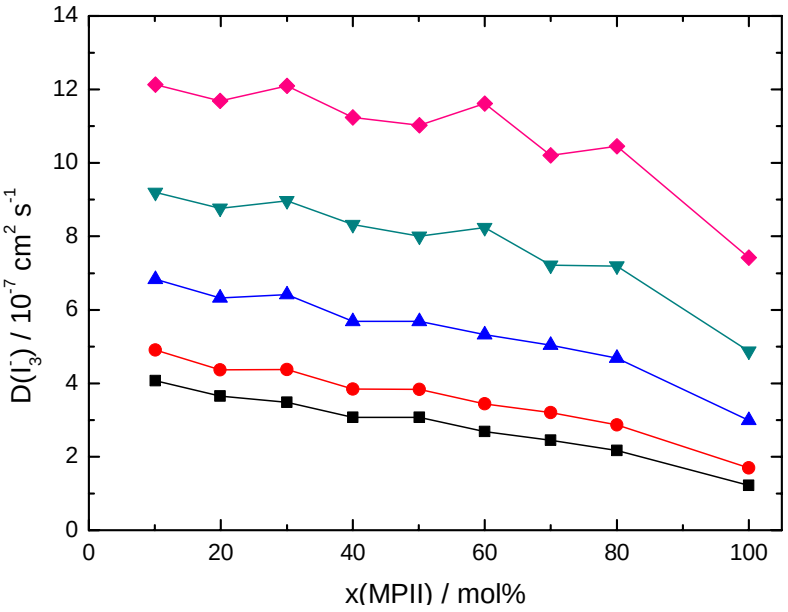

Figure 4-15: I_3^--diffusion coefficients of 0.05 mol L^{-1} I_2 in mixtures of EMINTf$_2$/MPII as a function of the MPII concentration at different temperatures; θ: (—■—) 25 °C, (—●—) 30 °C, (—▲—) 40 °C, (—▼—) 50 °C, (—◆—) 60 °C.

The system EMINTf$_2$/MPII has the second highest I_3^--diffusion coefficients of all examined systems, but again the limiting value of $1 \cdot 10^{-6}$ cm^2 s^{-1} is only exceeded at 60 °C. Since high iodide concentrations are beneficial for application in DSSCs and due to the fact that there is only little difference between the I_3^--diffusion coefficients in the region from 10 mol% MPII to 60 mol% MPII at higher temperatures, the blends with 10-60 mol% MPII would be the preferred electrolyte compositions for application in DSSCs.

In Figure 4-16 the behaviour of the Einstein-Stokes ratios as a function of the MPII concentration at varying temperatures is shown. In line with the previously examined electrolyte systems the Einstein-Stokes ratios for the system EMINTf$_2$/MPII increase

strongly with rising MPII concentration. The magnitude of the increase is the largest of all examined systems and decreases with rising temperature from 760% at 25 °C passing 620% at 40 °C to 500% at 60 °C.

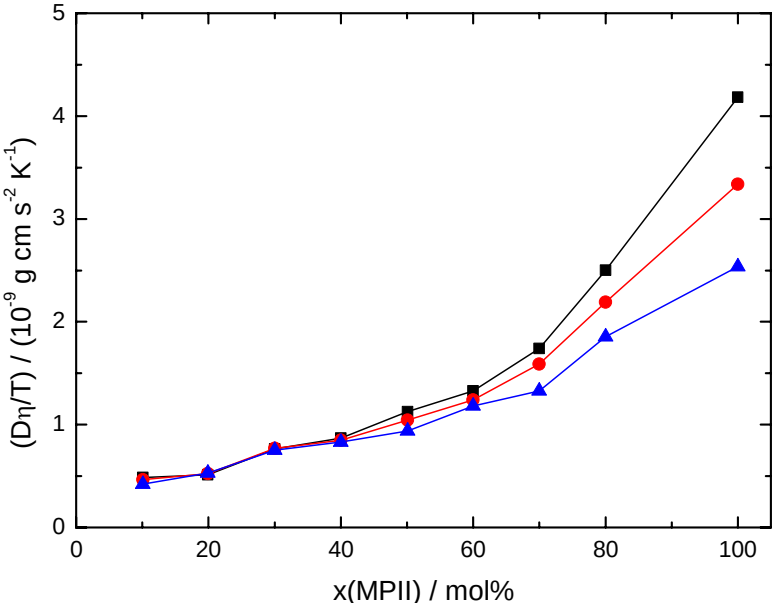

Figure 4-16: Einstein-Stokes ratios of 0.05 mol L^{-1} I_2 in mixtures of $EMINTf_2$/MPII as a function of the MPII concentration at different temperatures; *θ*: (—■—) 25 °C, (—●—) 40 °C, (—▲—) 60 °C.

This behaviour indicates again the enhancement of the overall I_3^--diffusion by a non-Stokesian charge transport.

4.5 Summary and Appraisal of Results

The influence of MPII concentration and temperature on I_3^--diffusion was examined at constant I_2 concentration for the electrolyte systems EMIDCA/MPII, $EMIBF_4$/MPII, EMIOTf/MPII, and $EMINTf_2$/MPII. Additionally, the influence of I_2 concentration on I_3^--diffusion was examined for EMIDCA/MPII and $EMIBF_4$/MPII at 80 mol% MPII and varying temperatures.

Compared to the other examined electrolyte systems the system EMIDCA/MPII has the highest I_3^--diffusion coefficients over the whole mixing and temperature range. The critical value of $1 \cdot 10^{-6}$ cm^2 s^{-1} for diffusion limitation of the DSSC is exceeded for every blend of the examined systems at 60 °C, except for the blend with 100 mol% MPII. It is already exceeded at 40 °C and 50 °C in EMIDCA based blends with high EMIDCA contents.

A comparison of I_3^--diffusion coefficients of the four examined electrolyte systems at 25 °C and 60 °C is shown in Figure 4-17 A and B. It proves that the exceptionally fast I_3^--diffusion in EMIDCA based blends compared to the other blends is also valid at higher temperatures. The I_3^--diffusion coefficients in the system EMIDCA/MPII increase continuously with decreasing MPII concentration, reaching the maximum values for all measurement temperatures at the lowest MPII concentration. This stays in clear contrast to the other electrolyte systems where the I_3^--diffusion coefficients often stay constant over a broad MPII concentration range or even reaches their maximum at medial MPII concentrations.

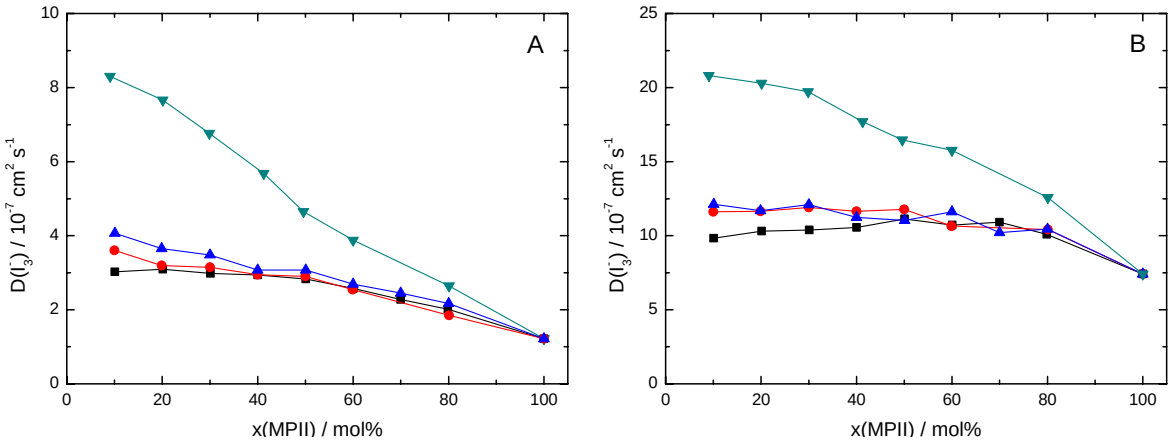

Figure 4-17: I_3^--diffusion coefficients of ≈ 0.05 mol L^{-1} I_2 in mixtures of MPII and varying solvent ILs at 25 °C (A) and 60 °C (B) as a function of the MPII concentration; (—■—) EMIOTf/MPII, (—●—) $EMIBF_4$/MPII, (—▲—) $EMINTf_2$/MPII, (—▼—) EMIDCA/MPII.

The Einstein-Stokes ratios for all examined electrolyte systems strongly increase with increasing MPII concentration and viscosity and do not obey the Einstein-Stokes equation, as shown in Figure 4-18 for the Einstein-Stokes ratios at 25 °C (A) and 60 °C (B). The Einstein-Stokes ratios for the two higher viscous electrolyte systems (EMIOTf/MPII and $EMIBF_4$/MPII) increase nearly linearly whereas for EMIDCA/MPII and $EMINTf_2$/MPII they show a rather exponential increase with increasing MPII concentration.

A possible explanation for the generally non-Stokesian behaviour is a change in the mechanism of mass- or charge-transport from a pure physical diffusion process to a chemical or electronic exchange mechanism, similar to the Grotthus-mechanism. This non-Stokesian charge transport occurs additionally to the diffusive charge transport and enhances the overall I_3^--diffusion. The impact of the non-Stokesian charge transport on the overall I_3^--diffusion is reduced with increasing temperature and thereby decreasing viscosity as well as increasing physical diffusion.

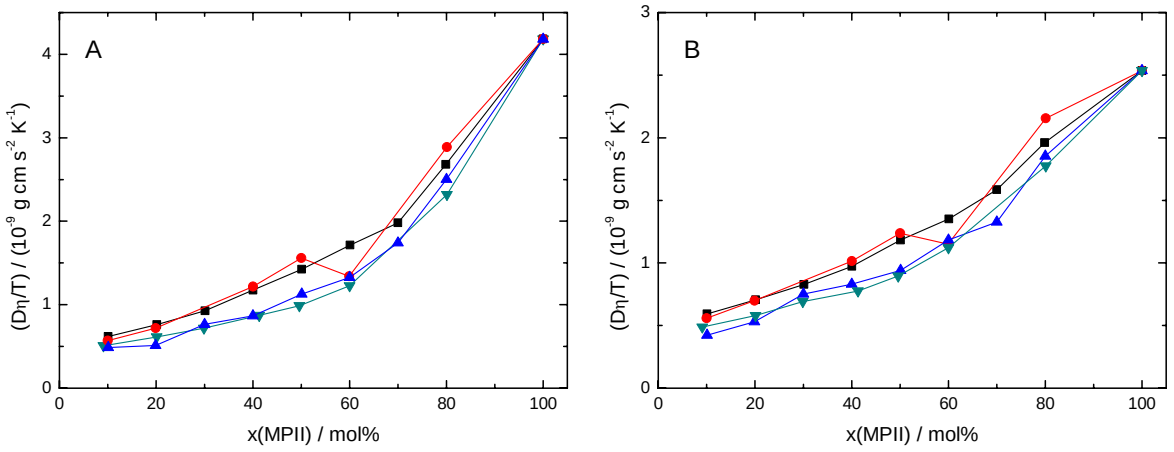

Figure 4-18: Einstein-Stokes ratios of ≈ 0.05 mol L^{-1} I_2 in mixtures of MPII and varying solvent ILs at 25 °C (A) and 60 °C (B) as a function of the MPII concentration; (—■—) EMIOTf/MPII, (—●—) $EMIBF_4$/MPII, (—▲—) $EMINTf_2$/MPII, (—▼—) EMIDCA/MPII.

The temperature dependence of the I_3^--diffusion coefficients was analysed according to the VFT-equation. Due to less accurate data points yielded by diffusion measurements and a too small temperature range and quantity of data points, the accuracy and therefore the significance of this analysis is not as high as for viscosity or conductivity data. Another critical point is the occurrence of the non-Stokesian charge transport and its varying impact on I_3^--diffusion at varying temperatures (Figure 4-19), for which reason the overall I_3^--diffusion coefficient is not exclusively viscosity dependent. Since the VFT-theory was introduced for temperature dependence of viscosity, rigorous analysis of other electrolyte

parameters like diffusion and conductivity according to the VFT-equation is only valid if non-Stokesian behaviour or strong temperature dependent ionic association can be excluded. Therefore, interpolation of I_3^--diffusion coefficients within the examined temperature range is possible with high accuracy, extrapolation of I_3^--diffusion coefficients to lower or higher temperatures yields results with lower reliability.

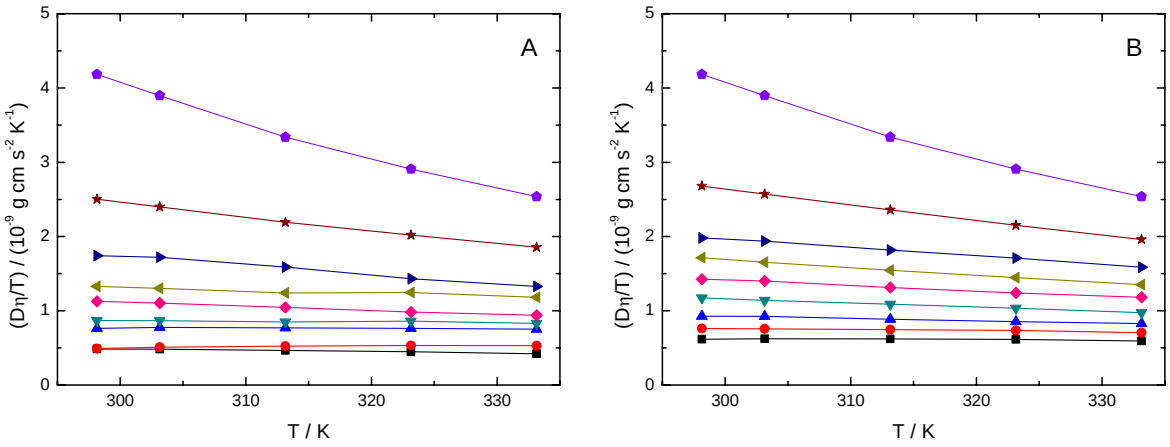

Figure 4-19: Temperature dependence of Einstein-Stokes ratios of 0.05 mol L^{-1} I_2 in mixtures of $EMINTf_2$/MPII (A) and EMIOTf/MPII (B) at varying MPII concentrations; (—■—) 10 mol% MPII, (—●—) 20 mol% MPII, (—▲—) 30 mol% MPII, (—▼—) 40 mol% MPII, (—◆—) 50 mol% MPII, (—◀—) 60 mol% MPII, (—▶—) 70 mol% MPII, (—★—) 80 mol% MPII, (—⬟—) 100 mol% MPII.

The influence of the I_2 concentration on I_3^--diffusion is small. The small increase of the I_3^--diffusion coefficients with increasing I_2 concentration is not based on a change of the charge transport mechanism but on a decrease of viscosity in the same magnitude. This effect increases with increasing electrolyte viscosity, and is therefore more distinct for the system $EMIBF_4$/MPII than for EMIDCA/MPII. Application of high I_2 concentrations in electrolytes for DSSCs abolishes diffusion limitations, since the limiting current is also proportional to the I_3^--concentration, but leads to enhanced light absorption by the electrolyte and enhanced recombination processes and therefore reduced efficiencies and stabilities. Due to these drawbacks and the little increase of I_3^--diffusion with increasing I_2 concentration, the I_2 concentration 0.05 mol L^{-1} was defined as standard I_2 concentration for all following measurements.

Simultaneous to the diffusion measurements at UMEs presented in Chap. 4, I_3^--diffusion coefficients in the same electrolyte blends were also examined with polarisation measurements at thin layer cells (TLCs) by Zistler [54]. Similar to steady-state measurements at UMEs, polarisation measurements at TLCs are also a frequently used and reliable

technique for determination of diffusion coefficients. [13,22,27,130] Advantages and disadvantages as well as measurement accuracy for both methods are compared in Ref. [130]. For both measurement techniques, the determined I_3^--diffusion coefficients show the same behaviour. The diffusion coefficients determined with UMEs are typically about 10% lower than the ones determined at TLCs. [27,54] A comparison of I_3^--diffusion coefficients determined at UMEs and TLCs for the systems EMIOTf/MPII (A) and EMIDCA/MPII (B) at varying temperatures is shown in Figure 4-20.

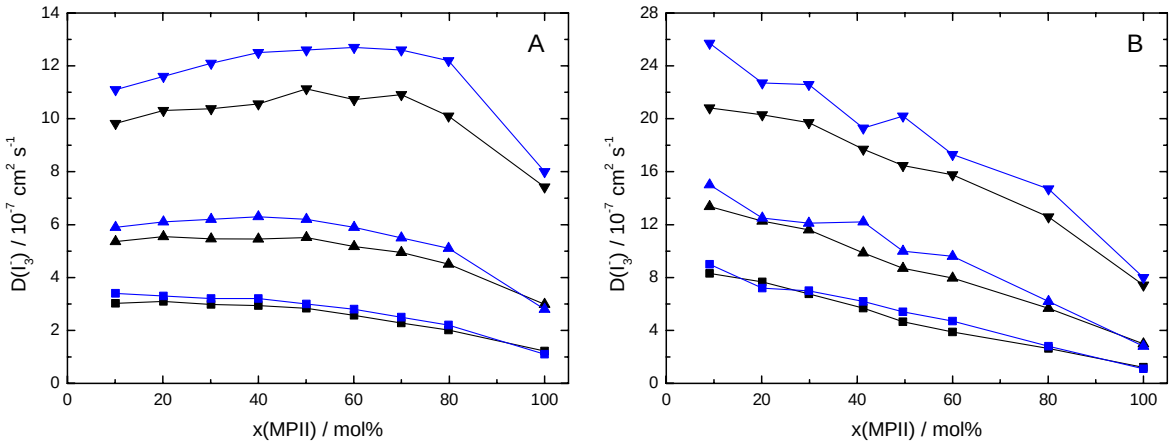

Figure 4-20: I_3^--diffusion coefficients of 0.05 mol L^{-1} I_2 in mixtures of EMIOTf/MPII (A) and EMIDCA/MPII (B) as a function of the MPII concentration determined at UMEs (—) and TLCs (—) at varying temperatures; *θ*: (—■—) and (—■—) 25 °C, (—▲—) and (—▲—) 40 °C, (—▼—) and (—▼—) 60 °C; TLC data from Ref. [54].

Larger deviations between I_3^--diffusion coefficients determined at UMEs and TLCs occur only for high iodine concentrations and elevated temperatures. At these conditions the Pt electrode of the TLCs is assumed to be corroded by the iodine, reducing the effective electrode surface and the resulting limiting current. [27,54]

5 Conductivity Measurements

For this study two different kinds of conductivity measurements were applied: a) a stationary and highly accurate method at constant temperature; b) a dynamic method with simultaneous recording of conductivity and temperature as a function of time. Both methods are explained in detail in Chaps. 3.3 and 3.4.

Advantages and disadvantages of both methods are also explained in detail and discussed in Chaps. 3.3 and 3.4. The main advantage of the stationary method is the high accuracy due to accurate calibration, frequency-dependent resistance measurement, and high precise temperature control. However, this involves time-consuming measurements. The main advantage of the dynamic method is the fast and automated recording of measurement data. The major drawback is the sample volume-dependent cell constant. The two methods do not only have different advantages and disadvantages but also serve different purposes. The results obtained with the stationary method were used for evaluation of charge transport properties and comparison with the results obtained by diffusion measurements. Additionally, the determined specific conductivities were used for calibration of the G(t)-T(t)-measuring cells. These cells were used for continuous and simultaneous conductivity and temperature measurements which should facilitate determination of hardly detectable phase transition points and solubility limits in electrolyte mixtures.

To realise a meaningful comparison of the results obtained by diffusion and conductivity measurements, the examined mixtures have nearly identical compositions or were in fact identical.

5.1 Stationary Conductivity Measurements

In general, stationary conductivity measurements were performed in a similar temperature range as diffusion measurements in Chap. 4, but slightly expanded to lower temperatures. If conductivity was sufficient large for detection and no solidification of the substance or blend occurred, the lower limit of the measurement range was at 5 °C otherwise it was shifted to higher temperatures until the before mentioned requirements were fulfilled. The upper limit at 50 °C was set due to restrictions of the cryostat used and the temperature control medium.

5.1.1 Pure Ionic Liquids

In general, the specific conductivity is a critical parameter for application of ILs in electrochemical devices. [148] Despite its obvious importance, for many ILs, little or no data has been published, especially with respect to the temperature dependence of the conductivity. On the other hand, for some ILs, extensive but inconsistent data has been published, mainly based on insufficient temperature regulation and strongly varying purity grades. [149]

Due to the lack of reliable conductivity data the specific conductivities of the single IL components of the potential electrolyte mixtures for DSSCs were examined to clarify the impact of specific ILs on the resulting specific conductivities of the blends. In addition, the influence of cation and anion on the conductivity was studied for several low and high viscous ILs. As mentioned above, determination of specific conductivities at various temperatures was also necessary for calibration of the later applied G(t)-T(t)-measuring cells. Supplier, purity, water contents, and viscosities of the examined ILs are listed in Table 5-1. If no supplier is given, the ILs were synthesised by Schreiner or Gerhard (see Chap. 3.1). Low and comparable water contents are crucial since they have a major influence on the viscosity and therefore also on the conductivity [149].

Table 5-1: Supplier, purities, water contents, and viscosities at 25 °C $\eta_{25\,°C}$ of the examined ILs.

Substance	Supplier	Purity	Water content [ppm]	$\eta_{25\,°C}$ [mPa s]
$BMIBF_4$	-	-	40	180 [143]
BMPlFAP	Merck	high-purity®	41	-
$BMPlNTf_2$	Merck	ultra pure®	18	85 [150]
BMPlOTf	Merck	high-purity®	-	-
$EMIBF_4$	-	-	23	37 [143]
EMIDCA	-	-	20	21 [136]
$EMINTf_2$	-	-	21	34 [145]
EMIOTf	Solvent Innovation	> 99%	108	42.7 [144]
$HMINTf_2$	Merck	ultra pure®	52	87.3[a] [151]
Me_3SDCA	-	-	-	27.2[a] [152]
MPII	-	-	75	1620[a] [130]

[a] At 20 °C.

The determined specific conductivities at each temperature are listed in Table 5-2. The absence of some values at lower temperatures results from conductivities that are too low

for the applied measuring cells or from melting points that are too high. Solidification of samples within the measuring cell may become a problem, because some solids slightly expand with increasing temperature before melting, resulting in damage to the measuring cell. [153]

Table 5-2: Temperature dependence of specific conductivities of pure ionic liquids.

κ [mS cm^{-1}]						
T [K] / Substance	**278.148**	**288.152**	**298.149**	**303.152**	**313.152**	**323.152**
$BMIBF_4$	1.123	2.088	3.538	4.469	6.79	9.75
BMPlFAP	-	0.676	1.201	1.547	2.438	3.600
$BMPlNTf_2$	-	1.762	2.786	3.409	4.914	6.749
BMPlOTf	-	1.187	1.989	2.498	3.775	5.40
$EMIBF_4$	-	-	15.57	18.29	24.44	31.42
EMIDCA	15.49	21.80	29.19	33.25	42.05	51.66
$EMINTf_2$	4.310	6.466	9.13	10.63	14.00	17.81
EMIOTf	3.902	5.894	8.42	9.88	13.20	17.06
$HMINTf_2$	-	1.375	2.205	2.719	3.973	5.52
Me_3SDCA	12.45	18.31	25.40	29.40	38.30	48.29
MPII	-	-	0.6099	0.893	1.760	3.139

For BMPlFAP and BMPlOTf no conductivity data have been published yet; for Me_3SDCA the only conductivity data yet published is the specific conductivity at 25 °C [152]. Comparison of conductivity data of the remaining ILs (Table 5-2) with values from literature is difficult because for some ILs extensive, but inconsistent data have been published, as shown in Table 5-3 for EMINTf2.

Table 5-3: Comparison of the determined specific conductivity of $EMINTf_2$ with literature values.

T [K]	κ [mS cm^{-1}]	Ref.
299	8.4	[146]
298	10.8	[154]
298	9.2	[145]
298	9.13	-
298	9.12	[149]
295	8.6	[155]
293	8.8	[70]

The temperature dependence of the determined specific conductivities was analysed by fitting the measurement data according to the VFT-equation (Eq. (5.1)) introduced in Chap. 2.2.1:

$$\kappa(T) = \kappa_0 \exp\left[\frac{-B}{T - T_0}\right] \tag{5.1}$$

To obtain a better resolution the specific conductivities and corresponding fits are shown in separate figures for low viscous ILs (Figure 5-1) and high viscous ILs (Figure 5-2). The corresponding fitting parameters for both kinds of ILs are listed in Table 5-9.

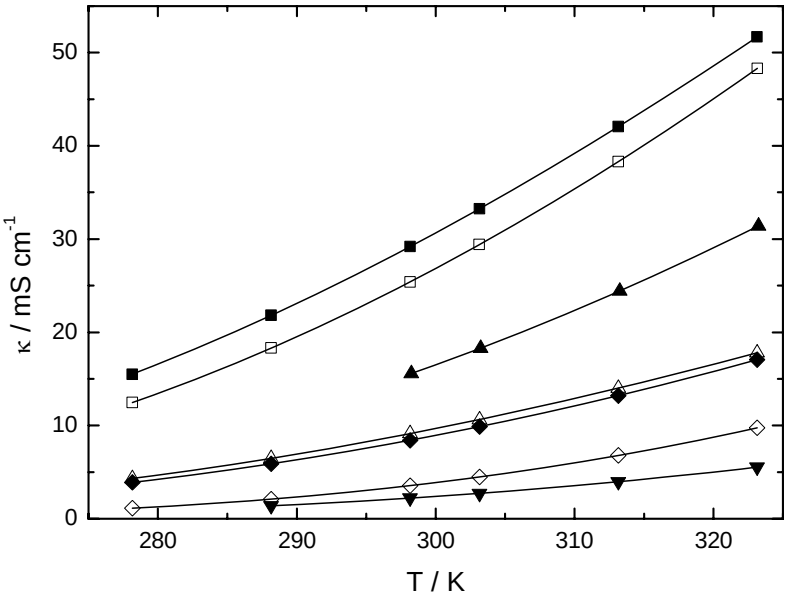

Figure 5-1: Specific conductivities of comparably low viscous ionic liquids with varying cations and anions as a function of temperature and corresponding fits according to the VFT-equation (Eq. (5.1)); (—■—) EMIDCA, (—□—) Me_3SDCA, (—▲—) $EMIBF_4$, (—△—) $EMINTf_2$, (—◆—) EMIOTf, (—◇—) $BMIBF_4$, (—▼—) $HMINTf_2$.

As shown in Figure 5-1 the specific conductivity of an imidazolium based IL strongly decreases with increasing alkyl chain length in the 1-alkyl-3-methylimidazolium-cation ($EMBF_4$ ➞ $BMIBF_4$, $EMINTf_2$ ➞ $HMINTf_2$). One reason for the decreasing conductivity is that the growing alkyl chain length causes an increase in viscosity (Table 5-1) based on increasing van der Waals interactions. The simultaneously increasing ion radius additionally decreases the ion mobility and therefore also the conductivity. A third reason

is that growing alkyl chains in the imidazolium cation typically also entail decreasing densities of the ILs and therefore ion concentrations. [69,156,157]

As an IL based on an aliphatic onium cation, Me_3SDCA, shows a very high conductivity. Its difference from the conductivity of EMIDCA is based on a slightly higher viscosity (23.4 mPa s at 25 °C, calculated according to Eq. (2.17) from viscosity data in Ref. [152]) and a more distinct tendency to ionic association. In general, higher conductivity and lower viscosity of trialkylsulfonium salts compared to corresponding ILs also based on aliphatic onium cations, such as tetraalkylammonium or pyrrolidinium salts, are basically related to the planarity of the sulfonium-cation. [157-159]

The specific conductivity of ILs also strongly varies with variation of the anionic species as shown in Figure 5-1 for 1-ethyl-3-methylimidazolium (EMI) based ILs and in Figure 5-2 for 1-butyl-1-methylpyrrolidinium (BMPl) based ILs. The conductivity for the EMI based ILs follows the order EMIDCA > $EMIBF_4$ > $EMINTf_2$ > EMIOTf and resembles therefore only partially the trend of the viscosity (EMIDCA > $EMINTf_2$ > $EMIBF_4$ > EMIOTf, see Table 5-1). According to Noda et al. [68] the larger tendency to ionic association in bis(trifluoromethylsulfonyl)imide (NTf_2) based ILs, when compared with tetrafluoroborate (BF_4) based ILs, has major but contrary impact on viscosity and conductivity of these ILs. Formation of ion pairs and larger neutral aggregates reduces the concentration of charge carriers and increases consequently the mean distance between charged species. Thus, Coulombic interactions between the ionic species are reduced and may cause a decrease of the viscosity. [68] Despite a reduced viscosity the conductivity decreases due to the reduced concentration of charge carriers. A similar behaviour can be assumed for trifluoromethanesulfonate (OTf) based IL since ionic association in EMIOTf was found to be more distinct than in $EMINTf_2$. [69,71]

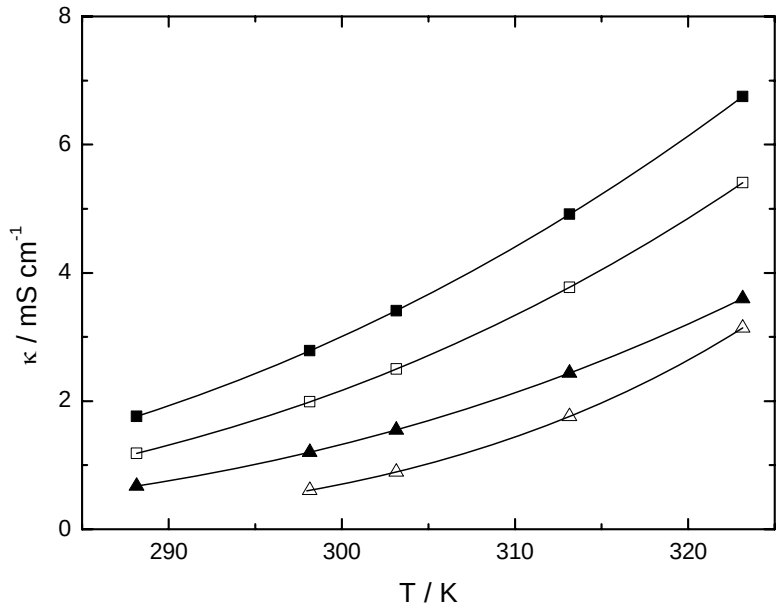

Figure 5-2: Specific conductivities of comparably high viscous ionic liquids as a function of temperature and corresponding fits according to the VFT-equation (Eq. (5.1)); (—■—) BMPlNTf$_2$, (—□—) BMPlOTf, (—▲—) BMPlFAP, (—△—) MPII.

The conductivity for the BMPl based ILs (Figure 5-2) follows the order BMPlNTf$_2$ > BMPlOTf > BMPlFAP. Ignat'ev et al. [147] reported a similar behaviour for the conductivities of the corresponding EMI based ILs and related it basically to viscosity differences. Despite the much larger anion radius the conductivity of BMPlFAP is only slightly lower than for BMPlOTf due to the weak tendency of the tris(pentafluoroethyl)-trifluorophosphate (FAP)-anion to ionic association compared to the smaller but more basic OTf-anion. [147]

MPII shows the lowest conductivity of all investigated ILs primarily based on its comparatively high viscosity (Table 5-1).

5.1.2 EMIDCA/MPII

Similar to the diffusion measurements for the system EMIDCA/MPII the influence of the MPII concentration on the specific conductivity was examined as well as its temperature dependence. To study the influence of the MPII concentration on the specific conductivity, the system EMIDCA/MPII was examined over a broad IL mixing range, varying from 11 mol% MPII to 100 mol% MPII, at a constant I_2 concentration of ≈ 0.05 mol L^{-1}. The accurate I_2 concentrations for each blend are given in Table 8-48 (Chap. 8.2.1). The lower limit of the studied temperature range was at 5 °C, the upper limit at 50 °C. The determined specific conductivities at each MPII concentration and temperature are listed in Table 5-4. The value of the blend with 100 mol% MPII at 5 °C could not be determined, since at this temperature the specific conductivity was too low for the applied measuring cells.

Table 5-4: Specific conductivities of ≈ 0.05 mol L^{-1} I_2 in mixtures of EMIDCA/MPII at varying MPII concentrations.

κ [mS cm^{-1}]					
T [K] / Mol% MPII	**278.151**	**298.151**	**303.152**	**313.150**	**323.150**
10.9	11.81	23.70	27.30	35.26	44.11
20.8	8.811	18.88	22.03	29.02	36.89
30.6	6.376	14.82	17.55	23.76	30.90
41.0	4.258	10.94	13.21	18.48	24.68
50.5	2.838	8.12	10.01	14.49	19.91
60.7	1.670	5.487	6.94	10.53	15.03
81.0	0.4834	2.175	2.932	4.971	7.79
100.0	-	0.6556	0.956	1.867	3.306

Due to the very low viscosity and high conductivity of EMIDCA, blends based on EMIDCA not only show the highest I_3^--diffusion coefficients of all examined electrolyte systems, but also the highest specific conductivities.

As for the pure ionic liquids, the temperature dependence of the specific conductivities was analysed according to the VFT-equation (Eq. (5.1)). The determined specific conductivities and the resulting VFT-plots are shown in Figure 5-3, the corresponding fitting parameters

of these plots are summarised in Table 8-49. The blend with 100 mol% and ≈ 0.05 mol L^{-1} I_2 has generally a slightly higher conductivity than pure MPII based on a reduced viscosity by adding iodine to an IL and a binary blend of ILs respectively [27,130].

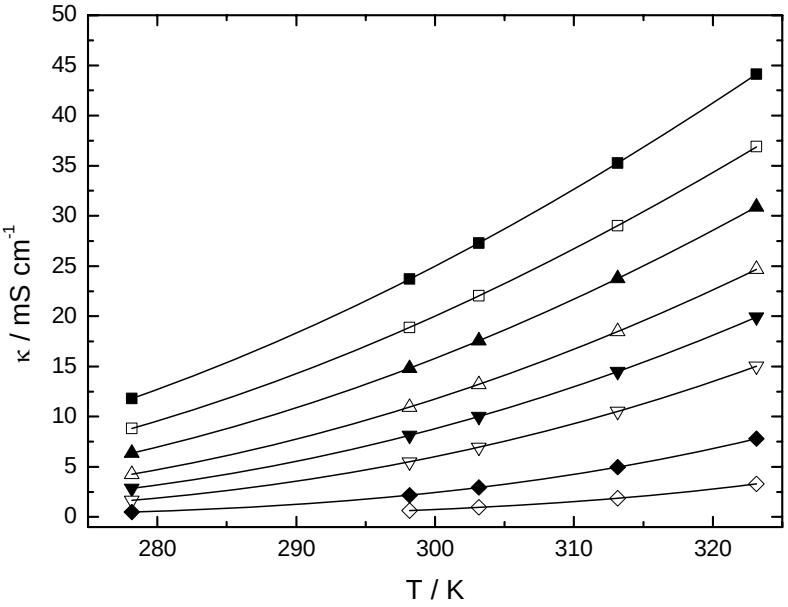

Figure 5-3: Specific conductivities of ≈ 0.05 mol L^{-1} I_2 in mixtures of EMIDCA/MPII as a function of temperature at varying MPII concentrations and corresponding fits according to the VFT-equation (Eq. (5.1)); (—■—) 11 mol% MPII, (—□—) 21 mol% MPII, (—▲—) 31 mol% MPII, (—△—) 41 mol% MPII, (—▼—) 51 mol% MPII, (—▽—) 61 mol% MPII, (—◆—) 81 mol% MPII, (—◇—) 100 mol% MPII.

The influence of the MPII concentration on the specific conductivity at varying temperatures is displayed in Figure 5-4. In contrast to the iodide concentration dependence of the I_3^--diffusion coefficients, analysing the iodide concentration dependence of the specific conductivity by means of mathematical expressions was possible. For this purpose several approaches were examined; fitting the measurement data according to a third grade polynomial (Eq. (5.2)) yielded the best results.

$$\kappa(x) = A + B_1 \cdot x + B_2 \cdot x^2 + B_3 \cdot x^3 \tag{5.2}$$

In Eq. (5.2) A, B_1, B_2, and B_3 are fitting parameters and x is the MPII concentration in mol%. The resulting plots of fitting the measurement data according to Eq. (5.2) are shown in Figure 5-4 along with the measured values, the corresponding fitting parameters are listed in Table 8-50. Since analysis of the conductivity data according to Eq. (5.2) yielded

good results, interpolation of conductivity values to Eq. (5.2) within the examined mixing range is accurate. The magnitude of the relative growth of the conductivity increases strongly with increasing MPII concentration, whereas the absolute value of the growth decreases strongly with increasing MPII concentration. In general, the tendency of conductivity with increasing MPII concentration correlates with the simultaneously increasing viscosity, but the viscosity increase is about 1.5 times larger than the conductivity loss [27].

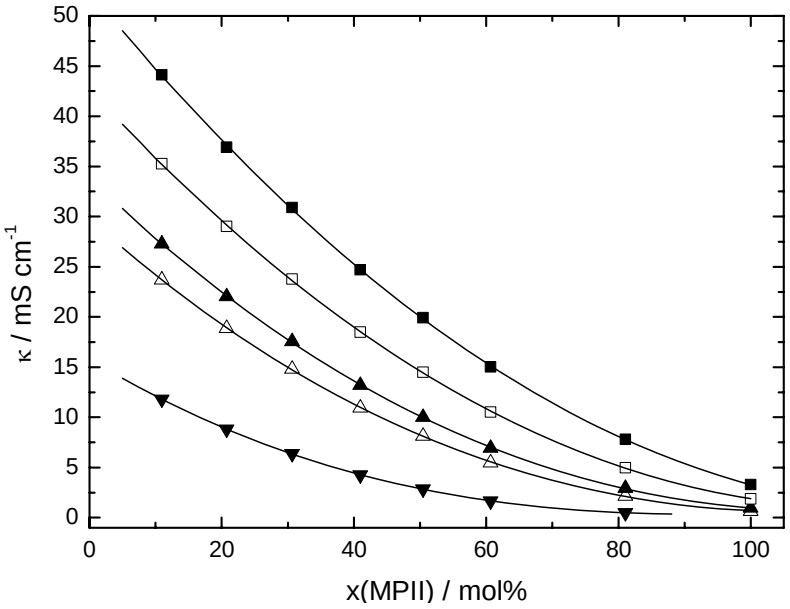

Figure 5-4: Specific conductivities of ≈ 0.05 mol L^{-1} I_2 in mixtures of EMIDCA/MPII as a function of the MPII concentration at varying temperatures and corresponding fits according to Eq. (5.2); *θ*: (—▼—) 5 °C, (—△—) 25 °C, (—▲—) 30 °C, (—□—) 40 °C, (—■—) 50 °C.

5.1.3 $EMIBF_4$/MPII

The specific conductivity in the system $EMIBF_4$/MPII was examined at a constant I_2 concentration of ≈ 0.05 mol L^{-1} and at varying iodide concentrations ranging from 10 mol% MPII to 100 mol% MPII. The accurate I_2 concentrations for each blend are given in Table 8-51 (Chap. 8.2.2). The lower limit of the studied temperature range was at 5 °C, the upper limit at 50 °C. The determined specific conductivities at each MPII concentration and temperature are listed in Table 5-5. The values of the blends with 80 mol% MPII and 100 mol% MPII at 5 °C could not be determined, since at this temperature the specific conductivity was too low for the applied measuring cell. At 15 °C the conductivities for only two blends are given because these blends were examined later in separate measurements.

Table 5-5: Specific conductivities of ≈ 0.05 mol L^{-1} I_2 in mixtures of $EMIBF_4$/MPII at varying MPII concentrations.

κ [mS cm^{-1}]						
T [K] / Mol% MPII	**278.151**	**288.152**	**298.151**	**303.152**	**313.150**	**323.150**
10.1	5.245	-	12.43	14.81	20.29	26.70
19.9	3.720	-	9.60	11.62	16.38	22.05
30.0	2.610	4.620	7.449	9.186	13.37	18.49
39.8	1.782	-	5.595	7.034	10.55	14.95
50.1	1.139	-	4.035	5.194	8.13	11.92
60.1	0.710	-	2.847	3.757	6.134	9.324
80.0	-	0.737	1.523	2.099	3.713	6.035
100.0	-	-	0.6556	0.956	1.867	3.306

As expected, the conductivities for the $EMIBF_4$ based blends are clearly lower than for the corresponding EMIDCA based blends, but on the $EMIBF_4$ rich side of the mixing range their conductivities are clearly higher than for the corresponding EMIOTf and $EMINTf_2$ based blends. The temperature dependence of the specific conductivities for the $EMIBF_4$ based blends was also analysed according to the VFT-equation (Eq. (5.1)). The determined specific conductivities and the resulting VFT-plots are shown in Figure 5-5, the corresponding fitting parameters of these plots are summarised in Table 8-52.

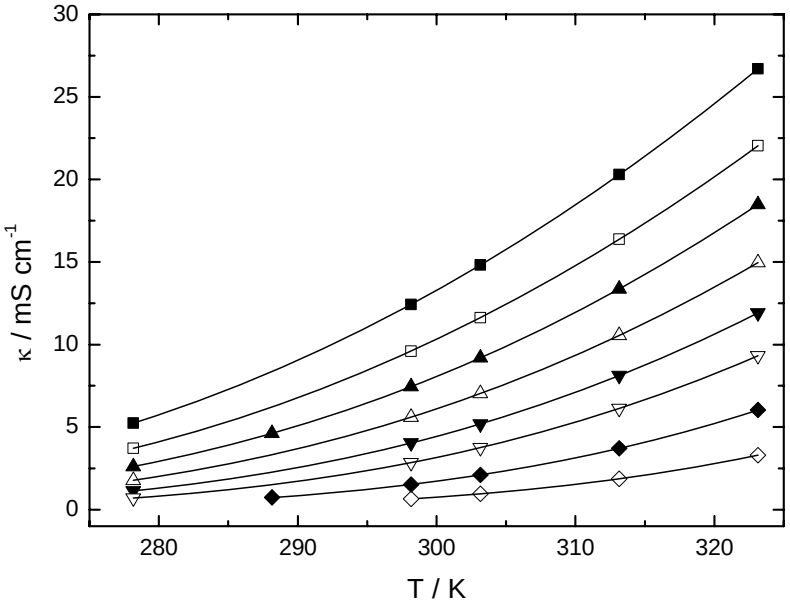

Figure 5-5: Specific conductivities of ≈ 0.05 mol L^{-1} I_2 in mixtures of $EMIBF_4$/MPII as a function of temperature at varying MPII concentrations and corresponding fits according to the VFT-equation (Eq. (5.1)); (—■—) 10 mol% MPII, (—□—) 20 mol% MPII, (—▲—) 30 mol% MPII, (—△—) 40 mol% MPII, (—▼—) 50 mol% MPII, (—▽—) 60 mol% MPII, (—◆—) 80 mol% MPII, (—◇—) 100 mol% MPII.

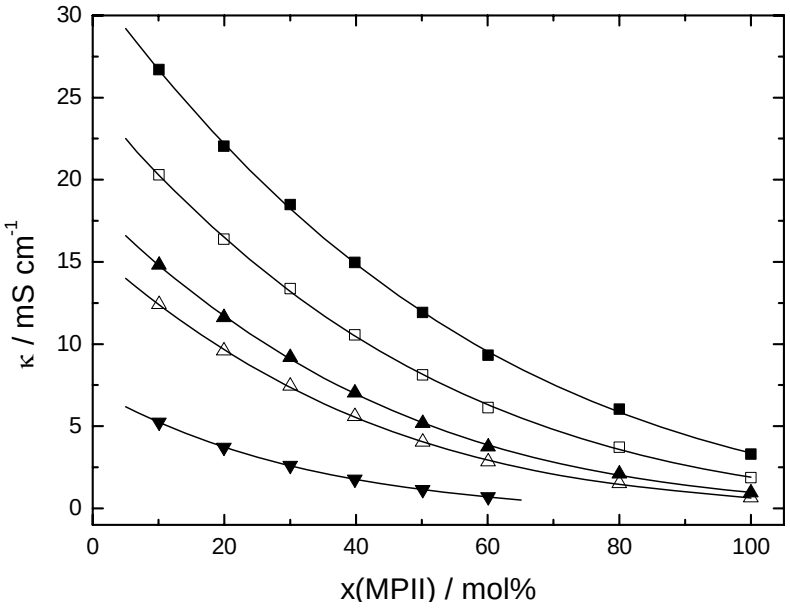

Figure 5-6: Specific conductivities of ≈ 0.05 mol L^{-1} I_2 in mixtures of $EMIBF_4$/MPII as a function of the MPII concentration at varying temperatures and corresponding fits according to Eq. (5.2); θ: (—▼—) 5 °C, (—△—) 25 °C, (—▲—) 30 °C, (—□—) 40 °C, (—■—) 50 °C.

The influence of the MPII concentration on the specific conductivity at varying temperatures is displayed in Figure 5-6. The resulting plots from analysing the conductivity data according to Eq. (5.2) are also shown in Figure 5-6, the corresponding fitting

parameters are summarised in Table 8-53. In contrast to its behaviour in the EMIDCA based blends, the conductivity of the $EMIBF_4$ based blends decreases in nearly equal magnitude as the viscosity increases with increasing MPII concentration.

5.1.4 EMIOTf/MPII

As for the two previously discussed systems, the specific conductivity in the system EMIOTf/MPII was examined at a constant I_2 concentration of ≈ 0.05 mol L^{-1} and at varying iodide concentrations ranging from 10 mol% MPII to 100 mol% MPII. The accurate I_2 concentrations for each blend are given in Table 8-54 (Chap. 8.2.3). The lower limit of the studied temperature range was at 5 °C, the upper limit at 50 °C. The determined specific conductivities at each MPII concentration and temperature are listed in Table 5-6. The values of the blends with 80 mol% MPII and 100 mol% MPII at 5 °C could not be determined since at this temperature the specific conductivity was too low for the applied measuring cells.

Table 5-6: Specific conductivities of ≈ 0.05 mol L^{-1} I_2 in mixtures of EMIOTf/MPII at varying MPII concentrations.

κ [mS cm^{-1}]					
T [K] / Mol% MPII	**278.148**	**298.151**	**303.151**	**313.151**	**323.149**
10.1	3.179	7.296	8.667	11.83	15.53
19.8	2.470	6.07	7.30	10.20	13.65
40.1	1.381	4.045	5.032	7.444	10.42
50.1	1.002	3.234	4.104	-	9.04
60.1	0.697	2.516	3.262	5.181	7.69
80.0	-	1.384	1.890	3.290	5.264
100.0	-	0.6556	0.956	1.867	3.306

Similar to the I_3^--diffusion coefficients the specific conductivities for the EMIOTf based blends are lower than for the corresponding blends of the other examined electrolyte systems. The temperature dependence of the conductivity was analysed according to the VFT-equation (Eq. (5.1)). The resulting VFT-plots and the measured conductivities are shown in Figure 5-7, the corresponding fitting parameters are summarised in Table 8-55.
The influence of the MPII concentration on the specific conductivity at varying temperatures is displayed in Figure 5-8 along with the results of fitting the measurement data according to Eq. (5.2). The corresponding fitting parameters are summarised in Table 8-56. Similar to the EMIDCA based blends, the tendency of conductivity of the EMIOTf

based blends with increasing MPII concentration correlates with the simultaneously increasing viscosity, but the viscosity increase is about 1.5 times larger than the conductivity loss at all investigated temperatures.

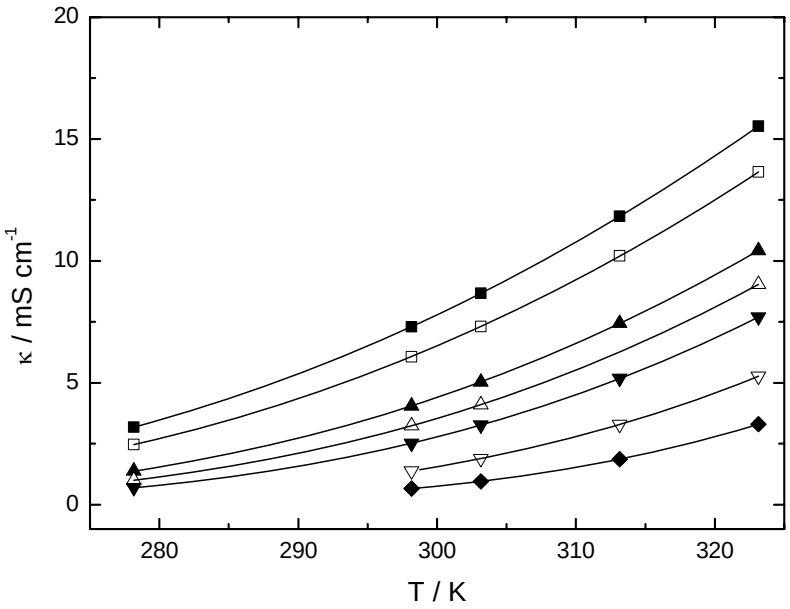

Figure 5-7: Specific conductivities of ≈ 0.05 mol L^{-1} I_2 in mixtures of EMIOTf/MPII as a function of temperature at varying MPII concentrations and corresponding fits according to the VFT-equation (Eq. (5.1)); (—■—) 10 mol% MPII, (—□—) 20 mol% MPII, (—▲—) 40 mol% MPII, (—△—) 50 mol% MPII, (—▼—) 60 mol% MPII, (—▽—) 80 mol% MPII, (—◆—) 100 mol% MPII.

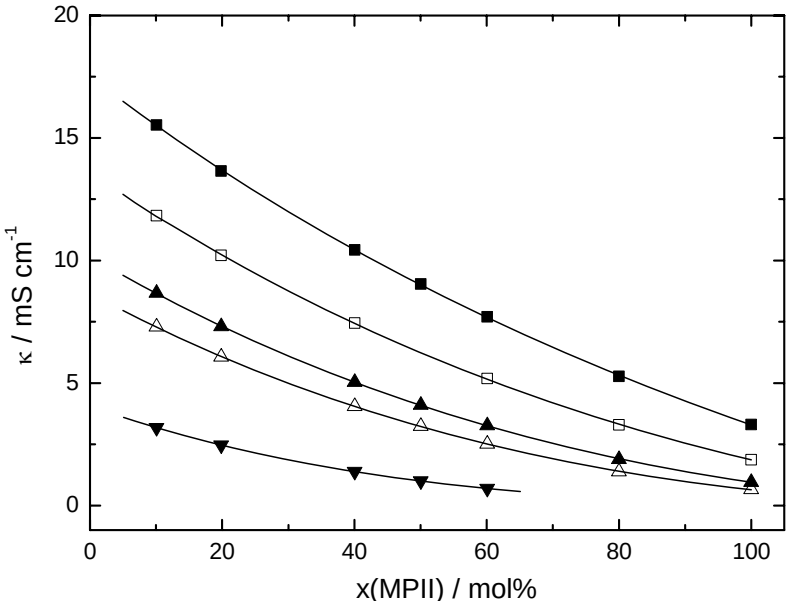

Figure 5-8: Specific conductivities of ≈ 0.05 mol L^{-1} I_2 in mixtures of EMIOTf/MPII as a function of the MPII concentration at varying temperatures and corresponding fits according to Eq. (5.2); θ: (—▼—) 5 °C, (—△—) 25 °C, (—▲—) 30 °C, (—□—) 40 °C, (—■—) 50 °C.

5.1.5 $EMINTf_2$/MPII

The specific conductivity in the system $EMINTf_2$/MPII was examined at a constant I_2 concentration of $\approx 0.05\ mol\ L^{-1}$ and at varying iodide concentrations ranging from 10 mol% MPII to 100 mol% MPII. The I_2 concentrations for each blend are given in Table 8-57 (Chap. 8.2.4). Although the lower (5 °C) and upper (50 °C) limit of the studied temperature range were the same as for the other evaluated electrolyte systems, the $EMINTf_2$ based blends were additionally examined at 15 °C. The determined specific conductivities at each MPII concentration and temperature are listed in Table 5-7. The values of the blend with 100 mol% MPII at 5 °C and 15 °C could not be determined since at these temperatures the specific conductivity was too low for the applied measuring cell.

Table 5-7: Specific conductivities of ≈ 0.05 mol L^{-1} I_2 in mixtures of $EMINTf_2$/MPII at varying MPII concentrations.

κ [mS cm^{-1}]						
T [K] / Mol% MPII	**278.148**	**288.152**	**298.149**	**303.152**	**313.152**	**323.152**
10.0	3.639	5.604	8.071	9.490	12.70	16.38
30.0	2.248	3.700	5.63	6.78	9.47	12.65
40.0	1.697	2.910	4.581	5.60	8.02	10.96
50.0	1.248	2.243	3.677	4.572	6.75	9.46
60.0	0.887	1.683	2.887	3.663	5.603	8.08
80.0	0.3666	0.802	1.557	2.087	3.514	5.495
100.0	-	-	0.6556	0.956	1.867	3.306

The specific conductivities of the $EMINTf_2$ based blends are slightly higher than for the corresponding EMIOTf based blends, but clearly lower than for the corresponding EMIDCA and $EMIBF_4$ based blends.

The temperature dependence of the determined specific conductivities and the resulting plots from fitting the measurement data according to the VFT-equation (Eq. (5.1)) are shown in Figure 5-9. The corresponding fitting parameters are listed in Table 8-58.

The influence of the MPII concentration on the specific conductivity at varying temperatures is displayed in Figure 5-10. The resulting plots from analysing the conductivity data according to Eq. (5.2) are also shown in Figure 5-10, the corresponding fitting parameters

are summarised in Table 8-59. The magnitude of the viscosity increase is about 2.5 times larger than the loss of the specific conductivity with increasing MPII concentration at all measurement temperatures. This is the largest value of all examined systems and primarily based on a comparative low conductivity of $EMINTf_2$ despite its also low viscosity.

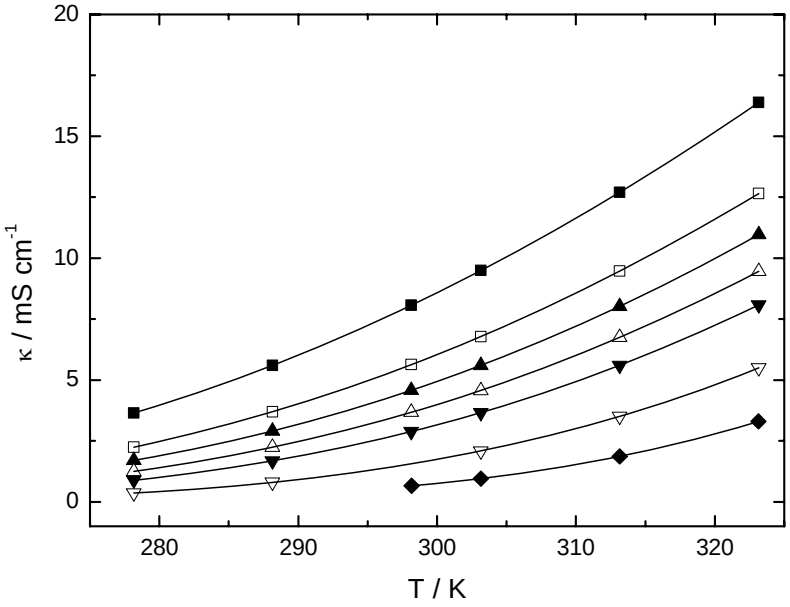

Figure 5-9: Specific conductivities of ≈ 0.05 mol L^{-1} I_2 in mixtures of $EMINTf_2$/MPII as a function of temperature at varying MPII concentrations and corresponding fits according to the VFT-equation (Eq. (5.1)); (—■—) 10 mol% MPII, (—□—) 30 mol% MPII, (—▲—) 40 mol% MPII, (—△—) 50 mol% MPII, (—▼—) 60 mol% MPII, (—▽—) 80 mol% MPII, (—◆—) 100 mol% MPII.

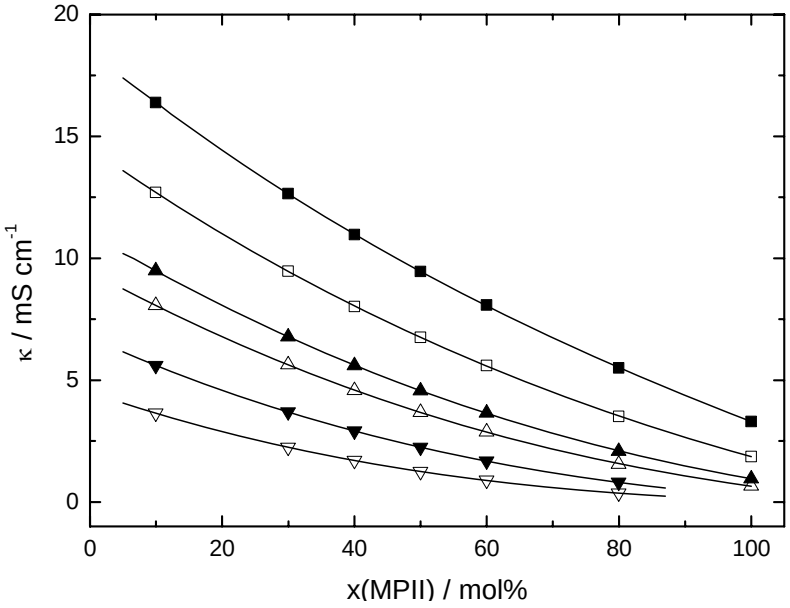

Figure 5-10: Specific conductivities of ≈ 0.05 mol L^{-1} I_2 in mixtures of $EMINTf_2$/MPII as a function of the MPII concentration at varying temperatures and corresponding fits according to Eq. (5.2); θ: (—▽—) 5 °C, (—▼—) 15 °C, (—△—) 25 °C, (—▲—) 30 °C, (—□—) 40 °C, (—■—) 50 °C.

5.1.6 Consideration of Fragility of Ionic Liquids

As discussed in Chap. 2.2.1 the validity of the applied working equation is determined by the type of glass forming liquid. An estimation of the fragility of several glass forming liquids was first performed by analysis of the temperature dependence of their viscosities in reduced plots of $log(\eta) = f(T_g/T)$ [81]. A similar illustration is shown in Figure 5-11 for three ILs. Despite the small temperature range of the given viscosities, it is obvious that all three ILs show a strong non-Arrhenius type behaviour and must be ranked under the fragile glass formers. That corresponds to the extremely low values for the strength index D calculated from the VFT-parameters B and T_0 in Table 5-8. However, for more detailed conclusions, viscosities over a wider temperature range and determined at higher accuracy are necessary.

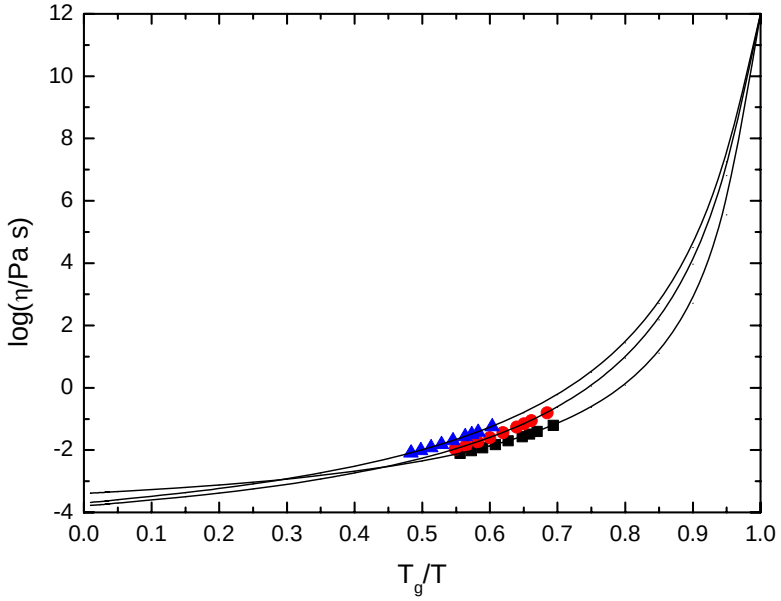

Figure 5-11: Arrhenius plot of IL viscosities with reduced temperature according to Angell [81], the inverse temperature is scaled by $T_g := T(\eta = 10^{12}$ Pa s). The viscosities of $EMINTf_2$ (■) [160], $HMINTf_2$ (●) [160], and $EMIBF_4$ (▲) [68] are obtained from literature. The viscosities for the solid lines are calculated using the VFT-equation (Eq. (2.17)) and the parameters in Table 5-8.

Table 5-8: VFT-Equation parameters of viscosity data of pure ionic liquids and calculated values of the strength *D* of the ionic liquids.

Substance	η_0 [mPa s]	B [K]	T_0 [K]	D
$EMIBF_4$ [68]	0.20[a]	750[a]	150[a]	5[a]
$EMINTf_2$ [160]	0.4 ± 0.13	509 ± 81	182 ± 10	2.8 ± 0.5
$HMINTf_2$ [160]	0.16 ± 0.02	757 ± 39	173 ± 3	4.4 ± 0.2

[a] No standard deviations given.

The clearly non-Arrhenius type behaviour of $EMINTf_2$, $HMINTf_2$, and $EMIBF_4$ in Figure 5-11 proves the validity of analysis of conductivity data of ILs according to the VFT-equation as performed in the preceding chapters. This approach is only valid if the temperature dependence of ionic association in ILs is negligible and the variation of conductivity with temperature is solely dependent on the varying viscosity. This approximation enables the estimation of fragilities of ILs from specific conductivity data. In Table 5-9 VFT-equation parameters of specific conductivity data and calculated strength *D* of pure ILs are summarised along with their corresponding standard deviations. Generally, the *D* values calculated from VFT-equation parameters of specific conductivity data (Table 5-9) show good agreement with the ones calculated from VFT-equation parameters of viscosity (Table 5-8).

Table 5-9: VFT-Equation parameters of specific conductivity data of pure ionic liquids and calculated values of the strength *D* of the ionic liquids.

Substance	κ_0 [mS cm^{-1}]	B [K]	T_0 [K]	R^2	D
$BMIBF_4$	1700 ± 60	786 ± 10	170.9 ± 1.0	1	4.60 ± 0.06
BMPIFAP	750 ± 70	780 ± 30	176 ± 2	1	4.43 ± 0.18
$BMPINTf_2$	680 ± 30	717 ± 14	167.8 ± 1.4	1	4.27 ± 0.09
BMPIOTf	1030 ± 40	819 ± 12	167.0 ± 1.1	1	4.90 ± 0.08
$EMIBF_4$	1170 ± 60	556 ± 15	169.5 ± 1.9	1	3.28 ± 0.10
EMIDCA	1185 ± 12	508 ± 3	161.1 ± 0.4	1	3.15 ± 0.02
$EMINTf_2$	614 ± 4	556.8 ± 1.7	165.9 ± 0.2	1	3.356 ± 0.011
EMIOTf	1049 ± 6	702.5 ± 1.9	152.6 ± 0.2	1	4.604 ± 0.014
$HMINTf_2$	700 ± 40	760 ± 18	166.3 ± 1.8	1	4.57 ± 0.12
Me_3SDCA	1620 ± 30	568 ± 5	161.5 ± 0.6	1	3.52 ± 0.03
MPII	5100 ± 400	1020 ± 20	185.5 ± 1.4	1	5.50 ± 0.12

The low *D* values (Table 5-9) indicate that all examined ILs are fragile liquids albeit there are small differences. As discussed in Chap. 2.2.1 the fragility of a liquid correlates with the type of interactions between atoms, molecules, and ions in the liquid. The fragility decreases with increasing strength and directional character of interactions and decreasing coordination number as well. An extremely low strength *D* as for EMIDCA and $EMIBF_4$ matches the assumption of weak Coulombic interactions and weak hydrogen bonding for these ILs (see. Chap. 5.1). Me_3SDCA and $EMINTf_2$ both show stronger Coulombic interactions, reducing the coordination number and its fluctuation. In the case of Me_3SDCA this is caused by a smaller cation when compared to EMIDCA; in the case of

$EMINTf_2$ it is based on the increased basic character of the anion when compared to $EMIBF_4$. A further increasing basic character of the anion as for EMIOTf leads consequently to a higher strength *D*. A longer alkyl side chain at the cation as it is the case for $BMIBF_4$ and $HMINTf_2$, when compared to $EMIBF_4$ and $EMINTf_2$, results in increased van der Waals interactions and consequently decreases the fragile character of the liquid. This matches the results of a comprehensive study on tetraalkylammonium and BMI based ILs by Angell and co-workers [86]. They also found a strong increase of fragility of ILs at increasing aromaticity of the cation from tetraalkylammonium- over 1-alkyl-3-methylimidazolium- to alkylpyridinium-cations. A similar behaviour can be found for BMPl based ILs when compared to EMI based ILs, albeit a comparison with corresponding BMI based salts would be more significant. The highest value for *D* is obtained for MPII. This is primarily based on the fact that the iodide anion can be easily polarised enabling comparably strong Coulombic interactions. Despite the fact that fragility and strength of ILs calculated from conductivity data are only approximations, they yield additional and useful information on the extent of ionic interactions and association in ILs.
Consideration of fragility for the ionic liquid blends is probably not adequate since, as shown in Chap. 6.2, many blends show partly solidification before reaching the glass transition temperature. A measurement setup with higher sensitivity for glass-transitions and extremely high cooling rates would be necessary to check the behaviour of the mixtures at their glass-transition points.

5.1.7 Comparison of Results from Diffusion and Conductivity Measurements

A brief comparison of the examined transport properties, I_3^--diffusion and conductivity for the system EMIOTf/MPII follows in this section. Both parameters are coupled to the viscosity, however in the case of ILs non-Stokesian charge transport plays an important role for the diffusion and ionic association for the conductivity.

The temperature dependence of I_3^--diffusion coefficients and of specific conductivities of ≈ 0.05 mol L^{-1} I_2 in blends of two ILs was analysed in both cases using VFT-equations. In Table 5-10 and Table 5-11 VFT-equation parameters of specific conductivity data and I_3^--diffusion coefficients of ≈ 0.05 mol L^{-1} I_2 in mixtures of EMIOTf and MPII are listed. EMIOTf was chosen because VFT-parameters of I_3^--diffusion coefficients for this system show the smallest standard deviations when compared to the other systems, due to a slightly modified measurement procedure (see Chap. 4.3).

The examined temperature ranges for both parameters were almost equal. Nevertheless, the standard deviations of the VFT-parameters for conductivity are clearly smaller than for I_3^--diffusion and κ_0, B, and T_0 show a continuous and uniform behaviour. One major reason for these deviations is the reduced accuracy of diffusion measurements when compared to conductivity measurements. The decreasing magnitude of the non-Stokesian portion on the overall diffusion with increasing temperature is the other major reason.

Table 5-10: VFT-Equation parameters of specific conductivity data of ≈ 0.05 mol L^{-1} I_2 in mixtures of EMIOTf and MPII at varying MPII concentrations.

Mol% MPII	κ_0 [mS cm^{-1}]	B [K]	T_0 [K]	R^2
10.1	1040 ± 40	689 ± 10	159.0 ± 1.4	1
19.8	1110 ± 40	707 ± 11	162.4 ± 1.1	1
40.1	1220 ± 90	720 ± 20	172 ± 2	1
50.1	1570 ± 60	775 ± 10	172.8 ± 0.9	1
60.1	1700 ± 200	790 ± 30	177 ± 3	1
80.0	1800 ± 200	790 ± 30	189 ± 3	1
100.0	4700 ± 500	1000 ± 30	185.9 ± 1.9	1

Table 5-11: VFT-Equation parameters of I_3^--diffusion coefficients of 0.05 mol L^{-1} I_2 in mixtures of EMIOTf/MPII at varying MPII concentrations.

Mol% MPII	$A \cdot 10^3$ [cm^2 s^{-1}]	B [K]	T_0 [K]	R^2
10.1	0.09 ± 0.005	778 ± 16	162.6 ± 1.6	1
20.1	0.08 ± 0.03	690 ± 110	173 ± 12	0.99995
30.1	0.24 ± 0.13	1000 ± 200	144 ± 17	0.99995
40.0	0.14 ± 0.03	810 ± 60	166 ± 6	0.99999
50.1	0.34 ± 0.17	1000 ± 200	151 ± 14	0.99996
60.1	0.19 ± 0.009	840 ± 13	171.0 ± 1.3	1
70.0	0.18 ± 0.006	754 ± 9	184.7 ± 0.9	1
79.9	0.14 ± 0.007	694 ± 13	191.7 ± 1.3	1
100.0	0.23 ± 0.02	840 ± 30	187 ± 2	1

Both parameters were analysed with respect to the MPII concentration as well. The behaviour of the specific conductivity with decreasing MPII concentration was similar for all examined systems, i.e. the conductivity continuously increased with decreasing MPII concentration. The measurement data were analysed by fitting according to a third grade polynomial (Figure 5-12B for the system EMIOTf/MPII). No uniform behaviour for decreasing MPII concentrations was found for the I_3^--diffusion coefficients (Figure 5-12A for the system EMIOTf/MPII) in the different systems. EMIDCA/MPII is the only system where the I_3^--diffusion coefficients continuously increase with decreasing MPII concentration whereas in the other electrolyte systems the I_3^--diffusion coefficients often stay constant over a broad MPII concentration range. The maximum for I_3^--diffusion coefficients at comparably high MPII concentrations for the system EMIOTf/MPII (Figure 5-12A) is unique.

As discussed in Chap. 2.2.3 the charge transfer among ions with negative charges is facilitated by the high ionic strength in ILs. The ionic strength generally correlates with the concentration of charge carriers that is reduced by ionic association. EMIOTf has the highest viscosity of the examined solvent ILs and the largest addiction to ionic association. Thus, the constancy of the I_3^--diffusion coefficients is probably caused by two opposite effects. On the one hand, the decreasing viscosity enhances the physical diffusion; on the other hand the increasing ionic association decreases the ionic strength and consequently the charge transfer rate. The occurrence of these constant I_3^--diffusion coefficients at higher temperatures corresponds to the assumption of increasing ionic association at increasing temperatures [86]. A similar behaviour is assumed for the system

EMIBF$_4$/MPII, whereas for the systems EMIDCA/MPII and EMINTf$_2$/MPII the viscosity loss is too large to be counterbalanced by a decreasing magnitude of the charge transfer.

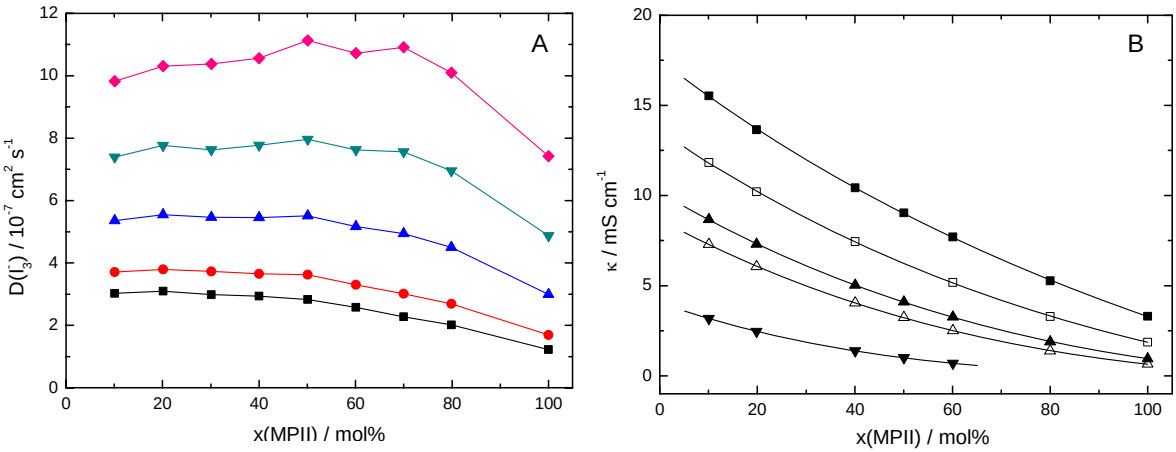

Figure 5-12: A) I_3^--diffusion coefficients of 0.05 mol L^{-1} I_2 in mixtures of EMIOTf/MPII as a function of the MPII concentration at different temperatures; θ: (—■—) 25 °C, (—●—) 30 °C, (—▲—) 40 °C, (—▼—) 50 °C, (—◆—) 60 °C. B) Specific conductivities of ≈ 0.05 mol L^{-1} I_2 in mixtures of EMIOTf/MPII as a function of the MPII concentration at varying temperatures and corresponding fits according to Eq. (5.2); θ: (—▼—) 5 °C, (—△—) 25 °C, (—▲—) 30 °C, (—□—) 40 °C, (—■—) 50 °C.

5.2 Dynamic (Continuous) Conductivity Measurements

The primary purpose of simultaneous recording of conductivity and temperature as a function of time, was to obtain an additional indication besides T(t)-curves for phase transitions during cooling and heating of a sample (see Chaps. 3.4.2 and 6). After consideration of few precautions the recorded conductivity can, though at reduced accuracy, also be used for analysis of the temperature dependence of the specific conductivity.

In contrast to the cell constants of conductivity cells used for stationary conductivity measurements, the cell constants of the G(t)-T(t)-measuring cells are temperature dependent (see also Chap. 3.4.1.2). Several approaches were examined for analysis of this temperature dependence. A quadratic fit of the measurement data as shown in Figure 5-13 for the cell constants of three measuring cells calculated from conductivities and specific conductivities of three blends of the system EMIOTf/MPII yields sufficient accurate results and can be easily performed.

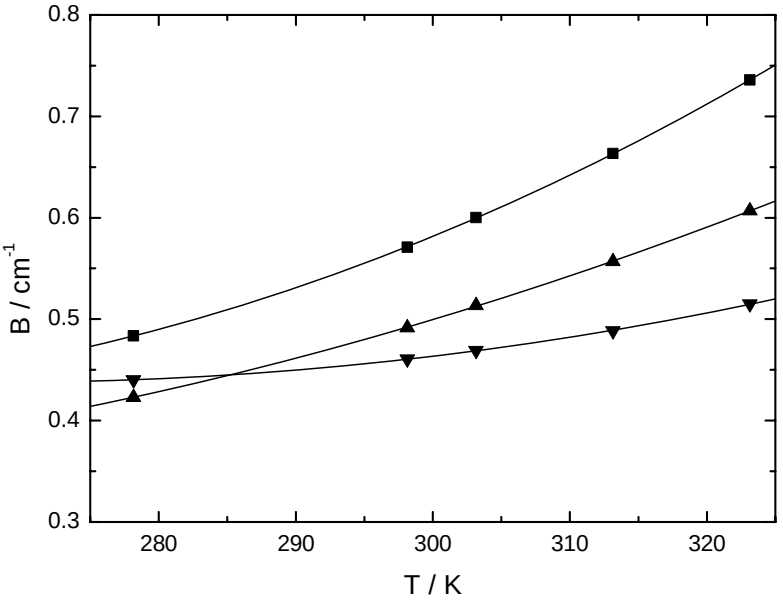

Figure 5-13: Cell constants of G(t)-T(t)-measuring cells determined with blends of the system EMIOTf/MPII as a function of temperature and corresponding quadratic fits; (—■—) 20 mol% MPII, (—▲—) 40 mol% MPII, (—▼—) 60 mol% MPII.

Analysis of the recorded conductivity with the calculated cell constants yields specific conductivities that are typically in good agreement with specific conductivities obtained by stationary conductivity measurements. In Figure 5-14 specific conductivities of

≈ 0.05 mol L^{-1} I_2 in mixtures of EMIOTf/MPII are compared. The conductivities are calculated from G(t)-T(t)-measurement data and according to the VFT-equation (Eq. (5.1)) from conductivity data obtained from stationary measurements respectively. Deviations are only obtained at high temperatures which is mainly based on interfering signals for G(t)-T(t)-measurements. The main disadvantage of this method is that at least three values for specific conductivities of the sample, distributed over a broad temperature range, are necessary to obtain accurate cell constants.

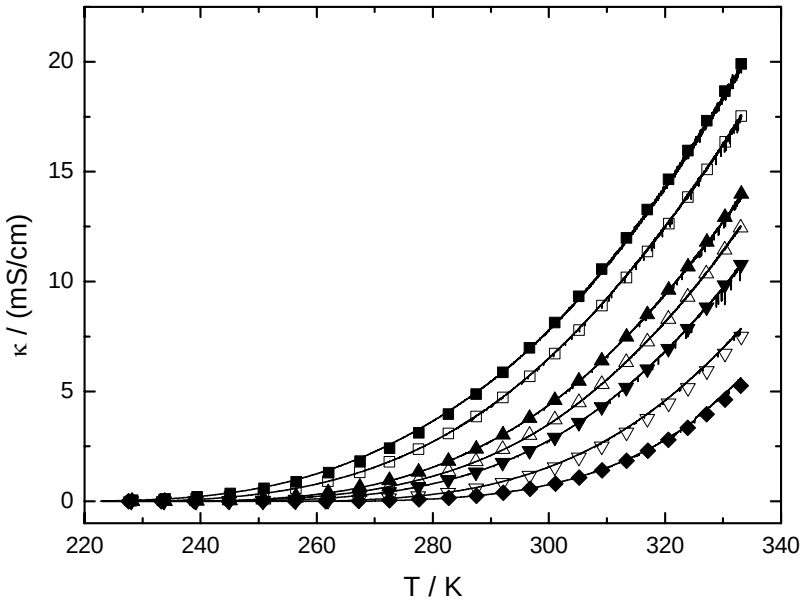

Figure 5-14: Specific conductivities of ≈ 0.05 mol L^{-1} I_2 in mixtures of EMIOTf/MPII calculated from conductivity data from dynamic conductivity measurements (—) as a function of temperature at varying MPII concentrations and corresponding fits according to the VFT-equation (Eq. (5.1)) calculated from conductivity data obtained by stationary conductivity measurements; (—■—) 10 mol% MPII, (—□—) 20 mol% MPII, (—▲—) 40 mol% MPII, (—△—) 50 mol% MPII, (—▼—) 60 mol% MPII, (—▽—) 80 mol% MPII, (—◆—) 100 mol% MPII.

If the temperature coefficient of the applied glass is disregarded, the temperature dependence of the cell constant is primarily based on the fill level (h_l) that is inversely proportional to the density (ρ):

$$B(T) \sim h_l(T) = \frac{m_s}{r_c^2 \pi} \frac{1}{\rho(T)} \tag{5.3}$$

where m_s is the mass of the sample and r_c the medial radius of the cell. The cell constants analysed in Figure 5-13 with regard to their temperature dependence are also inversely

proportional to the density of the sample. In Figure 5-15 the results from analysis of this relation according to linear and quadratic fits are shown for three blends of the system EMIOTf/MPII. With the proportional factor and the mass of the sample, the cell constant can be directly calculated from the density of the sample according to Eq. (5.3).

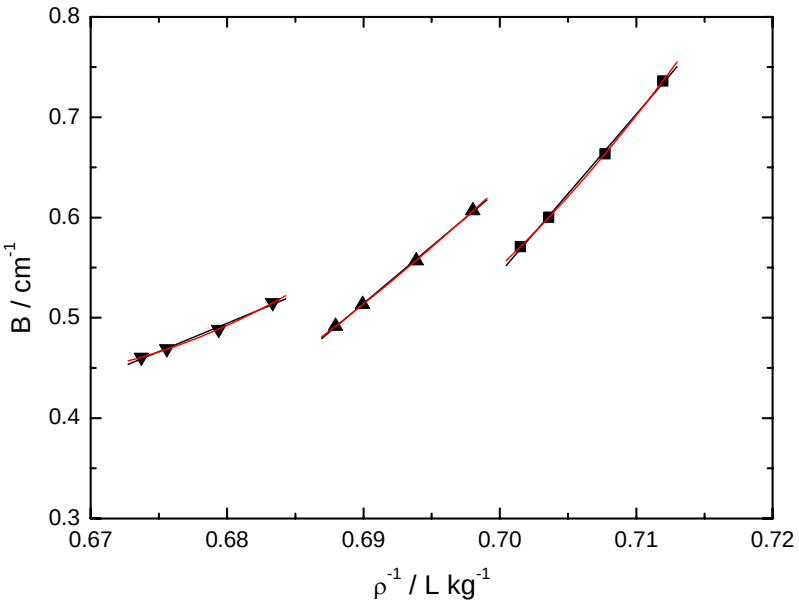

Figure 5-15: Cell constants of G(t)-T(t)-measuring cells determined with blends of the system EMIOTf/MPII as a function of density and corresponding linear (—) and quadratic (—) fits; (■) 20 mol% MPII, (▲) 40 mol% MPII, (▼) 60 mol% MPII.

Thus, after determination of the proportional factor of the cell constant by calibration, the specific conductivity can be directly calculated from the recorded conductivity and the density of the sample and vice versa. Calculation of densities from conductivity data can be of special interest for highly viscous ILs due to viscosity induced errors for common vibrating tube densitometry [161]. As discussed in Chap. 3.4.1.2 the cell constant may be altered by crystallising samples and during cleaning of the cell. Therefore, it is necessary to regularly calibrate the cell to obtain sufficient accurate results.

5.3 Summary and Appraisal of Results

Specific conductivities of eleven ILs were determined in a temperature range between 5 °C and 50 °C, for the ILs BMPlFAP, BMPlOTf, and Me_3SDCA for the first time. Analysis of the conductivity for several EMI and BMPl based ILs showed a strong influence of the anion and its varying size, basicity, and tendency to formation of hydrogen bridge bonds. The impact of the alkyl chain length in the 1-alkyl-3-methylimidazolium-cation on the conductivity was examined as well. A growing chain length causes increasing van der Waals interactions, increasing ion radii and consequently decreasing ion mobilities. Additionally, the density decreases and consequently the charge carrier concentration. These factors cause a strong decrease of conductivity. The planarity and aromaticity of the cation has additional influence on the conductivity, i.e.: the conductivity increases with increasing planarity and aromaticity of the cation.

Evaluation of the fragility, based on the determined specific conductivities, yielded similar results as analysis of viscosity data from literature. The values for the strength *D* calculated from VFT-parameters are in the fragile range for all examined ILs. Thus, they show a strong non-Arrhenius behaviour and the validity of analysis of the temperature dependence of conductivity according to the VFT-equation is confirmed. The slight variations of *D* with varying anions at fixed cations and vice versa were addressed in terms of varying ionic interactions and coordination numbers. They generally match the assumptions discussed above. The strength *D* increases with increasing alkyl chain length in the cation due to increasing van der Waals interactions. By variation of the anion the magnitude of Coulombic interactions increases in the order $DCA < BF_4 < NTf_2 < OTf$ resulting in increasing strength as well.

Evaluation of conductivity data with respect to fragility is based on the assumption that conductivity variations with temperature depend exclusively on viscosity changes. Despite this approximation, it is a useful method for classification of ILs since conductivities are often more accurate than viscosities determined with common rheometer devices and can be obtained much faster than highly accurate viscosities determined with an Ubbelhode viscometer.

The conductivities of the electrolyte mixtures are generally in the same order as are the conductivities of the applied solvent ILs. Analysis of the temperature dependence of the specific conductivities according to the VFT-equation yields accurate results in contrast to analysis of the temperature dependence of I_3^--diffusion coefficients. All examined systems

showed continuously increasing conductivities with decreasing MPII concentration. Analysis of the measurement data according to a third grade polynomial yielded sufficient results for accurate interpolation of conductivities of MPII concentrations within the examined mixing range.

Specific conductivities obtained from conductivity data recorded with G(t)-T(t)-measuring cells showed good agreement with those calculated by the VFT-equation from specific conductivities obtained from stationary conductivity measurements. The temperature dependence of the cell constants was analysed and two possibilities for processing of conductivity data from continuous conductivity measurements were shown. The more time-consuming but also more reliable method is a separate determination of the specific conductivity of the sample for at least three different temperatures and calibration of the cell for each specific measurement. The other possibility is a temperature dependent calibration of the cell to obtain the proportional factor that correlates the cell constant and the reciprocal value of the density. Thus, after determination of this proportional factor, the specific conductivity can be directly calculated from the recorded conductivity and the density of the sample and vice versa. For this method regular calibration of the cell is necessary to obtain sufficient accurate results.

6 Determination of Phase Transition Points in Pure Ionic Liquids and their Binary Mixtures

In the following chapters the results from simultaneous T(t)- and-G(t) measurements (Chap. 3.4) in pure ILs and blends of ILs are summarised and discussed. The obtained (l)-(s)-phase transition points are crucial factors for application of electrolytes, since they determine the lower limit of the operating range of these electrolytes.

The accuracy of phase transition points of organic solvents and their binary mixtures determined by evaluation of T(t)-measurements along with the reliability of the measurement technique has been extensively discussed in Refs. [103,107,108]. The accuracy of the conductivity data obtained by simultaneous T(t)- and G(t)-measurements was analysed in Chap. 5.2. Analysis of the accuracy and comparison of phase transition points of ILs determined by evaluation of T(t)-curves and G(t)-curves follows in Chap. 6.1. The results of examination of potential DSSC-electrolytes with the verified measurement techniques are summarised in Chap. 6.2.

6.1 Phase Transition Points of Pure Ionic Liquids

Phase transition points of common imidazolium based ILs measured by DSC are frequently reported. [68,109,136,162-165] However, similar as for the conductivity, for some ILs extensive but inconsistent data have been published as shown in Table 6-3 for $EMINTf_2$. Only little or no data have been published for ILs with tendency to large supercooling since, in combination with the generally applied high cooling and heating rates and resulting short time frames, no crystallisation of these ILs occurs within the working range of common DSC devices. Therefore, often only glass-transition points are determined. These transitions at comparably low temperatures often lead to the wrong assumption of extremely broad liquid ranges for specific ILs, as later shown for MPII. To obtain reliable phase transition points, the impact of various measurement parameters was accurately checked. That includes investigation of the influence of impurities, crystallisation aids, and heating and cooling rates on freezing and melting points of ILs. The influence of the anion on the phase transition points of EMI based ILs was analysed as well.

As already discussed in Chap. 3.4.2 evaluation of T(t)-curves is generally the method of choice for determination of phase transition points. Phase transition points of organic solvents and their binary mixtures obtained by this procedure were in good conformity with values from literature. [103,107,108] However, one of the main objectives of this study is the determination of phase diagrams of the electrolyte systems already examined in Chaps. 4 and 5. With regard to these systems and the expected weakly pronounced changes in their blends during cooling and heating, the conductivity that is simultaneously recorded with the sample temperature was checked in pure ILs as additional indicator for phase transition points and other temperature dependent changes in the sample.
Origin and purity of the examined ILs are listed in Table 5-1 (Chap. 5.1.1) apart from two deviations. EMIOTf (10 ppm H_2O) and trioctylmethylammonium trifluoroacetate (TOMATFA, 48 ppm H_2O) were purchased at *Merck* (no purity specifications were given).

6.1.1 Measurement Parameters that Influence Freezing and Melting Points

The most important parameter that influences freezing and melting points is the purity of the sample. The freezing and melting point of a sample dramatically decreases with increasing amount of impurities, as shown in Table 6-1 for two different batches of $EMIBF_4$ with different amounts of detected impurities. Since the type of impurity is based on the synthesis route and purification of ILs is a laborious task that often does not achieve as high purity grades as for many common inorganic and organic materials, impurities therefore have a major influence on reliability and consistency of published phase transition points of ILs [166].

Table 6-1: Freezing points $\theta_{f,\,T(t)}$, melting points $\theta_{m,\,T(t)}$ and magnitude of supercooling $\Delta\theta_s$ of EMIBF4 with varying quantities of detected impurities determined at cooling and heating rate v of -/+ 5 K h^{-1}.

v [K h^{-1}]	$\theta_{f,\,T(t)}$ [°C]	$\Delta\theta_s$ [°C]	$\theta_{m,\,T(t)}$ [°C]	Impurities
5.00	-14.6	50.1	13.4	23 ppm H_2O, 36 ppm Cl^-
5.00	-17.0	41.0	7.3	70 ppm H_2O, 330 ppm Br^-

The influence of cooling and heating rates on freezing and melting points of organic solvents has been discussed in Refs. [107,108]. For ILs a similar behaviour was expected, i.e. increased supercooling with an increasing cooling rate and no clear effect on freezing

and melting points by variation of cooling and heating rates. In fact, no generally valid conclusion of the effect of varying cooling and heating rates can be given in the case of ILs.

The most uniform behaviour was found for the melting points θ_m that generally decrease slightly with increasing heating rate. Two examples for this behaviour are shown in Figure 6-1. The tendency of the melting points of organic solvents with increasing heating rates was neither as distinct nor as uniform as for ILs. [107,108]

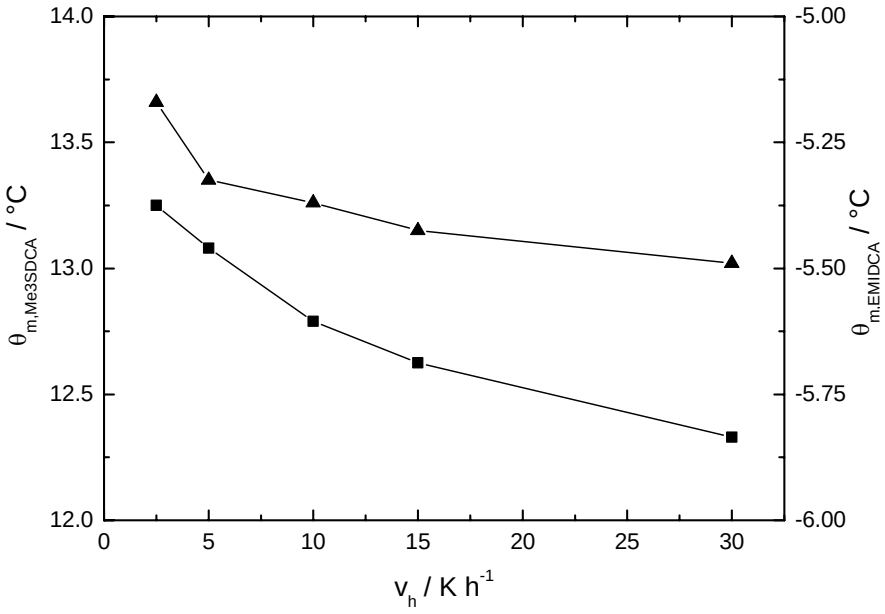

Figure 6-1: Melting points of Me_3SDCA (—■—) and EMIDCA (—▲—) as function of the applied heating rate v_h.

The determined freezing points θ_f generally decrease slightly with increasing cooling rate, as shown in Figure 6-2 for $EMINTf_2$. This correlates strongly with the increasing supercooling $\Delta\theta_s$ of $EMINTf_2$ (Figure 6-2) at an increasing cooling rate. Generally, supercooling is defined as the temperature difference between the freezing point and the temperature where the sample starts to crystallise. [107,108] In the case of ILs, the melting point is chosen as reference and not the freezing point because the melting point is more stable than the freezing point and not influenced by the occurring supercooling itself.

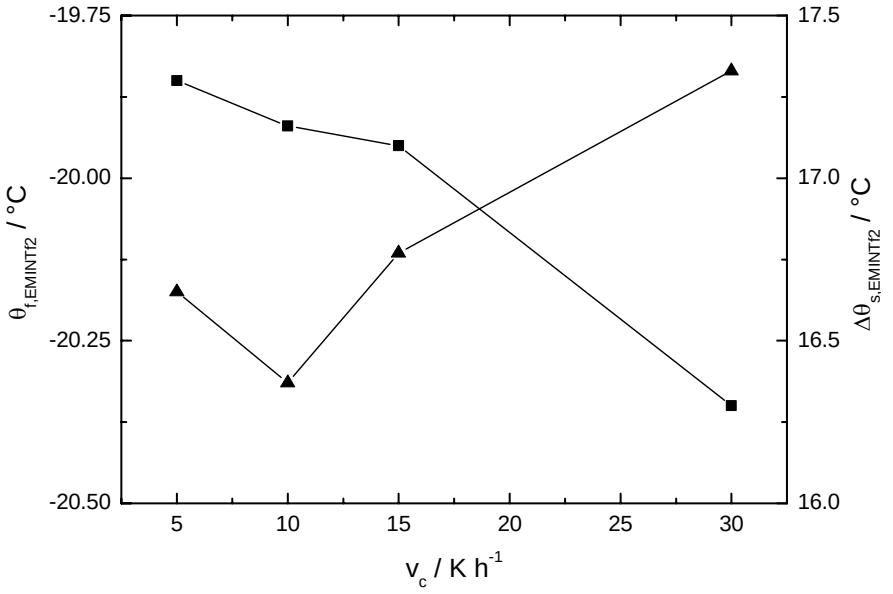

Figure 6-2: Freezing points (—■—) and supercooling (—▲—) of $EMINTf_2$ as function of the applied cooling rate v_c.

A different behaviour was found for Me_3SDCA (Figure 6-3) where the freezing point increases with increasing cooling rate in spite of a simultaneously increasing supercooling. Additionally, Me_3SDCA is the only IL where the freezing point was found to be higher than the melting point (Table 6-3 and Table 8-62).

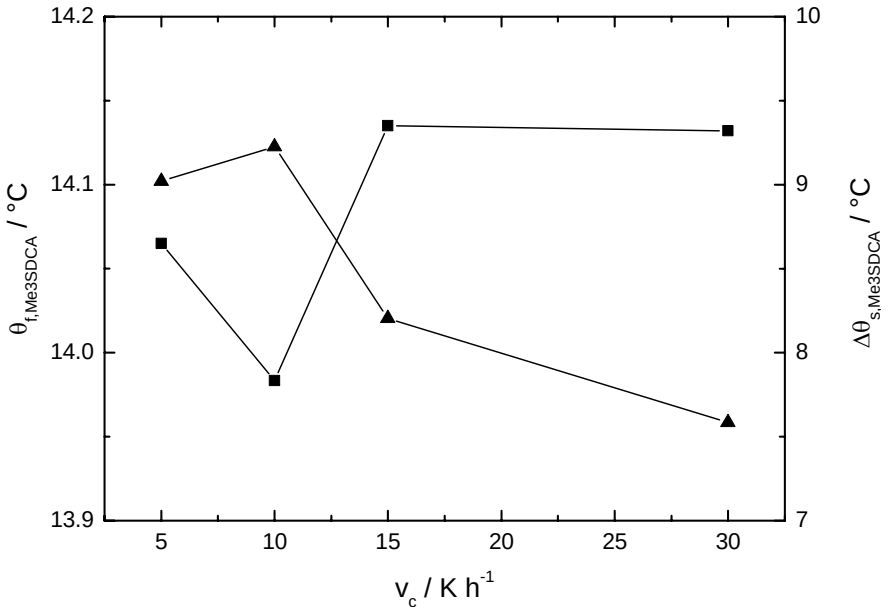

Figure 6-3: Freezing points (—■—) and supercooling (—▲—) of Me_3SDCA as function of the applied cooling rate v_c.

Since DSC-devices have to be calibrated for every applied scan rate, determination of phase transition points with DSC measurements is generally performed at fixed scan rates. In few cases, a dependence of the phase transition points and the magnitude of super-cooling on the applied scan rate is assumed [160,166] but mostly no further information is given if a dependence of phase transition points on the magnitude of the applied scan rate was observed or at least investigated. [109,163] Due to unavailable studies on the effect of the scan rate of DSC measurements on the determined phase transition points and as result of comparing the few published melting points of ILs determined at varying scan rates (e.g. EMINTf$_2$: θ_m = -17 °C at 10 K min^{-1} [166] and θ_m = -21 °C at 30 K min^{-1} [162]), an influence of the scan rate on the measurement results can not be excluded. This confirms doubts on the reliability of published phase transition points of ILs determined by DSC-measurements.

Carbon fibres, proposed by Ding et al. [167] as crystallisation aids, have proved to be useful in the case of organic solvents. [107,108] Thus, their influence on supercooling, freezing and melting points of ILs was also investigated. The results for EMIOTf (Table 8-69) are similar to the ones for organic solvents, i.e. a clear reduction of supercooling was found, but no distinct influence on freezing and melting points. In the case of TOMATFA (Table 8-70) application of carbon fibres had no effects.

6.1.2 Comparison and Discussion of Phase Transition Points Obtained by Evaluation of T(t)- and G(t)-Measurements

As discussed in Chap. 3.4.2, on cooling the conductivity of the samples often inclines to zero prior to crystallisation due to supercooling and insufficient sensitivity of the measuring equipment. Therefore, evaluation of G(t)-curves and *lnG*-plots was performed exclusively with respect to determination of melting points.

Contrary to melting points obtained from T(t)-curves, no distinct tendency with increasing heating rate could be observed for melting points obtained by evaluation of conductivity data, as shown in Figure 6-4 for EMIDCA. These studies show increasing differences at increasing heating rates between the melting points obtained from temperature and conductivity data (Figure 6-4 and Table 8-60 to Table 8-63). Due to that and due to a lower percentage of ILs crystallising at high than at low cooling rates, most of the measurements were conducted at a fixed and comparatively low cooling and heating rate v of -/+ 5 K h^{-1}.

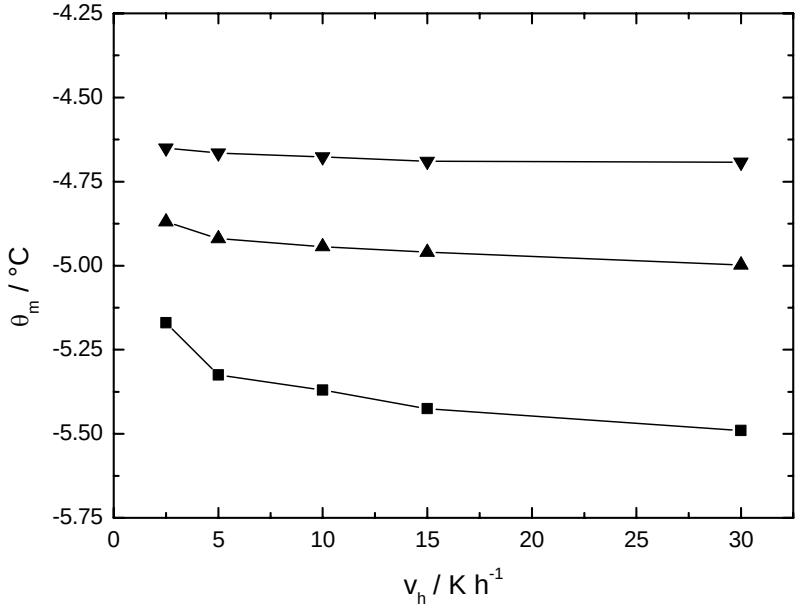

Figure 6-4: Melting points of EMIDCA determined by evaluation of T(t)-curves (—■—), G(t)-curves (—▲—) and *lnG*-plots (—▼—) as function of the applied heating rate v_h.

The mean values of the melting points determined by evaluation of T(t)- and G(t)-curves and *lnG*-plots are listed in Table 6-2 along with the corresponding standard deviations.

Table 6-2: Melting points obtained by evaluation of T(t)-curves $\theta_{m,\,T(t)}$, G(t)-curves $\theta_{m,\,G(t)}$, and *lnG*-plots $\theta_{m,\,lnG}$, the differences $\Delta\theta_{m,\,G(t)}$ and $\Delta\theta_{m,\,lnG}$ to $\theta_{m,\,T(t)}$, and the corresponding standard deviations.

Substance	$\theta_{m,T(t)}$ [°C]	$\theta_{m,\,G(t)}$ [°C]	$\Delta\theta_{m,\,G(t)}$ [°C]	$\theta_{m,\,lnG}$ [°C]	$\Delta\theta_{m,\,lnG}$ [°C]
$BMIBF_4$	-	-	-	-	-
BMPlFAP	1.9 ± 0.5	2.6 ± 0.3	0.6 ± 0.2	2.84 ± 0.14	0.9 ± 0.4
$BMPlNTf_2$[a]	-8.46	-	-	-	-
BMPlOTf	4.41 ± 0.04	5.17 ± 0.03	0.76 ± 0.06	5.60 ± 0.06	1.20 ± 0.08
$EMIBF_4$	13.42 ± 0.16	13.825 ± 0.007	0.310 ± 0.014	14.08 ± 0.02	0.66 ± 0.18
EMIDCA	-5.46 ± 0.15	-4.95 ± 0.04	0.44 ± 0.06	-4.680 ± 0.019	0.72 ± 0.08
$EMINTf_2$	-17.2 ± 0.4	-16.6 ± 0.2	0.5 ± 0.3	-16.34 ± 0.05	0.7 ± 0.5
EMIOTf[a]	-11.10 ± 0.15	-	-	-	-
$HMINTf_2$[a]	-1.85	-	-	-	-
Me_3SDCA	12.7 ± 0.4	13.85 ± 0.19	1.1 ± 0.3	15.33 ± 0.06	2.6 ± 0.3
MPII	16.9 ± 0.2	17.8 ± 0.3	0.8 ± 0.3	18.6 ± 0.3	1.5 ± 0.4
TOMATFA[a]	12.55 ± 0.09	-	-	-	-

[a] No conductivity recorded.

Additionally, the mean values of the differences between the melting points from T(t)-curves and G(t)-curves and between the melting points from T(t)-curves and *lnG*-plots are given with the corresponding standard deviations. The values determined for specific measurements are summarised for each IL in Chap. 8.3 (Table 8-60 to Table 8-70). For $BMIBF_4$ no phase transition was detected. EMIOTf and TOMATFA were exclusively measured in T(t)-measuring cells. The G(t)-T(t)-measuring cells for $BMPlNTf_2$ and $HMINTf_2$ were damaged at the end of the first cooling-heating cycle and thus, no useful conductivity data were obtained.

Generally, the melting points obtained from G(t)-curves and *lnG*-plots show very small standard deviations even for values determined at varying heating rates. Both melting points are always higher than the corresponding value from T(t)-curves primarily based on the non-ideal steplike increase of the conductivity at incipient melting. The difference between the melting points from T(t)- and G(t)-curves is typically in the range from 0.3 to 1 °C, the difference between the melting points from T(t)-curves and *lnG*-plots is a bit larger, i.e. typically in the range from 0.6 to 1.5 °C. Both deviations from the melting point obtained from T(t)-curves are much smaller than the differences among published melting points of specific ILs (Table 6-3). The corresponding values are also typically within the error margins calculated from literature values.

To sum it up, if a phase transition point can not be directly obtained from T(t)-measurements, simultaneously recorded conductivity data can yield a very accurate and useful approximation of the searched value.

6.1.3 Comparison and Discussion of the Determined Phase Transition Points with Corresponding Values from Literature

Generally, three different types of behaviour were observed for the ILs during cooling and heating. The first group of ILs has a distinct freezing point on cooling with varying strong supercooling and a distinct melting point on heating, as observed for EMIDCA and EMIOTf. The second group shows no phase transition but formation of an amorphous glass is assumed at the lower limit of the operating range, transforming into a liquid again during heating. $BMIBF_4$ is a compound that shows such behaviour [166]. The third group of ILs behaves like the second group during cooling. However, upon heating the IL is assumed to pass from the glass to a supercooled liquid phase and then crystallisation

occurs. If the sample is heated further it melts at θ_m. MPII and TOMATFA are two examples that belong to this last group.

In Table 6-3 the mean values of freezing and melting points determined by evaluation of T(t)-curves are listed along with the corresponding standard deviations and literature values. As mentioned above, supercooling was defined as temperature difference between the melting point and the temperature where the sample starts to crystallise. The exact values determined for the specific measurements are summarised for each IL in Chap. 8.3 (Table 8-60 to Table 8-70).

Table 6-3: Freezing $\theta_{f,\,T(t)}$ and melting points $\theta_{m,\,T(t)}$ obtained by evaluation of T(t)-curves with corresponding standard deviations, supercooling $\Delta\theta_s$, and literature values $\theta_{f,\,lit}$ and $\theta_{m,\,lit}$.

Substance	$\theta_{f,\,T(t)}$ [°C]	$\theta_{f,\,lit}$ [°C]	$\Delta\theta_s$ [°C]	$\theta_{m,\,T(t)}$ [°C]	$\theta_{m,\,lit}$ [°C]
$BMIBF_4$	-	-	-	-	-71[c] [165], -81[c] [168], -85[c] [166]
BMPIFAP	-8.9 ± 1.8	-	18.2 ± 1.1	1.9 ± 0.5	-
$BMPINTf_2$[a]	-39.15	-	44.17	-8.46	-18 [159], -22 [169]
BMPIOTf	-2.0 ± 0.9	-	18.3 ± 1.8	4.41 ± 0.04	-
$EMIBF_4$	-15 ± 3	-50.5 [170], -58 [143], -63 [109]	50 ± 2	13.42 ± 0.16	11 [109], 13 [143], 14.6 [170], 15 [68]
EMIDCA	-14 ± 3	-54 [140]	32 ± 6	-5.46 ± 0.15	-12 [140], -21 [136]
$EMINTf_2$	-19 ± 2	-50 [109]	32.2 ± 1.6[a] 16.3 ± 0.9	-2.44 ± 0.12[a] -17.2 ± 0.4	-3 [70], -12 [145], -15 [109], -16 [68], -17 [166], -18 [69], -21 [162]
EMIOTf[a]	-12.77 ± 0.17	-	5.9 ± 0.9	-11.10 ± 0.15	-9 [70], -10 [144], -15 [69]
$HMINTf_2$[a]	-42.00[b]	-	40.15	-1.85	-6 [160], -7 [171]
Me_3SDCA	13.8 ± 0.4	-	10 ± 3	12.7 ± 0.4	-1 [152]
MPII	-14.3 ± 1.5[b]	-	31.2 ± 1.6	16.9 ± 0.2	-70[c] [69]
TOMATFA[a]	-16.6 ± 0.6[b]	-	29.2 ± 0.6	12.55 ± 0.09	-

[a] No conductivity recorded.
[b] Crystallisation during heating.
[c] Glass-transition temperature.

The large differences between the determined freezing points and the literature values arise from different definitions of the freezing point. Generally, the freezing point is defined as the temperature of the halt obtained during crystallisation of the sample (see Chap. 2.3). For ILs the halt is often very short due to the occurring large supercooling. Therefore, instead of determination by extrapolation, the freezing point is defined as highest reached temperature during crystallisation [107]. For DSC-measurements the freezing point is

generally defined as onset of the crystallisation. [140,166] These freezing points are still 10 to 20 °C lower than the corresponding onset temperatures obtained from T(t)-curves.

For $BMIBF_4$ no phase transition point was observed. The applied measurement technique may not have been sensitive enough for detection of a glass-transition.

The melting points for BMPlFAP, BMPlOTf, MPII, and TOMATFA are determined for the first time and except for BMPlFAP with very low standard deviations. The comparatively high melting point of MPII is of special interest since MPII is a frequently used IL for DSSC-electrolytes. Up to the present a broad liquid range was assumed for this specific IL, mainly based on its low glass-transition temperature [69] and unavailable melting points due to inadequate measurement equipment.

In the case of $BMPlNTf_2$ and $HMINTf_2$ the determined melting points for both ILs are considerable higher than those given in literature. These large differences are possibly based on varying purity grades, as discussed in Chap. 6.1.1. However, both ILs should be examined again due to large differences vs. literature values and the fact that for each IL only one melting point could be determined without supporting conductivity data before the measuring cell was damaged.

A better conformity with literature values was obtained for $EMIBF_4$ and EMIOTf. The melting points for both ILs show comparably small standard deviations and are in the range of the corresponding literature values. The different literature values are primarily the result of varying purity grades. Especially for $EMIBF_4$ varying quantities of halide based impurities are obtained in our laboratory caused by different synthesis-routes. [113]

The melting points for EMIDCA and Me_3SDCA are, similar to $BMPlNTf_2$ and $HMINTf_2$, both considerably higher than the corresponding literature values but confirmed by a huge quantity of measurements and evaluation of additionally recorded conductivity data. Since both ILs are comparably new only few literature values are published. Me_3SDCA was, apart from drying on high vacuum, used as received from Gerhard[a] who reported a melting point for Me_3SDCA of -1 °C [152]. In Ref. [152] no details on impurities or measurement conditions are given. Since the melting point of -1 °C matches the temperature of beginning crystallisation for high cooling rates (Table 8-62) an inaccurate evaluation of the DSC-measurements in Ref. [152] is possible. Me_3SDCA is the only examined IL where the determined freezing point is higher than the melting point. The melting point of EMIDCA is, similar as for MPII, of special interest for researchers interested in DSSCs since EMIDCA is also a frequently used and promising IL for formation of DSSC-electrolytes.

[a] Thanks to Dr. D. Gerhard, Chemical Reaction Engineering, Friedrich-Alexander-University Erlangen-Nürnberg, now with BASF.

[13,27,139] Up to the present only two groups reported melting points for EMIDCA. The difference of 9 °C between the two published values is comparably large. The melting point determined in this work is even higher. The reason for these large differences is most likely varying purity grades of the examined samples. This assumption is confirmed by the more often published and also strongly varying viscosities of EMIDCA (Table 6-4), since the viscosity of ILs is also strongly affected by impurities [172], such as halides, organic solvents or water.

Table 6-4: Published viscosities η of EMIDCA with measurement temperature θ and source.

θ [°C]	η [mPa s]	Ref.
20	21	[138]
22	17	[140]
25	21	[136]
25	28.09	[139]

The results obtained for $EMINTf_2$ are not as clear as for the other examined ILs. Since the G(t)-T(t)-measuring cells are very damageable and due to inconsistent results after the first measurement series, $EMINTf_2$ was examined four times in four different measuring cells, all samples were from the same batch. The results from three measuring cells (14 measurements; 9 with simultaneous recorded conductivity, 5 without) were consistent and used for calculation of the mean value of -17.2 ± 0.4 °C. This value is in good accordance with the majority of literature values (Table 6-3). For the fourth measuring cell (8 measurements without recorded conductivity) the same freezing points were determined as for the other measurements but for seven of the eight measurements different melting points were obtained (Table 8-61). There is also one value from literature (-3 °C [70]) that is in conformity with the mean value of -2.44 ± 0.12 °C calculated from the results of these seven measurements. Such huge differences between melting points of one substance were not detected in any other case in over three years of almost consecutive measurements. The generally occurring deviations are at least one dimension smaller (Table 6-3, and Refs. [107,108]). Permeated air, moisture, and other impurities can be disregarded because these would decrease the melting point instead of increasing it. If measurement errors can be disregarded, the only remaining explanation is that solid $EMINTf_2$ exists in at least two different crystal structures with different melting points as well. ILs with two different crystal structures in the solid state are reported [173,174], albeit without detection of different melting points. If the different crystal structures occur in the case for $EMINTf_2$,

there must be a solid-solid phase transition because the freezing point and the temperature of the beginning crystallisation are almost identical for all measurements. Due to the lack of additional analytical data, no definite explanation can be given for the behaviour of $EMINTf_2$.

As done for the conductivity, the influence of the anion on the freezing point, melting point, and supercooling of EMI based ILs was examined. The freezing point in its original definition is strongly influenced by supercooling and shows comparably large standard deviations in the case of ILs (Table 6-3). The highest freezing point can be attributed to EMIOTf followed by EMIDCA, $EMIBF_4$, and $EMINTf_2$. For ILs the more significant phase transition point is the melting point. The order of ILs at the melting point meets the expectations much more. $EMIBF_4$ with the comparably small and highly symmetric BF_4-anion has the highest melting point, followed by EMIDCA with the also small but angulate and thus less symmetric DCA-anion. EMOITf has the second lowest melting point despite the strong tendency of the OTf-anion to formation of hydrogen-bonds. $EMINTf_2$ with the largest and most flexible anion [150] has the lowest melting point. Upon cooling EMIOTf is the first IL starting crystallisation followed by $EMINTf_2$ at much lower temperature that is followed at only slightly lower temperature by $EMIBF_4$ and EMIDCA. This behaviour and the order of ILs with regard to the magnitude of supercooling are in clear contrast to the behaviour at the melting point.

6.2 Phase Diagrams of Potential DSSC-Electrolytes

The theory for determination of phase transition points for construction of phase diagrams has already been discussed in Chap. 2.3, determination of phase transition points in Chap. 3.4.2. The reliability of phase transition points obtained from G(t)-curves and *lnG*-plots was analysed and discussed in Chap. 6.1.2, yielding that melting points obtained from conductivity data are typically 0.3-1.5 °C higher than melting points obtained from T(t)-curves. In this chapter a short overview is given over phase diagrams on the basis of their simplest case, i.e. a phase diagram of a binary, eutectic mixture. A generalized example is shown as temperature-mol fraction diagram in Figure 6-5. For this system (components A and B) the following conditions are valid:

- A and B are completely miscible for each molar ratio in the liquid phase (= phase α).
- A and B are completely immiscible in the solid phase (= phase β), i.e. no formation of mixed crystals, but a mixture of crystals of components A and B.
- The pressure stays constant.

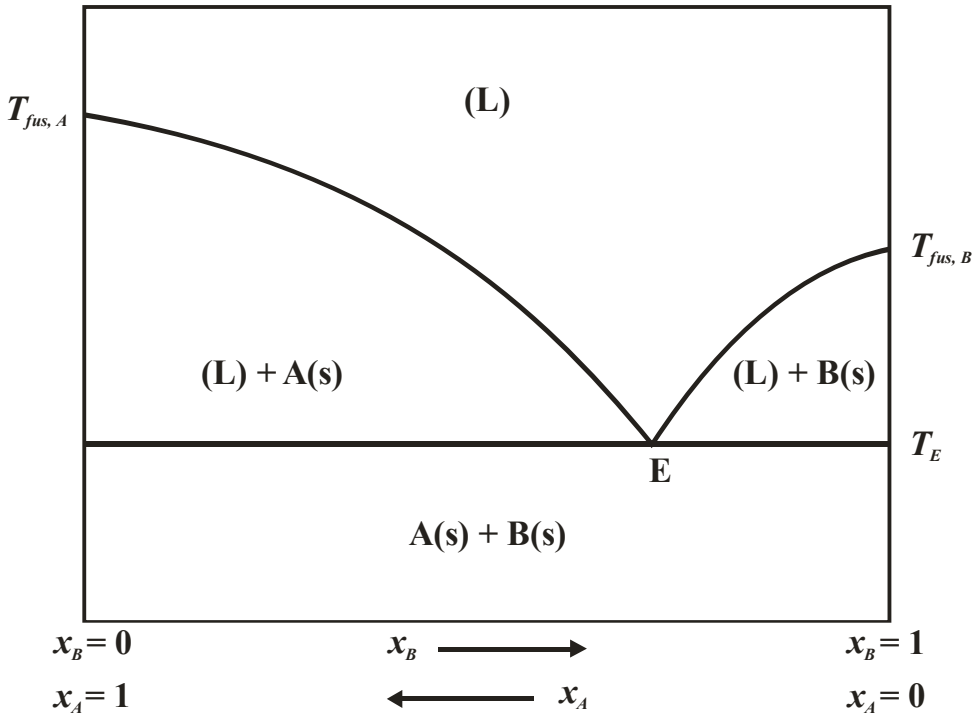

Figure 6-5: Ideal phase diagram of a binary, eutectic mixture.

The phase diagram contains several regions of varying composition:

- (L): homogeneous liquid mixture of components A and B;
- (L) + A(s): coexistence of (L) and solid component A;
- (L) + B(s): coexistence of (L) and solid component B;
- A(s) + B(s): coexistence of the solid components A and B;

The lines $T_{fus,A}E$ (solidus curve of A = melting curve of A = solubility curve of A) and $T_{fus,B}E$ (solidus curve of B = melting curve of B = solubility curve of B) are defined by the breaking points obtained from cooling- and heating-curves (Chap. 2.3). The halts obtained from these measurements define the eutectic isotherm through E and the melting point of the pure components A and B, $T_{fus,A}$ and $T_{fus,B}$ (at $x_A = 1$ and $x_B = 1$) (Chap. 2.3). The discussed lines confine the different regions. The charge transport in an electrolyte dramatically declines upon solidification (as shown in Chap. 3.4.2 for conductivity) and as a consequence also the energy output of the electrochemical device. Solidification of the electrolyte may also damage some component parts or the whole device. The liquid range of the electrolyte can be enlarged by the appropriate choice of composition.

Considered from a traditional point of view the examined DSSC-electrolytes typically consist of three components (iodine, MPII, solvent IL) and therefore have to be described by means of ternary phase diagrams. Since the iodine concentration stays nearly constant and at low values the systems can be also approximately described by binary phase diagrams.

However, one of the most unique features of ILs is that they consist completely of ions and their aggregates. Thus, a mixture of ILs consists not only of the original ILs that were mixed together but also of various other potential combinations of cations and anions. That means a common DSSC-electrolyte blend, e.g. EMIDCA/MPII that was made up of iodine, EMIDCA, and MPII can also be described as blend of EMIDCA, EMII, $EMII_3$, MPIDCA, MPII, and $MPII_3$ and hence as a six component system. The large quantity of components complicates evaluation of cooling and heating curves because only comparably small parts of the blend crystallize and melt resulting in indistinct phase transition points. Therefore, the determined phase transition points of DSSC-electrolyte blends are by far not as accurate as for pure ILs despite additionally recorded conductivity. The most accurate values were obtained for the two blends at both ends of the mixing range, i.e. with ≈ 10 mol% and 100 mol% MPII. In addition, the already low addiction of ILs to crystallise

is further reduced by adding other components. That leads to broad mixing ranges for some of the electrolyte systems where no phase transitions were observed.
In general, if at all only breaking points were obtained, no eutectic halts were observed. As shown in Figure 6-5 the breaking points define the solidus line that confines the liquid region of the electrolyte system. Thus, the breaking points are sufficient for definition of the liquid and consequently operating range of the DSSC-electrolyte mixtures.

6.2.1 EMIDCA/MPII

For construction of a phase diagram for the system EMIDCA/MPII the same blends were examined as used for conductivity measurements in Chap. 5.1.2; and two additional blends were tested. The accurate compositions of the blends are given in Table 8-71. Three cooling-heating cycles were performed with cooling and heating rates v of -/+ 5 K h^{-1} and the bath temperature ranging from -80 °C to +65 °C. The mean values of the breaking points for the melting process determined by evaluation of the heating branches of T(t)-($\theta_{b,\,T(t)}$) and G(t)-curves ($\theta_{b,\,G(t)}$), and lnG-plots ($\theta_{b,\,lnG}$) as well are summarised in Table 6-5 along with the corresponding standard deviations. The breaking points for crystallisation $\theta_{fc,\,T(t)}$ obtained from the cooling branch of T(t)-curves are also listed in Table 6-5. The accurate values for each blend and specific measurements are summarised in Chap. 8.3.2 (Table 8-72 to Table 8-76).

Table 6-5: Phase transition points of ≈ 0.05 mol L^{-1} I_2 in mixtures of EMIDCA/MPII with varying MPII concentrations determined at a cooling and heating rate v of -/+ 5 K h^{-1}.

Mol% MPII	$\theta_{fc,\,T(t)}$ [°C]	$\theta_{b,\,T(t)}$ [°C]	$\theta_{b,\,G(t)}$ [°C]	$\theta_{b,\,lnG}$ [°C]
5.4[a]	-43.31	-7.63	-	-
10.9	-53 ± 4[b]	-14.4 ± 0.2	-12.1 ± 0.9	-13.96 ± 0.17
15.1[a]	-49.01	-17.09	-	-
20.8	-	-	-	-15.26 ± 0.13
30.6	-	-	-	-
41.0	-	-	-	-
50.5	-	-	-	-
60.7	-	-	-	22.25 ± 0
81.0	-	-	-	-
100.0	-29.3 ± 1.8[b]	16.70 ± 0.10	17.93 ± 0.04	18.560 ± 0.014

[a] No conductivity recorded.
[b] Crystallisation during heating.

The phase transition point of 0.05 mol L^{-1} I_2 in MPII is assumed to be a melting point rather than a breaking point due to enormous excess of MPII and the characteristic of the phase transition. That is of interest for evaluation of the specific phase transition since the melting point is defined as beginning of the melting process whereas a breaking point is defined as its end.

Similar to pure ILs the phase transition points obtained from conductivity data are higher than phase transition points from T(t)-curves. The melting point of 0.05 mol L^{-1} I_2 in MPII is only slightly lower than for pure MPII. Between 21 mol% MPII and 81 mol% MPII no phase transition could be detected by evaluation of T(t)- and G(t)-curves. The two breaking points determined from the *lnG*-plots of the blends with 21 mol% MPII and 61 mol% MPII were only weakly pronounced. The phase diagram constructed from breaking points obtained from heating curves (Table 6-5) is shown in Figure 6-6.

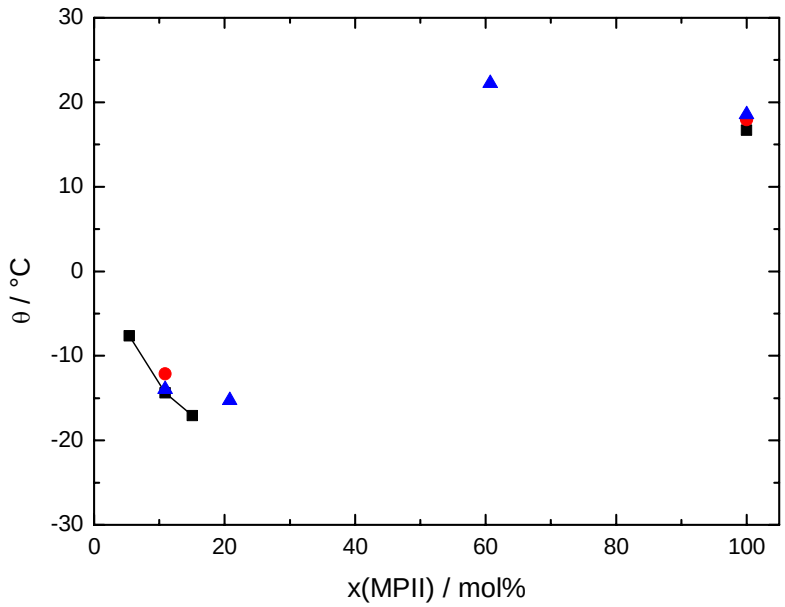

Figure 6-6: Phase diagram of the system EMIDCA/MPII; breaking points obtained from T(t)-curves (—■—), G(t)-curves (—●—), and *lnG*-plots (—▲—).

The absence of phase transition points for a broad mixing range is not definitely based on a corresponding broad liquid range. Especially on the MPII-rich side of the system behaviour of the blends similar to the one of pure MPII is assumed, i.e. a very low addiction to crystallisation that is further reduced by addition of EMIDCA despite a comparably high melting point of the resulting blend. However, both originally employed ILs and the potentially formed new combinations are strongly hydrophilic and should therefore show a high solubility in the actual solvent IL.

6.2.2 $EMIBF_4$/MPII

For construction of a phase diagram for the system $EMIBF_4$/MPII the same blends were examined as used for conductivity measurements (Chap. 5.1.3). The exact compositions of the blends are listed in Table 8-51. Only two cooling-heating cycles with cooling and heating rates v of -/+ 5 K h^{-1} were performed due to a large number of damaged measuring cells and other breakdowns. During these cycles the bath temperature was varied between -80 °C and +65 °C. In Table 6-6 the calculated mean values of the breaking points for crystallisation during cooling θ_{fc} and heating θ_{fh} and for melting θ_b are summarised along with the corresponding standard deviations. The exact values for the specific measurements are listed in Chap. 8.3.2 (Table 8-77 to Table 8-84). For some of the blends in the middle of the mixing range two potential breaking points (θ_{b1} and θ_{b2}) were obtained by evaluation of conductivity data. Since an accurate assignment of the determined phase transition temperature to a specific process was not possible, it was assumed to be equal for both breaking points if only one of them was observed. That was generally the case for the blends at the boundaries of the mixing range.

Table 6-6: Phase transition points of ≈ 0.05 mol L^{-1} I_2 in mixtures of $EMIBF_4$/MPII with varying MPII concentrations determined at a cooling and heating rate v of -/+ 5 K h^{-1}.

Mol% MPII	$\theta_{fc,\,T(t)}$ [°C]	$\theta_{fh,\,T(t)}$ [°C]	$\theta_{fc,\,G(t)}$ [°C]	$\theta_{fc,\,lnG}$ [°C]	$\theta_{b,\,T(t)}$ [°C]	$\theta_{b1,\,G(t)}$ [°C]	$\theta_{b2,\,G(t)}$ [°C]	$\theta_{b1,\,lnG}$ [°C]	$\theta_{b2,\,lnG}$ [°C]
10.1[a]	-42.3 ± 0.3	-	-42.3 ± 0.3	-42.3 ± 0.3	12.28 ± 0.04	13.62 ± 0.05	-	12.1 ± 0.3	-
19.9[a]	-38.6 ± 0.3	-	-38.5 ± 0.4	-38.5 ± 0.4	12.96 ± 0	13.72 ± 0	-	12.43 ± 0	-
30.0	-37.6 ± 1.7	-50.75 ± 0.05	-36.4 ± 0	-36.4 ± 0	-9.92 ± 0.08	-8.34 ± 0	13.0 ± 1.8	-	10.7 ± 0.5
39.8	-12.64 ± 0	-48.80 ± 0	-12.26 ± 0	-4.87 ± 0	-6.74 ± 0	-4.9 ± 0.4	10.2 ± 1.4	-5.7 ± 1.3	10.41 ± 0.06
50.1	-30 ± 6	-	-25.28 ± 0	-	-4 ± 3	-0.7 ± 0	14.32 ± 0	-1.7 ± 0.7	16.7 ± 1.5
60.1	-	-27 ± 4	-	-	3.2 ± 0.2	5.7 ± 1.5	22.58 ± 0	3.1 ± 0.7	21.4 ± 0.8
80.0[b]	-	-34.30 ± 0	-	-	7.53 ± 0	-	-	-	-
100.0[a]	-	-29.3 ± 1.8	-	-	16.70 ± 0.10	17.93 ± 0.04	-	18.560 ± 0.014	-

[a] Only one breaking point observed.
[b] No conductivity recorded.

Evaluation of T(t)-curves yielded one breaking point for each blend that correlates comparably well with the values for the first breaking point obtained by evaluation of the corresponding conductivity data. The values for these breaking points at the $EMIBF_4$-rich side of the mixing range are nearly as high as the melting point of pure $EMIBF_4$. Despite

an extraordinarily large supercooling occurs for pure $EMIBF_4$ (Table 6-3), the blends at the $EMIBF_4$-rich side mainly crystallise during cooling. For the blends at the MPII-rich side the breaking points are clearly lower than the melting point for pure MPII, but the blends generally show a similar behaviour as MPII; i.e. crystallisation during heating and a comparably high melting point. Supercooling is generally large except for the blend with 40 mol% MPII. The second breaking point was only observed for blends in the middle of the mixing range and only determined by evaluation of conductivity data. For the blend with 60 mol% MPII a nearly identical value was obtained as for the corresponding blend of the system EMIDCA/MPII. A similar behaviour was also observed for the system $EMINTf_2$/MPII.

The phase diagram constructed from the breaking points for melting obtained from T(t)-curves and from conductivity data is shown in Figure 6-7. If only the breaking points from T(t)-curves and the lower breaking points from G(t)-curves and *lnG*-plots are considered, the maximum for the liquid range of the system $EMIBF_4$/MPII is around a MPII concentration of 30 mol%. With regard to the higher breaking points obtained from conductivity data, the liquid range of the blends resembles the ones for the two pure ILs and no distinct maximum can be observed. However, for both cases the liquid range of this system stays comparably narrow over the whole mixing range.

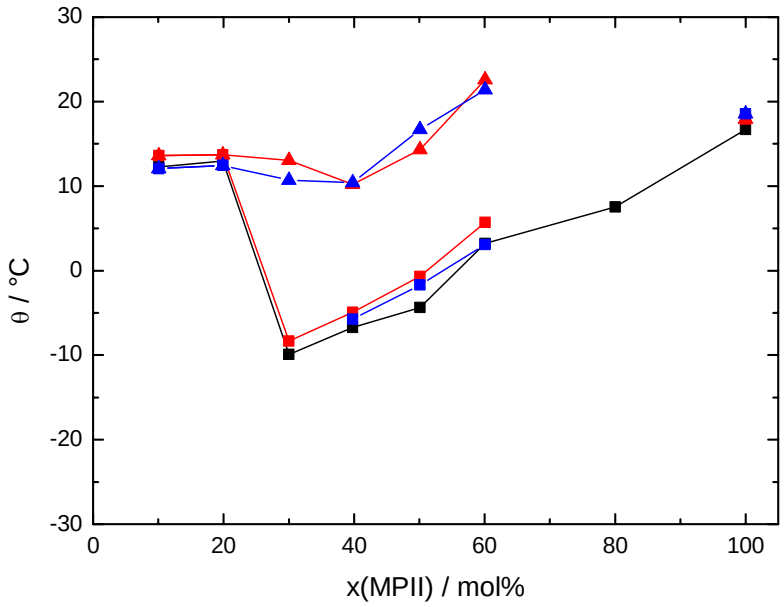

Figure 6-7: Phase diagram of the system $EMIBF_4$/MPII; breaking points obtained from T(t)-curves (—■—), θ_{b1} (—■—) and θ_{b2} (—▲—) from G(t)-curves, and θ_{b1} (—■—) and θ_{b2} (—▲—) from *lnG*-plots.

6.2.3 EMIOTf/MPII

As for the two previous electrolyte systems the blends that were examined with regard to conductivity (Chap. 5.1.4) were also examined for construction of a phase diagram for the system EMIOTf/MPII. The accurate compositions of the blends are given in Table 8-54. Three cooling-heating cycles were performed with cooling and heating rates v of -/+ 5 K h^{-1} and the bath temperature ranging from -80 °C to +65 °C. The calculated mean values of the determined breaking points (Table 8-85 and Table 8-86) are summarised in Table 6-7 with the corresponding standard deviations.

Table 6-7: Phase transition points of ≈ 0.05 mol L^{-1} I_2 in mixtures of EMIOTf/MPII with varying MPII concentrations determined at a cooling and heating rate v of -/+ 5 K h^{-1}.

Mol% MPII	$\theta_{fh,\,T(t)}$ [°C]	$\theta_{b,\,T(t)}$ [°C]	$\theta_{b,\,G(t)}$ [°C]	$\theta_{b,\,lnG}$ [°C]
10.1	-48 ± 4	-17.947 ± 0.015	-15.57 ± 0.08	-16.88 ± 0.12
19.8	-	-	-23.44 ± 0	-23.2 ± 0.2
40.1	-	-	-	-
50.1	-	-	-	-
60.1	-	-	-	-
80.0	-	-	-	-
100.0	-29.3 ± 1.8	16.70 ± 0.10	17.93 ± 0.04	18.560 ± 0.014

The phase diagram constructed from the breaking points for melting in Table 6-7 is shown in Figure 6-8. No breaking points could be observed for the largest part of the mixing range. Since EMIOTf is an IL with comparably low melting point but only little addiction to supercooling (Table 6-3), a larger number of detectable breaking points was expected for EMIOTf-rich blends. The behaviour of the blends at the MPII-rich side is assumed to be similar as for pure MPII. Despite the absence of breaking points in the examined temperature range, solidification of the blends cannot be definitely excluded. However, EMIOTf and MPII are both very hydrophilic ILs and the potentially formed combinations are as well. The resulting good solubility in the quantitative dominating IL may enable a broad liquid range of the blends.

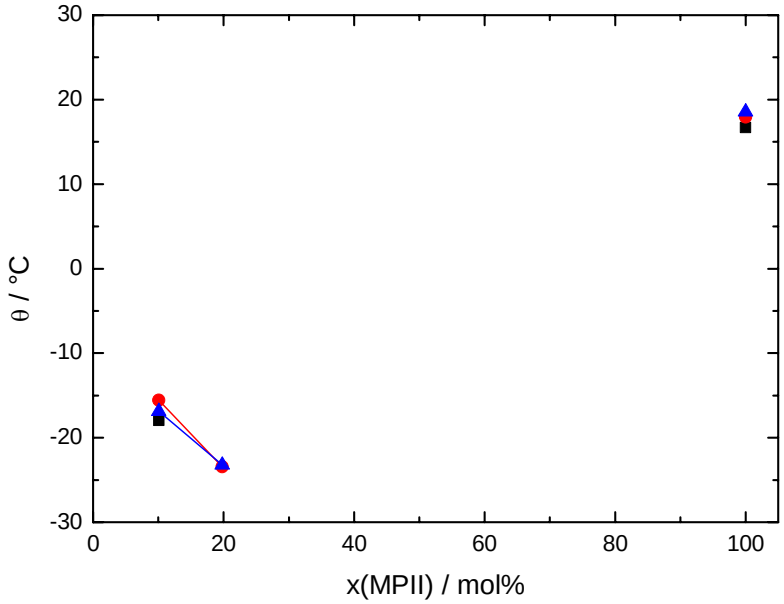

Figure 6-8: Phase diagram of the system EMIOTf/MPII; breaking points obtained from T(t)-curves (—■—), G(t)-curves (—●—), and *lnG*-plots (—▲—).

6.2.4 $EMINTf_2$/MPII

As already mentioned in Chap. 4.4, $EMINTf_2$ has an exceptional position among the studied solvent ILs since it is hydrophobic. Insolubilities of hydrophobic $EMINTf_2$ in hydrophilic MPII and vice versa at lower temperatures and specific electrolyte compositions were expected and sometimes qualitatively observed for the blends examined in Chap. 4.4.

For detailed examination of this behaviour and generally for construction of a phase diagram for the system $EMINTf_2$/MPII the same blends were examined as were used for the conductivity measurements in Chap. 5.1.5. The accurate compositions of the blends are given in Table 8-57. Since only few breakdowns occurred during the measurements, seven cooling-heating cycles with cooling and heating rates v of -/+ 5 K h^{-1} were performed. The bath-temperature was varied between -80 °C and +65 °C. In Table 6-8 the calculated mean values of the breaking points obtained for crystallisation during cooling θ_{fc} and heating θ_{fh} and for melting θ_b, θ_{b1} and θ_{b2} as well are summarised along with the corresponding standard deviations for each specific evaluation method. The exact values for the specific measurements are listed in Chap. 8.3.5 (Table 8-87 to Table 8-93).

Table 6-8: Phase transition points of ≈ 0.05 mol L^{-1} I_2 in mixtures of $EMINTf_2$/MPII with varying MPII concentrations determined at a cooling and heating rate *v* of -/+ 5 K h^{-1}.

Mol% MPII	$\theta_{fh,\,T(t)}$ [°C]	$\theta_{fc,\,G(t)}$ [°C]	$\theta_{fh,\,G(t)}$ [°C]	$\theta_{fc,\,lnG}$ [°C]	$\theta_{fh,\,lnG}$ [°C]	$\theta_{b,\,T(t)}$ [°C]	$\theta_{b1,\,G(t)}$ [°C]	$\theta_{b2,\,G(t)}$ [°C]	$\theta_{b1,\,lnG}$ [°C]	$\theta_{b2,\,lnG}$ [°C]
10.0	-50.7 ± 0.3	-	-	-	-	-7.3 ± 0.2	-4.61 ± 0.07	-4.03 ± 0.15	-7.29 ± 0.05	-4.12 ± 0.16
20.0	-	-	-22.1 ± 0.2	-	-22.0 ± 0.4	-10.72 ± 0.15	-8.30 ± 0.12	26.0 ± 1.2	-10.0 ± 0.3	26.1 ± 1.8
30.0	-	-	-10 ± 2	-	-8.37 ± 0	-23.80 ± 0	-23.0 ± 0.9	-	-23.59 ± 0.02	-
40.0	-	7.04 ± 0.15	-21.51 ± 0	0 ± 11	-22.21 ± 0	-	-	38.2 ± 0.4	-	36.4 ± 1.7
50.0	-	4 ± 3	-15.6 ± 0.9	4 ± 4	-16.8 ± 0.5	-	-	38.9 ± 0.3	-	36.5 ± 1.9
60.0	-	10 ± 3	-	10 ± 3	-21.7 ± 0.6	-	-	34.43 ± 0.11	-	34.8 ± 1.3
80.0	-	-	1 ± 2	-	0 ± 2	-	-	17.73 ± 0.08	-	18.5 ± 0.3
100.0	-29.3 ± 1.8	-				16.70 ± 0.10	17.93 ± 0.04	-	18.560 ± 0.014	-

The breaking points for crystallisation obtained from cooling and heating curves vary strongly. The values obtained from heating curves show significantly smaller standard deviations. Addiction to supercooling is generally high for all blends. Similar to the system $EMIBF_4$/MPII two different breaking points for melting were observed. The lower or first breaking point was only obtained for $EMINTf_2$-rich blends. The values obtained from the three different evaluation methods are in good conformity. The first breaking point for the two blends with 10 and 20 mol% MPII is significantly higher than the lower melting point of pure $EMINTf_2$ (Table 6-3). Since the melting point of a pure substance generally decreases by adding a second component, the occurrence of a second and higher melting point for pure $EMINTf_2$ is once more confirmed by the phase transition temperatures of these two blends. The higher or second breaking point was observed over almost the whole mixing range. The values for the blend with 80 mol% MPII are assigned to this second breaking point due to similar characteristics and the fact that no phase transition was determined with T(t)-curves.

The phase diagram constructed from the breaking points for melting from Table 6-8 is shown in Figure 6-9. The liquid range of this system stays comparably narrow over the whole mixing range. The maxima can be observed at both boundaries of the mixing range where the blends have similar liquid ranges as the pure ILs.

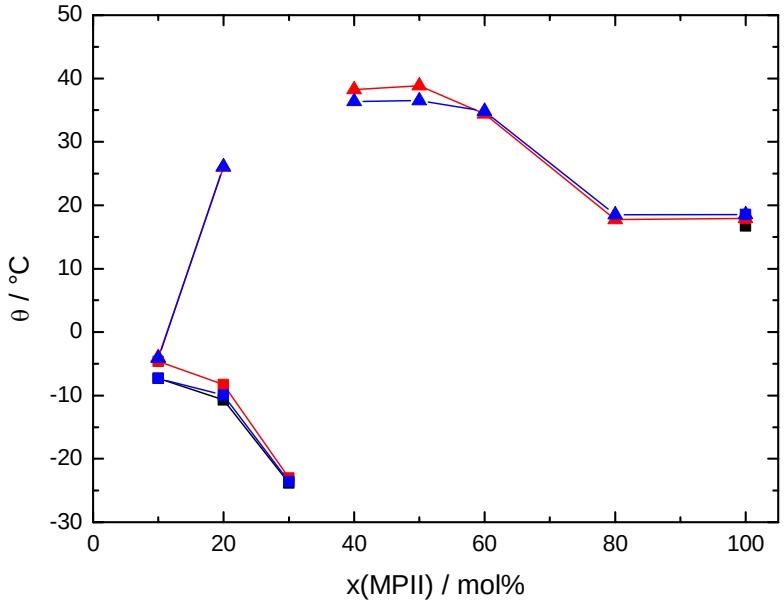

Figure 6-9: Phase diagram of the system EMINTf$_2$/MPII; breaking points obtained from T(t)-curves (—■—), θ_{b1} (—■—) and θ_{b2} (—▲—) from G(t)-curves, and θ_{b1} (—■—) and θ_{b2} (—▲—) from *lnG*-plots.

The second breaking points for this system are higher than for the systems EMIDCA/MPII and EMIBF$_4$/MPII. The constant parameters for all three systems are the cations (EMI and MPI) and two of the anions (iodide and triiodide). Thus, the part of the mixture that finishes its melting process at the second breaking point consists with high probability of a combination of two of these four components. For the system EMIBF$_4$/MPII the second breaking points are still in the temperature range of the melting point of pure MPII or MPII$_3$. Both salts can be excluded for the system EMINTf$_2$/MPII because they are liquid at nearly all determined phase transition temperatures. Another possible combination of these components that is solid up to comparably high temperatures is EMII (θ_m = 79 °C [109]). It especially can be assumed for the system EMINTf$_2$/MPII that the precipitate consists most likely of EMII due to its high melting point and the stronger hydrophilic character of EMII compared to MPII.

6.3 Summary and Appraisal of Results

Phase transition points of several pure ILs were determined by three different evaluation methods. After comparison and verification of the obtained results, determination of phase transition points of blends of the electrolyte systems EMIDCA/MPII, $EMIBF_4$/MPII, EMIOTf/MPII, and $EMINTf_2$/MPII was performed in a uniform manner.

Investigation of the various parameters that influence freezing and melting points showed that the purity of the sample is of extraordinary importance. Already minor impurities cause a dramatic decrease of the melting point of $EMIBF_4$. The influence of the cooling rate on freezing points and magnitude of supercooling is comparably small and non-uniform. The melting points of ILs slightly decrease with increasing heating rates. Since DSC-measurements are generally performed at a fixed and comparably high scan rate this is a potential source of error. Application of carbon fibres as crystallisation aids in ILs reduces the magnitude of supercooling but has no distinct influence on determined freezing and melting points.

Comparison of phase transition points determined by evaluation of T(t)-curves, G(t)-curves, and *lnG*-plots showed that the values obtained from G(t)-curves and *lnG*-plots are typically 0.3 to 1 °C and 0.6 to 1.5 °C higher than the corresponding values obtained from T(t)-curves. Since both differences are much smaller than common deviations among published melting points of specific ILs, it can be assumed that evaluation of conductivity data also yields reliable phase transition points.

The determined phase transition points of $EMIBF_4$ and EMIOTf are in good conformity with values from literature. The melting points for BMPlFAP, BMPlOTf, MPII, and TOMATFA were determined for the first time, confirmed by either a larger number of measurements, additional recorded conductivity data or a combination of both. For the ILs $BMPlNTf_2$, $HMINTf_2$, EMIDCA and Me_3SDCA the determined melting points are clearly higher than the corresponding values from literature, primarily based on varying purity grades and inadequate data-evaluation. However, $BMPlNTf_2$ and $HMINTf_2$ should be examined again since for both ILs only one value could be determined due to a damaged measuring cell. A surprising result was obtained for $EMINTf_2$ since two clearly different melting points were observed for this salt. The lower melting point is frequently published in literature the higher one was additionally confirmed by results obtained by examination of the system $EMINTf_2$/MPII.

Examination of the blends of the electrolyte systems EMIDCA/MPII, $EMIBF_4$/MPII, EMIOTf/MPII, and $EMINTf_2$/MPII yielded only breaking points. For the systems EMIDCA/MPII and EMIOTf/MPII no phase transition points were obtained over a broad mixing range. Several blends of the systems $EMIBF_4$/MPII and $EMINTf_2$/MPII showed two breaking points, partially above the melting points of the originally employed pure ILs. The higher breaking points of these blends are primarily based on the formation of insoluble and high melting compounds, such as EMII, from cations and anions that are present in the melt. The phase diagrams for the four electrolyte systems, constructed with the mean values from the breaking points for melting obtained from T(t)-curves, G(t)-curves, and *lnG*-plots, are shown in Figure 6-10.

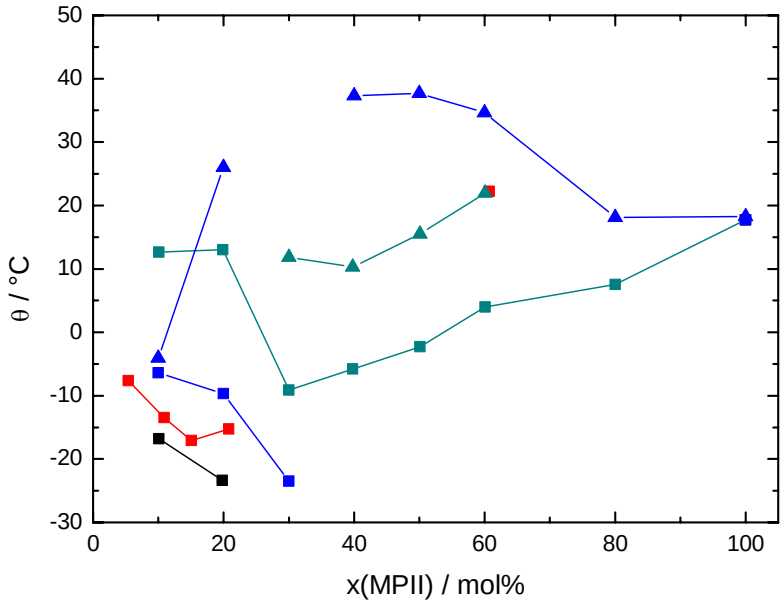

Figure 6-10: Phase diagrams of the systems EMIOTf/MPII (—■—), EMIDCA/MPII (—■—), $EMIBF_4$/MPII θ_{b1} (—■—) and θ_{b2} (—▲—), and $EMINTf_2$/MPII θ_{b1} (—■—) and θ_{b2} (—▲—) constructed with mean values calculated from the breaking points obtained from T(t)-curves, G(t)-curves, and *lnG*-plots.

No definite conclusion can be drawn for the liquid range of the systems EMIDCA/MPII and EMIOTf/MPII since only breaking points for blends at the boundaries of the mixing range were obtained. However, for these blends with low MPII concentraion the liquid range is clearly larger than for the corresponding pure ILs. Thus, for both systems its maximum is assumed at this boundary of the mixing range. The liquid range of the two other systems stays comparably narrow over the whole mixing range and has a minimum at

medium MPII concentrations. The maxima can be observed at both boundaries of the specific mixing ranges where the blends have similar liquid ranges as the pure ILs.

To sum it up, simultaneous recording of temperature and conductivity during cooling and heating of a sample has been proven to be a useful tool, especially for examination of mixtures of ILs. The higher breaking points of blends of the systems $EMIBF_4$/MPII and $EMINTf_2$/MPII were for instance exclusively determined by evaluation of conductivity data. However, the low durability of the applied G(t)-T(t)-measuring cells is a major problem especially for investigation of expensive materials. Smaller cell constants and consequently higher sensitivities would be a further improvement of the measuring cells as well as temperature and fill level independent cell constants.

7 Summary

The primary objective of this work was to characterise and optimise ionic liquid based electrolytes for application in DSSCs with respect to different properties and parameters. The examined electrolytes generally consist of iodine, 1-methyl-3-propylimidazolium iodide (MPII) and one of the following solvent ionic liquids: 1-ethyl-3-methylimidazolium bis(trifluoromethylsulfonyl)imide ($EMINTf_2$), 1-ethyl-3-methylimidazolium dicyanamide (EMIDCA), 1-ethyl-3-methylimidazolium tetrafluoroborate ($EMIBF_4$), or 1-ethyl-3-methylimidazolium trifluoromethanesulfonate (EMIOTf). These electrolyte mixtures were examined with respect to the following parameters:

- Charge transport by I_3^--diffusion was examined by steady-state cyclic voltammetry at ultramicroelectrodes.
- Charge transport by migration was examined by stationary and dynamic conductivity measurements.
- The liquid range of the electrolytes was examined by thermal analysis backed up by simultaneously recorded conductivity data.

All three parameters were studied over the whole mixing range of two ionic liquids to obtain the optimum mixing ratio with respect to charge transport and liquid range for each electrolyte system. For later application of DSSCs varying operating temperatures reaching values up to 60 °C are expected depending on location, season and time of day. To enable reliable predictions of the performance of DSSCs the single components have to be examined over a similar temperature range as expected for later application. Thus, examination of conductivity and I_3^--diffusion was performed in a temperature range from 5 °C to 50 °C and from 25 °C to 60 °C. It was shown that mixing ratio and temperature both have a strong influence on the electrolyte and thus, on the efficiency and operating range of the DSSC. An additional examination of the influence of I_3^--concentration on the diffusion yielded no distinct effects.

Systematic investigation of I_3^--diffusion over the whole mixing range of an ionic liquid based electrolyte at varying temperatures is a new approach that differs clearly to most published work in this field of research. The general approach is to examine a specific electrolyte composition at 25 °C or even without controlling the temperature. Examination of the liquid range of a potential DSSC-electrolyte was performed for the first time.

Actually, there is often not even reliable data available for the liquid range of the single components of these electrolytes up to now.

The largest I_3^--diffusion coefficients were obtained for the blends of the system EMIDCA/MPII. The I_3^--diffusion coefficients of the corresponding blends of the remaining systems are clearly lower and in the order $EMINTf_2$/MPII, $EMIBF_4$/MPII, and EMIOTf/MPII. It was shown that the I_3^--transport in all systems does not obey the Einstein-Stokes-equation and thus a non-Stokesian I_3^--transport occurs. The temperature dependence of this non-Stokesian I_3^--transport confirms the assumption of a Grotthus-type charge transfer mechanism in ionic liquids that occurs in addition to the diffusive charge transport and thus enhances the overall charge transport.

As for I_3^--diffusion the largest specific conductivities were obtained for the system EMIDCA/MPII. In contrast to I_3^--diffusion coefficients, the tendency of the conductivity with decreasing MPII concentration was similar for all systems and was analysed according to a third grade polynomial.

Investigation of the liquid range yielded strongly different results for specific electrolyte systems. On the one hand no breaking points could be observed for most of the mixing range of the systems EMIDCA/MPII and EMIOTf/MPII. The maximum of the liquid range for both systems is assumed to be at the boundary of the mixing range at low MPII concentrations, since no definite conclusion can be given for the other blends. On the other hand the systems $EMIBF_4$/MPII and $EMINTf_2$/MPII show two breaking points mostly at medium MPII concentrations and at least one observed breaking point for the remaining blends. If only the lower breaking points obtained from temperature and conductivity measurements are considered, the liquid range of both systems is clearly wider than for the pure ionic liquids. However, if the higher breaking points obtained solely from conductivity data are considered, the liquid range for both systems is clearly narrower than for the pure ionic liquids with its minimum at medium MPII concentrations. That means that partly solidification of the electrolyte occurs at temperatures up to 23 °C for the system $EMIBF_4$/MPII and up to 39 °C for the system $EMINTf_2$/MPII.

For the final appraisal of the electrolyte systems only the results obtained from diffusion measurements and investigation of the liquid ranges were considered. Despite the second highest I_3^--diffusion coefficients of the examined electrolyte systems, the system $EMINTf_2$/MPII can not be recommended for a later application in DSSCs due to its extremely narrow liquid range over the whole mixing range. A similar conclusion can be drawn for the system $EMIBF_4$/MPII. However, the blends at the $EMIBF_4$ rich side of the

mixing range are subject to extremely large supercooling, thus application in DSSCs may be still possible. The determined liquid ranges of the EMIOTf rich blends are the largest of all blends, but also have the lowest I_3^--diffusion coefficients of all comparable blends. The best combination of diffusion and liquid range feature two blends at the EMIDCA rich side of the system EMIDCA/MPII, due to the largest I_3^--diffusion coefficients at a comparably broad liquid range.

The same electrolyte systems were rated by Zistler [54] by the use of an overall parameter (OP) calculated from results yielded by determination of I_3^--diffusion coefficients and charge transfer resistances at thin layer cells. The highest OP-values were obtained for the blends of the system $EMINTf_2$/MPII, followed by blends with medium MPII concentrations in EMIOTf, and blends with low MPII concentrations of the systems EMIDCA/MPII and $EMIBF_4$/MPII.

Consideration of the results from both studies yielded the conclusion that two of the systems are not suitable for later application in DSSCs; the system $EMINTf_2$/MPII due to the insufficient liquid range that is the predominant parameter for a later application and the system $EMIBF_4$/MPII due to weak performances in both studies. The systems EMIDCA/MPII and EMIOTf/MPII showed a better overall performance with different advantages concerning specific parameters. Thus, blends with low MPII concentrations of these two systems are recommended for later application in DSSCs in the order EMIDCA/MPII > EMIOTf/MPII.

The examination of pure ionic liquids with respect to their conductivities and liquid ranges yielded additional and reliable information for their characterisation. The commonly published conductivities of ionic liquids are typically less accurate due to inadequate temperature control, lacking purity specifications, and insufficient calibration of the measuring cell. Additionally, their temperature dependence is often analysed in an inadequate manner. It was shown that viscosity is a major but not the only parameter that influences conductivity. Additionally, specific conductivity data of three ionic liquids was reported for the first time. Analysis of viscosity and conductivity data yielded that all examined ionic liquids are fragile glass formers. That means strong non-Arrhenius type behaviour of viscosity and conductivity occur. This is in clear contrast to the common assumptions concerning the evaluation of the temperture dependence of these parameters in ionic liquids (see Refs. [71,143,149,175]). The influence of cation and anion on conductivity and fragility were analysed and discussed as well.

It has been shown that thermal analysis with simultaneous recording of conductivity yields highly accurate and confirmed melting points of ionic liquids compared to values commonly obtained by DSC-measurements. The melting points of four ionic liquids were determined for the first time. The determined melting points of four additional ionic liquids are much higher than the corresponding values from literature primarily based on lower purity grades, inadequate measurement or evaluation technique for the published values. For one ionic liquid two melting points were obtained; tentative interpretation: two different solid phases. This observation was not yet reported in literature.

The comprehensive approach for characterisation and optimisation of new DSSC-electrolytes and the close cooperation with scientists from our research group and project partners within the DSSC-network-project as well enabled finishing of several publications dealing with results from this dissertation. Several additional publications based on this dissertation are in preperation but not listed below.

- P. Wachter, M. Zistler, C. Schreiner, M. Berginc, U. Opara Krašovec, D. Gerhard, P. Wasserscheid, A. Hinsch, H. J. Gores, "Characterisation of DSSC-electrolytes based on 1-ethyl-3-methylimidazolium dicyanamide: Measurement of triiodide diffusion coefficient, viscosity, and photovoltaic performance", *J. Photochem. Photobiol. A*, available online, doi:10.1016/j.jphotochem.2007.12.001, (2007).
- P. Wachter, C. Schreiner, M. Zistler, D. Gerhard, P. Wasserscheid, H. J. Gores, "A microelectrode study of triiodide diffusion coefficients in mixtures of room temperature ionic liquids, useful for dye-sensitised solar cells", *Microchim. Acta*, **160**, 125 (2008).
- M. Zistler, P. Wachter, C. Schreiner, M. Fleischmann, D. Gerhard, P. Wasserscheid, A. Hinsch, H. J. Gores, "Temperature Dependent Impedance Analysis of Binary Ionic Liquid Electrolytes for Dye-Sensitized Solar Cells", *J. Electrochem. Soc*., **154**, B925 (2007).
- A. Hinsch, S. Behrens, M. Berginc, H. Bönnemann, H. Brandt, A. Drewitz, F. Einsele, D. Faßler, D. Gerhard, H. Gores, T. Herzig, S. Himmler, G. Khelashvili, D. Koch, G. Nasmudinova, U. Opara-Krašovec, P. Putyra, U. Rau, R. Sastrawan, T. Schauer, C. Schreiner, S. Sensfuß, C. Siegers, K. Skupien, P. Wachter, J. Walter, P. Wasserscheid, U. Würfel, M. Zistler, "Material development for dye solar modules; results from an integrated approach", *Prog. Photovolt.: Res. Appl*., in press.

- P. Wachter, H.-G. Schweiger, F. Wudy, H. J. Gores, "Check of a novel equipment for efficient determinations of solid-liquid phase equilibria enabling measurements at low temperature change rates", *J. Chem. Thermodyn.*, submitted.

Additional publications dealing with results from prior work:

- M. Zistler, C. Schreiner, P. Wachter, P. Wasserscheid, D. Gerhard, H. J. Gores, "Electrochemical Characterization of 1-Ethyl-3-methylimidazolium Thiocyanate and Measurement of Triiodide Diffusion Coefficients in Blends of two Ionic Liquids.", *Int. J. Electrochem. Sci*., **3**, 236 (2008).
- M. Zistler, P. Wachter, P. Wasserscheid, D. Gerhard, A. Hinsch, R. Sastrawan, H. J. Gores, "Comparison of electrochemical methods for triiodide diffusion coefficient measurements and observation of non-Stokesian diffusion behaviour in binary mixtures of two ionic liquids", *Electrochim. Acta,* **52**, 161 (2006).

The results of this work were also presented in the following lectures:

Presentation on the occasion of "Tag der Naturwissenschaften" (Day of Sciences) at the Universität Regensburg:

- "Ionische Flüssigkeiten – Elektrolyte für Farbstoffsolarzellen" (Regensburg, 11/2006)

Presentations within the DSSC-network-project:

- "Characterisation of DSSC-Electrolytes at various Temperatures – Diffusion and Impedance Studies" (Freiburg, 5/2006).
- "Characterisation of DSSC-Electrolytes at various Temperatures – Diffusion and Impedance Studies" (Cracow, 10/2006).
- "Characterisation of DSSC-Electrolytes at various Temperatures – Diffusion and Impedance Studies" (Freiburg, 3/2007).

8 Appendix

8.1 Determination of Diffusion Coefficients

Determination of I_3^--diffusion coefficients was performed by steady-state cyclic voltammetry at UMEs with nominal radii of 5 µm. To obtain steady-state behaviour even for comparably small I_3^--diffusion coefficients as in MPII, cyclic voltammograms in ILs and their mixtures were recorded with a scan rate of 5 mV s^{-1}. Start and end potential was typically 0 V since Pt pseudo-reference electrode and Pt working electrode were immersed into the same solution. The reverse potentials were chosen in such a manner that diffusion-limited steady-state currents for I_3^--reduction were obtained without occurring side reactions. They vary for different blends and electrodes. To prevent electrical interference all measurements were conducted within a Faraday cage. During the measurements temperature was regulated by a thermostat (RK 8 KP, *Lauda*, ± 0.05 °C) and controlled by a temperature sensor that is connected to a thermometer. Every value for a specific blend and temperature was determined at least three times to enable calculation of an accurate mean value. The calculated standard deviations of these mean values were always smaller than the estimated maximum error of 5% (Chap. 3.2.4). In the following paragraphs the determined I_3^--diffusion coefficients are summarised for each blend. Since illustration of all recorded cyclic-voltammograms would be too extensive only one measurement is shown exemplary for each blend and temperature.

8.1.1 EMIDCA/MPII

8.1.1.1 0.05 mol L^{-1} I_2 in EMIDCA/MPII with 9.1 mol% MPII

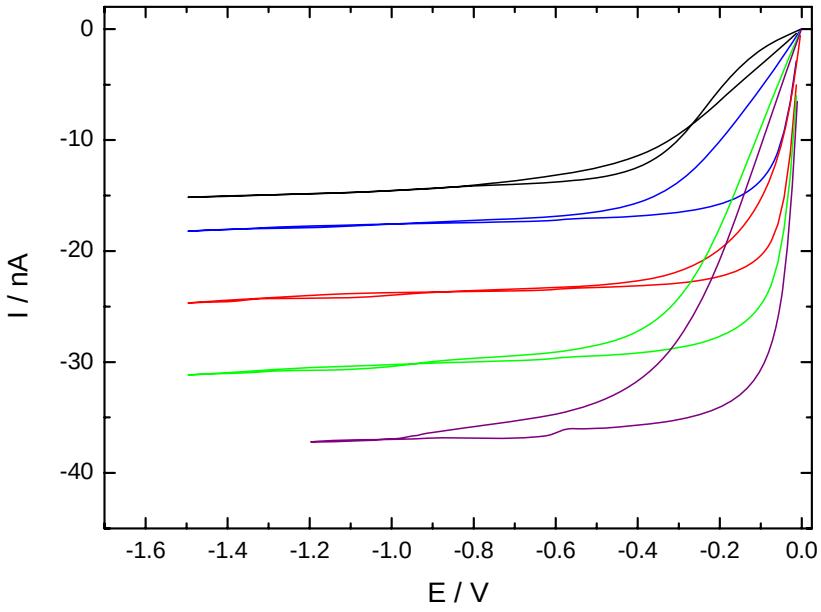

Figure 8-1: Steady-state cyclic voltammograms of 0.05 mol L^{-1} I_2 in EMIDCA/MPII with 9.1 mol% MPII; v = 5 mV s^{-1}; θ: (—) 25 °C, (—) 30 °C, (—) 40 °C, (—) 50 °C, (—) 60 °C.

Table 8-1: Measurement parameters and determined I_3^--diffusion coefficients of 0.05 mol L^{-1} I_2 in EMIDCA/MPII with 9.1 mol% MPII.

θ [°C]	$c(I_3^-)$ [mol L^{-1}]	$r_0 \cdot 10^4$ [cm]	$I \cdot 10^9$ [A]	$D' \cdot 10^7$ [cm^2 s^{-1}]	$D \cdot 10^7$ [cm^2 s^{-1}]
25	0.0465	5.03	-14.893	8.24892	8.30 ± 0.04
	0.0465	5.03	-14.999	8.30768	
	0.0465	5.03	-15.067	8.34546	
	0.0465	5.03	-14.988	8.30192	
30	0.0463	5.03	-17.564	9.77068	9.84 ± 0.04
	0.0463	5.03	-17.610	9.79627	
	0.0463	5.03	-17.671	9.82998	
	0.0463	5.03	-17.726	9.86085	
	0.0463	5.03	-17.771	9.88588	
	0.0463	5.03	-17.746	9.87187	
	0.0463	5.03	-17.724	9.85991	
40	0.0461	5.03	-23.410	13.0795	13.37 ± 0.13
	0.0461	5.03	-23.879	13.3411	
	0.0461	5.03	-24.072	13.4492	
	0.0461	5.03	-24.072	13.4488	
	0.0461	5.03	-24.007	13.4125	
	0.0461	5.03	-24.076	13.4511	
	0.0461	5.03	-23.976	13.3954	
50	0.0458	5.03	-29.420	16.5447	16.9 ± 0.3
	0.0458	5.03	-29.928	16.8306	
	0.0458	5.03	-30.297	17.038	
	0.0458	5.03	-30.534	17.1713	

60	0.0455	5.03	-35.922	20.3343	20.8 ± 0.4
	0.0455	5.03	-37.005	20.9472	
	0.0455	5.03	-37.431	21.1888	

8.1.1.2 0.05 mol L^{-1} I_2 in EMIDCA/MPII with 20.1 mol% MPII

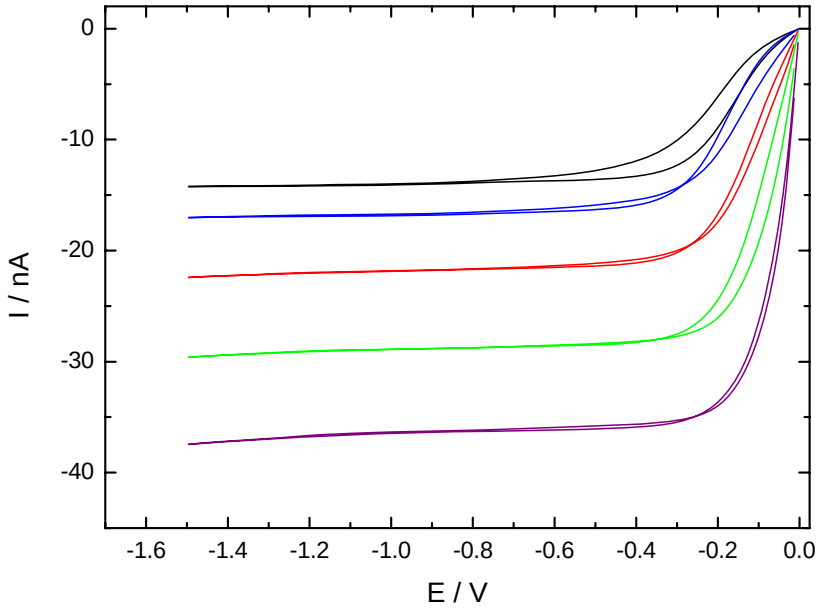

Figure 8-2: Steady-state cyclic voltammograms of 0.05 mol L^{-1} I_2 in EMIDCA/MPII with 20.1 mol% MPII; v = 5 mV s^{-1}; θ: (—) 25 °C, (—) 30 °C, (—) 40 °C, (—) 50 °C, (—) 60 °C.

Table 8-2: Measurement parameters and determined I_3^--diffusion coefficients of 0.05 mol L^{-1} I_2 in EMIDCA/MPII with 20.1 mol% MPII.

θ [°C]	$c(I_3^-)$ [mol L^{-1}]	$r_0 \cdot 10^4$ [cm]	$I \cdot 10^9$ [A]	$D' \cdot 10^7$ [cm^2 s^{-1}]	$D \cdot 10^7$ [cm^2 s^{-1}]
25	0.0476	4.99	-13.993	7.6324	7.665 ± 0.018
	0.0476	4.99	-14.066	7.6719	
	0.0476	4.99	-14.070	7.6743	
	0.0476	4.99	-14.061	7.6692	
	0.0476	4.99	-14.072	7.6752	
30	0.0474	4.99	-16.757	9.17825	9.17 ± 0.02
	0.0474	4.99	-16.731	9.16412	
	0.0474	4.99	-16.690	9.14171	
	0.0474	4.99	-16.793	9.19802	
40	0.0472	4.99	-22.740	12.5081	12.3 ± 0.3
	0.0472	4.99	-22.845	12.5659	
	0.0472	4.99	-22.849	12.5681	
	0.0472	4.99	-21.741	11.9587	
	0.0472	4.99	-21.816	12.0001	
	0.0472	4.99	-21.823	12.0038	
50	0.0469	4.99	-28.557	15.8082	15.87 ± 0.07
	0.0469	4.99	-28.629	15.8484	
	0.0469	4.99	-28.804	15.9452	
60	0.0466	4.99	-36.457	20.3117	20.29 ± 0.03
	0.0466	4.99	-36.462	20.3145	
	0.0466	4.99	-36.352	20.2532	

8.1.1.3 0.05 mol L^{-1} I_2 in EMIDCA/MPII with 29.9 mol% MPII

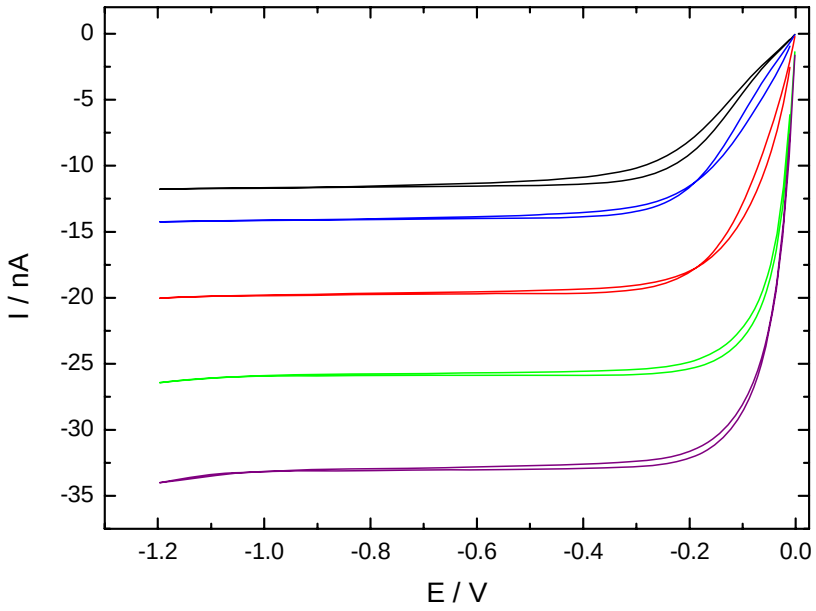

Figure 8-3: Steady-state cyclic voltammograms of 0.04 mol L^{-1} I_2 in EMIDCA/MPII with 29.9 mol% MPII; v = 5 mV s^{-1}; θ: (—) 25 °C, (—) 30 °C, (—) 40 °C, (—) 50 °C, (—) 60 °C.

Table 8-3: Measurement parameters and determined I_3^--diffusion coefficients of 0.04 mol L^{-1} I_2 in EMIDCA/MPII with 29.9 mol% MPII.

θ [°C]	$c(I_3^-)$ [mol L^{-1}]	$r_0 \cdot 10^4$ [cm]	$I \cdot 10^9$ [A]	$D' \cdot 10^7$ [cm^2 s^{-1}]	$D \cdot 10^7$ [cm^2 s^{-1}]
25	0.0443	5.03	-11.601	6.74458	6.763 ± 0.015
	0.0443	5.03	-11.652	6.77441	
	0.0443	5.03	-11.655	6.77621	
	0.0443	5.03	-11.619	6.75528	
30	0.0441	5.03	-14.167	8.27406	8.24 ± 0.03
	0.0441	5.03	-14.073	8.21904	
	0.0441	5.03	-14.093	8.2309	
40	0.0439	5.03	-19.746	11.5849	11.602 ± 0.017
	0.0439	5.03	-19.803	11.6185	
	0.0439	5.03	-19.774	11.6013	
50	0.0436	5.03	-25.744	15.2080	15.30 ± 0.09
	0.0436	5.03	-25.907	15.3044	
	0.0436	5.03	-26.047	15.3869	
60	0.0434	5.03	-33.340	19.7857	19.71 ± 0.10
	0.0434	5.03	-33.392	19.8170	
	0.0434	5.03	-33.100	19.6436	
	0.0434	5.03	-33.042	19.6092	

8.1.1.4 0.05 mol L^{-1} I_2 in EMIDCA/MPII with 41.3 mol% MPII

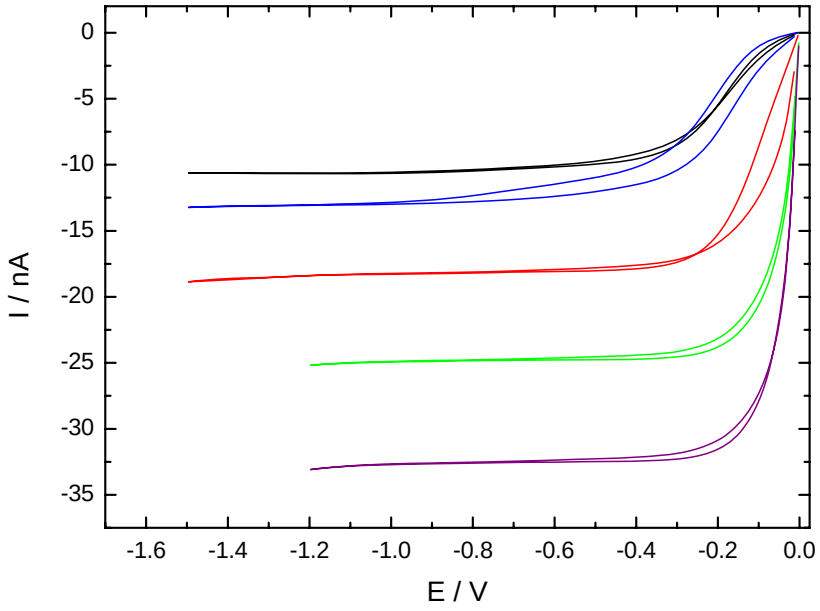

Figure 8-4: Steady-state cyclic voltammograms of 0.05 mol L^{-1} I_2 in EMIDCA/MPII with 41.3 mol% MPII; v = 5 mV s^{-1}; θ: (—) 25 °C, (—) 30 °C, (—) 40 °C, (—) 50 °C, (—) 60 °C.

Table 8-4: Measurement parameters and determined I_3^--diffusion coefficients of 0.05 mol L^{-1} I_2 in EMIDCA/MPII with 41.3 mol% MPII.

θ [°C]	$c(I_3^-)$ [mol L^{-1}]	$r_0 \cdot 10^4$ [cm]	$I \cdot 10^9$ [A]	$D' \cdot 10^7$ [cm^2 s^{-1}]	$D \cdot 10^7$ [cm^2 s^{-1}]
25	0.0451	5.37	-10.594	5.66729	5.68 ± 0.013
	0.0451	5.37	-10.622	5.68184	
	0.0451	5.37	-10.642	5.69270	
30	0.0450	5.37	-13.042	6.99205	6.988 ± 0.006
	0.0450	5.37	-13.025	6.98309	
40	0.0447	5.37	-18.011	9.72079	9.86 ± 0.09
	0.0447	5.37	-18.272	9.86149	
	0.0447	5.37	-18.484	9.97607	
	0.0447	5.37	-18.474	9.97084	
	0.0447	5.37	-18.302	9.87811	
	0.0447	5.37	-17.982	9.70513	
	0.0447	5.37	-18.321	9.88821	
	0.0447	5.37	-18.511	9.99086	
	0.0447	5.37	-18.215	9.83111	
	0.0447	5.37	-18.232	9.83996	
	0.0447	5.37	-18.212	9.82949	
50	0.0445	5.37	-24.690	13.3853	13.41 ± 0.02
	0.0445	5.37	-24.699	13.3903	
	0.0445	5.37	-24.743	13.4143	
	0.0445	5.37	-24.777	13.4325	
60	0.0442	5.37	-32.224	17.5885	17.69 ± 0.06
	0.0442	5.37	-32.428	17.7001	
	0.0442	5.37	-32.426	17.6987	
	0.0442	5.37	-32.472	17.7239	
	0.0442	5.37	-32.536	17.7591	

8.1.1.5 0.04 mol L^{-1} I_2 in EMIDCA/MPII with 49.6 mol% MPII

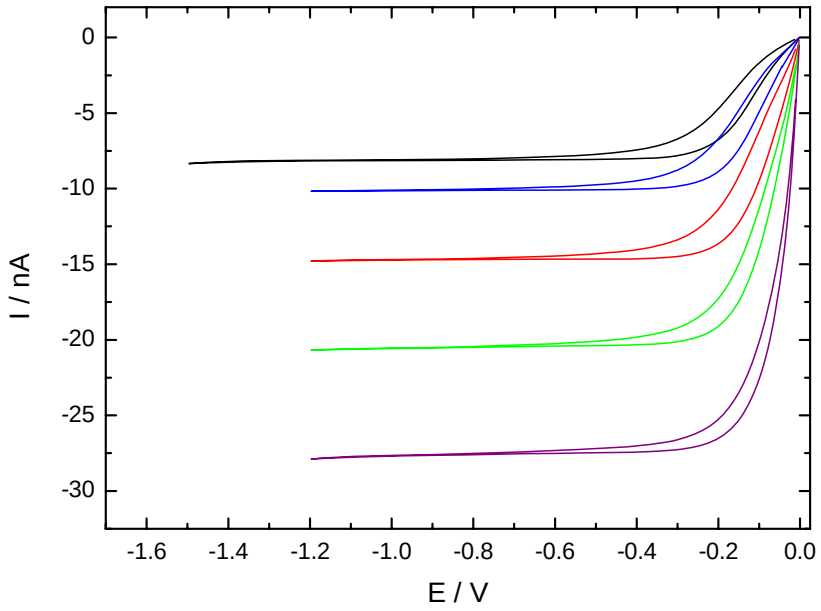

Figure 8-5: Steady-state cyclic voltammograms of 0.04 mol L^{-1} I_2 in EMIDCA/MPII with 49.6 mol% MPII; v = 5 mV s^{-1}; θ: (—) 25 °C, (—) 30 °C, (—) 40 °C, (—) 50 °C, (—) 60 °C.

Table 8-5: Measurement parameters and determined I_3^--diffusion coefficients of 0.04 mol L^{-1} I_2 in EMIDCA/MPII with 49.6 mol% MPII.

θ [°C]	$c(I_3^-)$ [mol L^{-1}]	$r_0 \cdot 10^4$ [cm]	$I \cdot 10^9$ [A]	$D' \cdot 10^7$ [cm^2 s^{-1}]	$D \cdot 10^7$ [cm^2 s^{-1}]
25	0.0410	5.37	-7.663	4.50882	4.65 ± 0.13
	0.0410	5.37	-7.785	4.58067	
	0.0410	5.37	-8.046	4.73426	
	0.0410	5.37	-8.120	4.77784	
30	0.0409	5.37	-10.070	5.94000	5.952 ± 0.012
	0.0409	5.37	-10.091	5.95239	
	0.0409	5.37	-10.110	5.96348	
40	0.0407	5.37	-14.637	8.67646	8.694 ± 0.016
	0.0407	5.37	-14.681	8.70230	
	0.0407	5.37	-14.684	8.70432	
50	0.0405	5.37	-20.420	12.1640	12.18 ± 0.02
	0.0405	5.37	-20.482	12.2008	
	0.0405	5.37	-20.422	12.1653	
60	0.0402	5.37	-27.300	16.3837	16.47 ± 0.09
	0.0402	5.37	-27.452	16.4751	
	0.0402	5.37	-27.585	16.5548	

8.1.1.6 0.05 mol L^{-1} I_2 in EMIDCA/MPII with 60.0 mol% MPII

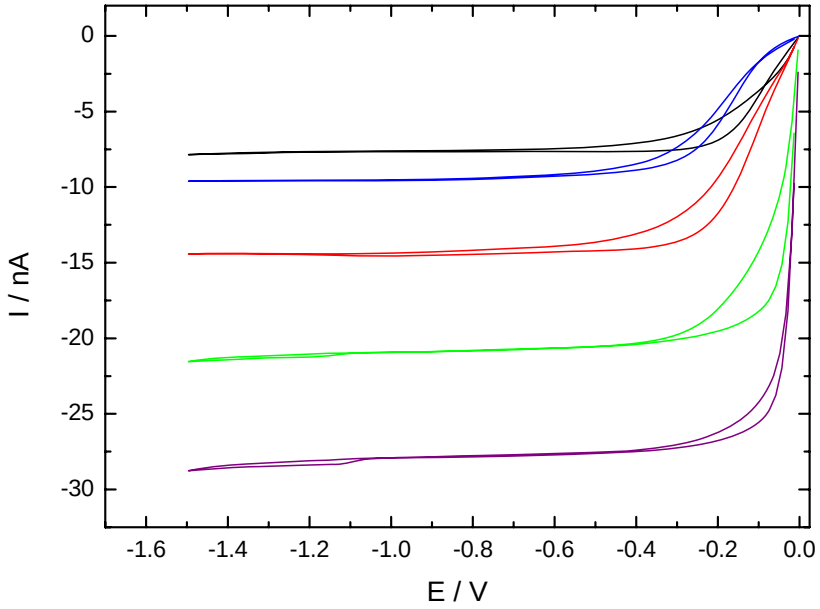

Figure 8-6: Steady-state cyclic voltammograms of 0.05 mol L^{-1} I_2 in EMIDCA/MPII with 60.0 mol% MPII; v = 5 mV s^{-1}; θ: (—) 25 °C, (—) 30 °C, (—) 40 °C, (—) 50 °C, (—) 60 °C.

Table 8-6: Measurement parameters and determined I_3^--diffusion coefficients of 0.05 mol L^{-1} I_2 in EMIDCA/MPII with 60.0 mol% MPII.

θ [°C]	$c(I_3^-)$ [mol L^{-1}]	$r_0 \cdot 10^4$ [cm]	$I \cdot 10^9$ [A]	$D' \cdot 10^7$ [cm^2 s^{-1}]	$D \cdot 10^7$ [cm^2 s^{-1}]
25	0.0468	5.03	-6.797	3.74092	3.88 ± 0.16
	0.0468	5.03	-6.750	3.71455	
	0.0468	5.03	-7.243	3.98638	
	0.0468	5.03	-7.393	4.06852	
	0.0468	5.03	-7.311	4.02368	
	0.0468	5.03	-6.823	3.75480	
30	0.0466	5.03	-8.559	4.73066	5.1 ± 0.3
	0.0466	5.03	-8.593	4.74961	
	0.0466	5.03	-9.640	5.32797	
	0.0466	5.03	-9.322	5.15209	
	0.0466	5.03	-9.364	5.17554	
	0.0466	5.03	-9.537	5.27122	
40	0.0464	5.03	-14.460	8.02645	7.96 ± 0.07
	0.0464	5.03	-14.262	7.91643	
	0.0464	5.03	-14.203	7.88368	
	0.0464	5.03	-14.457	8.02484	
50	0.0461	5.03	-20.731	11.5822	11.58 ± 0.12
	0.0461	5.03	-20.494	11.4499	
	0.0461	5.03	-20.759	11.5982	
	0.0461	5.03	-20.564	11.4890	
	0.0461	5.03	-21.049	11.7600	
60	0.0459	5.03	-28.334	15.8992	15.8 ± 0.2
	0.0459	5.03	-27.898	15.6543	
	0.0459	5.03	-27.994	15.7085	
	0.0459	5.03	-27.680	15.5323	
	0.0459	5.03	-28.580	16.0374	

8.1.1.7 0.05 mol L^{-1} I_2 in EMIDCA/MPII with 80.1 mol% MPII

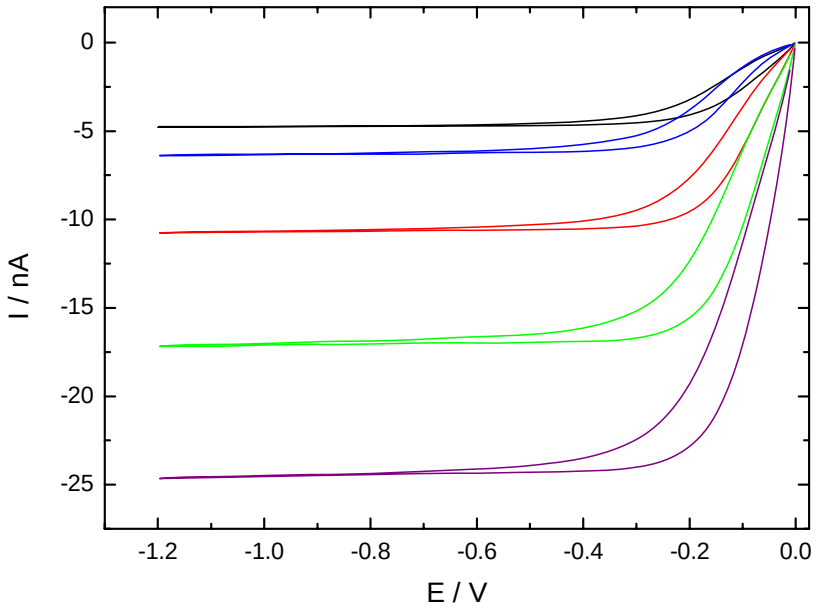

Figure 8-7: Steady-state cyclic voltammograms of 0.05 mol L^{-1} I_2 in EMIDCA/MPII with 80.1 mol% MPII; v = 5 mV s^{-1}; θ: (—) 25 °C, (—) 30 °C, (—) 40 °C, (—) 50 °C, (—) 60 °C.

Table 8-7: Measurement parameters and determined I_3^--diffusion coefficients of 0.05 mol L^{-1} I_2 in EMIDCA/MPII with 80.1 mol% MPII.

θ [°C]	$c(I_3^-)$ [mol L^{-1}]	$r_0 \cdot 10^4$ [cm]	$I \cdot 10^9$ [A]	$D' \cdot 10^7$ [cm^2 s^{-1}]	$D \cdot 10^7$ [cm^2 s^{-1}]
25	0.0502	5.03	-4.748	2.43578	2.47 ± 0.03
	0.0502	5.03	-4.841	2.48367	
	0.0502	5.03	-4.867	2.49689	
30	0.0500	5.03	-6.243	3.21582	3.25 ± 0.04
	0.0500	5.03	-6.329	3.25995	
	0.0500	5.03	-6.379	3.28589	
40	0.0498	5.03	-10.493	5.42712	5.47 ± 0.04
	0.0498	5.03	-10.615	5.49006	
	0.0498	5.03	-10.645	5.50557	
50	0.0495	5.03	-16.743	8.71190	8.78 ± 0.07
	0.0495	5.03	-16.882	8.78423	
	0.0495	5.03	-17.024	8.85811	
60	0.0492	5.03	-24.055	12.5926	12.70 ± 0.10
	0.0492	5.03	-24.286	12.7135	
	0.0492	5.03	-24.430	12.7889	

8.1.1.8 0.10 mol L^{-1} I_2 in EMIDCA/MPII with 80 mol% MPII

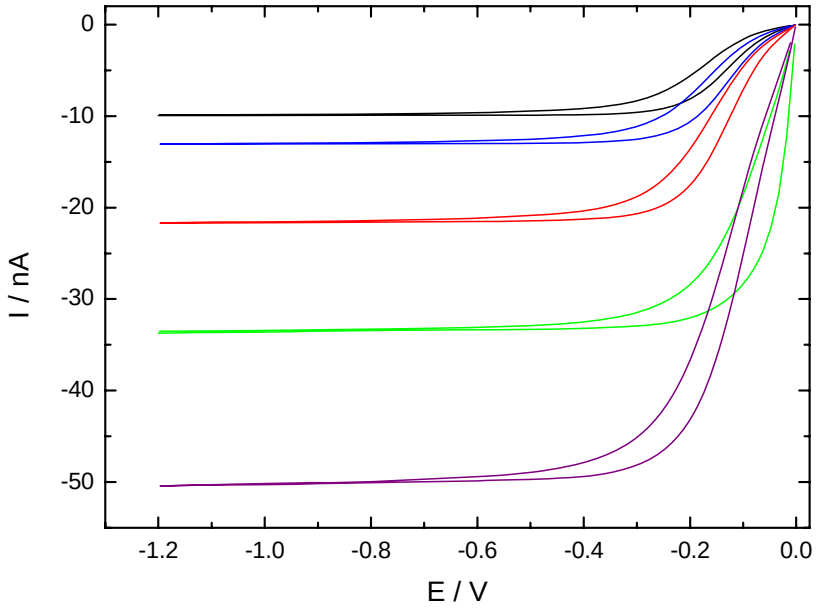

Figure 8-8: Steady-state cyclic voltammograms of 0.10 mol L^{-1} I_2 in EMIDCA/MPII with 80 mol% MPII; v = 5 mV s^{-1}; θ: (—) 25 °C, (—) 30 °C, (—) 40 °C, (—) 50 °C, (—) 60 °C.

Table 8-8: Measurement parameters and determined I_3^--diffusion coefficients of 0.10 mol L^{-1} I_2 in EMIDCA/MPII with 80 mol% MPII.

θ [°C]	$c(I_3^-)$ [mol L^{-1}]	$r_0 \cdot 10^4$ [cm]	$I \cdot 10^9$ [A]	$D' \cdot 10^7$ [cm^2 s^{-1}]	$D \cdot 10^7$ [cm^2 s^{-1}]
25	0.101	5.03	-9.764	2.48988	2.516 ± 0.019
	0.101	5.03	-9.925	2.53095	
	0.101	5.03	-9.924	2.53075	
	0.101	5.03	-9.858	2.5139	
30	0.101	5.03	-13.055	3.32911	3.323 ± 0.005
	0.101	5.03	-13.019	3.32011	
	0.101	5.03	-13.017	3.31939	
40	0.101	5.03	-21.581	5.50352	5.499 ± 0.006
	0.101	5.03	-21.537	5.49209	
	0.101	5.03	-21.574	5.50158	
50	0.100	5.03	-33.557	8.64309	8.83 ± 0.16
	0.100	5.03	-34.622	8.91735	
	0.100	5.03	-34.651	8.92489	
60	0.0994	5.03	-50.093	13.0325	13.02 ± 0.02
	0.0994	5.03	-49.935	12.9912	
	0.0994	5.03	-50.044	13.0197	

8.1.1.9 0.20 mol L^{-1} I_2 in EMIDCA/MPII with 80 mol% MPII

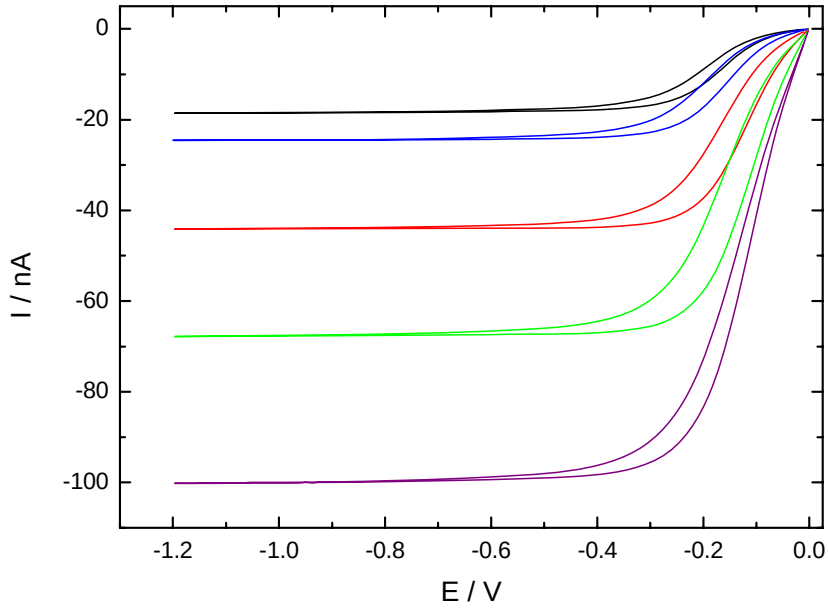

Figure 8-9: Steady-state cyclic voltammograms of 0.20 mol L^{-1} I_2 in EMIDCA/MPII with 80 mol% MPII; v = 5 mV s^{-1}; θ: (—) 25 °C, (—) 30 °C, (—) 40 °C, (—) 50 °C, (—) 60 °C.

Table 8-9: Measurement parameters and determined I_3^--diffusion coefficients of 0.20 mol L^{-1} I_2 in EMIDCA/MPII with 80 mol% MPII.

θ [°C]	$c(I_3^-)$ [mol L^{-1}]	$r_0 \cdot 10^4$ [cm]	$I \cdot 10^9$ [A]	$D' \cdot 10^7$ [cm^2 s^{-1}]	$D \cdot 10^7$ [cm^2 s^{-1}]
25	0.201	5.03	-18.108	2.31915	2.35 ± 0.02
	0.201	5.03	-18.410	2.35783	
	0.201	5.03	-18.433	2.36083	
30	0.201	5.03	-24.461	3.14068	3.17 ± 0.04
	0.201	5.03	-24.692	3.17034	
	0.201	5.03	-25.012	3.21144	
40	0.200	5.03	-43.456	5.61030	5.65 ± 0.04
	0.200	5.03	-43.948	5.67383	
	0.200	5.03	-43.951	5.67418	
50	0.198	5.03	-67.413	8.75152	8.745 ± 0.018
	0.198	5.03	-67.210	8.72523	
	0.198	5.03	-67.467	8.75849	
60	0.197	5.03	-99.022	12.9267	12.96 ± 0.04
	0.197	5.03	-99.153	12.9438	
	0.197	5.03	-99.666	13.0108	

8.1.1.10 0.30 mol L^{-1} I_2 in EMIDCA/MPII with 80 mol% MPII

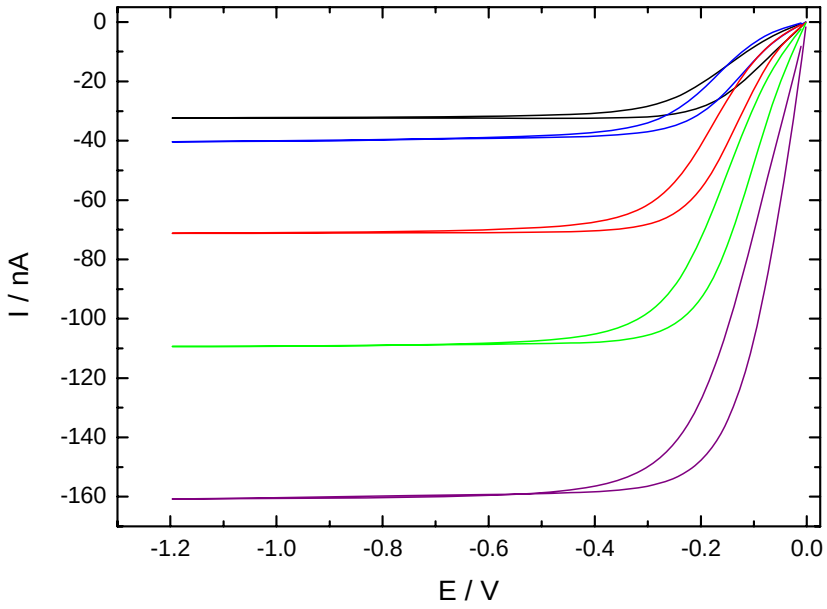

Figure 8-10: Steady-state cyclic voltammograms of 0.30 mol L^{-1} I_2 in EMIDCA/MPII with 80 mol% MPII; v = 5 mV s^{-1}; θ: (—) 25 °C, (—) 30 °C, (—) 40 °C, (—) 50 °C, (—) 60 °C.

Table 8-10: Measurement parameters and determined I_3^--diffusion coefficients of 0.30 mol L^{-1} I_2 in EMIDCA/MPII with 80 mol% MPII.

θ [°C]	$c(I_3^-)$ [mol L^{-1}]	$r_0 \cdot 10^4$ [cm]	$I \cdot 10^9$ [A]	$D' \cdot 10^7$ [cm^2 s^{-1}]	$D \cdot 10^7$ [cm^2 s^{-1}]
25	0.296	5.37	-31.929	2.59882	2.615 ± 0.018
	0.296	5.37	-32.092	2.61216	
	0.296	5.37	-32.356	2.63365	
30	0.296	5.37	-39.908	3.25713	3.258 ± 0.011
	0.296	5.37	-39.742	3.24357	
	0.296	5.37	-39.997	3.26440	
	0.296	5.37	-40.050	3.26868	
40	0.294	5.37	-70.555	5.78968	5.81 ± 0.02
	0.294	5.37	-71.088	5.83340	
	0.294	5.37	-70.943	5.82156	
50	0.292	5.37	-109.812	9.06352	9.01 ± 0.04
	0.292	5.37	-108.929	8.99064	
	0.292	5.37	-108.871	8.98585	
60	0.291	5.37	-157.623	13.0813	13.15 ± 0.09
	0.291	5.37	-158.061	13.1176	
	0.291	5.37	-159.623	13.2473	

8.1.1.11 0.40 mol L^{-1} I_2 in EMIDCA/MPII with 80 mol% MPII

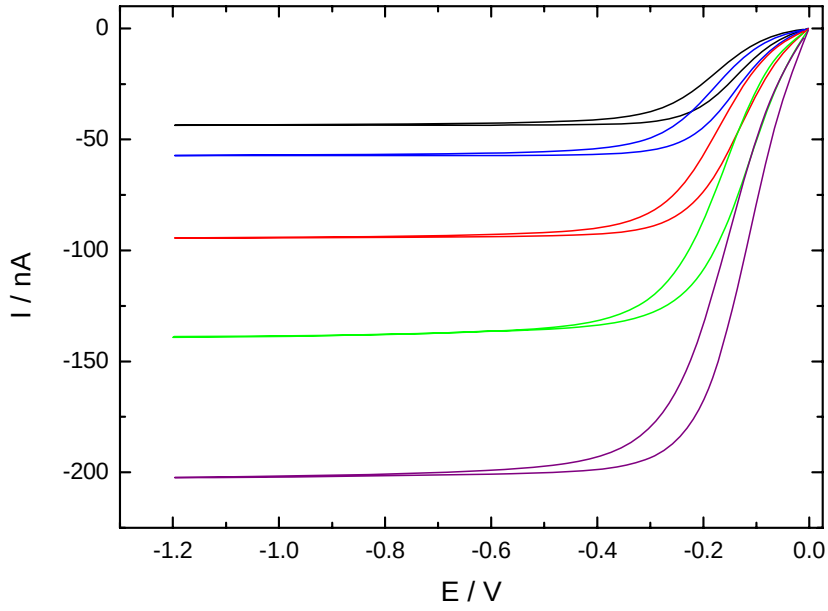

Figure 8-11: Steady-state cyclic voltammograms of 0.40 mol L^{-1} I_2 in EMIDCA/MPII with 80 mol% MPII; v = 5 mV s^{-1}; θ: (—) 25 °C, (—) 30 °C, (—) 40 °C, (—) 50 °C, (—) 60 °C.

Table 8-11: Measurement parameters and determined I_3^--diffusion coefficients of 0.40 mol L^{-1} I_2 in EMIDCA/MPII with 80 mol% MPII.

θ [°C]	$c(I_3^-)$ [mol L^{-1}]	$r_0 \cdot 10^4$ [cm]	$I \cdot 10^9$ [A]	$D' \cdot 10^7$ [cm^2 s^{-1}]	$D \cdot 10^7$ [cm^2 s^{-1}]
25	0.396	5.03	-43.603	2.83600	2.833 ± 0.004
	0.396	5.03	-43.585	2.83480	
	0.396	5.03	-43.499	2.82924	
30	0.395	5.03	-57.244	3.73356	3.726 ± 0.009
	0.395	5.03	-56.968	3.71555	
	0.395	5.03	-57.149	3.72737	
40	0.393	5.03	-93.649	6.14222	6.14 ± 0.02
	0.393	5.03	-93.971	6.16334	
	0.393	5.03	-93.244	6.11563	
50	0.391	5.37	-137.607	8.50150	8.56 ± 0.06
	0.391	5.37	-138.230	8.53999	
	0.391	5.37	-138.570	8.56099	
	0.391	5.37	-139.835	8.63915	
60	0.388	5.37	-199.677	1.24029	12.44 ± 0.05
	0.388	5.37	-199.852	1.24138	
	0.388	5.37	-201.262	1.25014	

8.1.1.12 0.49 mol L^{-1} I_2 in EMIDCA/MPII with 80 mol% MPII

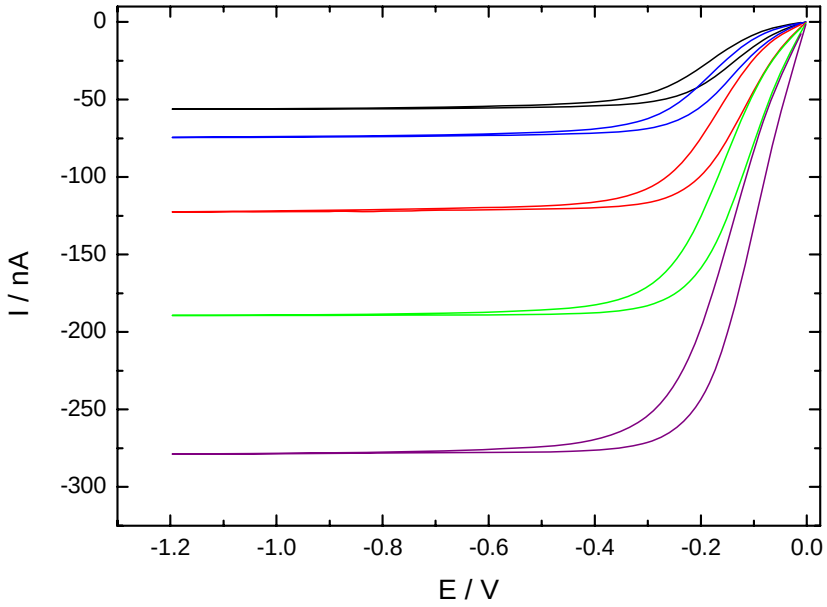

Figure 8-12: Steady-state cyclic voltammograms of 0.49 mol L^{-1} I_2 in EMIDCA/MPII with 80 mol% MPII; v = 5 mV s^{-1}; θ: (—) 25 °C, (—) 30 °C, (—) 40 °C, (—) 50 °C, (—) 60 °C.

Table 8-12: Measurement parameters and determined I_3^--diffusion coefficients of 0.49 mol L^{-1} I_2 in EMIDCA/MPII with 80 mol% MPII.

θ [°C]	$c(I_3^-)$ [mol L^{-1}]	$r_0 \cdot 10^4$ [cm]	$I \cdot 10^9$ [A]	$D' \cdot 10^7$ [cm^2 s^{-1}]	$D \cdot 10^7$ [cm^2 s^{-1}]
25	0.493	5.37	-55.028	2.69450	2.72 ± 0.02
	0.493	5.37	-55.697	2.72725	
	0.493	5.37	-55.978	2.74101	
30	0.491	5.37	-73.768	3.62240	3.632 ± 0.008
	0.491	5.37	-74.097	3.63856	
	0.491	5.37	-73.992	3.63339	
40	0.489	5.37	-122.280	6.03779	6.029 ± 0.011
	0.489	5.37	-122.173	6.03251	
	0.489	5.37	-121.835	6.01582	
50	0.486	5.37	-187.339	9.30159	9.35 ± 0.04
	0.486	5.37	-188.840	9.37612	
	0.486	5.37	-188.933	9.38073	
60	0.483	5.37	-275.471	13.7539	13.81 ± 0.06
	0.483	5.37	-276.555	13.8080	
	0.483	5.37	-277.774	13.8689	

8.1.1.13 VFT-Equation Parameters

Table 8-13: VFT-Equation parameters of I_3^--diffusion coefficients of ≈ 0.05 mol L^{-1} I_2 in mixtures of EMIDCA/MPII at varying MPII concentrations.

Mol% MPII	$A \cdot 10^3$ [cm^2 s^{-1}]	B [K]	T_0 [K]	R^2
9.1	0.020 ± 0.005	280 ± 50	211 ± 9	0.99988
20.1	0.2 ± 0.2	1000 ± 400	130 ± 40	0.99981
29.9	0.05 ± 0.02	480 ± 100	189 ± 13	0.9999
41.3	0.19 ± 0.08	840 ± 150	153 ± 15	0.99995
49.6	0.15 ± 0.1	700 ± 200	170 ± 20	0.99987
60.0	0.050 ± 0.003	413 ± 12	212.6 ± 1.6	1
80.1	0.51 ± 0.14	1020 ± 90	163 ± 7	0.99999
100.0	0.23 ± 0.02	840 ± 30	187 ± 2	1

Table 8-14: VFT-Equation parameters of I_3^--diffusion coefficients of I_2 in mixtures of EMIDCA/MPII with 80 mol% MPII at varying I_2 concentrations.

$c(I_3^-)$ [mol L^{-1}]	$A \cdot 10^3$ [cm^2 s^{-1}]	B [K]	T_0 [K]	R^2
0.05	0.51 ± 0.14	1020 ± 90	163 ± 7	0.99999
0.10	0.6 ± 0.7	1000 ± 300	170 ± 30	0.99984
0.20	0.13 ± 0.08	590 ± 140	200 ± 15	0.99985
0.30	0.15 ± 0.17	600 ± 300	200 ± 30	0.99956
0.40	0.2 ± 0.6	800 ± 800	170 ± 70	0.99826
0.49	0.57 ± 0.1	990 ± 50	168 ± 4	1

8.1.2 $EMIBF_4$/MPII

8.1.2.1 0.05 mol L^{-1} I_2 in $EMIBF_4$/MPII with 10.0 mol% MPII

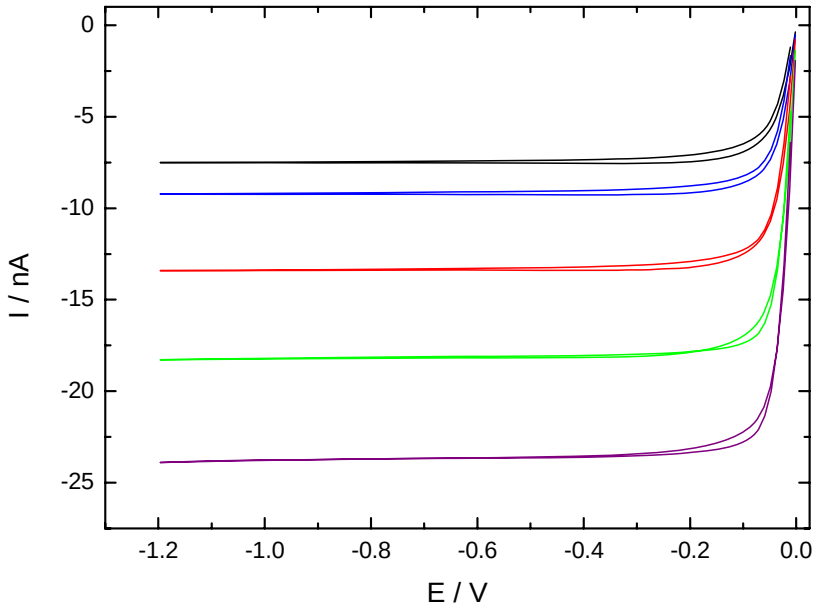

Figure 8-13: Steady-state cyclic voltammograms of 0.05 mol L^{-1} I_2 in $EMIBF_4$/MPII with 10.0 mol% MPII; v = 5 mV s^{-1}; θ: (—) 25 °C, (—) 30 °C, (—) 40 °C, (—) 50 °C, (—) 60 °C.

Table 8-15: Measurement parameters and determined I_3^--diffusion coefficients of 0.05 mol L^{-1} I_2 in $EMIBF_4$/MPII with 10.0 mol% MPII.

θ [°C]	$c(I_3^-)$ [mol L^{-1}]	$r_0 \cdot 10^4$ [cm]	$I \cdot 10^9$ [A]	$D' \cdot 10^7$ [cm^2 s^{-1}]	$D \cdot 10^7$ [cm^2 s^{-1}]
25	0.0542	4.99	-7.570	3.62463	3.607 ± 0.015
	0.0542	4.99	-7.519	3.60050	
	0.0542	4.99	-7.511	3.59676	
30	0.0541	4.99	-9.256	4.44541	4.439 ± 0.006
	0.0541	4.99	-9.242	4.43870	
	0.0541	4.99	-9.230	4.43277	
40	0.0538	4.99	-13.393	6.46921	6.460 ± 0.011
	0.0538	4.99	-13.382	6.46390	
	0.0538	4.99	-13.348	6.44743	
50	0.0534	4.99	-18.484	8.98150	8.88 ± 0.08
	0.0534	4.99	-18.185	8.83631	
	0.0534	4.99	-18.185	8.83607	
60	0.0531	4.99	-24.017	11.7379	11.62 ± 0.11
	0.0531	4.99	-23.681	11.5736	
	0.0531	4.99	-23.619	11.5433	

8.1.2.2 0.05 mol L^{-1} I_2 in $EMIBF_4$/MPII with 19.9 mol% MPII

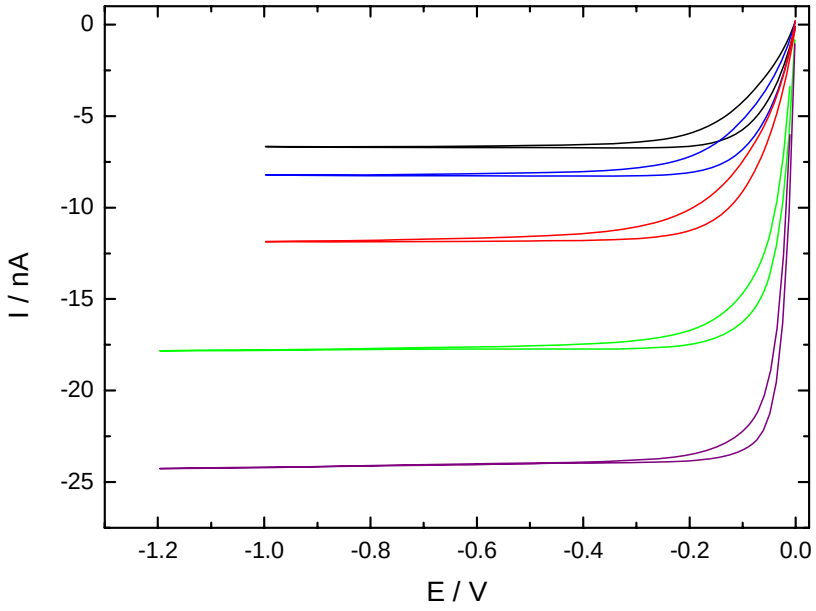

Figure 8-14: Steady-state cyclic voltammograms of 0.05 mol L^{-1} I_2 in $EMIBF_4$/MPII with 19.9 mol% MPII; v = 5 mV s^{-1}; θ: (—) 25 °C, (—) 30 °C, (—) 40 °C, (—) 50 °C, (—) 60 °C.

Table 8-16: Measurement parameters and determined I_3^--diffusion coefficients of 0.05 mol L^{-1} I_2 in $EMIBF_4$/MPII with 19.9 mol% MPII.

θ [°C]	$c(I_3^-)$ [mol L^{-1}]	$r_0 \cdot 10^4$ [cm]	$I \cdot 10^9$ [A]	$D' \cdot 10^7$ [cm^2 s^{-1}]	$D \cdot 10^7$ [cm^2 s^{-1}]
25	0.0507	5.37	-6.719	3.19705	3.1967 ± 0.0013
	0.0507	5.37	-6.720	3.19775	
	0.0507	5.37	-6.715	3.19518	
30	0.0506	5.37	-8.268	3.94547	3.940 ± 0.004
	0.0506	5.37	-8.251	3.93738	
	0.0506	5.37	-8.250	3.93687	
40	0.0503	5.37	-11.992	5.75538	5.70 ± 0.04
	0.0503	5.37	-11.831	5.67787	
	0.0503	5.37	-11.832	5.67864	
50	0.0500	5.37	-17.833	8.60970	8.59 ± 0.02
	0.0500	5.37	-17.745	8.56712	
	0.0500	5.37	-17.782	8.58474	
60	0.0497	5.37	-23.804	11.5590	11.64 ± 0.07
	0.0497	5.37	-24.075	11.6903	
	0.0497	5.37	-24.013	11.6601	

8.1.2.3 0.05 mol L^{-1} I_2 in $EMIBF_4$/MPII with 30.0 mol% MPII

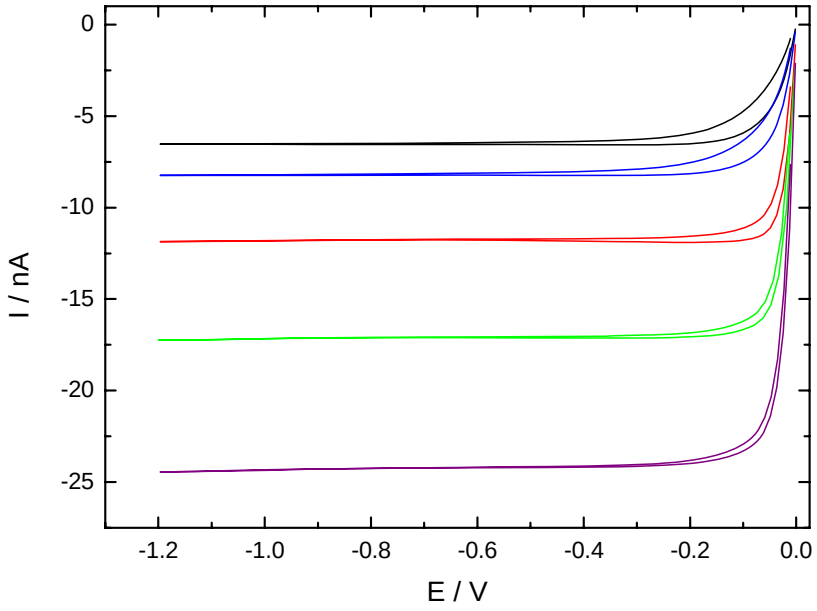

Figure 8-15: Steady-state cyclic voltammograms of 0.05 mol L^{-1} I_2 in $EMIBF_4$/MPII with 30.0 mol% MPII; v = 5 mV s^{-1}; θ: (—) 25 °C, (—) 30 °C, (—) 40 °C, (—) 50 °C, (—) 60 °C.

Table 8-17: Measurement parameters and determined I_3^--diffusion coefficients of 0.05 mol L^{-1} I_2 in $EMIBF_4$/MPII with 30.0 mol% MPII.

θ [°C]	$c(I_3^-)$ [mol L^{-1}]	$r_0 \cdot 10^4$ [cm]	$I \cdot 10^9$ [A]	$D' \cdot 10^7$ [cm^2 s^{-1}]	$D \cdot 10^7$ [cm^2 s^{-1}]
25	0.0539	4.99	-6.525	3.14110	3.150 ± 0.008
	0.0539	4.99	-6.548	3.15221	
	0.0539	4.99	-6.556	3.15622	
30	0.0538	4.99	-8.225	3.97089	3.973 ± 0.002
	0.0538	4.99	-8.230	3.97360	
	0.0538	4.99	-8.234	3.97541	
40	0.0535	4.99	-11.233	5.45334	5.64 ± 0.18
	0.0535	4.99	-11.819	5.73758	
	0.0535	4.99	-11.793	5.72515	
50	0.0532	4.99	-17.183	8.39025	8.378 ± 0.018
	0.0532	4.99	-17.132	8.36496	
60	0.0529	4.99	-24.140	11.8550	11.91 ± 0.05
	0.0529	4.99	-24.246	11.9069	
	0.0529	4.99	-24.351	11.9588	

8.1.2.4 0.05 mol L^{-1} I_2 in $EMIBF_4$/MPII with 40.0 mol% MPII

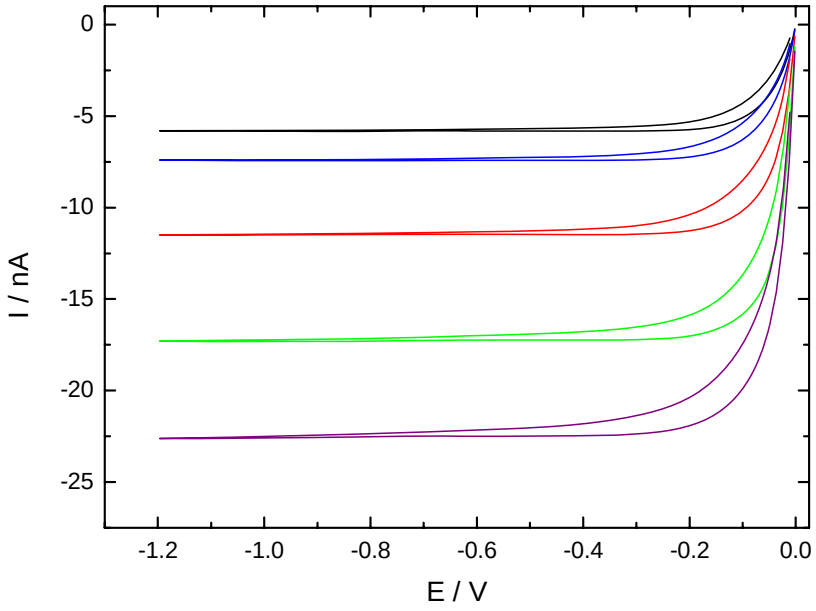

Figure 8-16: Steady-state cyclic voltammograms of 0.05 mol L^{-1} I_2 in $EMIBF_4$/MPII with 40.0 mol% MPII; v = 5 mV s^{-1}; θ: (—) 25 °C, (—) 30 °C, (—) 40 °C, (—) 50 °C, (—) 60 °C.

Table 8-18: Measurement parameters and determined I_3^--diffusion coefficients of 0.05 mol L^{-1} I_2 in $EMIBF_4$/MPII with 40.0 mol% MPII.

θ [°C]	$c(I_3^-)$ [mol L^{-1}]	$r_0 \cdot 10^4$ [cm]	$I \cdot 10^9$ [A]	$D' \cdot 10^7$ [cm^2 s^{-1}]	$D \cdot 10^7$ [cm^2 s^{-1}]
25	0.0509	5.03	-5.865	2.96545	2.948 ± 0.015
	0.0509	5.03	-5.815	2.94016	
	0.0509	5.03	-5.811	2.93819	
30	0.0508	5.03	-7.418	3.76142	3.766 ± 0.006
	0.0508	5.03	-7.422	3.76329	
	0.0508	5.03	-7.441	3.77307	
40	0.0505	5.03	-11.424	5.82546	5.835 ± 0.011
	0.0505	5.03	-11.466	5.84673	
	0.0505	5.03	-11.439	5.83281	
50	0.0502	5.03	-17.476	8.96285	8.86 ± 0.10
	0.0502	5.03	-17.263	8.85320	
	0.0502	5.03	-17.076	8.75771	
60	0.0499	5.03	-23.137	11.9335	11.6 ± 0.3
	0.0499	5.03	-22.513	11.6117	
	0.0499	5.03	-22.102	11.3999	

8.1.2.5 0.05 mol L^{-1} I_2 in $EMIBF_4$/MPII with 50.0 mol% MPII

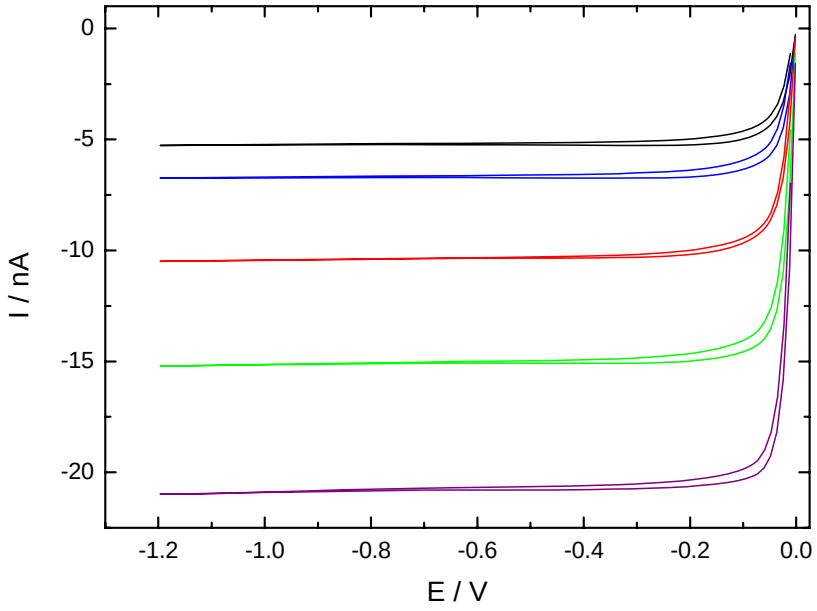

Figure 8-17: Steady-state cyclic voltammograms of 0.05 mol L^{-1} I_2 in $EMIBF_4$/MPII with 50.0 mol% MPII; v = 5 mV s^{-1}; θ: (—) 25 °C, (—) 30 °C, (—) 40 °C, (—) 50 °C, (—) 60 °C.

Table 8-19: Measurement parameters and determined I_3^--diffusion coefficients of 0.05 mol L^{-1} I_2 in $EMIBF_4$/MPII with 50.0 mol% MPII.

θ [°C]	$c(I_3^-)$ [mol L^{-1}]	$r_0 \cdot 10^4$ [cm]	$I \cdot 10^9$ [A]	$D' \cdot 10^7$ [cm^2 s^{-1}]	$D \cdot 10^7$ [cm^2 s^{-1}]
25	0.0469	4.99	-5.251	2.90675	2.9051 ± 0.0016
	0.0469	4.99	-5.247	2.90476	
	0.0469	4.99	-5.245	2.90366	
30	0.0468	4.99	-6.712	3.72629	3.723 ± 0.015
	0.0468	4.99	-6.729	3.73570	
	0.0468	4.99	-6.676	3.70661	
40	0.0465	4.99	-10.364	5.78635	5.789 ± 0.011
	0.0465	4.99	-10.390	5.80092	
	0.0465	4.99	-10.354	5.78043	
50	0.0462	4.99	-15.051	8.45122	8.466 ± 0.015
	0.0462	4.99	-15.105	8.48137	
	0.0462	4.99	-15.078	8.46644	
60	0.0460	4.99	-20.922	11.8148	11.78 ± 0.03
	0.0460	4.99	-20.819	11.7569	
	0.0460	4.99	-20.825	11.7598	

8.1.2.6 0.05 mol L^{-1} I_2 in $EMIBF_4$/MPII with 59.9 mol% MPII

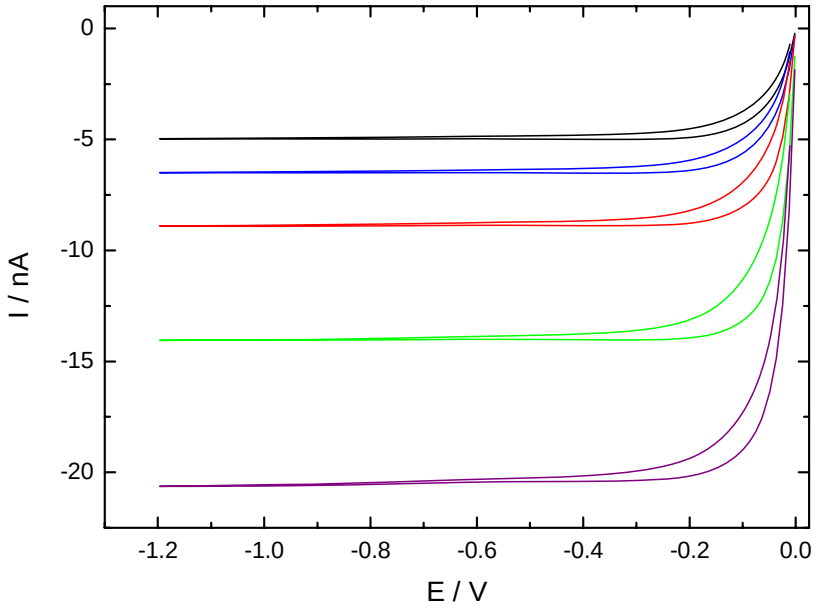

Figure 8-18: Steady-state cyclic voltammograms of 0.05 mol L^{-1} I_2 in $EMIBF_4$/MPII with 59.9 mol% MPII; v = 5 mV s^{-1}; θ: (—) 25 °C, (—) 30 °C, (—) 40 °C, (—) 50 °C, (—) 60 °C.

Table 8-20: Measurement parameters and determined I_3^--diffusion coefficients of 0.05 mol L^{-1} I_2 in $EMIBF_4$/MPII with 59.9 mol% MPII.

θ [°C]	$c(I_3^-)$ [mol L^{-1}]	$r_0 \cdot 10^4$ [cm]	$I \cdot 10^9$ [A]	$D' \cdot 10^7$ [cm^2 s^{-1}]	$D \cdot 10^7$ [cm^2 s^{-1}]
25	0.0473	5.37	-5.012	2.55447E-07	2.544 ± 0.009
	0.0473	5.37	-4.977	2.53634E-07	
	0.0473	5.37	-4.986	2.54116E-07	
30	0.0472	5.37	-6.579	3.36268E-07	3.30 ± 0.08
	0.0472	5.37	-6.501	3.32233E-07	
	0.0472	5.37	-6.268	3.20345E-07	
40	0.0469	5.37	-8.805	4.52491E-07	4.55 ± 0.02
	0.0469	5.37	-8.885	4.56619E-07	
	0.0469	5.37	-8.875	4.56090E-07	
50	0.0467	5.37	-13.885	7.17612E-07	7.24 ± 0.06
	0.0467	5.37	-14.020	7.24594E-07	
	0.0467	5.37	-14.127	7.30140E-07	
60	0.0464	5.37	-20.491	1.06492E-06	10.643 ± 0.013
	0.0464	5.37	-20.497	1.06523E-06	
	0.0464	5.37	-20.451	1.06285E-06	

8.1.2.7 0.05 mol L^{-1} I_2 in $EMIBF_4$/MPII with 80.1 mol% MPII

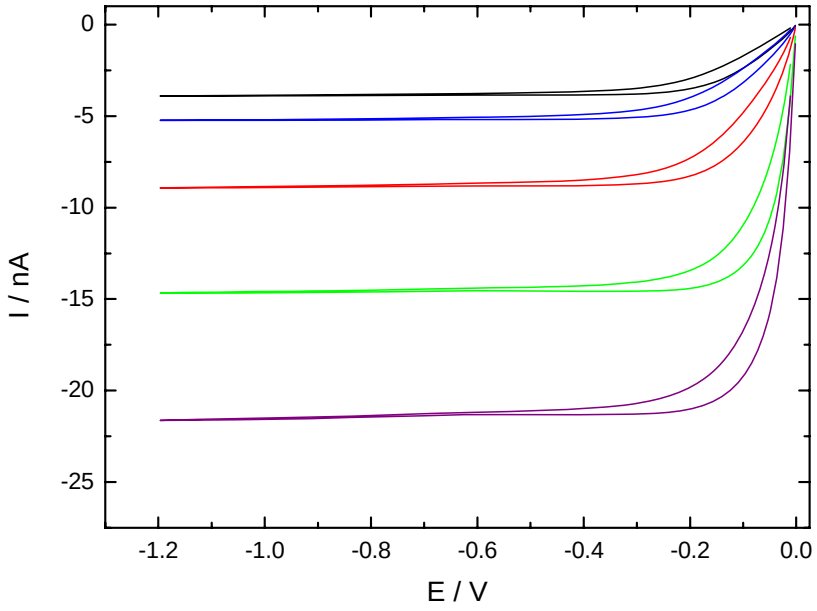

Figure 8-19: Steady-state cyclic voltammograms of 0.05 mol L^{-1} I_2 in $EMIBF_4$/MPII with 80.1 mol% MPII; v = 5 mV s^{-1}; θ: (—) 25 °C, (—) 30 °C, (—) 40 °C, (—) 50 °C, (—) 60 °C.

Table 8-21: Measurement parameters and determined I_3^--diffusion coefficients of 0.05 mol L^{-1} I_2 in $EMIBF_4$/MPII with 80.1 mol% MPII.

θ [°C]	$c(I_3^-)$ [mol L^{-1}]	$r_0 \cdot 10^4$ [cm]	$I \cdot 10^9$ [A]	$D' \cdot 10^7$ [cm^2 s^{-1}]	$D \cdot 10^7$ [cm^2 s^{-1}]
25	0.0506	5.37	-3.865	1.84259	1.847 ± 0.005
	0.0506	5.37	-3.873	1.84646	
	0.0506	5.37	-3.886	1.85295	
30	0.0505	5.37	-5.216	2.49391	2.490 ± 0.004
	0.0505	5.37	-5.208	2.48986	
	0.0505	5.37	-5.201	2.48665	
40	0.0502	5.37	-8.800	4.22995	4.244 ± 0.014
	0.0502	5.37	-8.858	4.25762	
	0.0502	5.37	-8.832	4.24512	
50	0.0499	5.37	-14.690	7.10051	7.08 ± 0.02
	0.0499	5.37	-14.598	7.0558	
	0.0499	5.37	-14.637	7.07499	
60	0.0496	5.37	-21.482	10.4408	10.41 ± 0.03
	0.0496	5.37	-21.424	10.4127	
	0.0496	5.37	-21.357	10.3803	

8.1.2.8 0.10 mol L^{-1} I_2 in $EMIBF_4$/MPII with 80.0 mol% MPII

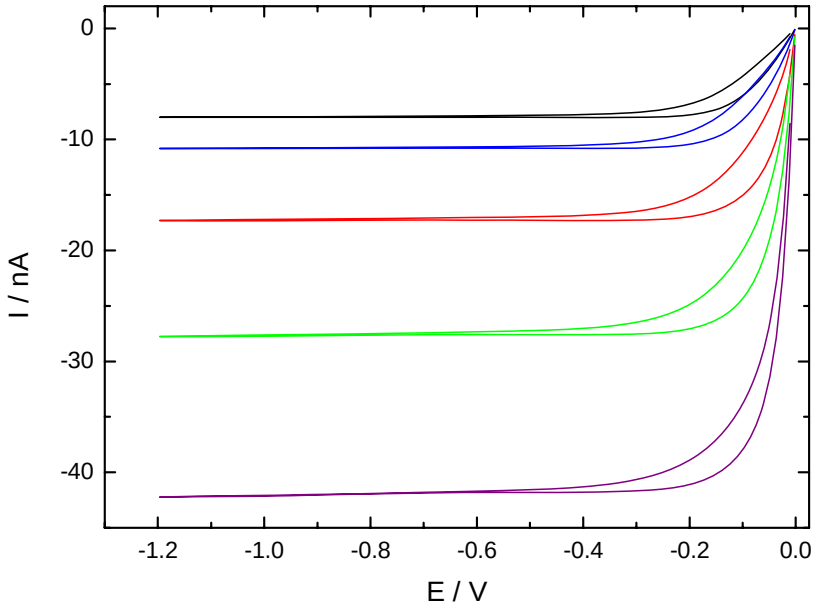

Figure 8-20: Steady-state cyclic voltammograms of 0.10 mol L^{-1} I_2 in $EMIBF_4$/MPII with 80.0 mol% MPII; v = 5 mV s^{-1}; θ: (—) 25 °C, (—) 30 °C, (—) 40 °C, (—) 50 °C, (—) 60 °C.

Table 8-22: Measurement parameters and determined I_3^--diffusion coefficients of 0.10 mol L^{-1} I_2 in $EMIBF_4$/MPII with 80.0 mol% MPII.

θ [°C]	$c(I_3^-)$ [mol L^{-1}]	$r_0 \cdot 10^4$ [cm]	$I \cdot 10^9$ [A]	$D' \cdot 10^7$ [cm^2 s^{-1}]	$D \cdot 10^7$ [cm^2 s^{-1}]
25	0.1000	5.03	-8.090	2.08392	2.067 ± 0.016
	0.1000	5.03	-8.006	2.06218	
	0.1000	5.03	-7.971	2.05338	
30	0.0997	5.03	-10.844	2.80117	2.794 ± 0.007
	0.0997	5.03	-10.794	2.7882	
	0.0997	5.03	-10.815	2.79363	
40	0.0992	5.03	-17.264	4.48342	4.486 ± 0.002
	0.0992	5.03	-17.283	4.48833	
	0.0992	5.03	-17.273	4.48571	
50	0.0986	5.03	-27.392	7.15359	7.20 ± 0.04
	0.0986	5.03	-27.632	7.21603	
	0.0986	5.03	-27.713	7.23739	
60	0.0981	5.03	-41.929	11.0098	11.04 ± 0.06
	0.0981	5.03	-41.920	11.0074	
	0.0981	5.03	-42.302	11.1079	

8.1.2.9 0.20 mol L^{-1} I_2 in $EMIBF_4$/MPII with 80.0 mol% MPII

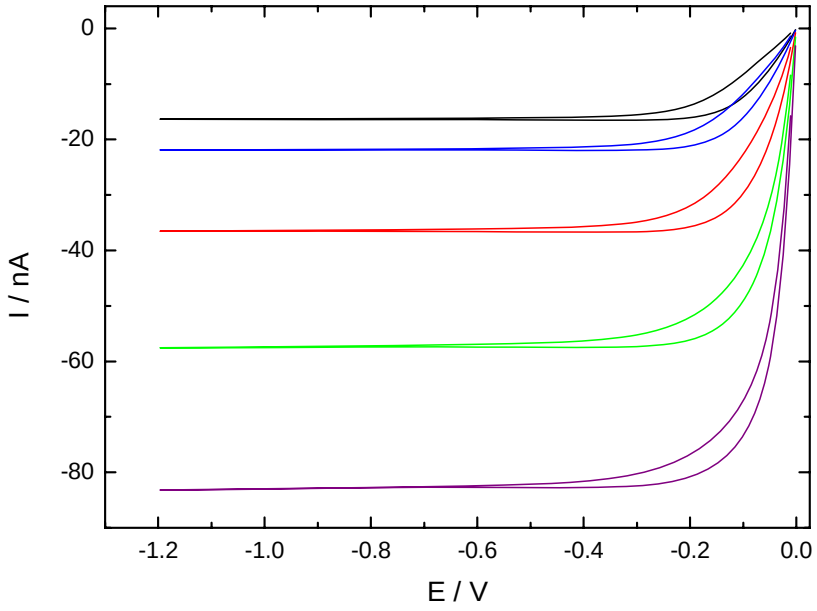

Figure 8-21: Steady-state cyclic voltammograms of 0.20 mol L^{-1} I_2 in $EMIBF_4$/MPII with 80.0 mol% MPII; v = 5 mV s^{-1}; θ: (—) 25 °C, (—) 30 °C, (—) 40 °C, (—) 50 °C, (—) 60 °C.

Table 8-23: Measurement parameters and determined I_3^--diffusion coefficients of 0.20 mol L^{-1} I_2 in $EMIBF_4$/MPII with 80.0 mol% MPII.

θ [°C]	$c(I_3^-)$ [mol L^{-1}]	$r_0 \cdot 10^4$ [cm]	$I \cdot 10^9$ [A]	$D' \cdot 10^7$ [cm^2 s^{-1}]	$D \cdot 10^7$ [cm^2 s^{-1}]
25	0.198	4.99	-16.541	2.16915	2.159 ± 0.009
	0.198	4.99	-16.424	2.15379	
	0.198	4.99	-16.426	2.15411	
30	0.197	4.99	-21.828	2.87039	2.876 ± 0.005
	0.197	4.99	-21.907	2.88087	
	0.197	4.99	-21.885	2.87789	
40	0.196	4.99	-36.574	4.83566	4.840 ± 0.007
	0.196	4.99	-36.576	4.83589	
	0.196	4.99	-36.666	4.84781	
50	0.195	4.99	-57.353	7.62544	7.635 ± 0.010
	0.195	4.99	-57.425	7.63495	
	0.195	4.99	-57.500	7.64494	
60	0.194	4.99	-83.073	11.1007	11.07 ± 0.02
	0.194	4.99	-82.768	11.0600	
	0.194	4.99	-82.769	11.0601	

8.1.2.10 0.30 mol L^{-1} I_2 in $EMIBF_4$/MPII with 80.1 mol% MPII

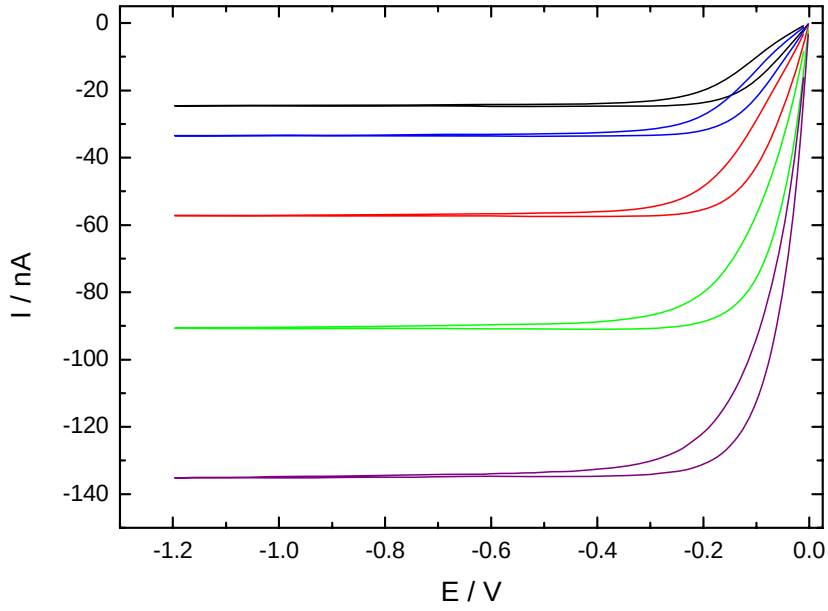

Figure 8-22: Steady-state cyclic voltammograms of 0.30 mol L^{-1} I_2 in $EMIBF_4$/MPII with 80.1 mol% MPII; ν = 5 mV s^{-1}; θ: (—) 25 °C, (—) 30 °C, (—) 40 °C, (—) 50 °C, (—) 60 °C.

Table 8-24: Measurement parameters and determined I_3^--diffusion coefficients of 0.30 mol L^{-1} I_2 in $EMIBF_4$/MPII with 80.1 mol% MPII.

θ [°C]	$c(I_3^-)$ [mol L^{-1}]	$r_0 \cdot 10^4$ [cm]	$I \cdot 10^9$ [A]	$D' \cdot 10^7$ [cm^2 s^{-1}]	$D \cdot 10^7$ [cm^2 s^{-1}]
25	0.296	5.03	-24.831	2.15969	2.150 ± 0.009
	0.296	5.03	-24.635	2.14265	
	0.296	5.03	-24.682	2.14676	
30	0.295	5.03	-33.533	2.92452	2.921 ± 0.003
	0.295	5.03	-33.487	2.92049	
	0.295	5.03	-33.468	2.91888	
40	0.294	5.03	-57.783	5.06657	5.05 ± 0.02
	0.294	5.03	-57.306	5.02479	
	0.294	5.03	-57.685	5.05801	
50	0.292	5.03	-91.534	8.07103	8.04 ± 0.03
	0.292	5.03	-90.763	8.00297	
	0.292	5.03	-91.202	8.04175	
60	0.290	5.03	-134.764	11.9485	11.93 ± 0.03
	0.290	5.03	-134.746	11.9469	
	0.290	5.03	-134.173	11.8961	

8.1.2.11 0.39 mol L^{-1} I_2 in $EMIBF_4$/MPII with 80.0 mol% MPII

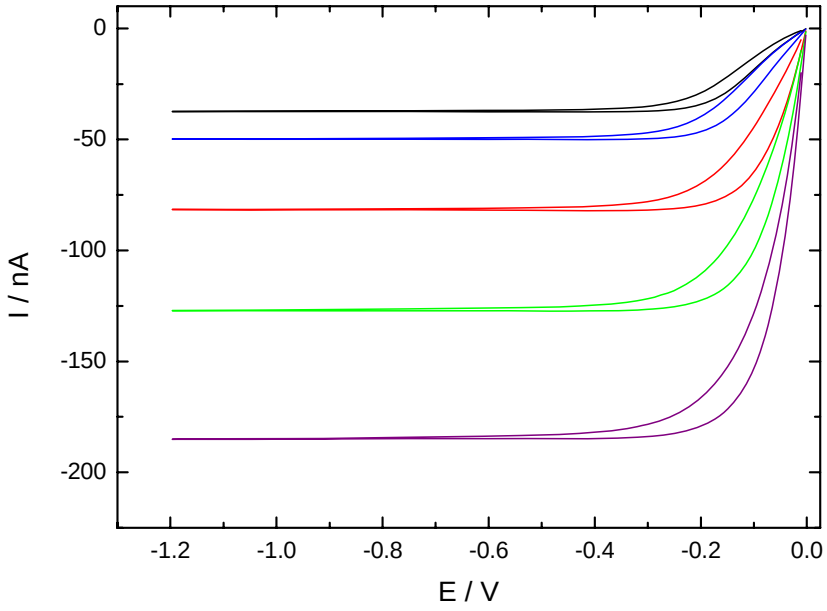

Figure 8-23: Steady-state cyclic voltammograms of 0.39 mol L^{-1} I_2 in $EMIBF_4$/MPII with 80.0 mol% MPII; v = 5 mV s^{-1}; θ: (—) 25 °C, (—) 30 °C, (—) 40 °C, (—) 50 °C, (—) 60 °C.

Table 8-25: Measurement parameters and determined I_3^--diffusion coefficients of 0.39 mol L^{-1} I_2 in $EMIBF_4$/MPII with 80.0 mol% MPII.

θ [°C]	$c(I_3^-)$ [mol L^{-1}]	$r_0 \cdot 10^4$ [cm]	$I \cdot 10^9$ [A]	$D' \cdot 10^7$ [cm^2 s^{-1}]	$D \cdot 10^7$ [cm^2 s^{-1}]
25	0.392	5.37	-37.566	2.31114	2.308 ± 0.003
	0.392	5.37	-3.7475	2.30558	
	0.392	5.37	-3.7499	2.30703	
30	0.391	5.37	-49.819	3.07350	3.078 ± 0.005
	0.391	5.37	-49.900	3.07855	
	0.391	5.37	-49.975	3.08312	
40	0.389	5.37	-81.801	5.07429	5.0736 ± 0.0009
	0.389	5.37	-81.772	5.07249	
	0.389	5.37	-81.796	5.07395	
50	0.387	5.37	-127.089	7.92900	7.936 ± 0.010
	0.387	5.37	-127.120	7.93093	
	0.387	5.37	-127.388	7.94765	
60	0.384	5.37	-184.829	11.5978	11.57 ± 0.05
	0.384	5.37	-184.715	11.5907	
	0.384	5.37	-183.463	11.5121	

8.1.2.12 0.49 mol L^{-1} I_2 in $EMIBF_4$/MPII with 80.0 mol% MPII

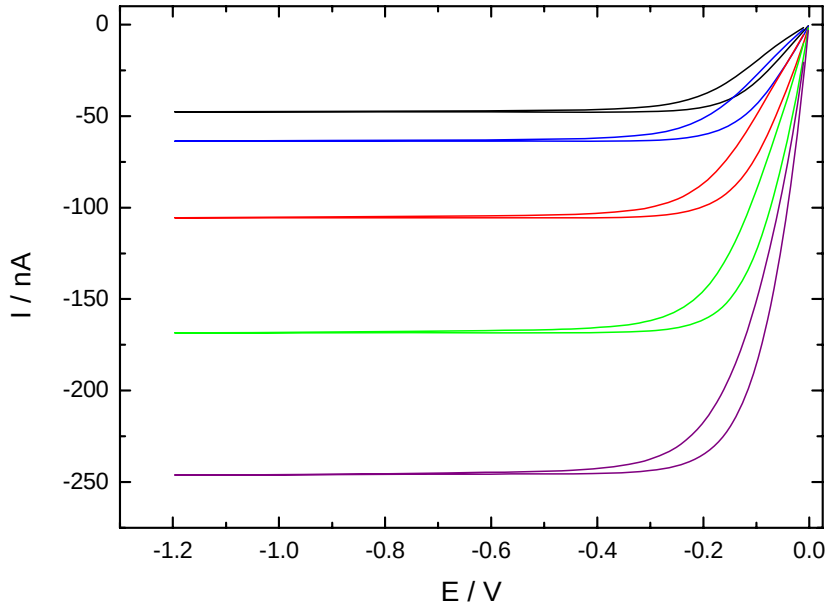

Figure 8-24: Steady-state cyclic voltammograms of 0.49 mol L^{-1} I_2 in $EMIBF_4$/MPII with 80.0 mol% MPII; v = 5 mV s^{-1}; θ: (—) 25 °C, (—) 30 °C, (—) 40 °C, (—) 50 °C, (—) 60 °C.

Table 8-26: Measurement parameters and determined I_3^--diffusion coefficients of 0.49 mol L^{-1} I_2 in $EMIBF_4$/MPII with 80.0 mol% MPII.

θ [°C]	$c(I_3^-)$ [mol L^{-1}]	$r_0 \cdot 10^4$ [cm]	$I \cdot 10^9$ [A]	$D' \cdot 10^7$ [cm^2 s^{-1}]	$D \cdot 10^7$ [cm^2 s^{-1}]
25	0.485	5.37	-47.553	2.36576	2.368 ± 0.004
	0.485	5.37	-47.689	2.37249	
	0.485	5.37	-47.522	2.36422	
30	0.484	5.37	-63.482	3.16687	3.173 ± 0.005
	0.484	5.37	-63.650	3.17527	
	0.484	5.37	-63.671	3.17632	
40	0.481	5.37	-105.661	5.29961	5.300 ± 0.011
	0.481	5.37	-105.444	5.28873	
	0.481	5.37	-105.900	5.3116	
50	0.478	5.37	-166.096	8.37787	8.45 ± 0.06
	0.478	5.37	-168.256	8.48682	
	0.478	5.37	-168.274	8.48773	
60	0.476	5.37	-246.095	12.4818	12.467 ± 0.015
	0.476	5.37	-245.491	12.4512	
	0.476	5.37	-245.843	12.4691	

8.1.2.13 VFT-Equation Parameters

Table 8-27: VFT-Equation parameters of I_3^--diffusion coefficients of 0.05 mol L^{-1} I_2 in mixtures of $EMIBF_4$/MPII at varying MPII concentrations.

Mol% MPII	$A \cdot 10^3$ [$cm^2\ s^{-1}$]	B [K]	T_0 [K]	R^2
10.1	0.040 ± 0.005	480 ± 40	194 ± 5	0.99999
20.1	0.6 ± 1.9	1300 ± 1300	130 ± 100	0.99883
30.1	0.1 ± 0.4	700 ± 800	180 ± 90	0.99714
40.0	0.02 ± 0.02	300 ± 200	220 ± 30	0.99861
50.1	0.130 ± 0.002	725 ± 5	179.8 ± 0.5	1
60.1	0.2 ± 0.8	800 ± 1300	180 ± 130	0.99403
79.9	0.2 ± 0.2	700 ± 300	200 ± 30	0.99951
100.0	0.23 ± 0.02	840 ± 30	187 ± 2	1

Table 8-28: VFT-Equation parameters of I_3^--diffusion coefficients of I_2 in mixtures of $EMIBF_4$/MPII with 80 mol% MPII at varying I_2 concentrations.

$c(I_3^-)$ [mol L^{-1}]	$A \cdot 10^3$ [$cm^2\ s^{-1}$]	B [K]	T_0 [K]	R^2
0.05	0.2 ± 0.2	700 ± 300	200 ± 30	0.99951
0.10	0.2 ± 0.5	800 ± 600	190 ± 60	0.99866
0.20	0.10 ± 0.06	660 ± 120	196 ± 11	0.99993
0.30	0.20 ± 0.02	720 ± 30	194 ± 3	1
0.39	0.30 ± 0.1	830 ± 110	180 ± 10	0.99997
0.49	0.4 ± 0.2	890 ± 170	178 ± 14	0.99994

8.1.3 EMIOTf/MPII

8.1.3.1 0.05 mol L^{-1} I_2 in EMIOTf/MPII with 10.1 mol% MPII

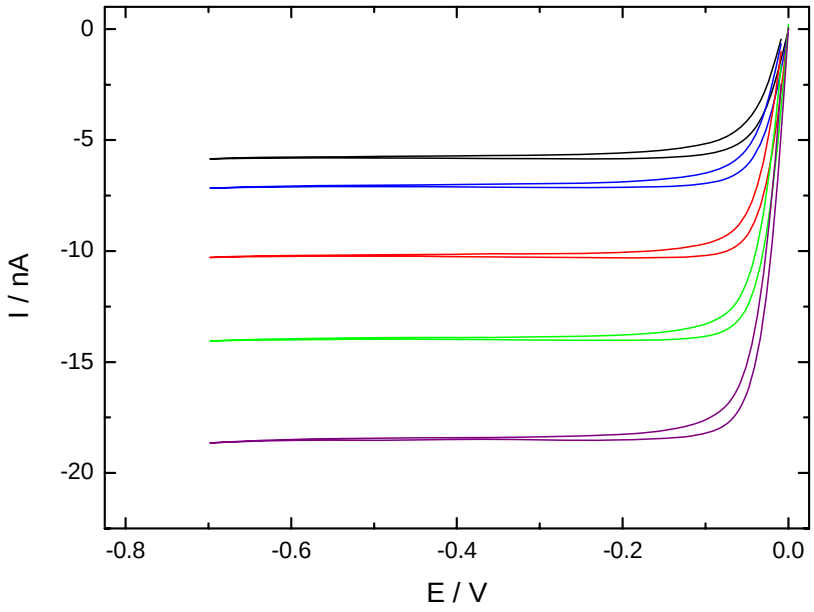

Figure 8-25: Steady-state cyclic voltammograms of 0.05 mol L^{-1} I_2 in EMIOTf/MPII with 10.1 mol% MPII; v = 5 mV s^{-1}; θ: (—) 25 °C, (—) 30 °C, (—) 40 °C, (—) 50 °C, (—) 60 °C.

Table 8-29: Measurement parameters and determined I_3^--diffusion coefficients of 0.05 mol L^{-1} I_2 in EMIOTf/MPII with 10.1 mol% MPII.

θ [°C]	$c(I_3^-)$ [mol L^{-1}]	$r_0 \cdot 10^4$ [cm]	$I \cdot 10^9$ [A]	$D' \cdot 10^7$ [cm^2 s^{-1}]	$D \cdot 10^7$ [cm^2 s^{-1}]
25	0.0495	5.03	-5.812	3.02160	3.025 ± 0.003
	0.0495	5.03	-5.822	3.02640	
	0.0495	5.03	-5.823	3.02734	
30	0.0494	5.03	-7.098	3.70060	3.704 ± 0.005
	0.0494	5.03	-7.118	3.71123	
	0.0494	5.03	-7.100	3.70150	
40	0.0491	5.03	-10.173	5.33511	5.36 ± 0.02
	0.0491	5.03	-10.179	5.33831	
	0.0491	5.03	-10.186	5.34235	
	0.0491	5.03	-10.262	5.38221	
	0.0491	5.03	-10.260	5.38105	
	0.0491	5.03	-10.242	5.37145	
50	0.0488	5.03	-14.040	7.40773	7.394 ± 0.012
	0.0488	5.03	-13.994	7.38330	
	0.0488	5.03	-14.010	7.39163	
60	0.0485	5.03	-18.539	9.83956	9.825 ± 0.015
	0.0485	5.03	-18.511	9.82501	
	0.0485	5.03	-18.482	9.80930	

8.1.3.2 0.05 mol L^{-1} I_2 in EMIOTf/MPII with 20.1 mol% MPII

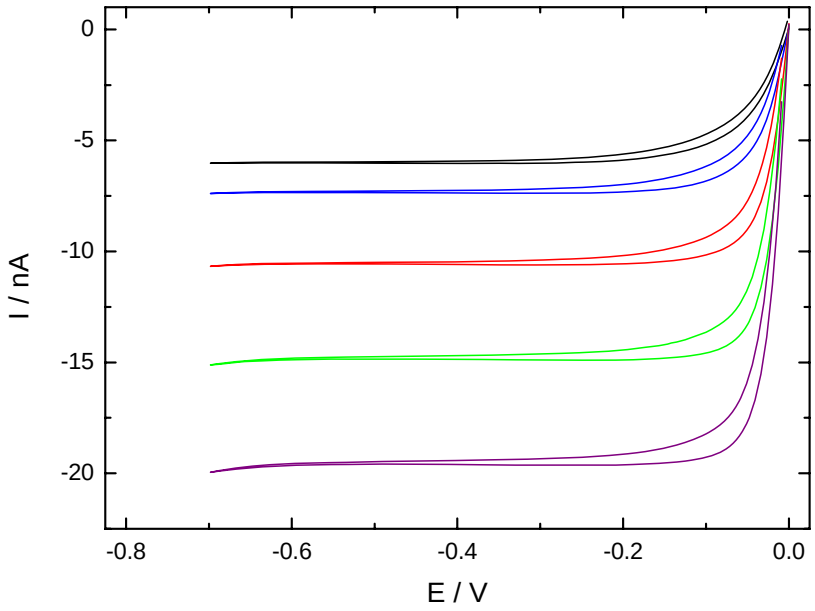

Figure 8-26: Steady-state cyclic voltammograms of 0.05 mol L^{-1} I_2 in EMIOTf/MPII with 20.1 mol% MPII; v = 5 mV s^{-1}; θ: (—) 25 °C, (—) 30 °C, (—) 40 °C, (—) 50 °C, (—) 60 °C.

Table 8-30: Measurement parameters and determined I_3^--diffusion coefficients of 0.05 mol L^{-1} I_2 in EMIOTf/MPII with 20.1 mol% MPII.

θ [°C]	$c(I_3^-)$ [mol L^{-1}]	$r_0 \cdot 10^4$ [cm]	$I \cdot 10^9$ [A]	$D' \cdot 10^7$ [cm^2 s^{-1}]	$D \cdot 10^7$ [cm^2 s^{-1}]
25	0.0505	4.99	-6.019	3.09495	3.096 ± 0.003
	0.0505	4.99	-6.016	3.09361	
	0.0505	4.99	-6.027	3.09913	
30	0.0503	4.99	-7.353	3.79194	3.794 ± 0.002
	0.0503	4.99	-7.354	3.79249	
	0.0503	4.99	-7.361	3.79621	
40	0.0500	4.99	-10.587	5.49184	5.54 ± 0.06
	0.0500	4.99	-10.583	5.48987	
	0.0500	4.99	-10.577	5.4866	
	0.0500	4.99	-10.800	5.60223	
	0.0500	4.99	-10.807	5.60601	
	0.0500	4.99	-10.778	5.59092	
50	0.0497	4.99	-14.839	7.74409	7.763 ± 0.013
	0.0497	4.99	-14.882	7.76663	
	0.0497	4.99	-14.890	7.77065	
	0.0497	4.99	-14.888	7.76929	
60	0.0495	4.99	-19.614	10.2976	10.306 ± 0.007
	0.0495	4.99	-19.639	10.3106	
	0.0495	4.99	-19.635	10.3085	

8.1.3.3 0.05 mol L^{-1} I_2 in EMIOTf/MPII with 30.1 mol% MPII

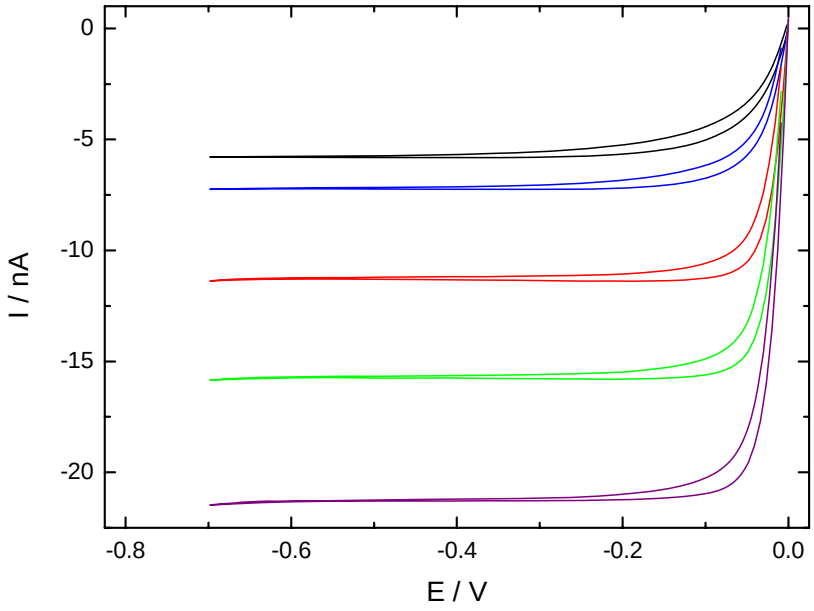

Figure 8-27: Steady-state cyclic voltammograms of 0.05 mol L^{-1} I_2 in EMIOTf/MPII with 30.1 mol% MPII; v = 5 mV s^{-1}; θ: (—) 25 °C, (—) 30 °C, (—) 40 °C, (—) 50 °C, (—) 60 °C.

Table 8-31: Measurement parameters and determined I_3^--diffusion coefficients of 0.05 mol L^{-1} I_2 in EMIOTf/MPII with 30.1 mol% MPII.

θ [°C]	$c(I_3^-)$ [mol L^{-1}]	$r_0 \cdot 10^4$ [cm]	$I \cdot 10^9$ [A]	$D' \cdot 10^7$ [cm^2 s^{-1}]	$D \cdot 10^7$ [cm^2 s^{-1}]
25	0.0505	4.99	-5.813	2.98924	2.983 ± 0.007
	0.0505	4.99	-5.804	2.98417	
	0.0505	4.99	-5.788	2.97608	
30	0.0503	4.99	-7.241	3.7342	3.728 ± 0.007
	0.0503	4.99	-7.230	3.72855	
	0.0503	4.99	-7.215	3.72051	
40	0.0501	4.99	-10.490	5.44059	5.458 ± 0.012
	0.0501	4.99	-10.551	5.47234	
	0.0501	4.99	-10.542	5.46746	
	0.0501	5.37	-11.302	5.44700	
	0.0501	5.37	-11.331	5.46092	
	0.0501	5.37	-11.322	5.45692	
50	0.0498	5.37	-15.697	7.61063	7.626 ± 0.015
	0.0498	5.37	-15.759	7.64059	
	0.0498	5.37	-15.733	7.62808	
60	0.0495	5.37	-21.283	10.3803	10.377 ± 0.006
	0.0495	5.37	-21.285	10.3810	
	0.0495	5.37	-21.263	10.3707	

8.1.3.4 0.05 mol L^{-1} I_2 in EMIOTf/MPII with 40.0 mol% MPII

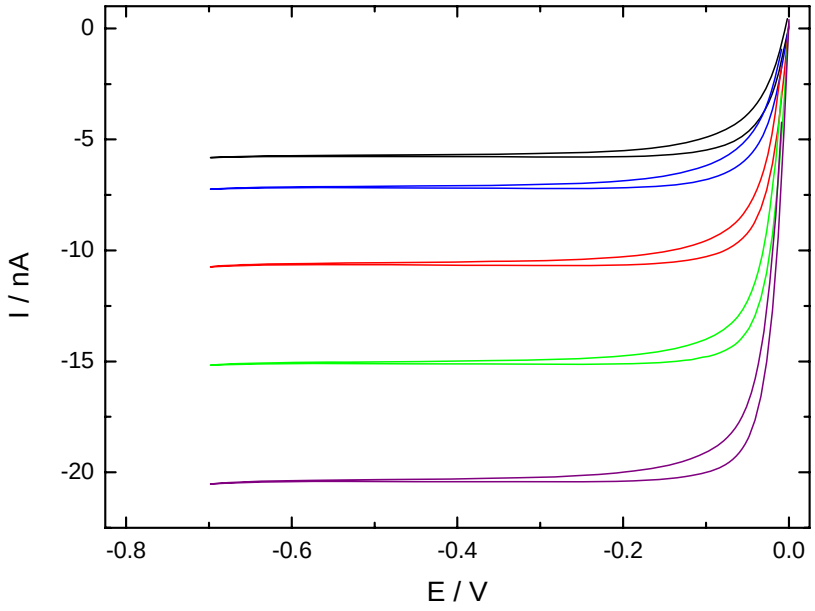

Figure 8-28: Steady-state cyclic voltammograms of 0.05 mol L^{-1} I_2 in EMIOTf/MPII with 40.0 mol% MPII; v = 5 mV s^{-1}; θ: (—) 25 °C, (—) 30 °C, (—) 40 °C, (—) 50 °C, (—) 60 °C.

Table 8-32: Measurement parameters and determined I_3^--diffusion coefficients of 0.05 mol L^{-1} I_2 in EMIOTf/MPII with 40.0 mol% MPII.

θ [°C]	$c(I_3^-)$ [mol L^{-1}]	$r_0 \cdot 10^4$ [cm]	$I \cdot 10^9$ [A]	$D' \cdot 10^7$ [cm^2 s^{-1}]	$D \cdot 10^7$ [cm^2 s^{-1}]
25	0.0512	4.99	-5.796	2.94168	2.937 ± 0.005
	0.0512	4.99	-5.776	2.93151	
	0.0512	4.99	-5.786	2.93673	
30	0.0510	4.99	-7.167	3.6479	3.653 ± 0.005
	0.0510	4.99	-7.180	3.6545	
	0.0510	4.99	-7.184	3.65662	
40	0.0507	4.99	-10.644	5.4489	5.458 ± 0.011
	0.0507	4.99	-10.682	5.46835	
	0.0507	4.99	-10.695	5.4747	
	0.0507	4.99	-10.643	5.44833	
	0.0507	4.99	-10.664	5.45898	
	0.0507	4.99	-10.648	5.45089	
50	0.0504	4.99	-15.073	7.76188	7.772 ± 0.009
	0.0504	4.99	-15.102	7.77708	
	0.0504	4.99	-15.104	7.77764	
60	0.0501	4.99	-20.329	10.5298	10.56 ± 0.03
	0.0501	4.99	-20.406	10.5695	
	0.0501	4.99	-20.447	10.5906	

8.1.3.5 0.05 mol L^{-1} I_2 in EMIOTf/MPII with 50.1 mol% MPII

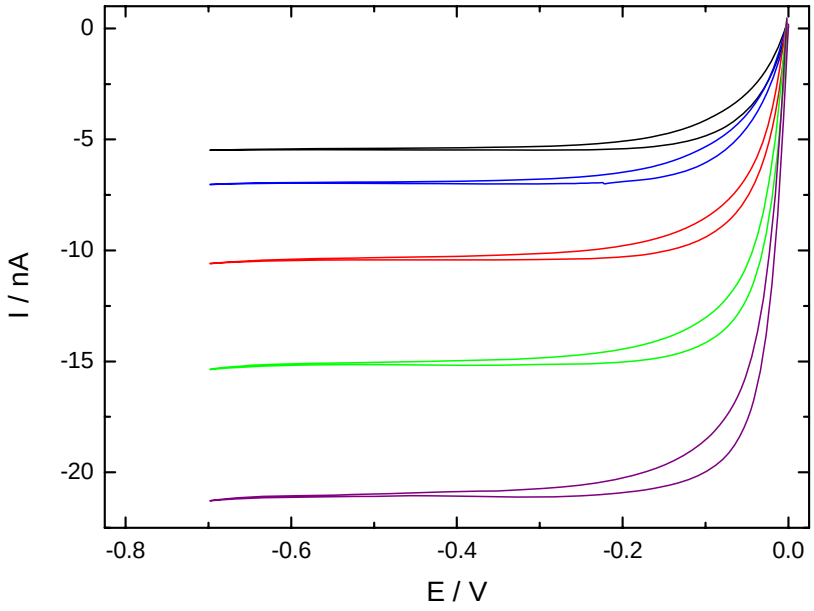

Figure 8-29: Steady-state cyclic voltammograms of 0.05 mol L^{-1} I_2 in EMIOTf/MPII with 50.1 mol% MPII; v = 5 mV s^{-1}; θ: (—) 25 °C, (—) 30 °C, (—) 40 °C, (—) 50 °C, (—) 60 °C.

Table 8-33: Measurement parameters and determined I_3^--diffusion coefficients of 0.05 mol L^{-1} I_2 in EMIOTf/MPII with 50.1 mol% MPII.

θ [°C]	$c(I_3^-)$ [mol L^{-1}]	$r_0 \cdot 10^4$ [cm]	$I \cdot 10^9$ [A]	$D' \cdot 10^7$ [cm^2 s^{-1}]	$D \cdot 10^7$ [cm^2 s^{-1}]
25	0.0498	5.03	-5.465	2.8294	2.833 ± 0.006
	0.0498	5.03	-5.466	2.82998	
	0.0498	5.03	-5.484	2.83936	
30	0.0496	5.03	-6.982	3.62509	3.6257 ± 0.00010
	0.0496	5.03	-6.986	3.62686	
	0.0496	5.03	-6.983	3.62525	
40	0.0493	5.03	-10.685	5.57869	5.51 ± 0.09
	0.0493	5.03	-10.699	5.58615	
	0.0493	5.03	-10.705	5.58913	
	0.0493	5.03	-10.347	5.40221	
	0.0493	5.03	-10.441	5.45139	
	0.0493	5.03	-10.443	5.45259	
50	0.0490	5.03	-15.127	7.94423	7.960 ± 0.014
	0.0490	5.03	-15.171	7.96713	
	0.0490	5.03	-15.175	7.96933	
60	0.0488	5.03	-21.023	11.1041	11.125 ± 0.019
	0.0488	5.03	-21.090	11.1398	
	0.0488	5.03	-21.075	11.1318	

8.1.3.6 0.05 mol L^{-1} I_2 in EMIOTf/MPII with 60.1 mol% MPII

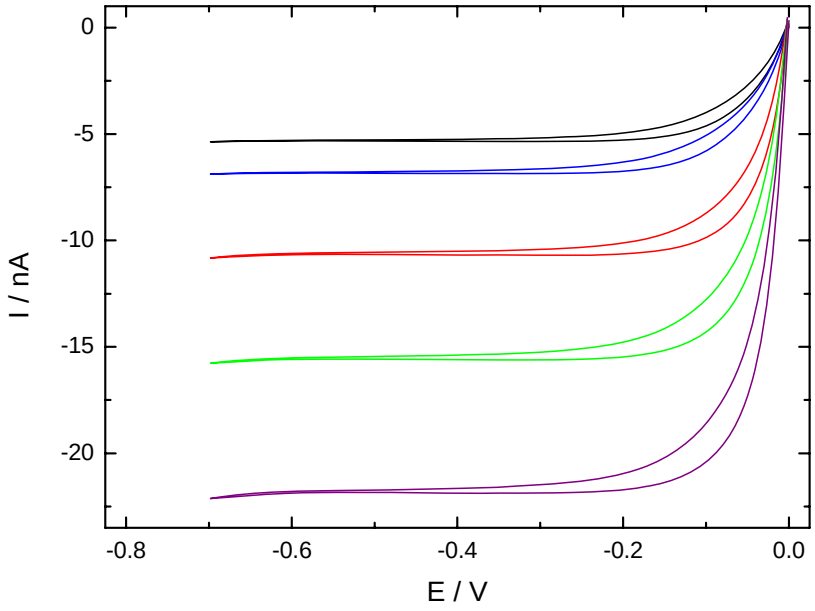

Figure 8-30: Steady-state cyclic voltammograms of 0.05 mol L^{-1} I_2 in EMIOTf/MPII with 60.1 mol% MPII; v = 5 mV s^{-1}; θ: (—) 25 °C, (—) 30 °C, (—) 40 °C, (—) 50 °C, (—) 60 °C.

Table 8-34: Measurement parameters and determined I_3^--diffusion coefficients of 0.05 mol L^{-1} I_2 in EMIOTf/MPII with 60.1 mol% MPII.

θ [°C]	$c(I_3^-)$ [mol L^{-1}]	$r_0 \cdot 10^4$ [cm]	$I \cdot 10^9$ [A]	$D' \cdot 10^7$ [cm^2 s^{-1}]	$D \cdot 10^7$ [cm^2 s^{-1}]
25	0.0501	5.37	-5.363	2.8294	2.576 ± 0.006
	0.0501	5.37	-5.337	2.82998	
	0.0501	5.37	-5.346	2.83936	
30	0.0500	5.37	-6.805	3.62509	3.301 ± 0.013
	0.0500	5.37	-6.846	3.62686	
	0.0500	5.37	-6.853	3.62525	
40	0.0497	5.37	-10.629	5.57869	5.170 ± 0.015
	0.0497	5.37	-10.606	5.58615	
	0.0497	5.37	-10.625	5.58913	
	0.0497	5.37	-10.674	5.40221	
	0.0497	5.37	-10.687	5.45139	
	0.0497	5.37	-10.647	5.45259	
50	0.0494	5.37	-15.677	7.94423	7.63 ± 0.03
	0.0494	5.37	-15.598	7.96713	
	0.0494	5.37	-15.562	7.96933	
60	0.0491	5.37	-21.760	11.1041	10.72 ± 0.03
	0.0491	5.37	-21.864	11.1398	
	0.0491	5.37	-21.843	11.1318	

8.1.3.7 0.05 mol L^{-1} I_2 in EMIOTf/MPII with 70.0 mol% MPII

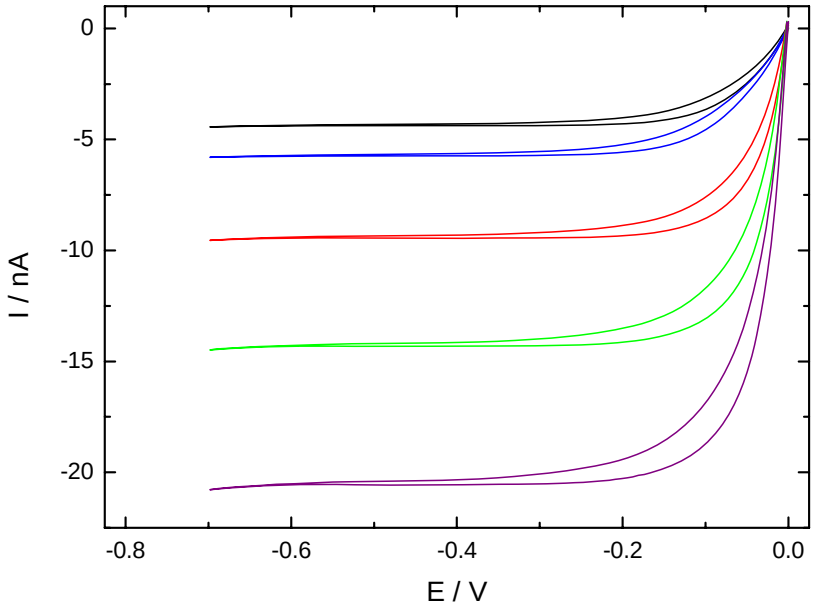

Figure 8-31: Steady-state cyclic voltammograms of 0.05 mol L^{-1} I_2 in EMIOTf/MPII with 70.0 mol% MPII; v = 5 mV s^{-1}; θ: (—) 25 °C, (—) 30 °C, (—) 40 °C, (—) 50 °C, (—) 60 °C.

Table 8-35: Measurement parameters and determined I_3^--diffusion coefficients of 0.05 mol L^{-1} I_2 in EMIOTf/MPII with 70.0 mol% MPII.

θ [°C]	$c(I_3^-)$ [mol L^{-1}]	$r_0 \cdot 10^4$ [cm]	$I \cdot 10^9$ [A]	$D' \cdot 10^7$ [cm^2 s^{-1}]	$D \cdot 10^7$ [cm^2 s^{-1}]
25	0.0495	5.03	-4.365	2.27169	2.278 ± 0.005
	0.0495	5.03	-4.384	2.28176	
	0.0495	5.03	-4.380	2.27983	
30	0.0493	5.03	-5.777	3.01519	3.010 ± 0.010
	0.0493	5.03	-5.746	2.99914	
	0.0493	5.03	-5.780	3.01688	
40	0.0491	5.03	-9.381	4.92350	4.946 ± 0.015
	0.0491	5.03	-9.401	4.93377	
	0.0491	5.03	-9.425	4.94646	
	0.0491	5.03	-9.435	4.95156	
	0.0491	5.03	-9.444	4.95655	
	0.0491	5.03	-9.460	4.96466	
50	0.0488	5.03	-14.334	7.56611	7.560 ± 0.005
	0.0488	5.03	-14.317	7.55729	
	0.0488	5.03	-14.318	7.55782	
60	0.0485	5.03	-20.532	10.8988	10.911 ± 0.012
	0.0485	5.03	-20.560	10.9136	
	0.0485	5.03	-20.575	10.9215	

8.1.3.8 0.05 mol L^{-1} I_2 in EMIOTf/MPII with 79.9 mol% MPII

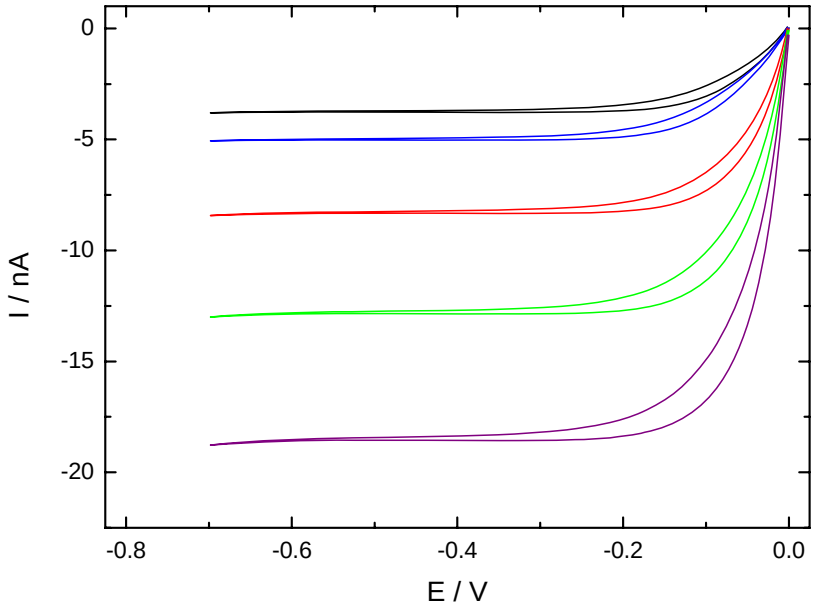

Figure 8-32: Steady-state cyclic voltammograms of 0.05 mol L^{-1} I_2 in EMIOTf/MPII with 79.9 mol% MPII; v = 5 mV s^{-1}; θ: (—) 25 °C, (—) 30 °C, (—) 40 °C, (—) 50 °C, (—) 60 °C.

Table 8-36: Measurement parameters and determined I_3^--diffusion coefficients of 0.05 mol L^{-1} I_2 in EMIOTf/MPII with 79.9 mol% MPII.

θ [°C]	$c(I_3^-)$ [mol L^{-1}]	$r_0 \cdot 10^4$ [cm]	$I \cdot 10^9$ [A]	$D' \cdot 10^7$ [cm^2 s^{-1}]	$D \cdot 10^7$ [cm^2 s^{-1}]
25	0.0487	4.99	-3.798	2.02328	2.015 ± 0.007
	0.0487	4.99	-3.770	2.00866	
	0.0487	4.99	-3.781	2.01418	
30	0.0486	4.99	-5.051	2.6985	2.691 ± 0.007
	0.0486	4.99	-5.026	2.68475	
	0.0486	4.99	-5.036	2.69056	
40	0.0483	4.99	-8.443	4.53512	4.50 ± 0.03
	0.0483	4.99	-8.417	4.52138	
	0.0483	4.99	-8.453	4.54048	
	0.0483	4.99	-8.304	4.46073	
	0.0483	4.99	-8.336	4.4776	
	0.0483	4.99	-8.355	4.48785	
50	0.0481	4.99	-12.868	6.95116	6.953 ± 0.007
	0.0481	4.99	-12.862	6.94754	
	0.0481	4.99	-12.885	6.96039	
60	0.0478	4.99	-18.534	10.0676	10.10 ± 0.03
	0.0478	4.99	-18.575	10.0899	
	0.0478	4.99	-18.659	10.1354	

8.1.3.9 VFT-Equation Parameters

Table 8-37: VFT-Equation parameters of I_3^--diffusion coefficients of 0.05 mol L^{-1} I_2 in mixtures of EMIOTf/MPII at varying MPII concentrations.

Mol% MPII	$A \cdot 10^3$ [cm^2 s^{-1}]	B [K]	T_0 [K]	R^2
10.1	0.090 ± 0.005	778 ± 16	162.6 ± 1.6	1
20.1	0.08 ± 0.03	690 ± 110	173 ± 12	0.99995
30.1	0.24 ± 0.13	1000 ± 200	144 ± 17	0.99995
40.0	0.14 ± 0.03	810 ± 60	166 ± 6	0.99999
50.1	0.34 ± 0.17	1000 ± 200	151 ± 14	0.99996
60.1	0.190 ± 0.009	840 ± 13	171.0 ± 1.3	1
70.0	0.180 ± 0.006	754 ± 9	184.7 ± 0.9	1
79.9	0.140 ± 0.007	694 ± 13	191.7 ± 1.3	1
100.0	0.23 ± 0.02	840 ± 30	187 ± 2	1

8.1.4 EMINTf$_2$/MPII

8.1.4.1 0.05 mol L^{-1} I$_2$ in EMINTf$_2$/MPII with 10.1 mol% MPII

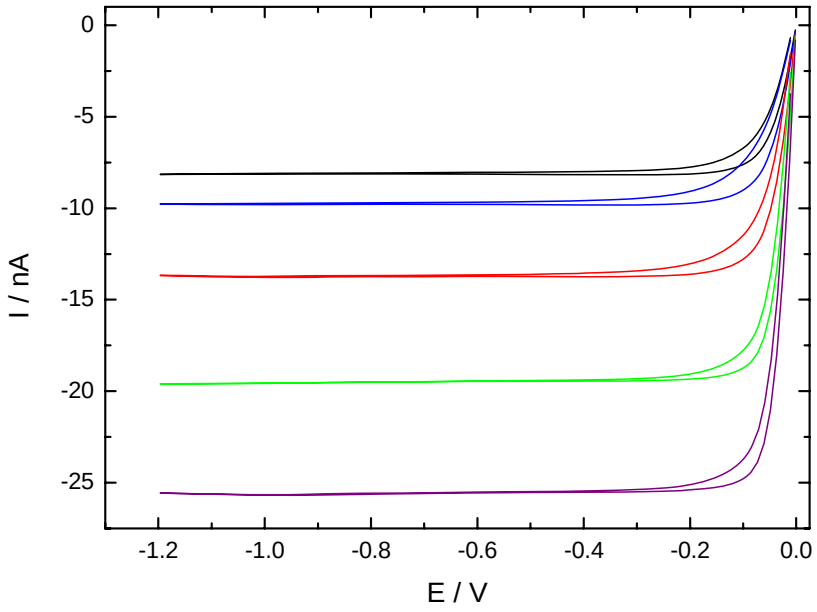

Figure 8-33: Steady-state cyclic voltammograms of 0.05 mol L^{-1} I$_2$ in EMINTf$_2$/MPII with 10.1 mol% MPII; v = 5 mV s^{-1}; θ: (—) 25 °C, (—) 30 °C, (—) 40 °C, (—) 50 °C, (—) 60 °C.

Table 8-38: Measurement parameters and determined I_3^--diffusion coefficients of 0.05 mol L^{-1} I$_2$ in EMINTf$_2$/MPII with 10.1 mol% MPII.

θ [°C]	$c(I_3^-)$ [mol L^{-1}]	$r_0 \cdot 10^4$ [cm]	$I \cdot 10^9$ [A]	$D' \cdot 10^7$ [cm^2 s^{-1}]	$D \cdot 10^7$ [cm^2 s^{-1}]
25	0.0520	4.99	-8.152	4.06736	4.069 ± 0.006
	0.0520	4.99	-8.145	4.06376	
	0.0520	4.99	-8.169	4.07583	
30	0.0519	4.99	-9.789	4.90077	4.9027 ± 0.0019
	0.0519	4.99	-9.793	4.90270	
	0.0519	4.99	-9.797	4.90461	
40	0.0515	5.37	-14.398	6.74168	6.84 ± 0.09
	0.0515	5.37	-14.432	6.75731	
	0.0515	5.37	-14.452	6.76663	
	0.0515	4.99	-13.727	6.91691	
	0.0515	4.99	-13.731	6.91888	
	0.0515	4.99	-13.721	6.91364	
50	0.0512	5.37	-19.522	9.20196	9.199 ± 0.011
	0.0512	5.37	-19.490	9.18688	
	0.0512	5.37	-19.536	9.20880	
60	0.0508	5.37	-25.559	12.1278	12.134 ± 0.009
	0.0508	5.37	-25.561	12.1291	
	0.0508	5.37	-25.594	12.1446	

8.1.4.2 0.05 mol L^{-1} I_2 in $EMINTf_2$/MPII with 19.9 mol% MPII

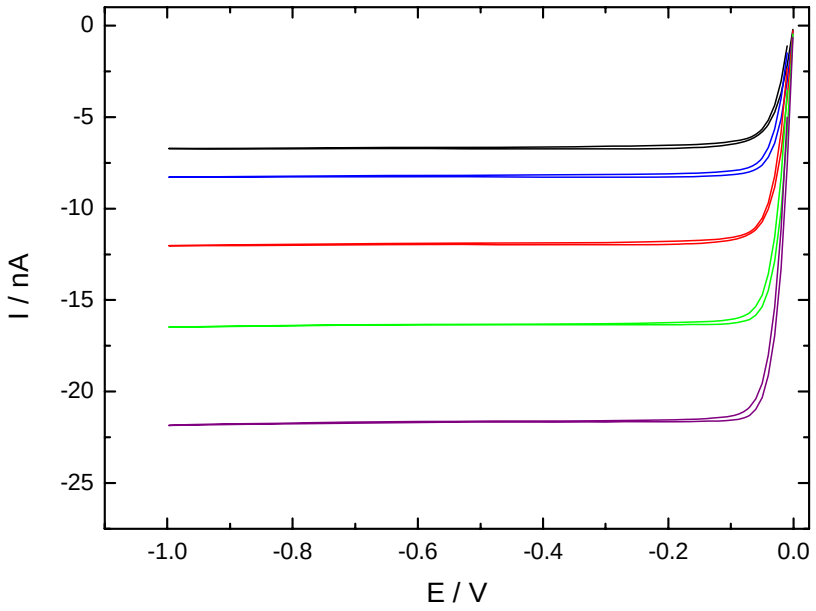

Figure 8-34: Steady-state cyclic voltammograms of 0.05 mol L^{-1} I_2 in $EMINTf_2$/MPII with 19.9 mol% MPII; v = 5 mV s^{-1}; θ: (—) 25 °C, (—) 30 °C, (—) 40 °C, (—) 50 °C, (—) 60 °C.

Table 8-39: Measurement parameters and determined I_3^--diffusion coefficients of 0.05 mol L^{-1} I_2 in $EMINTf_2$/MPII with 19.9 mol% MPII.

θ [°C]	$c(I_3^-)$ [mol L^{-1}]	$r_0 \cdot 10^4$ [cm]	$I \cdot 10^9$ [A]	$D' \cdot 10^7$ [cm^2 s^{-1}]	$D \cdot 10^7$ [cm^2 s^{-1}]
25	0.0489	5.03	-6.518	3.43319	3.51 ± 0.07
	0.0489	5.03	-6.728	3.54388	
	0.0489	5.03	-6.749	3.55509	
30	0.0487	5.03	-8.218	4.34304	4.363 ± 0.017
	0.0487	5.03	-8.266	4.36810	
	0.0487	5.03	-8.282	4.37661	
40	0.0484	5.03	-11.814	6.28427	6.33 ± 0.04
	0.0484	5.03	-11.833	6.29422	
	0.0484	5.03	-11.853	6.30502	
	0.0484	5.03	-11.878	6.31842	
	0.0484	5.03	-11.976	6.37039	
	0.0484	5.03	-12.002	6.38422	
50	0.0481	5.03	-16.340	8.74794	8.77 ± 0.02
	0.0481	5.03	-16.369	8.76342	
	0.0481	5.03	-16.425	8.79324	
60	0.0478	5.03	-21.683	11.6830	11.689 ± 0.005
	0.0478	5.03	-21.699	11.6915	
	0.0478	5.03	-21.701	11.6926	

8.1.4.3 0.05 mol L^{-1} I_2 in $EMINTf_2$/MPII with 30.0 mol% MPII

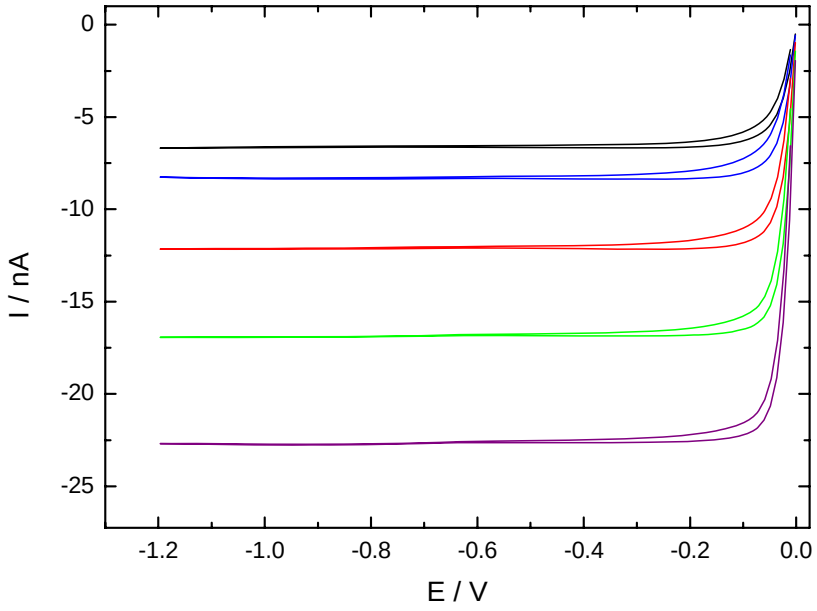

Figure 8-35: Steady-state cyclic voltammograms of 0.05 mol L^{-1} I_2 in $EMINTf_2$/MPII with 30.0 mol% MPII; v = 5 mV s^{-1}; θ: (—) 25 °C, (—) 30 °C, (—) 40 °C, (—) 50 °C, (—) 60 °C.

Table 8-40: Measurement parameters and determined I_3^--diffusion coefficients of 0.05 mol L^{-1} I_2 in $EMINTf_2$/MPII with 30.0 mol% MPII.

θ [°C]	$c(I_3^-)$ [mol L^{-1}]	$r_0 \cdot 10^4$ [cm]	$I \cdot 10^9$ [A]	$D' \cdot 10^7$ [cm^2 s^{-1}]	$D \cdot 10^7$ [cm^2 s^{-1}]
25	0.0493	5.03	-6.683	3.49460	3.481 ± 0.013
	0.0493	5.03	-6.649	3.47691	
	0.0493	5.03	-6.636	3.47009	
30	0.0491	5.03	-8.309	4.35878	4.371 ± 0.012
	0.0491	5.03	-8.332	4.37092	
	0.0491	5.03	-8.356	4.38350	
40	0.0488	5.03	-12.145	6.41166	6.411 ± 0.006
	0.0488	5.03	-12.131	6.40406	
	0.0488	5.03	-12.155	6.41684	
50	0.0485	5.03	-16.900	8.97959	8.969 ± 0.009
	0.0485	5.03	-16.872	8.96477	
	0.0485	5.03	-16.870	8.96370	
60	0.0482	5.03	-22.655	12.1153	12.10 ± 0.02
	0.0482	5.03	-22.655	12.1156	
	0.0482	5.03	-22.583	12.0771	

8.1.4.4 0.05 mol L^{-1} I_2 in $EMINTf_2$/MPII with 40.0 mol% MPII

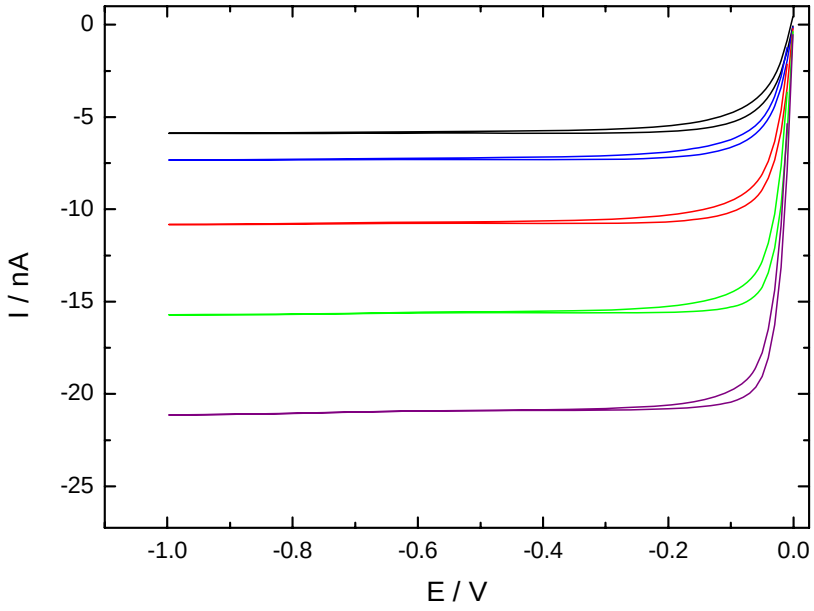

Figure 8-36: Steady-state cyclic voltammograms of 0.05 mol L^{-1} I_2 in $EMINTf_2$/MPII with 40.0 mol% MPII; v = 5 mV s^{-1}; θ: (—) 25 °C, (—) 30 °C, (—) 40 °C, (—) 50 °C, (—) 60 °C.

Table 8-41: Measurement parameters and determined I_3^--diffusion coefficients of 0.05 mol L^{-1} I_2 in $EMINTf_2$/MPII with 40.0 mol% MPII.

θ [°C]	$c(I_3^-)$ [mol L^{-1}]	$r_0 \cdot 10^4$ [cm]	$I \cdot 10^9$ [A]	$D' \cdot 10^7$ [cm^2 s^{-1}]	$D \cdot 10^7$ [cm^2 s^{-1}]
25	0.0496	4.99	-5.850	3.06363	3.072 ± 0.007
	0.0496	4.99	-5.872	3.07522	
	0.0496	4.99	-5.874	3.07638	
30	0.0494	4.99	-7.296	3.83329	3.838 ± 0.005
	0.0494	4.99	-7.304	3.83741	
	0.0494	4.99	-7.315	3.84310	
40	0.0491	4.99	-10.722	5.66806	5.684 ± 0.014
	0.0491	4.99	-10.771	5.69401	
	0.0491	4.99	-10.764	5.69016	
50	0.0488	4.99	-15.713	8.35932	8.33 ± 0.03
	0.0488	4.99	-15.628	8.31426	
	0.0488	4.99	-15.613	8.30639	
60	0.0485	4.99	-21.014	11.2498	11.24 ± 0.02
	0.0485	4.99	-20.950	11.2159	
	0.0485	4.99	-21.032	11.2595	

8.1.4.5 0.05 mol L^{-1} I_2 in $EMINTf_2$/MPII with 50.1 mol% MPII

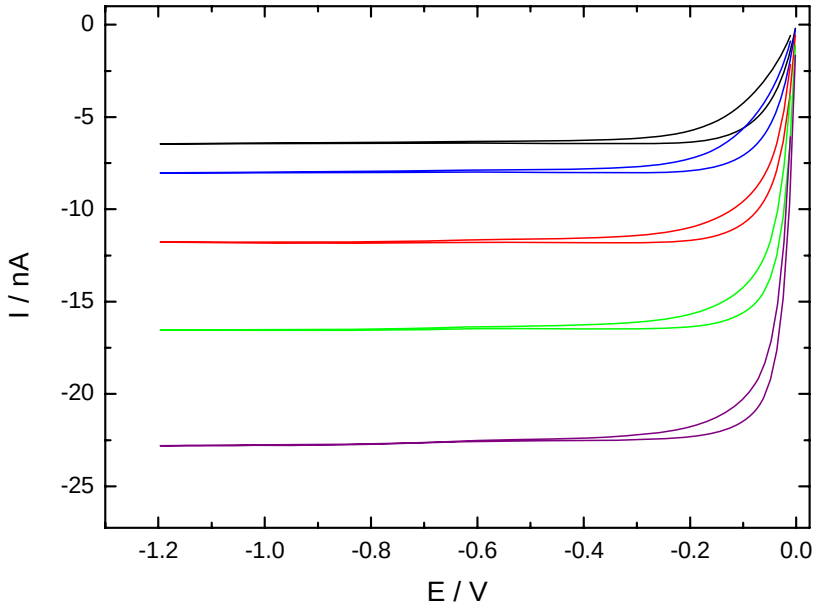

Figure 8-37: Steady-state cyclic voltammograms of 0.05 mol L^{-1} I_2 in $EMINTf_2$/MPII with 50.1 mol% MPII; v = 5 mV s^{-1}; θ: (—) 25 °C, (—) 30 °C, (—) 40 °C, (—) 50 °C, (—) 60 °C.

Table 8-42: Measurement parameters and determined I_3^--diffusion coefficients of 0.05 mol L^{-1} I_2 in $EMINTf_2$/MPII with 50.1 mol% MPII.

θ [°C]	$c(I_3^-)$ [mol L^{-1}]	$r_0 \cdot 10^4$ [cm]	$I \cdot 10^9$ [A]	$D' \cdot 10^7$ [cm^2 s^{-1}]	$D \cdot 10^7$ [cm^2 s^{-1}]
25	0.0505	5.37	-6.405	3.05938	3.070 ± 0.011
	0.0505	5.37	-6.428	3.07036	
	0.0505	5.37	-6.449	3.08048	
30	0.0504	5.37	-8.005	3.83554	3.8351 ± 0.0017
	0.0504	5.37	-8.001	3.83328	
	0.0504	5.37	-8.008	3.83658	
40	0.0500	5.37	-11.815	5.69522	5.689 ± 0.006
	0.0500	5.37	-11.799	5.68789	
	0.0500	5.37	-11.792	5.68413	
50	0.0497	5.37	-16.489	7.99853	8.006 ± 0.009
	0.0497	5.37	-16.500	8.00426	
	0.0497	5.37	-16.524	8.01561	
60	0.0494	5.37	-22.573	11.0179	11.034 ± 0.018
	0.0494	5.37	-22.646	11.0534	
	0.0494	5.37	-22.597	11.0294	

8.1.4.6 0.05 mol L^{-1} I_2 in $EMINTf_2$/MPII with 60.0 mol% MPII

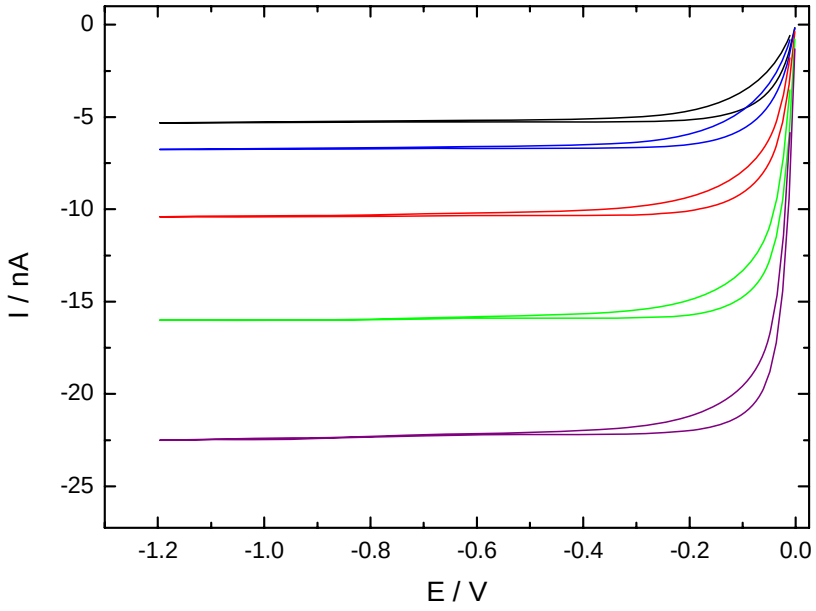

Figure 8-38: Steady-state cyclic voltammograms of 0.05 mol L^{-1} I_2 in $EMINTf_2$/MPII with 60.0 mol% MPII; v = 5 mV s^{-1}; θ: (—) 25 °C, (—) 30 °C, (—) 40 °C, (—) 50 °C, (—) 60 °C.

Table 8-43: Measurement parameters and determined I_3^--diffusion coefficients of 0.05 mol L^{-1} I_2 in $EMINTf_2$/MPII with 60.0 mol% MPII.

θ [°C]	$c(I_3^-)$ [mol L^{-1}]	$r_0 \cdot 10^4$ [cm]	$I \cdot 10^9$ [A]	$D' \cdot 10^7$ [cm^2 s^{-1}]	$D \cdot 10^7$ [cm^2 s^{-1}]
25	0.0505	5.03	-5.273	2.68785	2.6893 ± 0.0016
	0.0505	5.03	-5.276	2.68902	
	0.0505	5.03	-5.280	2.69107	
30	0.0504	5.03	-6.731	3.44130	3.439 ± 0.006
	0.0504	5.03	-6.713	3.43191	
	0.0504	5.03	-6.736	3.44374	
40	0.0501	5.03	-10.354	5.32506	5.324 ± 0.004
	0.0501	5.03	-10.360	5.32794	
	0.0501	5.03	-10.345	5.32023	
50	0.0498	5.03	-15.896	8.22565	8.244 ± 0.017
	0.0498	5.03	-15.936	8.24599	
	0.0498	5.03	-15.961	8.25903	
60	0.0495	5.03	-22.336	11.6280	11.615 ± 0.012
	0.0495	5.03	-22.308	11.6135	
	0.0495	5.03	-22.291	11.6046	

8.1.4.7 0.05 mol L^{-1} I_2 in $EMINTf_2$/MPII with 70.0 mol% MPII

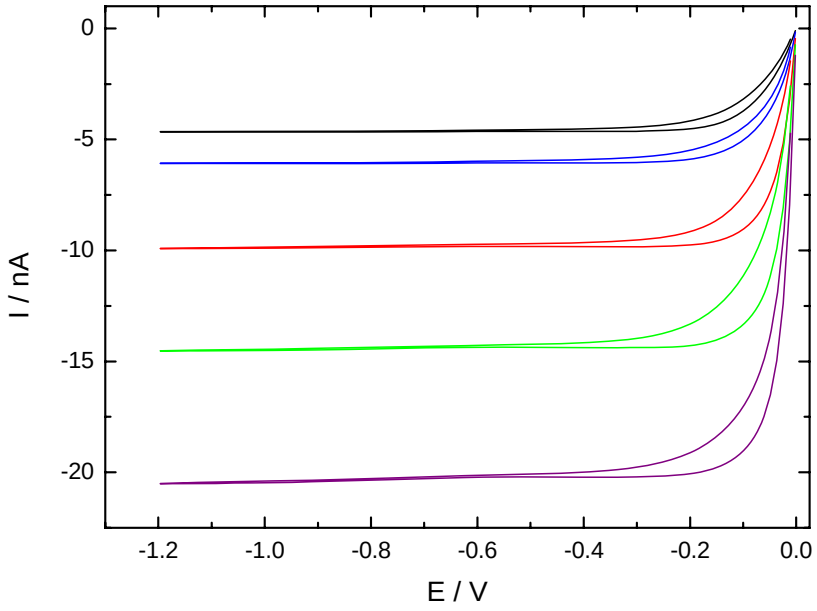

Figure 8-39: Steady-state cyclic voltammograms of 0.05 mol L^{-1} I_2 in $EMINTf_2$/MPII with 70.0 mol% MPII; v = 5 mV s^{-1}; θ: (—) 25 °C, (—) 30 °C, (—) 40 °C, (—) 50 °C, (—) 60 °C.

Table 8-44: Measurement parameters and determined I_3^--diffusion coefficients of 0.05 mol L^{-1} I_2 in $EMINTf_2$/MPII with 70.0 mol% MPII.

θ [°C]	$c(I_3^-)$ [mol L^{-1}]	$r_0 \cdot 10^4$ [cm]	$I \cdot 10^9$ [A]	$D' \cdot 10^7$ [cm^2 s^{-1}]	$D \cdot 10^7$ [cm^2 s^{-1}]
25	0.0490	5.03	-4.664	2.45316	2.449 ± 0.004
	0.0490	5.03	-4.647	2.4444	
	0.0490	5.03	-4.655	2.44841	
30	0.0488	5.03	-6.071	3.20295	3.204 ± 0.003
	0.0488	5.03	-6.069	3.20188	
	0.0488	5.03	-6.080	3.20754	
40	0.0485	5.03	-9.758	5.17843	5.03 ± 0.17
	0.0485	5.03	-9.795	5.19774	
	0.0485	5.03	-9.787	5.19371	
	0.0485	5.37	-9.800	4.87153	
	0.0485	5.37	-9.853	4.89765	
	0.0485	5.37	-9.786	4.86446	
50	0.0482	5.37	-14.420	7.2108	7.216 ± 0.006
	0.0482	5.37	-14.427	7.21415	
	0.0482	5.37	-14.442	7.2217	
60	0.0480	5.37	-20.239	10.1804	10.21 ± 0.03
	0.0480	5.37	-20.322	10.2222	
	0.0480	5.37	-20.350	10.2360	

8.1.4.8 0.05 mol L^{-1} I_2 in $EMINTf_2$/MPII with 80.0 mol% MPII

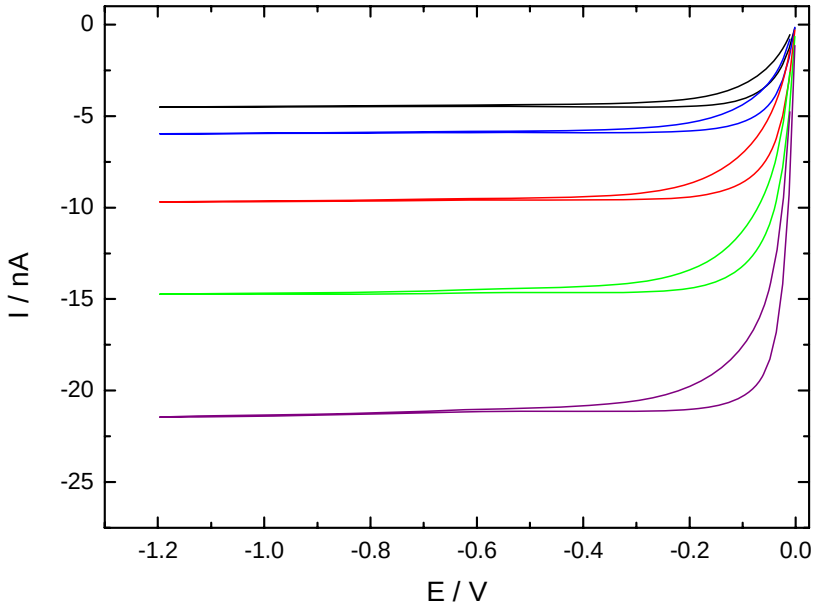

Figure 8-40: Steady-state cyclic voltammograms of 0.05 mol L^{-1} I_2 in $EMINTf_2$/MPII with 80.0 mol% MPII; v = 5 mV s^{-1}; θ: (—) 25 °C, (—) 30 °C, (—) 40 °C, (—) 50 °C, (—) 60 °C.

Table 8-45: Measurement parameters and determined I_3^--diffusion coefficients of 0.05 mol L^{-1} I_2 in $EMINTf_2$/MPII with 80.0 mol% MPII.

θ [°C]	$c(I_3^-)$ [mol L^{-1}]	$r_0 \cdot 10^4$ [cm]	$I \cdot 10^9$ [A]	$D' \cdot 10^7$ [cm^2 s^{-1}]	$D \cdot 10^7$ [cm^2 s^{-1}]
25	0.0499	5.37	-4.522	2.18419	2.173 ± 0.009
	0.0499	5.37	-4.489	2.16823	
	0.0499	5.37	-4.488	2.16775	
30	0.0498	5.37	-5.890	2.85313	2.866 ± 0.012
	0.0498	5.37	-5.925	2.87014	
	0.0498	5.37	-5.935	2.87515	
40	0.0495	5.37	-9.633	4.69312	4.689 ± 0.004
	0.0495	5.37	-9.624	4.68889	
	0.0495	5.37	-9.618	4.6856	
50	0.0492	5.37	-14.685	7.19665	7.193 ± 0.004
	0.0492	5.37	-14.682	7.19508	
	0.0492	5.37	-14.668	7.18837	
60	0.0489	5.37	-21.171	10.4358	10.453 ± 0.019
	0.0489	5.37	-21.247	10.4735	
	0.0489	5.37	-21.196	10.4482	

8.1.4.9 0.05 mol L^{-1} I_2 in MPII

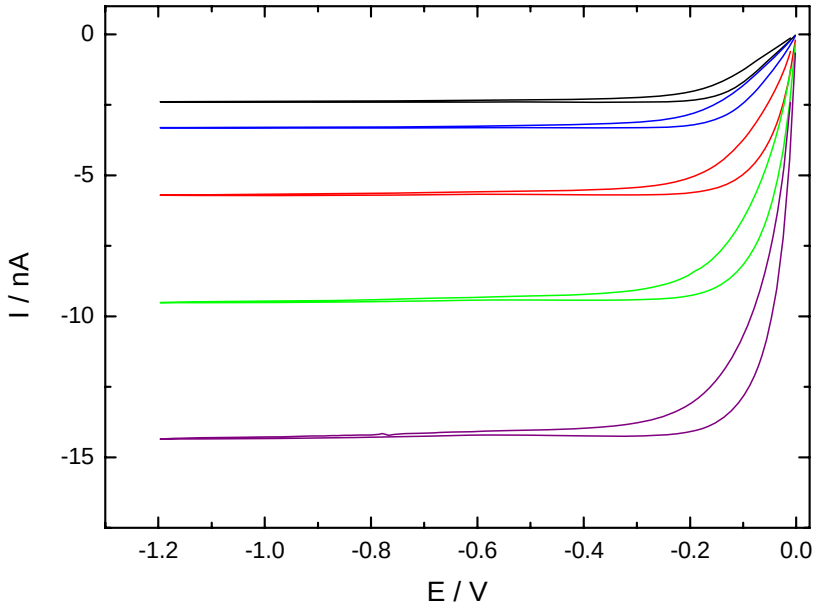

Figure 8-41: Steady-state cyclic voltammograms of 0.05 mol L^{-1} I_2 in MPII; v = 5 mV s^{-1}; θ: (—) 25 °C, (—) 30 °C, (—) 40 °C, (—) 50 °C, (—) 60 °C.

Table 8-46: Measurement parameters and determined I_3^--diffusion coefficients of 0.05 mol L^{-1} I_2 in MPII.

θ [°C]	$c(I_3^-)$ [mol L^{-1}]	$r_0 \cdot 10^4$ [cm]	$I \cdot 10^9$ [A]	$D' \cdot 10^7$ [cm^2 s^{-1}]	$D \cdot 10^7$ [cm^2 s^{-1}]
25	0.0510	4.99	-2.391	1.21749	1.2194 ± 0.0016
	0.0510	4.99	-2.397	1.22058	
	0.0510	4.99	-2.396	1.22001	
30	0.0509	4.99	-3.322	1.6959	1.695 ± 0.003
	0.0509	4.99	-3.312	1.69062	
	0.0509	4.99	-3.324	1.6971	
40	0.0506	4.99	-5.967	3.06223	2.99 ± 0.07
	0.0506	4.99	-5.936	3.04656	
	0.0506	4.99	-5.950	3.05356	
	0.0506	4.99	-5.696	2.92337	
	0.0506	4.99	-5.690	2.91995	
	0.0506	4.99	-5.682	2.91622	
50	0.0503	4.99	-9.405	4.85266	4.873 ± 0.017
	0.0503	4.99	-9.458	4.88013	
	0.0503	4.99	-9.467	4.88487	
60	0.0500	4.99	-14.287	7.41163	7.42 ± 0.02
	0.0500	4.99	-14.271	7.40317	
	0.0500	4.99	-14.355	7.44649	

8.1.4.10 VFT-Equation Parameters

Table 8-47: VFT-Equation parameters of I_3^--diffusion coefficients of 0.05 mol L^{-1} I_2 in mixtures of $EMINTf_2$/MPII at varying MPII concentrations.

Mol% MPII	$A \cdot 10^3$ [$cm^2\ s^{-1}$]	B [K]	T_0 [K]	R^2
10.1	0.4 ± 0.2	1300 ± 200	110 ± 20	0.99997
19.9	0.1 ± 0.02	720 ± 50	170 ± 6	0.99999
30.0	0.13 ± 0.04	770 ± 100	168 ± 10	0.99997
40.0	0.13 ± 0.15	800 ± 300	170 ± 30	0.99965
50.1	0.5 ± 0.3	1200 ± 300	130 ± 20	0.99994
60.0	0.4 ± 0.7	1000 ± 500	160 ± 50	0.99955
70.0	0.15 ± 0.17	800 ± 300	170 ± 30	0.9997
80.0	0.290 ± 0.008	897 ± 8	173.2 ± 0.7	1
100.0	0.23 ± 0.02	840 ± 30	187 ± 2	1

8.2 Conductivity Measurements

Conductivity measurements were performed with previously calibrated conductivity cells connected to a conductivity bridge. The electrolyte resistances were determined at four frequencies in a range between 3 and 8 kHz at each temperature to enable extrapolation of the determined electrolyte resistances to infinite frequencies. The examined temperature range was typically between 5 °C and 50 °C with a temperature stability of ± 2 mK for each measurement temperature. In the following paragraphs the exact compositions of the blends and the fitting parameters for analysis of conductivity data with respect to temperature and MPII concentration are summarised for the electrolyte systems EMIDCA/MPII, $EMIBF_4$/MPII, EMIOTf/MPII, and $EMINTf_2$/MPII.

8.2.1 EMIDCA/MPII

Table 8-48: I_2-molonities and MPII concentrations of the blends of the system EMIDCA/MPII.

Mol% MPII	10.9	20.8	30.6	41.0	50.5	60.7	81.0	100.0
$\tilde{m}$ (I_2) [mol kg^{-1}]	0.0428	0.0404	0.0396	0.0378	0.0372	0.0358	0.0331	0.0319

Table 8-49: VFT-Equation parameters of specific conductivity data of ≈ 0.05 mol L^{-1} I_2 in mixtures of EMIDCA and MPII at varying MPII concentrations.

Mol% MPII	κ_0 [mS cm^{-1}]	B [K]	T_0 [K]	R^2
10.9	1210 ± 30	523 ± 6	165.2 ± 0.8	1
20.8	1095 ± 11	514 ± 3	171.5 ± 0.4	1
30.6	1190 ± 15	544 ± 3	174.0 ± 0.4	1
41.0	1231 ± 15	568 ± 3	178.0 ± 0.4	1
50.5	1296 ± 12	591 ± 2	181.7 ± 0.3	1
60.7	1500 ± 40	641 ± 6	183.9 ± 0.6	1
81.0	2500 ± 200	800 ± 20	185.1 ± 1.8	1
100.0	4700 ± 500	1000 ± 30	185.9 ± 1.9	1

Table 8-50: Fit parameters of fitting specific conductivity data of ≈ 0.05 mol L^{-1} I_2 in mixtures of EMIDCA and MPII at varying temperatures according to Eq. (5.2).

T [K]	A [mS cm^{-1}]	B_1 [mS cm^{-1} K^{-1}]	$B_2 \cdot 10^3$ [mS cm^{-1} K^{-2}]	$B_3 \cdot 10^6$ [mS cm^{-1} K^{-3}]	R^2
278.151	15.81 ± 0.07	-0.399 ± 0.007	3.18 ± 0.16	-7.3 ± 1.1	0.99998
298.151	29.80 ± 0.16	-0.595 ± 0.012	3.5 ± 0.3	-4.8 ± 1.5	0.99995
303.152	33.87 ± 0.183	-0.637 ± 0.013	3.4 ± 0.3	-3.3 ± 1.7	0.99995
313.150	42.7 ± 0.2	-0.721 ± 0.019	3.2 ± 0.4	-1 ± 2	0.99995
323.150	52.5 ± 0.4	-0.80 ± 0.03	3.1 ± 0.6	0.3 ± 3	0.99992

8.2.2 $EMIBF_4$/MPII

Table 8-51: I_2-molonities and MPII concentrations of the blends of the system $EMIBF_4$/MPII.

Mol% MPII	10.1	19.9	30.0	39.8	50.1	60.1	80.0	100.0
$\tilde{m}$ (I_2) [mol kg^{-1}]	0.0390	0.0384	0.0367	0.0362	0.0356	0.0355	0.0340	0.0319

Table 8-52: VFT-Equation parameters of specific conductivity data of ≈ 0.05 mol L^{-1} I_2 in mixtures of $EMIBF_4$ and MPII at varying MPII concentrations.

Mol% MPII	κ_0 [mS cm^{-1}]	B [K]	T_0 [K]	R^2
10.1	1410 ± 6	613.8 ± 1.1	168.44 ± 0.13	1
19.9	1465 ± 11	634 ± 2	172.0 ± 0.2	1
30.0	1576 ± 18	654 ± 3	175.9 ± 0.3	1
39.8	1570 ± 40	667 ± 6	179.8 ± 0.6	1
50.1	1890 ± 80	719 ± 11	181.2 ± 1.0	1
60.1	2200 ± 100	770 ± 15	182.6 ± 1.3	1
80.0	3500 ± 500	900 ± 40	182 ± 3	1
100.0	4700 ± 500	1000 ± 30	185.9 ± 1.9	1

Table 8-53: Fit parameters of fitting specific conductivity data of ≈ 0.05 mol L^{-1} I_2 in mixtures of $EMIBF_4$ and MPII at varying temperatures according to Eq. (5.2).

T [K]	A [mS cm^{-1}]	B_1 [mS cm^{-1} K^{-1}]	$B_2 \cdot 10^3$ [mS cm^{-1} K^{-2}]	$B_3 \cdot 10^6$ [mS cm^{-1} K^{-3}]	R^2
278.151	7.24 ± 0.09	-0.225 ± 0.010	2.7 ± 0.3	-13 ± 3	0.99992
298.151	15.76 ± 0.16	-0.362 ± 0.013	3.0 ± 0.2	-9.0 ± 1.6	0.99978
303.152	18.5 ± 0.2	-0.401 ± 0.015	3.1 ± 0.3	-9 ± 2	0.99976
313.150	24.8 ± 0.3	-0.48 ± 0.02	3.4 ± 0.5	-9 ± 3	0.99969
323.150	31.9 ± 0.4	-0.55 ± 0.03	3.5 ± 0.7	-8 ± 4	0.99962

8.2.3 EMIOTf/MPII

Table 8-54: I_2-molonities and MPII concentrations of the blends of the system EMIOTf/MPII.

Mol% MPII	10.1	19.8	30.6	40.1	50.1	60.1	80.0	100.0
$\tilde{m}$ (I_2) [mol kg^{-1}]	0.0349	0.0343	0.0396	0.0346	0.0338	0.0330	0.0324	0.0319

Table 8-55: VFT-Equation parameters of specific conductivity data of ≈ 0.05 mol L^{-1} I_2 in mixtures of EMIOTf and MPII at varying MPII concentrations.

Mol% MPII	κ_0 [mS cm^{-1}]	B [K]	T_0 [K]	R^2
10.1	1040 ± 40	689 ± 10	159.0 ± 1.4	1
19.8	1110 ± 40	707 ± 11	162.4 ± 1.1	1
40.1	1220 ± 90	720 ± 20	172 ± 2	1
50.1	1570 ± 60	775 ± 10	172.8 ± 0.9	1
60.1	1700 ± 200	790 ± 30	177 ± 3	1
80.0	1800 ± 200	790 ± 30	189 ± 3	1
100.0	4700 ± 500	1000 ± 30	185.9 ± 1.9	1

Table 8-56: Fit parameters of fitting specific conductivity data of ≈ 0.05 mol L^{-1} I_2 in mixtures of EMIOTf and MPII at varying temperatures according to Eq. (5.2).

T [K]	A [mS cm^{-1}]	B_1 [mS cm^{-1} K^{-1}]	$B_2 \cdot 10^3$ [mS cm^{-1} K^{-2}]	$B_3 \cdot 10^6$ [mS cm^{-1} K^{-3}]	R^2
278.148	4.064 ± 0.008	-0.0960 ± 0.0009	0.84 ± 0.02	-3.0 ± 0.3	1
298.151	8.66 ± 0.05	-0.144 ± 0.004	0.78 ± 0.08	-1.4 ± 0.5	0.99996
303.151	10.15 ± 0.06	-0.157 ± 0.005	0.77 ± 0.11	-1.3 ± 0.6	0.99995
313.151	13.58 ± 0.10	-0.183 ± 0.008	0.80 ± 0.18	-1.4 ± 1.1	0.99994
323.149	17.48 ± 0.13	-0.205 ± 0.010	0.8 ± 0.2	-1.6 ± 1.3	0.9999

8.2.4 $EMINTf_2$/MPII

Table 8-57: I_2-molonities and MPII concentrations of the blends of the system $EMINTf_2$/MPII.

Mol% MPII	10.0	20.0	30.0	40.0	50.0	60.0	80.0	100.0
$\tilde{m}$ (I_2) [mol kg^{-1}]	0.0324	0.0322	0.0323	0.0327	0.0322	0.0320	0.0322	0.0319

Table 8-58: VFT-Equation parameters of specific conductivity data of ≈ 0.05 mol L^{-1} I_2 in mixtures of $EMINTf_2$ and MPII at varying MPII concentrations.

Mol% MPII	κ_0 [mS cm^{-1}]	B [K]	T_0 [K]	R^2
10.0	678 ± 12	583 ± 5	166.7 ± 0.6	1
30.0	790 ± 6	631 ± 2	170.4 ± 0.2	1
40.0	913 ± 7	671 ± 2	171.5 ± 0.2	1
50.0	1058 ± 16	707 ± 4	173.4 ± 0.4	1
60.0	1310 ± 30	755 ± 6	174.7 ± 0.6	1
80.0	2400 ± 200	890 ± 20	177.3 ± 1.8	1
100.0	4700 ± 500	1000 ± 30	185.9 ± 1.9	1

Table 8-59: Fit parameters of fitting specific conductivity data of ≈ 0.05 mol L^{-1} I_2 in mixtures of $EMINTf_2$ and MPII at varying temperatures according to Eq. (5.2).

T [K]	A [mS cm^{-1}]	B_1 [mS cm^{-1} K^{-1}]	$B_2 \cdot 10^3$ [mS cm^{-1} K^{-2}]	$B_3 \cdot 10^6$ [mS cm^{-1} K^{-3}]	R^2
278.148	4.504 ± 0.010	-0.0930 ± 0.0009	0.63 ± 0.02	-1.41 ± 0.18	1
288.152	6.751 ± 0.016	-0.1219 ± 0.0016	0.71 ± 0.04	-1.4 ± 0.3	0.99999
298.149	9.48 ± 0.03	-0.148 ± 0.002	0.68 ± 0.05	-0.8 ± 0.3	0.99999
303.152	11.03 ± 0.03	-0.162 ± 0.003	0.71 ± 0.06	-0.9 ± 0.3	0.99998
313.152	14.52 ± 0.05	-0.191 ± 0.003	0.77 ± 0.08	-1.3 ± 0.5	0.99998
323.152	18.48 ± 0.06	-0.219 ± 0.004	0.88 ± 0.09	-2.0 ± 0.6	0.99998

8.3 Determination of Phase Transition Points

Determination of phase transition points was performed by evaluation of temperature and conductivity data that were simultaneously recorded during cooling and heating of the sample. The examined temperature range was typically between -80 °C and +65 °C. After finishing examination of the influence of cooling and heating rate on the determined phase transition points most of the measurements were conducted at a fixed and comparative low cooling and heating rate v of -/+ 5 K h^{-1}. That means for one cooling-heating cycle up to 12200 data points were recorded per sample. If possible, i.e. no damage or other breakdown of the measuring cell, every sample was examined at minimum three times to get reliable results. In the following paragraphs the determined phase transition points of pure ILs, blends of the electrolyte systems EMIDCA/MPII, $EMIBF_4$/MPII, EMIOTf/MPII, and $EMINTf_2$/MPII and the organic solvents dimethyl carbonate (DMC), ethylene carbonate (EC), and ethylpropionate (EP) are summarised.

8.3.1 Pure Ionic Liquids

The following tables (Table 8-60 - Table 8-63) summarise phase transition points and magnitude of supercooling of pure ILs determined at varying cooling and heating rates. For EMIDCA (Table 8-60) and Me_3SDCA (Table 8-62) values determined with T(t)-G(t)-measuring cells and T(t)-measuring cells are listed together in one table. For $EMINTf_2$ (Table 8-61) only values determined with a T(t)-measuring cell are listed, since the applied T(t)-G(t)-measuring cell was damaged during the first cooling-heating cycle. For MPII, measurements were conducted with a T(t)-G(t)-measuring cell only.

Table 8-60: Phase transition points and magnitude of supercooling of EMIDCA determined at varying cooling and heating rates.

v [K h^{-1}]	θ_f [°C]	$\Delta\theta_s$ [°C]	$\theta_{m,\,T(t)}$ [°C]	$\theta_{m,\,G(t)}$ [°C]	$\theta_{m,\,lnG}$ [°C]
2.50[a]	-	-	-5.17	-4.87	-4.65
2.50[b]	-	-	-5.54	-	-
5.00[a]	-11.86	27.50	-5.32	-4.92	-4.67
5.00[a]	-12.11	27.39	-5.33	-4.92	-4.66
5.00[b]	-13.40	42.15	-5.40	-	-
10.00[a]	-13.23	30.88	-5.37	-4.94	-4.66
10.00[a]	-12.36	28.51	-5.38	-4.95	-4.70

v [K h^{-1}]	θ_f [°C]	$\Delta\theta_s$ [°C]	$\theta_{m,\,T(t)}$ [°C]	$\theta_{m,\,G(t)}$ [°C]	$\theta_{m,\,lnG}$ [°C]
10.00[a]	-12.05	27.97	-5.36	-4.94	-4.67
10.00[b]	-16.69	38.79	-5.56	-	-
15.00[a]	-12.47	28.45	-5.42	-4.96	-4.68
15.00[a]	-12.82	28.92	-5.43	-4.96	-4.70
15.00[b]	-22.53	40.48	-5.59	-	-
30.00[a]	-12.91	28.19	-5.50	-5.00	-4.69
30.00[a]	-13.57	29.51	-5.47	-5.00	-4.71
30.00[a]	-13.31	28.94	-5.49	-4.99	-4.69
30.00[a]	-13.38	29.03	-5.48	-	-
30.00[a]	-13.00	28.69	-5.51	-5.00	-4.68
30.00[b]	-12.02	41.22	-5.45	-	-
30.00[b]	-14.52	41.72	-5.46	-	-
30.00[b]	-12.89	42.72	-5.92	-	-

[a] T(t)-G(t)-measuring cell.
[b] T(t)-measuring cell.

Table 8-61: Phase transition points and magnitude of supercooling of $EMINTf_2$ determined at varying cooling and heating rates in two different T(t)-measuring cells.

v [K h^{-1}]	θ_f [°C]	$\Delta\theta_s$ [°C]	$\theta_{m,\,T(t)}$ [°C]	θ_f [°C]	$\Delta\theta_s$ [°C]	$\theta_{m,\,T(t)}$ [°C]
2.50	-	-	-17.23	-	-	-
5.00	-19.85	16.65	-16.89	-19.73	30.44	-2.28
10.00	-19.92	16.37	-17.31	-20.89[a]	17.91[a]	-16.92[a]
10.00	-	-	-	-20.85	32.10	-2.38
15.00	-19.95	16.77	-17.63	-20.18	33.16	-2.41
30.00	-20.35	17.33	-17.85	-19.84	33.71	-2.50
30.00	-	-	-	-10.92	29.55	-2.36
30.00	-	-	-	-19.41	33.48	-2.54
30.00	-	-	-	-21.04	32.90	-2.62

[a] Not considered for calculation of mean value due.

Table 8-62: Phase transition points and magnitude of supercooling of Me_3SDCA determined at varying cooling and heating rates.

v [K h^{-1}]	θ_f [°C]	$\Delta\theta_s$ [°C]	$\theta_{m,\,T(t)}$ [°C]	$\theta_{m,\,G(t)}$ [°C]	$\theta_{m,\,lnG}$ [°C]
2.50[a]	-	-	13.25	13.79	15.37
2.50[b]	-	-	13.43	-	-
5.00[a]	13.99	9.33	13.10	13.94	15.34
5.00[a]	14.14	8.71	13.06	14.11	15.29
5.00[b]	13.56	12.87	13.23	-	-

v [K h^{-1}]	θ_f [°C]	$\Delta\theta_s$ [°C]	$\theta_{m,\,T(t)}$ [°C]	$\theta_{m,\,G(t)}$ [°C]	$\theta_{m,\,lnG}$ [°C]
10.00[a]	13.87	9.18	12.76	13.77	15.30
10.00[a]	13.89	10.20	12.75	13.50	15.34
10.00[a]	14.19	8.30	12.86	14.10	15.40
10.00[b]	13.49	13.40	12.84	-	-
15.00[a]	14.06	8.68	12.54	13.94	15.22
15.00[a]	14.21	7.73	12.71	14.03	15.42
15.00[b]	13.50	13.29	12.99	-	-
30.00[a]	14.05	8.40	12.52	13.75	15.25
30.00[a]	14.11	-	-	-	-
30.00[a]	14.14	7.24	12.20	13.74	15.28
30.00[a]	14.14	7.29	12.22	-	-
30.00[a]	14.22	7.41	12.38	13.70	15.37
30.00[b]	12.92	14.17	12.24	-	-
30.00[b]	13.19	-	-	-	-
30.00[b]	13.32	13.30	12.41	-	-

[a] T(t)-G(t)-measuring cell.
[b] T(t)-measuring cell.

Table 8-63: Phase transition points and magnitude of supercooling of MPII determined at varying cooling and heating rates.

v [K h^{-1}]	θ_f [°C]	$\Delta\theta_s$ [°C]	$\theta_{m,\,T(t)}$ [°C]	$\theta_{m,\,G(t)}$ [°C]	$\theta_{m,\,lnG}$ [°C]
2.50	-	-	16.96	17.49	18.95
5.00	-	-	15.33[b]	18.82[b]	20.00[b]
5.00	-15.95[a]	33.02	17.07	17.76	18.30
10.00	-	-	-	-	-
10.00	-	-	15.36[b]	19.33[b]	23.13[b]
10.00	-13.84[a]	30.85	17.01	18.05	18.42
15.00	-	-	-	-	-
15.00	-13.00[a]	29.8	16.80	-	-
30.00	-	-	-	-	-
30.00	-	-	-	-	-
30.00	-	-	15.91[b]	-	-
30.00	-	-	-	-	-
30.00	-	-	16.46	-	-

[a] Crystallisation during heating.
[b] Not considered for calculation of mean value due to rising halt line.

The following tables (Table 8-64 - Table 8-68) summarise phase transition points and magnitude of supercooling determined at fixed cooling and heating rate v of -/+ 5 K h^{-1}.

For $BMPlNTf_2$ and $HMINTf_2$ only one cooling and heating curve could be analysed since in both cases the measuring cell was damaged during the second cooling-heating cycle. The results for $BMPlNTf_2$ and $HMINTf_2$ are summarised in Table 8-64. In Table 8-67 values determined for two different purity grades of $EMIBF_4$ and otherwise identical measurement conditions are listed together for comparison. For EMIOTf (Table 8-69) and TOMATFA (Table 8-70) phase transition points determined with and without application of carbon fibres are listed together in one table. For these two ILs, measurements were conducted at a cooling and heating rate v of -/+ 10 K h^{-1}.

Table 8-64: Phase transition points and magnitude of supercooling of $BMPlNTf_2$ and $HMINTf_2$ determined at a cooling and heating rate v of -/+ 5 K h^{-1}.

Substance	v [K h^{-1}]	θ_f [°C]	$\Delta\theta_s$ [°C]	$\theta_{m,\,T(t)}$ [°C]	$\theta_{m,\,G(t)}$ [°C]	$\theta_{m,\,lnG}$ [°C]
$BMPlNTf_2$	5.00	-39.15	44.17	-8.46	-	-
$HMINTf_2$	5.00	-42.00[a]	40.15	-1.85	-	-

[a] Crystallisation during heating.

Table 8-65: Phase transition points and magnitude of supercooling of BMPlFAP determined at a cooling and heating rate v of -/+ 5 K h^{-1}.

v [K h^{-1}]	θ_f [°C]	$\Delta\theta_s$ [°C]	$\theta_{m,\,T(t)}$ [°C]	$\theta_{m,\,G(t)}$ [°C]	$\theta_{m,\,lnG}$ [°C]
5.00	-8.08	19.28	2.59	2.93	2.97
5.00	-8.10	18.00	2.45	2.88	2.99
5.00	-7.13	17.08	2.19	2.74	2.89
5.00	-7.41	16.76	1.93	2.58	2.92
5.00	-11.84	19.64	1.80	2.55	2.78
5.00	-10.64	18.96	1.27	2.20	2.71
5.00	-9.34	17.83	1.37	2.23	2.63

Table 8-66: Phase transition points and magnitude of supercooling of BMPlOTf determined at a cooling and heating rate v of -/+ 5 K h^{-1}.

v [K h^{-1}]	θ_f [°C]	$\Delta\theta_s$ [°C]	$\theta_{m,\,T(t)}$ [°C]	$\theta_{m,\,G(t)}$ [°C]	$\theta_{m,\,lnG}$ [°C]
5.00	-2.58	19.81	4.45	5.13	5.57
5.00	-0.49	15.66	4.36	5.17	5.56
5.00	-1.28	18.15	4.44	5.14	5.62
5.00	-2.20	17.72	4.41	5.16	5.52
5.00	-3.21	19.68	4.41	5.16	5.61
5.00	-1.46	20.36	4.43	5.23	5.65
5.00	-2.56	16.67	4.34	5.20	5.70

Table 8-67: Phase transition points and magnitude of supercooling of $EMIBF_4$ with varying purity grades determined at a cooling and heating rate v of -/+ 5 K h^{-1}.

v [K h^{-1}]	θ_f [°C]	$\Delta\theta_s$ [°C]	$\theta_{m,\,T(t)}$ [°C]	$\theta_{m,\,G(t)}$ [°C]	$\theta_{m,\,lnG}$ [°C]
5.00	-13.79[a]	49.34[a]	13.52[a]	13.82[a]	14.08[a]
5.00	-12.21[a]	48.16[a]	13.51[a]	13.83[a]	14.06[a]
5.00	-17.92[a]	52.76[a]	13.24[a]	-	14.10[a]
5.00	-7.17[b]	31.86[b]	7.26[b]	-	-
5.00	-20.40[b]	45.45[b]	7.52[b]	-	-
5.00	-23.43[b]	45.74[b]	7.10[b]	-	-

[a] $EMIBF_4$ with 23 ppm H_2O and 36 ppm Cl^-.
[b] $EMIBF_4$ with 70 ppm H_2O and 330 ppm Br^-.

Table 8-68: Phase transition points and magnitude of supercooling of $EMINTf_2$ determined at a cooling and heating rate v of -/+ 5 K h^{-1}.

v [K h^{-1}]	θ_f [°C]	$\Delta\theta_s$ [°C]	$\theta_{m,\,T(t)}$ [°C]	$\theta_{m,\,G(t)}$ [°C]	$\theta_{m,\,lnG}$ [°C]
5.00	-19.86	16.89	-16.69	-16.42	-16.32
5.00	-19.49	15.76	-16.71	-16.39	-16.31
5.00	-20.33	16.09	-16.68	-16.41	-16.30
5.00	-18.68	16.33	-16.66	-16.45	-16.33
5.00	-18.98	16.37	-16.81	-16.51	-16.35
5.00	-19.22	15.20	-17.01	-16.55	-16.30
5.00	-19.44	15.59	-17.21	-16.56	-16.34
5.00	-20.14	14.89	-17.98	-16.96	-16.47
5.00	-20.04	15.55	-17.85	-16.95	-16.37

Table 8-69: Phase transition points and magnitude of supercooling of EMIOTf and EMIOTf with added carbon fibres determined at a cooling and heating rate v of -/+ 10 K h^{-1}.

	Without carbon fibres			With carbon fibres		
v [K h^{-1}]	θ_f [°C]	$\Delta\theta_s$ [°C]	$\theta_{m,\,T(t)}$ [°C]	θ_f [°C]	$\Delta\theta_s$ [°C]	$\theta_{m,\,T(t)}$ [°C]
10.00	-12.68	5.91	-11.03	-12.07	2.82	-10.88
10.00	-12.65	6.18	-10.95	-12.50	2.89	-10.98
10.00	-12.66	6.87	-10.94	-12.94	2.71	-11.00
10.00	-12.80	6.58	-11.21	-13.18	2.50	-11.47
10.00	-13.09	5.47	-11.23	-13.19	2.89	-11.16
10.00	-12.71	4.42	-11.26	-13.34	2.62	-11.45

Table 8-70: Phase transition points and magnitude of supercooling of TOMATFA and TOMATFA with added carbon fibres determined at a cooling and heating rate v of -/+ 10 K h^{-1}.

	Without carbon fibres			With carbon fibres		
v [K h^{-1}]	θ_f [°C]	$\Delta\theta_s$ [°C]	$\theta_{m,T(t)}$ [°C]	θ_f [°C]	$\Delta\theta_s$ [°C]	$\theta_{m,T(t)}$ [°C]
10.00	-15.83[a]	28.32	12.49	-	-	-
10.00	-16.03[a]	28.46	12.43	-	-	-
10.00	-15.86[a]	28.30	12.44	-	-	-
10.00	-17.05[a]	29.54	12.49	-17.46[a]	29.79	12.33
10.00	-16.27[a]	28.79	12.52	-18.03[a]	30.41	12.38
10.00	-16.41[a]	28.90	12.49	-18.41[a]	30.75	12.34
10.00	-17.01[a]	29.58	12.57	-17.44[a]	29.92	12.48
10.00	-17.01[a]	29.61	12.60	-17.44[a]	29.95	12.51
10.00	-16.48[a]	29.09	12.61	-17.44[a]	29.95	12.51
10.00	-16.97[a]	29.65	12.68	-17.60[a]	30.06	12.46
10.00	-17.10[a]	29.79	12.69	-18.12[a]	30.59	12.47
10.00	-17.50[a]	30.16	12.66	-17.60[a]	30.08	12.48

[a] Crystallisation during heating.

8.3.2 EMIDCA/MPII

Table 8-71: I_2-molonities and MPII concentrations of the blends of the system EMIDCA/MPII.

Mol% MPII	5.4	10.9	15.1	20.8	30.6	41.0	50.5	60.7	81.0	100.0
$\tilde{m}$ (I_2) [mol kg^{-1}]	0.0485	0.0428	0.0454	0.0404	0.0396	0.0378	0.0372	0.0358	0.0331	0.0319

Table 8-72: Phase transition points of ≈ 0.05 mol L^{-1} I_2 in EMIDCA/MPII with 5.4 mol% MPII determined at a cooling and heating rate v of -/+ 5 K h^{-1}.

v [K h^{-1}]	$\theta_{fc,T(t)}$ [°C]	$\theta_{fh,T(t)}$ [°C]	$\theta_{b,T(t)}$ [°C]
5.00[a]	-43.31	-	-7.63
5.00[a]	-	-	-
5.00[a]	-	-	-

[a] No conductivity recorded.

Table 8-73: Phase transition points of ≈ 0.05 mol L^{-1} I_2 in EMIDCA/MPII with 10.9 mol% MPII determined at a cooling and heating rate *v* of -/+ 5 K h^{-1}.

v [K h^{-1}]	$\theta_{fc,\,T(t)}$ [°C]	$\theta_{fh,\,T(t)}$ [°C]	$\theta_{b,\,T(t)}$ [°C]	$\theta_{b,\,G(t)}$ [°C]	$\theta_{b,\,lnG}$ [°C]
5.00	-	-54.47	-14.66	-11.53	-14.08
5.00	-	-55.58	-14.26	-12.74	-13.84
5.00	-	-47.65	-14.26	-	-

Table 8-74: Phase transition points of ≈ 0.05 mol L^{-1} I_2 in EMIDCA/MPII with 15.1 mol% MPII determined at a cooling and heating rate *v* of -/+ 5 K h^{-1}.

v [K h^{-1}]	$\theta_{fc,\,T(t)}$ [°C]	$\theta_{fh,\,T(t)}$ [°C]	$\theta_{b,\,T(t)}$ [°C]
5.00[a]	-49.01	-	-17.09
5.00[a]	-	-	-
5.00[a]	-	-	-

[a] No conductivity recorded.

Table 8-75: Phase transition points of ≈ 0.05 mol L^{-1} I_2 in EMIDCA/MPII with 20.8 mol% MPII determined at a cooling and heating rate *v* of -/+ 5 K h^{-1}.

v [K h^{-1}]	$\theta_{fc,\,T(t)}$ [°C]	$\theta_{fh,\,T(t)}$ [°C]	$\theta_{b,\,T(t)}$ [°C]	$\theta_{b,\,G(t)}$ [°C]	$\theta_{b,\,lnG}$ [°C]
5.00	-	-	-	-	-15.16
5.00	-	-	-	-	-15.35
5.00	-	-	-	-	-

Table 8-76: Phase transition points of ≈ 0.05 mol L^{-1} I_2 in EMIDCA/MPII with 60.7 mol% MPII determined at a cooling and heating rate *v* of -/+ 5 K h^{-1}.

v [K h^{-1}]	$\theta_{fc,\,T(t)}$ [°C]	$\theta_{fh,\,T(t)}$ [°C]	$\theta_{b,\,T(t)}$ [°C]	$\theta_{b,\,G(t)}$ [°C]	$\theta_{b,\,lnG}$ [°C]
5.00	-	-	-	-	-
5.00	-	-	-	-	22.25
5.00	-	-	-	-	-

8.3.3 $EMIBF_4$/MPII

Table 8-77: Phase transition points of ≈ 0.05 mol L^{-1} I_2 in $EMIBF_4$/MPII with 10.1 mol% MPII determined at a cooling and heating rate *v* of -/+ 5 K h^{-1}.

v [K h^{-1}]	$\theta_{fc, T(t)}$ [°C]	$\theta_{fh, T(t)}$ [°C]	$\theta_{fc, G(t)}$ [°C]	$\theta_{fc, lnG}$ [°C]	$\theta_{b, T(t)}$ [°C]	$\theta_{b1, G(t)}$ [°C]	$\theta_{b2, G(t)}$ [°C]	$\theta_{b1, lnG}$ [°C]	$\theta_{b2, lnG}$ [°C]
5.00	-42.50	-	-42.50	-42.49	12.25	13.58	-	12.27	-
5.00	-42.01	-	-42.01	-42.01	12.31	13.65	-	11.84	-

Table 8-78: Phase transition points of ≈ 0.05 mol L^{-1} I_2 in $EMIBF_4$/MPII with 19.9 mol% MPII determined at a cooling and heating rate *v* of -/+ 5 K h^{-1}.

v [K h^{-1}]	$\theta_{fc, T(t)}$ [°C]	$\theta_{fh, T(t)}$ [°C]	$\theta_{fc, G(t)}$ [°C]	$\theta_{fc, lnG}$ [°C]	$\theta_{b, T(t)}$ [°C]	$\theta_{b1, G(t)}$ [°C]	$\theta_{b2, G(t)}$ [°C]	$\theta_{b1, lnG}$ [°C]	$\theta_{b2, lnG}$ [°C]
5.00	-38.37	-	-38.21	-38.22	12.96	13.72	-	12.43	-
5.00	-38.81	-	-38.81	-38.77	-	-	-	-	-

Table 8-79: Phase transition points of ≈ 0.05 mol L^{-1} I_2 in $EMIBF_4$/MPII with 30.0 mol% MPII determined at a cooling and heating rate *v* of -/+ 5 K h^{-1}.

v [K h^{-1}]	$\theta_{fc, T(t)}$ [°C]	$\theta_{fh, T(t)}$ [°C]	$\theta_{fc, G(t)}$ [°C]	$\theta_{fc, lnG}$ [°C]	$\theta_{b, T(t)}$ [°C]	$\theta_{b1, G(t)}$ [°C]	$\theta_{b2, G(t)}$ [°C]	$\theta_{b1, lnG}$ [°C]	$\theta_{b2, lnG}$ [°C]
5.00	-36.40	-	-36.40	-36.40	-9.98	-	-	-	-
5.00	-	-50.78	-	-	-9.86	-8.34	13.44	-	10.06
5.00	-	-	-	-	-	-	13.50	-	10.56
5.00	-	-50.71	-	-	-	-8.34	14.20	-	11.23
5.00	-38.76	-	-	-	-	-	14.00	-	11.38
5.00	-	-	-	-	-	-	13.65	-	10.70
5.00	-	-	-	-	-	-	9.46	-	10.24

Table 8-80: Phase transition points of ≈ 0.05 mol L^{-1} I_2 in $EMIBF_4$/MPII with 39.8 mol% MPII determined at a cooling and heating rate *v* of -/+ 5 K h^{-1}.

v [K h^{-1}]	$\theta_{fc, T(t)}$ [°C]	$\theta_{fh, T(t)}$ [°C]	$\theta_{fc, G(t)}$ [°C]	$\theta_{fc, lnG}$ [°C]	$\theta_{b, T(t)}$ [°C]	$\theta_{b1, G(t)}$ [°C]	$\theta_{b2, G(t)}$ [°C]	$\theta_{b1, lnG}$ [°C]	$\theta_{b2, lnG}$ [°C]
5.00	-	-48.80	-	-	-6.74	-4.63	9.18	-4.81	10.36
5.00	-12.64	-	-12.26	-4.87	-6.74	-5.24	11.22	-6.67	10.45

Table 8-81: Phase transition points of ≈ 0.05 mol L^{-1} I_2 in $EMIBF_4$/MPII with 50.1 mol% MPII determined at a cooling and heating rate *v* of -/+ 5 K h^{-1}.

v [K h^{-1}]	$\theta_{fc, T(t)}$ [°C]	$\theta_{fh, T(t)}$ [°C]	$\theta_{fc, G(t)}$ [°C]	$\theta_{fc, lnG}$ [°C]	$\theta_{b, T(t)}$ [°C]	$\theta_{b1, G(t)}$ [°C]	$\theta_{b2, G(t)}$ [°C]	$\theta_{b1, lnG}$ [°C]	$\theta_{b2, lnG}$ [°C]
5.00	-34.38	-	-	-	-2.48	-0.70	14.32	-2.19	15.64
5.00	-25.74	-	-25.28	-	-6.29	-	-	-1.19	-17.74

Table 8-82: Phase transition points of ≈ 0.05 mol L^{-1} I_2 in $EMIBF_4$/MPII with 60.1 mol% MPII determined at a cooling and heating rate *v* of -/+ 5 K h^{-1}.

v [K h^{-1}]	$\theta_{fc, T(t)}$ [°C]	$\theta_{fh, T(t)}$ [°C]	$\theta_{fc, G(t)}$ [°C]	$\theta_{fc, lnG}$ [°C]	$\theta_{b, T(t)}$ [°C]	$\theta_{b1, G(t)}$ [°C]	$\theta_{b2, G(t)}$ [°C]	$\theta_{b1, lnG}$ [°C]	$\theta_{b2, lnG}$ [°C]
5.00	-	-24.41	-	-	3.37	6.76	-	3.54	20.83
5.00	-	-30.49	-	-	3.07	4.65	22.58	2.61	21.94

Table 8-83: Phase transition points of ≈ 0.05 mol L^{-1} I_2 in $EMIBF_4$/MPII with 80.0 mol% MPII determined at a cooling and heating rate *v* of -/+ 5 K h^{-1}.

v [K h^{-1}]	$\theta_{fc, T(t)}$ [°C]	$\theta_{fh, T(t)}$ [°C]	$\theta_{fc, G(t}$ [°C]	$\theta_{fc, lnG}$ [°C]	$\theta_{b, T(t)}$ [°C]	$\theta_{b1, G(t)}$ [°C]	$\theta_{b2, G(t)}$ [°C]	$\theta_{b1, lnG}$ [°C]	$\theta_{b2, lnG}$ [°C]
5.00[a]	-	-34.30	-	-	7.53	-	-	-	-
5.00[a]	-	-	-	-	-	-	-	-	-

[a] No conductivity recorded.

Table 8-84: Phase transition points of ≈ 0.05 mol L^{-1} I_2 in MPII determined at a cooling and heating rate *v* of -/+ 5 K h^{-1}.

v [K h^{-1}]	$\theta_{fc, T(t)}$ [°C]	$\theta_{fh, T(t)}$ [°C]	$\theta_{fc, G(t)}$ [°C]	$\theta_{fc, lnG}$ [°C]	$\theta_{b, T(t)}$ [°C]	$\theta_{b1, G(t)}$ [°C]	$\theta_{b2, G(t)}$ [°C]	$\theta_{b1, lnG}$ [°C]	$\theta_{b2, lnG}$ [°C]
5.00	-	-30.62	-	-	16.63	17.95	-	18.55	-
5.00	-	-28.04	-	-	16.77	17.90	-	18.57	-

8.3.4 EMIOTf/MPII

Table 8-85: Phase transition points of ≈ 0.05 mol L^{-1} I_2 in EMIOTf/MPII with 10.1 mol% MPII determined at a cooling and heating rate *v* of -/+ 5 K h^{-1}.

v [K h^{-1}]	$\theta_{fh, T(t)}$ [°C]	$\theta_{b, T(t)}$ [°C]	$\theta_{b, G(t)}$ [°C]	$\theta_{b, lnG}$ [°C]
5.00	-43.88	-17.93	-15.48	-16.95
5.00	-50.94	-17.96	-15.64	-16.95
5.00	-51.22	-17.95	-15.59	-16.74

Table 8-86: Phase transition points of ≈ 0.05 mol L^{-1} I_2 in EMIOTf/MPII with 19.8 mol% MPII determined at a cooling and heating rate *v* of -/+ 5 K h^{-1}.

v [K h^{-1}]	$\theta_{fh,\ T(t)}$ [°C]	$\theta_{b,\ T(t)}$ [°C]	$\theta_{b,\ G(t)}$ [°C]	$\theta_{b,\ lnG}$ [°C]
5.00	-	-	-	-
5.00	-	-	-23.44	-23.38
5.00	-	-	-	-23.10

8.3.5 EMINTf$_2$/MPII

Table 8-87: Phase transition points of ≈ 0.05 mol L^{-1} I_2 in EMINTf$_2$/MPII with 10.0 mol% MPII determined at a cooling and heating rate *v* of -/+ 5 K h^{-1}.

v [K h^{-1}]	$\theta_{fh,\ T(t)}$ [°C]	$\theta_{fc,\ G(t)}$ [°C]	$\theta_{fh,\ G(t)}$ [°C]	$\theta_{fc,\ lnG}$ [°C]	$\theta_{fh,\ lnG}$ [°C]	$\theta_{b,\ T(t)}$ [°C]	$\theta_{b1,\ G(t)}$ [°C]	$\theta_{b2,\ G(t)}$ [°C]	$\theta_{b1,\ lnG}$ [°C]	$\theta_{b2,\ lnG}$ [°C]
5.00	-50.61	-	-	-	-	-7.18	-4.51	-3.84	-7.19	-3.81
5.00	-51.09	-	-	-	-	-7.48	-4.60	-3.90	-7.44	-4.08
5.00	-50.46	-	-	-	-	-7.13	-4.61	-4.00	-7.20	-4.24
5.00	-51.16	-	-	-	-	-7.15	-4.55	-4.05	-7.16	-4.17
5.00	-50.37	-	-	-	-	-7.24	-4.70	-4.30	-7.33	-4.33
5.00	-50.64	-	-	-	-	-7.18	-4.70	-4.11	-7.20	-4.15
5.00	-	-	-	-	-	-7.64	-4.62	-4.04	-7.50	-4.08

Table 8-88: Phase transition points of ≈ 0.05 mol L^{-1} I_2 in EMINTf$_2$/MPII with 20.0 mol% MPII determined at a cooling and heating rate *v* of -/+ 5 K h^{-1}.

v [K h^{-1}]	$\theta_{fh,\ T(t)}$ [°C]	$\theta_{fc,\ G(t)}$ [°C]	$\theta_{fh,\ G(t)}$ [°C]	$\theta_{fc,\ lnG}$ [°C]	$\theta_{fh,\ lnG}$ [°C]	$\theta_{b,\ T(t)}$ [°C]	$\theta_{b1,\ G(t)}$ [°C]	$\theta_{b2,\ G(t)}$ [°C]	$\theta_{b1,\ lnG}$ [°C]	$\theta_{b2,\ lnG}$ [°C]
5.00	-	-	-	-	-22.11	-	-	-	-	23.64
5.00	-	-	-	-	-21.47	-	-	-	-	25.89
5.00	-26.22	-	-	-	-	-10.55	-8.35	24.82	-9.84	25.34
5.00	-	-	-21.96	-	-22.38	-	-	27.26	-	27.96
5.00	-31.21	-	-	-	-	-10.76	-8.16	-	-9.75	-
5.00	-	-	-22.27	-	-22.22	-	-	25.99	-	27.60
5.00	-37.66	-	-	-	-	-10.85	-8.38	-	-10.34	-

Table 8-89: Phase transition points of ≈ 0.05 mol L^{-1} I_2 in $EMINTf_2$/MPII with 30.0 mol% MPII determined at a cooling and heating rate *v* of -/+ 5 K h^{-1}.

v [K h^{-1}]	$\theta_{fh,\,T(t)}$ [°C]	$\theta_{fc,\,G(t)}$ [°C]	$\theta_{fh,\,G(t)}$ [°C]	$\theta_{fc,\,lnG}$ [°C]	$\theta_{fh,\,lnG}$ [°C]	$\theta_{b,\,T(t)}$ [°C]	$\theta_{b1,\,G(t)}$ [°C]	$\theta_{b2,\,G(t)}$ [°C]	$\theta_{b1,\,lnG}$ [°C]	$\theta_{b2,\,lnG}$ [°C]
5.00	-	-	-7.60	-	-8.37	-	-	-	-	-
5.00	-	-	-	-	-	-	-	-	-	-
5.00	-	-	-9.82	-	-	-	-	-	-	-
5.00	-	-	-11.94	-	-	-	-	-	-	-
5.00	-	-	-	-	-	-	-	-	-	-
5.00	-	-	-	-	-	-	-23.70	-	-23.57	-
5.00	-	-	-	-	-	-23.80	-22.37	-	-23.60	-

Table 8-90: Phase transition points of ≈ 0.05 mol L^{-1} I_2 in $EMINTf_2$/MPII with 40.0 mol% MPII determined at a cooling and heating rate *v* of -/+ 5 K h^{-1}.

v [K h^{-1}]	$\theta_{fh,\,T(t)}$ [°C]	$\theta_{fc,\,G(t)}$ [°C]	$\theta_{fh,\,G(t)}$ [°C]	$\theta_{fc,\,lnG}$ [°C]	$\theta_{fh,\,lnG}$ [°C]	$\theta_{b,\,T(t)}$ [°C]	$\theta_{b1,\,G(t)}$ [°C]	$\theta_{b2,\,G(t)}$ [°C]	$\theta_{b1,\,lnG}$ [°C]	$\theta_{b2,\,lnG}$ [°C]
5.00	-		-21.51	-	-22.21	-	-	-	-	33.94
5.00	-	-	-	-	-	-	-	-	-	37.94
5.00	-	-	-	-12.85	-	-	-	38.50	-	37.90
5.00	-	7.14	-	7.22	-	-	-	-	-	36.63
5.00	-	6.93	-	6.56	-	-	-	37.96	-	35.38
5.00	-	-	-	-	-	-	-	-	-	-
5.00	-	-	-	-	-	-	-	-	-	-

Table 8-91: Phase transition points of ≈ 0.05 mol L^{-1} I_2 in $EMINTf_2$/MPII with 50.0 mol% MPII determined at a cooling and heating rate *v* of -/+ 5 K h^{-1}.

v [K h^{-1}]	$\theta_{fh,\,T(t)}$ [°C]	$\theta_{fc,\,G(t)}$ [°C]	$\theta_{fh,\,G(t)}$ [°C]	$\theta_{fc,\,lnG}$ [°C]	$\theta_{fh,\,lnG}$ [°C]	$\theta_{b,\,T(t)}$ [°C]	$\theta_{b1,\,G(t)}$ [°C]	$\theta_{b2,\,G(t)}$ [°C]	$\theta_{b1,\,lnG}$ [°C]	$\theta_{b2,\,lnG}$ [°C]
5.00	-	-	-16.08	-	-16.87	-	-	-	-	33.85
5.00	-	-	-16.10	-	-16.25	-	-	38.87	-	38.04
5.00	-	6.91	-	6.68	-	-	-	39.19	-	36.70
5.00	-	-	-15.74	-	-17.30	-	-	38.51	-	37.55
5.00	-	1.80	-	1.54	-	-	-	-	-	-
5.00	-	-	-14.28	-	-	-	-	-	-	-
5.00	-	-	-	-	-	-	-	-	-	-

Table 8-92: Phase transition points of ≈ 0.05 mol L^{-1} I_2 in $EMINTf_2$/MPII with 60.0 mol% MPII determined at a cooling and heating rate *v* of -/+ 5 K h^{-1}.

v [K h^{-1}]	$\theta_{fh, T(t)}$ [°C]	$\theta_{fc, G(t)}$ [°C]	$\theta_{fh, G(t)}$ [°C]	$\theta_{fc, lnG}$ [°C]	$\theta_{fh, lnG}$ [°C]	$\theta_{b, T(t)}$ [°C]	$\theta_{b1, G(t)}$ [°C]	$\theta_{b2, G(t)}$ [°C]	$\theta_{b1, lnG}$ [°C]	$\theta_{b2, lnG}$ [°C]
5.00	-	-	-	-	-22.10	-	-	-	-	34.51
5.00	-	-	-	-	-	-	-	-	-	-
5.00	-	6.93	-	6.62	-	-	-	-	-	33.38
5.00	-	-	-	-	-21.25	-	-	34.35	-	35.93
5.00	-	12.86	-	12.40	-	-	-	34.50	-	34.54
5.00	-	-	-	-	-	-	-	-	-	36.72
5.00	-	10.32	-	10.28	-	-	-	-	-	33.87

Table 8-93: Phase transition points of ≈ 0.05 mol L^{-1} I_2 in $EMINTf_2$/MPII with 80.0 mol% MPII determined at a cooling and heating rate *v* of -/+ 5 K h^{-1}.

v [K h^{-1}]	$\theta_{fh, T(t)}$ [°C]	$\theta_{fc, G(t)}$ [°C]	$\theta_{fh, G(t)}$ [°C]	$\theta_{fc, lnG}$ [°C]	$\theta_{fh, lnG}$ [°C]	$\theta_{b, T(t)}$ [°C]	$\theta_{b1, G(t)}$ [°C]	$\theta_{b2, G(t)}$ [°C]	$\theta_{b1, lnG}$ [°C]	$\theta_{b2, lnG}$ [°C]
5.00	-	-	-	-	-	-	-	-	-	-
5.00	-	-	2.82	-	2.88	-	-	17.67	-	18.83
5.00	-	-	0.11	-	0.05	-	-	17.78	-	18.36
5.00	-	-	-1.28	-	-1.67	-	-	-	-	18.29
5.00	-	-	-	-	-	-	-	-	-	-
5.00	-	-	-	-	-	-	-	-	-	-
5.00	-	-	-	-	-	-	-	-	-	-

8.3.6 Organic Solvents

The three organic solvents dimethyl carbonate (DMC, 45 ppm H_2O, *Merck* selectipur®), ethylene carbonate (EC, *Merck* selectipur®), and ethylpropionate (EP, 160 ppm H_2O, *Merck* selectipur®) are frequently used components for formulation of electrolytes for Li-ion-batteries. They were examined to complete previous studies of phase transition points of organic solvents [103,107] and to optimize the measuring procedures with regard to the later examined ILs. DMC and EC were examined with and without addition of carbon fibres as crystallisation aids, EP with added carbon fibres only. Melting points of DMC with and without added carbon fibres are clearly lower and show larger deviations than the corresponding freezing points. The mean values and corresponding standard deviations for all solvents are summarized in Table 8-94.

Table 8-94: Mean values of freezing θ_f and melting points θ_m with corresponding standard deviations, supercooling $\Delta\theta_s$, and literature values $\theta_{f,\,lit}$ and $\theta_{m,\,lit}$.

Substance	θ_f [°C]	$\theta_{f,\,lit}$ [°C]	$\Delta\theta_s$ [°C]	θ_m [°C]	$\theta_{m,\,lit}$ [°C]
DMC	4.46 ± 0.06	4.61 ± 0.1 [134]	1.9 ± 0.6	3.9 ± 0.3	4.6 [176]
DMC[a]	4.03 ± 0.14	-	0.49 ± 0.09	2.4 ± 0.7	-
EC	35.68 ± 0.18	36.35 ± 0.1 [134]	23 ± 3	35.38 ± 0.13	36.6 [177]
EC[a]	35.97 ± 0.09	-	5 ± 3	35.54 ± 0.10	-
EP[a]	-	-	-	-73.44 ± 0.03	-73.9 [178]

[a] With addition of carbon fibres as crystallisation aids.

Table 8-95: Phase transition points and magnitude of supercooling of DMC determined at varying cooling and heating rates.

v [K h^{-1}]	θ_f [°C]	$\Delta\theta_s$ [°C]	θ_m [°C]	θ_f [°C]	$\Delta\theta_s$ [°C]	θ_m [°C]	θ_f [°C]	$\Delta\theta_s$ [°C]	θ_m [°C]
30.00	4.54	2.30	4.20	4.52	3.19	3.89	4.46	2.20	3.63
30.00	4.53	2.44	4.14	4.50	2.40	3.97	4.46	1.75	3.81
30.00	4.52	2.14	4.14	4.48	1.73	4.05	4.47	2.36	3.65
30.00	4.48	1.11	4.13	4.49	2.16	4.07	4.46	2.21	3.72
30.00	4.51	2.44	4.17	4.48	2.16	4.13	4.39	0.79	3.86
30.00	4.53	1.75	4.13	4.48	2.64	3.90	4.35	1.39	4.00
30.00	4.48	1.25	4.10	4.49	2.50	4.04	4.38	1.09	3.81
30.00	4.50	1.48	4.04	4.49	2.70	3.72	4.39	1.55	4.00
30.00	4.52	2.32	4.12	4.47	2.12	3.88	4.38	1.70	3.61
30.00	4.52	2.61	4.17	4.42	0.79	4.05	4.42	2.02	3.43
30.00	4.50	1.30	4.09	4.48	2.27	3.69	4.35	0.90	3.94
30.00	4.50	2.11	4.09	4.48	2.54	3.69	4.40	2.81	3.45
30.00	4.51	1.87	4.04	4.43	2.38	3.94	4.40	1.97	3.37
30.00	4.45	1.14	4.12	4.41	1.23	3.93	4.34	1.34	3.73
30.00	4.54	2.30	4.20	4.47	2.40	3.77	4.38	1.89	3.48
30.00	4.53	2.44	4.14	4.47	1.99	3.70	4.39	1.85	3.50
30.00	4.52	2.14	4.14	4.46	1.67	3.84	4.32	1.03	3.65
10.00	4.53	1.28	4.36	4.55	2.31	4.38	4.45	2.79	3.65
10.00	4.53	1.39	4.36	4.54	2.04	4.24	4.42	2.28	4.04
10.00	4.51	1.18	4.37	4.47	2.17	3.64	4.39	2.56	3.86
10.00	4.54	2.03	4.36	4.46	2.47	3.67	4.40	2.57	3.63

Table 8-96: Phase transition points and magnitude of supercooling of DMC with added carbon fibres determined at varying cooling and heating rates.

v [K h^{-1}]	θ_f [°C]	$\Delta\theta_s$ [°C]	θ_m [°C]	θ_f [°C]	$\Delta\theta_s$ [°C]	θ_m [°C]	θ_f [°C]	$\Delta\theta_s$ [°C]	θ_m [°C]
30.00	4.23	0.52	3.82	4.04	0.63	2.12	4.00	0.47	3.07
30.00	4.15	0.44	2.92	4.06	0.47	2.66	4.02	0.53	2.67
30.00	4.14	0.39	2.98	4.14	0.75	2.25	3.95	0.59	2.36
30.00	4.18	0.59	3.51	4.02	0.51	1.90	3.97	0.50	2.35
30.00	4.12	0.38	2.66	4.01	0.49	2.22	3.95	0.76	1.23
30.00	4.13	0.45	3.68	4.01	0.40	2.11	3.96	0.45	2.38
30.00	4.11	0.52	2.74	4.07	0.56	2.58	3.91	0.58	2.67
30.00	4.08	0.59	2.71	4.06	0.53	2.76	3.86	0.38	2.58
30.00	4.10	0.50	2.57	4.05	0.60	2.42	3.91	0.64	2.21
30.00	4.12	0.61	2.10	4.05	0.54	2.64	3.88	0.51	1.70
30.00	4.07	0.55	2.42	4.01	0.27	2.33	3.83	0.40	2.16
30.00	4.02	0.42	2.52	4.05	0.50	1.78	3.88	0.57	2.72
30.00	4.08	0.56	2.72	4.06	0.60	3.70	3.84	0.47	1.60
30.00	4.02	0.46	2.70	4.03	0.51	2.02	3.85	0.39	1.21
30.00	4.23	0.52	3.82	4.02	0.49	2.45	3.89	0.56	2.39
30.00	4.15	0.44	2.92	3.98	0.50	1.59	3.87	0.50	2.18
30.00	4.14	0.39	2.98	4.02	0.55	1.81	3.83	0.47	1.41
10.00	4.42	0.40	3.97	4.25	0.37	2.85	3.93	0.43	1.67
10.00	4.39	0.45	3.78	4.24	0.40	3.05	3.90	0.47	2.00
10.00	4.35	0.42	3.31	3.99	0.42	2.18	3.86	0.44	1.13
10.00	4.30	0.40	3.52	3.89	0.41	1.52	3.87	0.33	0.69

Table 8-97: Phase transition points and magnitude of supercooling of EC determined at varying cooling and heating rates.

v [K h^{-1}]	θ_f [°C]	$\Delta\theta_s$ [°C]	θ_m [°C]	θ_f [°C]	$\Delta\theta_s$ [°C]	θ_m [°C]	θ_f [°C]	$\Delta\theta_s$ [°C]	θ_m [°C]
30.00	35.69	23.16	35.23	-	-	35.56	-	-	35.58
30.00	-	-	35.36	-	-	35.52	35.55	24.59	35.19
30.00	-	-	35.31	-	-	35.47	-	-	35.33
30.00	-	-	35.50	-	-	35.42	-	-	35.37
30.00	-	-	35.48	35.76	19.98	35.21	-	-	35.32
30.00	-	-	35.45	-	-	35.21	-	-	35.51
30.00	-	-	35.35	-	-	35.31	-	-	35.40
30.00	35.79	23.96	35.50	-	-	35.48	-	-	35.52
30.00	-	-	35.44	-	-	35.51	35.23	24.94	35.03
30.00	-	-	35.35	-	-	35.38	-	-	35.28

v [K h^{-1}]	θ_f [°C]	$\Delta\theta_s$ [°C]	θ_m [°C]	θ_f [°C]	$\Delta\theta_s$ [°C]	θ_m [°C]	θ_f [°C]	$\Delta\theta_s$ [°C]	θ_m [°C]
30.00	-	-	35.43	-	-	35.47	-	-	35.38
30.00	-	-	35.40	35.64	28.67	35.25	-	-	35.47
30.00	-	-	35.49	-	-	35.42	-	-	35.52
30.00	-	-	35.53	-	-	35.42	-	-	35.59
30.00	35.97	21.79	35.16	-	-	35.42	-	-	35.49
30.00	-	-	35.28	-	-	35.50	-	-	-
30.00	-	-	35.22	-	-	35.46	-	-	-
10.00	-	-	-	35.85	23.21	35.49	35.35	16.62	35.21
10.00	-	-	-	35.81	20.86	35.44	35.67	27.21	35.22
10.00	-	-	-	35.65	20.02	35.34	35.71	22.72	35.18
10.00	35.80	23.64	35.61	35.75	26.27	35.19	35.68	22.96	35.16

Table 8-98: Phase transition points and magnitude of supercooling of EC with added carbon fibres determined at varying cooling and heating rates.

v [K h^{-1}]	θ_f [°C]	$\Delta\theta_s$ [°C]	θ_m [°C]	θ_f [°C]	$\Delta\theta_s$ [°C]	θ_m [°C]	θ_f [°C]	$\Delta\theta_s$ [°C]	θ_m [°C]
30.00	36.02	7.94	35.48	-	-	35.62	-	-	35.57
30.00	35.82	0.74	35.51	-	-	35.50	35.97	5.79	35.37
30.00	35.79	0.46	35.55	-	-	35.47	-	-	35.68
30.00	35.85	0.70	35.54	-	-	35.39	-	-	35.35
30.00	35.89	0.66	35.68	35.93	6.26	35.54	-	-	35.32
30.00	35.89	0.44	35.61	-	-	35.47	-	-	35.51
30.00	35.82	0.35	35.53	-	-	35.53	-	-	35.49
30.00	36.04	5.78	35.57	-	-	35.54	-	-	35.51
30.00	-	-	35.63	-	-	35.51	35.94	7.13	35.59
30.00	-	-	35.55	-	-	35.62	-	-	35.43
30.00	-	-	35.56	-	-	35.58	-	-	35.47
30.00	-	-	35.59	36.00	6.80	35.57	-	-	35.51
30.00	-	-	35.32	-	-	35.56	-	-	35.54
30.00	-	-	35.52	-	-	35.43	-	-	35.57
30.00	35.95	6.82	35.40	-	-	35.49	-	-	35.49
30.00	-	-	35.45	-	-	35.54	-	-	-
30.00	-	-	35.46	-	-	35.57	-	-	-
10.00	36.06	3.98	35.87	36.06	6.04	35.76	35.98	5.85	35.56
10.00	36.06	3.92	35.72	36.03	5.92	35.66	35.98	6.19	35.55
10.00	36.07	3.50	35.71	36.01	5.92	35.55	35.96	4.19	35.59
10.00	36.11	9.56	35.50	35.90	4.35	35.56	36.02	4.44	35.51

Table 8-99: Phase transition points and magnitude of supercooling of EP with added carbon fibres determined at cooling and heating rate *v* of -/+ 10 K h^{-1}.

v [K h^{-1}]	θ_f [°C]	$\Delta\theta_s$ [°C]	θ_m [°C]	θ_f [°C]	$\Delta\theta_s$ [°C]	θ_m [°C]	θ_f [°C]	$\Delta\theta_s$ [°C]	θ_m [°C]
10.00	-	-	-	-	-	-73.40	-	-	-73.44
10.00	-	-	-	-	-	-73.47	-	-	-73.43
10.00	-	-	-73.49	-	-	-73.42	-	-	-73.45
10.00	-	-	-73.42	-	-	-73.43	-	-	-73.47
1.50	-	-	-73.41	-	-	-	-	-	-

8.4 Abbreviations and Acronyms

a.c.	alternating current
AN	acetonitrile
BAS	Bioanalytical Systems
$BMIBF_4$	1-butyl-3-methylimidazolium tetrafluoroborate
BMPlFAP	1-butyl-1-methylpyrrolidinium tris(pentafluoroethyl)trifluoro phosphate
BMPlNTf2	1-butyl-1-methylpyrrolidinium bis(trifluoromethylsulfonyl) imide
BMPlOTf	1-butyl-1-methylpyrrolidinium trifluoromethanesulfonate
CV	cyclic voltammetry
CE	counter electrode
DMC	dimethyl carbonate
DSC	differential scanning calorimetry
DSSC	dye-sensitised solar cell
DTA	differential thermal analysis
EC	ethylene carbonate
$EMIBF_4$	1-ethyl-3-methylimidazolium tetrafluoroborate
EMIDCA	1-ethyl-3-methylimidazolium dicyanamide
EMII	1-ethyl-3-methylimidazolium iodide
$EMII_3$	1-ethyl-3-methylimidazolium triiodide
$EMINTf_2$	1-ethyl-3-methylimidazolium bis(trifluoromethyl sulfonyl)imide
EMIOTf	1-ethyl-3-methylimidazolium trifluoromethanesulfonate
EP	ethylpropionate
$HMINTf_2$	1-hexyl-3-methylimidazolium bis(trifluoromethyl sulfonyl)imide
IL	ionic liquid
Me_3SDCA	trimethylsulfonium dicyanamide
MPIDCA	1-methyl-3-propyl¬imidazolium dicyanamide
MPII	1-methyl-3-propyl¬imidazolium iodide
$MPII_3$	1-methyl-3-propyl¬imidazolium triiodide

NMR	nuclear magnetic resonance
RE	reference electrode
SEM	scanning electrode microscopy
TCO	transparent conducting oxide
$TEABF_4$	tetraethylammonium tetrafluoroborate
TLC	thin layer cell
TOMATFA	trioctylmethylammonium trifluoroacetate
VFT	Vogel-Fulcher-Tamann
WE	working electrode

8.5 Physical Constants and Symbols

Physical Constants

Symbol	*Name*	*Value*
N_A	Avogadro constant	$6.0221 \cdot 10^{23}$ mol^{-1}
k	Boltzmann constant	$1.38065 \cdot 10^{-23}$ J K^{-1}
F	Faraday constant	96485 C mol^{-1}
R	gas constant	8.314 J K^{-1} mol^{-1}
e_0	unit of electron charge, charge of electron	$1.6022 \cdot 10^{-19}$ C

Main Symbols

Symbol	*Name*	*SI-Unit*
E_a	activation energy	J mol^{-1}
ω	angular frequency	s^{-1}
A	area	m^2
θ_b	breaking point	°C
C	capacitance	F = A s V^{-1}
B	cell constant	m^{-1}
r_c	cell radius	m
z	charge number of ions	-
G	conductance	S
v	cooling or heating rate	K h^{-1}
f	degree of freedom	-
ρ	density	Kg m^{-3}
D	diffusion coefficient	m² s^{-1}
x	distance	m
z	distance normal to the electrode	m
η	dynamic viscosity	Pa s
i, I	electric current	A

Symbol	*Name*	*SI-Unit*
E	electric field	V m^{-1}
Φ	electric potential	V
n_e	electrochemical valency	-
r_0	electrode radius	m
Λ	equivalent conductivity (electrolyte)	S m^2 mol^{-1}
λ	equivalent conductivity (ion)	S m^2 mol^{-1}
h_l	fill level	m
Δz	fluctuation of the mean coordination number	-
J	flux	mol m^{-2} s^{-1}
F	force	N = kg m s^{-2}
m	fragility (index)	-
θ_f	freezing point	°C
T_g	glass transition temperature	K
T_0	ideal glass transition temperature	K
Φ_i	incident optical power	W = V A
u	ion mobility	m^2 s^{-1} V^{-1}
l, l_0	length, path length, step length	m
z_0	mean coordination number	-
$\overline{\Delta}^2$	mean square of displacement	m^2
t	measurement time	s
θ_m	melting point	°C
$\overline{m}$	molality	mol kg^{-1}
M	molar mass	kg mol^{-1}
x	molar ratio	-, %
c	molarity	mol m^{-3}
$\tilde{m}$	molonity	mol kg^{-1}
δ	Nernst-diffusion layer	m
n	number of electrons participating in a reaction	-
m	number of time units	-
R	ohmic resistance	Ω

Symbol	***Name***	***SI-Unit***
P	power	W = V A
r	radial distance	m
R_i	radius of the ion	m
τ	relaxation time	s
v	scan/sweep rate	$V\ s^{-1}$
η_{sol}	solar efficiency	-
κ	specific conductivity	$S\ m^{-1}$
ρ	specific resistance	Ω m
σ	standard deviation	-
i_{ss}	steady-state current	A
ν	stoichiometric coefficients	-
D	strength (index)	-
$\Delta\theta_s$	supercooling	°C
T, Θ	temperature	K, °C
τ	time unit	s
$\vec{v}$	velocity	$m\ s^{-1}$
U, E	voltage/potential	V
V	volume	m^3

8.6 Figures

8.7 Tables

9 References

[1] www.stern.de.

[2] www.shell.com.

[3] www.bp.com.

[4] M. Grätzel, *Nature*, **414,** 338 (2001).

[5] N. Vlachopoulos, P. Liska, J. Augustynski, M. Grätzel, *J. Am. Chem. Soc.*, **110**, 1216 (1988).

[6] B. O'Regan, M. Grätzel, *Nature*, **353,** 737 (1991).

[7] http://www.solarserver.de/.

[8] http://emsolar.ee.tu-berlin.de/allgemein/enamort.html.

[9] M. Grätzel, *J. Photochem. Photobiol. A*, **164,** 3 (2004).

[10] Literature investigation with SciFinder Scholar 2006, direct hits for topic: "dye-sensitised solar cell" (duplicates removed).

[11] R. Martin, in: E. Hering, R. Martin (Eds.), *Photonik*, Springer, Berlin, Heidelberg, New York (2006).

[12] R. Kern, *dissertation*, Freiburg i. Brsg. (2001).

[13] A. Hinsch, S. Behrens, M. Berginc, H. Bönnemann, H. Brandt, A. Drewitz, F. Einsele, D. Faßler, D. Gerhard, H. Gores, T. Herzig, S. Himmler, G. Khelashvili, D. Koch, G. Nasmudinova, U. Opara-Krašovec, P. Putyra, U. Rau, R. Sastrawan, T. Schauer, C. Schreiner, S. Sensfuß, C. Siegers, K. Skupien, P. Wachter, J. Walter, P. Wasserscheid, U. Würfel, M. Zistler, „*Material development for dye solar modules; results from an integrated approach", Prog. Photovolt.: Res. Appl.*, in press.

[14] K. Tennakone, G. R. R. A. Kumara, I. R. M. Kottegoda, V. P. S. Perera, *Chem. Commun.*, 15 (1999).

[15] K. Sayama, H. Sugihara, H. Arakawa, *Chem. Mater.*, **10,** 3825 (1998).

[16] G. Kron, T. Egerter, J. H. Werner, U. Rau*, J. Phys. Chem. B*, **107,** 3556 (2003).

[17] Y. Tachibana, J. E. Moser, M. Grätzel, J. Z. Zhang, *J. Phys. Chem. B,* **100,** 20056 (1997).

[18] N. J. Cherepy, G. P. Smestad, M. Grätzel, J. Z. Zhang, *J. Phys. Chem. B*, **101,** 9342 (1997).

[19] M. Hilgendorff, V. Sundström, *J. Phys. Chem. B*, **102,** 10505 (1998).

[20] F. Cao, G. Oskam, G. J. Meyer, P. C. Searson, *J. Phys. Chem. B*, **100,** 17021 (1996).

[21] A. Hagfeldt, M. Grätzel, *Acc. Chem. Res.*, **33,** 269 (2000).

[22] A. Hauch, A. Georg, *Electrochim. Acta*, **46**, 3457 (2001).

[23] N. Papageorgiou, M. Grätzel, *Sol. Energy Mater. Sol. Cells*, **44,** 405 (1996).

[24] G. Kron, *dissertation*, Stuttgart (2003).

[25] M. Grätzel, *Inorg. Chem.*, **44**, 6841 (2005).

[26] G. Kron, T. Egerter, G. Nelles, A. Yasuda, J. H. Werner, U. Rau, *Thin Solid Films*, **403-404**, 242 (2002).

[27] P. Wachter, M. Zistler, C. Schreiner, M. Berginc, U. Opara Krašovec, D. Gerhard, P. Wasserscheid, A. Hinsch, H. J. Gores, *J. Photochem. Photobiol. A*, available online, doi:10.1016/j.jphotochem.2007.12.001, (2007).

[28] P. Wang, S. M. Zakeeruddin, J.-E. Moser, R. Humphry-Baker, M. Grätzel, *J. Am. Chem. Soc*., **126**, 7164 (2004).

[29] S. Nakade, Y. Makimoto, W. Kubo, T. Kitamaru, Y. Wada, S. Yanagadi, *J. Phys. Chem. B*, **109,** 3488 (2005).

[30] B. Mahrov, A. Hagfeldt, F. Lenzmann, G. Boschloo, *Sol. Energy Mat. & Sol. Cells*, **88,** 351 (2005).

[31] Q.-B. Meng, K. Takahashi, X.-T. Zhang, I. Sutanto, T. N. Rao, O. Sato, A. Fujishima, H. Watanabe, T. Nakamori, M. Uragami, *Langmuir*, **19,** 3572 (2003).

[32] R. Kawano, H. Matsui, C. Matsuyama, A. Sato, Md. A. B. H. Susan, N. Tanabe, M. Watanabe, *J. Photochem. Photobiol. A*, **164,** 87 (2004).

[33] A. Hinsch, J. M. Kroon, R. Kern, I. Uhlendorf, J. Holzbock, A. Meyer, J. Ferber, *Prog. Photovolt.*, **9**, 425 (2001).

[34] N. Papageorgiou, Y. Athanassov, M. Armand, P. Bonhôte, H. Petterson, A. Azam, M. Grätzel, *J. Electrochem. Soc.*, **143**, 3099 (1996).

[35] N. Yamanaka, R. Kawano, W. Kubo, T. Kitamura, Y. Wada, M. Watanabe, S. Yanagida, *Chem. Commun.*, 740 (2005).

[36] Q. Dai, D. R. MacFarlane, P. C. Howlett, M. Forsyth, *Angew. Chem. Int. Ed.*, **44**, 313 (2005).

[37] W. Kubo, S. Kambe, S. Nakade, T. Kitamura, K. Hanabusa, H. Shirai, Y. Wada, S. Yanagida, *J. Phys. Chem. B*, **107**, 4374 (2003).

[38] S. M. Zakeeruddin, P. Liska, M. Grätzel, *Chem. Mater.*, **15**, 1825 (2003).

[39] P. Wang, S. M. Zakeeruddin, P. Comte, I. Exnar, M. Grätzel, *J. Am. Chem. Soc.*, **125**, 1166 (2003).

[40] T. Kato, A. Okazaki, S. Hayase, *Chem. Commun.*, 363 (2005).

[41] W. Kubo, T. Kitamura, K. Hanabusa, Y. Wada, S. Yanagida, *Chem. Commun.*, 374 (2002).

[42] W. Kubo, K. Murakoshi, T. Kitamura, S. Yoshida, M. Haruki, K. Hanabusa, H. Shirai, Y. Wada, S. Yanagida, *J. Phys. Chem. B*, **105**, 12809 (2001).

[43] P. Wang, S. M. Zakeeruddin, J. E. Moser, M. Nazeeruddin, T. Sekiguchi, M. Grätzel, *Nature Materials*, **21**, 402 (2003).

[44] A. F. Nogueira, J. R. Durrant, M. A. De Paoli, *Adv. Mater.*, **13**, 826 (2001).

[45] W. Li, J. Kang, X. Li, S. Fang, Y. Lin, G. Wang, X. Xiao, *J. Photochem. Photobiol. A*, **170**, 1 (2005).

[46] F. Cao, G. Oskam, P. C. Searson, *J. Phys. Chem.*, **99**, 17071 (1995).

[47] P. Wasserscheid, W. Keim, *Angew. Chem.*, **112**, 3926 (2000).

[48] M. Galiński, A. Lewandowski, I. Stępniak, *Electrochim. Acta*, **51**, 5567 (2006).

[49] F. Mazille, Z. Fei, D. Kuang, D. Zhao, S. M. Zakeeruddin, M. Grätzel, P. J. Dyson, *Inorg. Chem*., **45,** 1585 (2006).

[50] J. Ferber, R. Stangl, J. Luther, *Sol. Energy Mater. Sol. Cells*, **53**, 29 (1998).

[51] N. Papageorgiou, *Coord. Chem. Rev.*, **248**, 1421 (2004).

[52] T. Asano, T. Kubo, Y.Nishikitani, *Jpn. J. Appl. Phys.,* **44**, 6776 (2005).

[53] U. Rau, M. Hlusiak, T. Kirchartz, F. Einsele, *"Modelling and characterization of dye sensitized solar cells (DSSCs)"*, BMBF-network-project DSSC-Meeting, 23.03.07, Freiburg.

[54] M. Zistler, *dissertation*, Regensburg (2008).

[55] D. Kuang, P. Wang, S. Ito, S. M. Zakeeruddin, M. Grätzel, *J. Am. Chem. Soc.*, **128**, 7732 (2006).

[56] P. Wang, B. Wenger, R. Humphry-Baker, J.-E. Moser, J. Teuscher, W. Kantlehner, J. Mezger, E. V. Stoyanov, S. M. Zakeeruddin, M. Grätzel, *J. Am. Chem. Soc.*, **127**, 6850 (2005).

[57] P. Wachter, C. Schreiner, M. Zistler, D. Gerhard, P. Wasserscheid, H. J. Gores, *Microchim. Acta*, **160**, 125 (2008).

[58] M. Zistler, P. Wachter, C. Schreiner, M. Fleischmann, D. Gerhard, P. Wasserscheid, A. Hinsch, H. J. Gores, *J. Electrochem. Soc.*, **154**, B925 (2007).

[59] M. Berginc, U. Opara Krašovec, M. Jankovec, M. Topič, *Sol. Energy Mat. & Sol. Cells*, **91**, 821 (2007).

[60] R. Wachter, J. Barthel, *Ber. Bunsenges. Phys. Chem.*, **83**, 634 (1979).

[61] J. Barthel, R. Wachter, H. J. Gores, in: B. E. Conway, J. O'M. Bockris (Eds.), *Modern Aspects of Electrochemistry*, Vol. 13, Chap. 1, Plenum, New York (1979).

[62] J. Barthel, H. J. Gores, in: J. O. Besenhard (Ed.), *Handbook of Battery Materials*, Wiley-VCH, Weinheim (1998).

[63] J. Barthel, H. J. Gores, in: G. Mamantov, A. I. Popov (Eds.), *Chemistry of Nonaqueous Solutions – Current Progress*, VCH, New York (1994).

[64] K. Izutsu, *Electrochemistry in Nonaqueous Solutions*, Wiley-VCH, Weinheim (2002).

[65] J. Barthel, H. Krienke, W. Kunz, *Physical Chemistry of Electrolyte Solutions*, Steinkopff - Springer, Darmstadt, Berlin (1998).

[66] C. H. Hamann, W. Vielstich, *Elektrochemie*, Wiley-VCH, Weinheim (2005).

[67] H. Ohno, M. Yoshizawa, *Solid State Ionics*, **154-155**, 303 (2002).

[68] A. Noda, K. Hayamizu, M. Watanabe, *J. Phys. Chem. B*, **105**, 4603 (2001).

[69] H. A. Every, A. G. Bishop, D. R. MacFarlane, G. Orädd, M. Forsyth, *Phys. Chem. Chem. Phys.*, **6**, 1758 (2004).

[70] P. Bonhôte, A.-P. Dias, N. Papageorgiou, K. Kalyanasundaram, M. Grätzel, *Inorg. Chem.*, **35**, 1168 (1996).

[71] H. A. Every, A. G. Bishop, M. Forsyth, D. R. MacFarlane, *Electrochim. Acta*, **45**, 1279 (2000).

[72] J. O'M. Bockris, A. K. Reddy, *Modern Aspects of Electrochemistry*, Vol. 1, Plenum, New York (1979).

[73] B. J. Alder, T. Einwohner, *J. Chem. Phys.*, **43**, 3399 (1965).

[74] J. Barthel, R. Gerber, H. J. Gores, *Ber. Bunsenges. Phys. Chem.*, **88**, 616 (1984).

[75] H. Vogel, *Phys. Z.*, **22**, 645 (1921).

[76] G. S. Fulcher, *J. Am. Ceram. Soc.*, **8**, 339 (1925).

[77] G. Tamann, W. Hesse, *Z. Anorg. All. Chem.*, **156**, 245 (1926).

[78] G. Adam, J. H. Gibbs, *J. Chem. Phys.*, **43**, 139 (1965).

[79] G. S. Crest, M. H. Cohen, in: I. Prigogine, S. A. Rice (Eds.), *Advances in Chemical Physics*, Vol. 48, Wiley & Sons, New York (1981).

[80] G. S. Crest, M. H. Cohen, in: T. Ashworth, D. R. Smith (Eds.), *Thermal Conductivity*, Vol. 18, Plenum Press, New York (1985).

[81] C. A. Angell, *J. Phys. Chem. Solids*, **49**, 863 (1988).

[82] C. A. Angell, *J. Noncryst. Solids*, **131**, 13 (1991).

[83] C. A. Angell, *Science*, **267**, 1924 (1995).

[84] R. Böhmer, K. L. Ngai, C. A. Angell, D. J. Plazek, *J. Chem. Phys.*, **99**, 4201 (1993).

[85] H. J. Gores, *postdoctoral lecture qualification thesis*, Regensburg (1997).

[86] W. Xu, E. I. Cooper, C. A. Angell, *J. Phys. Chem. B*, **107**, 6170 (2003).

[87] J. Barthel, R. Neueder, *Electrolyte Data Collection*, Dechema, Frankfurt (1999).

[88] T. A. Vilgis, *Phys. Rev. B*, **47**, 2882 (1993).

[89] A. J. Bard, L. R. Faulkner, *Electrochemical Methods: Fundamentals and Applications, 2nd ed.*, Wiley, New York (2001).

[90] R. A. Robinson, R. H. Stokes, *Electrolyte Solutions*, Butterworths, London (1959).

[91] P. W. Atkins, *Physikalische Chemie,* VCH, Weinheim (1996).

[92] R. A. Robinson, R. H. Stokes, *Annu. Rev. Phys. Chem*., **8,** 37 (1957).

[93] H. J. Hanson, C. W. Tobias, *J. Electrochem. Soc.,* **134**, 2204 (1987).

[94] C. F. T. de Grotthuss, *Ann. Chim.,* **58,** 54 (1806).

[95] R. Kawano, M. Watanabe, *Chem. Commun.*, 2107 (2005).

[96] N. Yamanaka, R. Kawano, W. Kubo, T. Kitamura, Y. Wada, M. Watanabe, S. Yanagida, *J. Phys. Chem. B*, **111**, 4763 (2007).

[97] I. Ruff, V. J. J. Friedrich, *Phys. Chem.*, **75**, 3297 (1971).

[98] H. J. Dahms, *Phys. Chem.*, **72**, 362 (1968).

[99] I. Ruff, L. J. Botár, *Chem. Phys.*, **83**, 1292 (1985).

[100] E. L. Skau, C. A. Arthur, Jr., in: A. Weissberger, B. W. Rossiter (Eds.), *Physical Methods of Chemistry*, Vol. 1, Part V, Wiley-Interscience, New York (1971).

[101] M. P. Mathieu, *Bul. Soc. Chim. Belges*, **63**, 333 (1954).

[102] H. Hammer, *diploma thesis*, Saarbrücken (1970).

[103] H.-G. Schweiger, *dissertation*, Regensburg (2004).

[104] M. S. Ding, K. Xu, T. R. Jow, *J. Therm. Anal. Cal.*, **62**, 177 (2000).

[105] M. S. Ding, K. Xu, T. R. Jow, *J. Electrochem. Soc.*, **147**, 1688 (2000).

[106] M. S. Ding, K. Xu, S. Zhang, T. R. Jow, *J. Electrochem. Soc.*, **148**, A299 (2001).

[107] P. Wachter, *diploma thesis*, Regensburg (2005).

[108] P. Wachter, H.-G. Schweiger, F. Wudy, H. J. Gores, *J. Chem. Thermodyn.*, submitted.

[109] H. L. Ngo, K. LeCompte, L. Hargens, A. B. McEwen, *Thermochim. Acta*, **357-358**, 97 (2000).

[110] D. H. Andrews, G. T. Kohman, J. Johnston, *J. Phys. Chem.*, **29**, 914 (1925).

[111] A. R. Glasgow, Jr., G. S. Ross, A. T. Horton, D. Enagonio, H. D. Dixon, C. P. Saylor, G. T. Furukawa, M. L. Reilly, J. M. Henning, *Anal. Chim. Acta*, **17**, 54 (1957).

[112] S. Schrödle, R. Buchner, W. Kunz, *Fluid Phase Equilibria,* **216**, 175 (2004).

[113] C. Schreiner, *dissertation*, Regensburg (2008).

[114] J. Heinze, *Angew. Chem. Int. Ed. Engl.*, **32**, 1268 (1993).

[115] K. Izutsu, M. Ito, E. Sarai, *Anal. Sci.*, **1**, 341 (1985).

[116] H. Bruglachner, *dissertation*, Regensburg (2004).

[117] R. M. Wightman, D. O. Wipf, in: A. J. Bard (Ed.), *Electroanalytical Chemistry*, Vol. 15, Marcel Dekker, New York (1989).

[118] K. Aoki, J. Osteryoung, *J. Electroanal. Chem.*, **122**, 19 (1981).

[119] K. Aoki, J. Osteryoung, *J. Electroanal. Chem.*, **160**, 335 (1984).

[120] J. E. Baur, R. M. Wightman, *J. Electroanal. Chem.*, **305**, 73 (1991).

[121] C. G. Zoski, A. M. Bond, E. T. Allison, K. B. Oldham, *Anal. Chem.*, **62**, 37 (1990).

[122] D. Shoup, A. Szabo, *J. Electroanal. Chem.*, **140**, 237 (1982).

[123] K. B. Oldham, *J. Electroanal. Chem.*, **250**, 1 (1988).

[124] A. M. Bond, D. Luscombe, K. B. Oldham, C. G. Zoski, *J. Electroanal. Chem.*, **249**, 1 (1988).

[125] K. B. Oldham, *J. Electroanal. Chem.*, **237**, 303 (1987).

[126] H. Kahlert, in: F. Scholz (Ed.), *Electroanalytical Methods*, Springer, Berlin (2002).

[127] J. F. Coetzee, C. W. Gardner, *Anal. Chem.*, **54**, 2530 (1982).

[128] J. F. Coetzee, C. W. Gardner, *Anal. Chem.*, **54**, 2625 (1982).

[129] R. Kawano, M. Watanabe, *Chem. Commun.*, 330 (2003).

[130] M. Zistler, P. Wachter, P. Wasserscheid, D. Gerhard, A. Hinsch, R. Sastrawan, H. J. Gores, *Electrochim. Acta*, **52**, 161 (2006).

[131] C. A. Brooks, A. P. Doherty, *Electrochem. Commun.*, **6**, 867 (2004).

[132] P. Wang, S. M. Zakeeruddin, R. Humphry-Baker, M. Grätzel, *Chem. Mater.*, **16**, 2694 (2004).

[133] J. Barthel, F. Feuerlein, R. Neueder, R. Wachter, *J. Sol. Chem.*, **9**, 209 (1980).

[134] E. S. Carl, *dissertation*, Regensburg (1998).

[135] H.-G. Schweiger, M. Multerer, H. J. Gores, *IEEE transactions on instrumentation and measurement*, **56**, 2002 (2007).

[136] D. R. MacFarlane, J. Golding, S. Forsyth, G. B. Deacon, *Chem. Commun.*, 1430 (2001).

[137] M. Zistler, C. Schreiner, P. Wachter, P. Wasserscheid, D. Gerhard, H. J. Gores, *Int. J. Electrochem. Sci.*, **3**, 236 (2008).

[138] D. R. MacFarlane, S. A. Forsyth, J. Golding, G. B. Deacon, *Green Chem.*, **4**, 444 (2002).

[139] Q. Dai, D. B. Menzies, D. R. MacFarlane, S. R. Batten, S. Forsyth, L. Spiccia, Y.-B. Cheng, *C. R. Chimie*, **9**, 617 (2006).

[140] Y. Yoshida, K. Muroi, A. Otsuka, G. Saito, M. Takahashi, T. Yoko, *Inorg. Chem.*, **43**, 1458 (2004).

[141] S. Eisele, M. Schwarz, B. Speiser, C. Tittel, *Electrochim. Acta*, **51**, 5304 (2006).

[142] L. Nagy, G. Gyetvia, L. Kollár, G. Nagy, *J. Biochem. Biophys. Methods*, **69**, 121 (2006).

[143] T. Nishida, Y Tashiro, M. Yamamoto, *J. Flourine Chem.*, **120**, 135 (2003).

[144] S. Zhang, N. Sun, X. He, X. Lu, X. Zhang, *J. Phys. Chem. Ref. Data*, **35**, 1475 (2006).

[145] H. Matsumoto, M. Yanagida, K. Tanimoto, M. Nomura, Y. Kitagawa, Y. Miyazaki, *Chem. Lett.*, 922 (2000).

[146] A. B. McEwen, H. L. Ngo, K. LeCompte, J. L. Goldman, *J. Electrochem. Soc.*, **146**, 1687 (1999).

[147] N. V. Ignat'ev, U. Welz-Biermann, A. Kucheryna, G. Bissky, H. Willner, *J. Flourine Chem.*, **126**, 1150 (2005).

[148] P. C. Trulove, R. A. Mantz, in: P. Wasserscheid, T. Welton (Eds.), *Ionic Liquids in Synthesis*, Wiley-VCH, Weinheim (2003).

[149] J. A. Widegren, E. M. Saurer, K. N. Marsh, J. W. Magee, *J. Chem. Thermodyn.*, **37**, 569 (2005).

[150] D. R. MacFarlane, J. Sun, J. Golding, P. Meakin, M. Forsyth, *Electrochim. Acta*, **45**, 1271 (2000).

[151] C. Hardacre, J. D. Holbrey, S. P. Katdare, K. R. Seddon, *Green Chem.*, **4**, 143 (2002).

[152] D. Gerhard, S. C. Alpaslan, H. J. Gores, M. Uerdingen, P. Wasserscheid, *Chem. Commun.*, 5080 (2005).

[153] C. Schreiner, *verbal communication*, Regensburg (2008).

[154] J. Fuller, R. T. Carlin, R. A. Osteryoung, *J. Electrochem. Soc.*, **144**, 3881 (1997).

[155] C. Nanjundiah, F. McDevitt, V. R. Koch, *J. Electrochem. Soc.*, **144**, 3392 (1997).

[156] Y. Yoshida, O. Baba, G. Saito, *J. Phys. Chem. B*, **111**, 4742 (2007).

[157] M. C. Buzzeo, R. G. Evans, R. G. Compton, *Chem. Phys. Chem.*, **5**, 1106 (2004).

[158] H. Matsumoto, T. Matsuda, Y. Miyazaki, *Chem. Lett.*, 1430 (2000).

[159] D. R. MacFarlane, P. Meakin, J. Sun, N. Amini, M. Forsyth, *J. Phys. Chem. B*, **103**, 4164 (1999).

[160] H. Tokuda, K. Hayamizu, K. Ishii, Md. A. B. H. Susan, M. Watanabe, *J. Phys. Chem. B*, **109**, 6103 (2005).

[161] Y. A. Sanmamed, D. González-Salgado, J. Troncoso, C. A. Cerdeiriña, L. Romaní, *Fluid Phase Equilibria*, **252**, 96 (2007).

[162] S. V. Dzyuba, R. A. Bartsch, *Chem. Phys. Chem.*, **3**, 161 (2002).

[163] J. G. Huddleston, A. E. Visser, W. M. Reichert, H. D. Willauer, G. A. Broker, R. D. Rogers, *Green Chem.*, **3**, 156 (2001).

[164] H. Matsumoto, H. Kageyama, Y. Miyazaki, *Chem. Commun.*, 1726 (2002).

[165] J. D. Holbrey, K. R. Seddon, *J. Chem. Soc.-Dalton Trans.*, 2133 (1999).

[166] C. P. Fredlake, J. M. Costhwaite, D. G. Hert, S. N. V. K. Aki, J. F. Brennecke, *J. Chem. Eng. Data*, **49**, 954 (2004).

[167] M. S. Ding, K. Xu, S. S. Zhang, T. R. Jow, K. Amine, G. L. Henriksen, *J. Electrochem. Soc.*, **146**, 3974 (1999).

[168] P. A. Z. Suarez, S. Einloft, J. E. L. Dullius, R. F. de Souza, J. Dupont, *J. Chim. Phys.-Chim. Biol.*, **95**, 1626 (1998).

[169] J. Sun, D. R. MacFarlane, M. Forsyth, *Electrochim. Acta*, **48**, 1707 (2003).

[170] A. Noda, M. Watanabe, *Electrochim. Acta*, **45**, 1265 (2000).

[171] J. M. Crosthwaite, M. J. Muldoon, J. K. Dixon, J. L. Anderson, J. F. Brennecke, *J. Chem. Thermodyn.*, **37**, 559 (2005).

[172] K. R. Seddon, A. Stark, M.-J. Torres, *Pure Appl. Chem.*, **72**, 2275 (2000).

[173] S. Hayashi, R. Ozawa, H. Hamaguchi, *Chem. Lett.*, **32**, 498 (2003).

[174] R. Ozawa, S. Hayashi, S. Saha, A. Kobayashi, H. Hamaguchi, *Chem. Lett.*, **32**, 948 (2003).

[175] Y. Yoshida, J. Fujii, K. Muroi, A. Otsuka, G. Saito, M. Takahashi, T. Yoko, *Synthetic Metals*, **153**, 421 (2005).

[176] E. Y. Menzel, *dissertation*, Regensburg (1998).

[177] M. S. Ding, T. R. Jow, *J. Electrochem. Soc.*, **152**, A1199 (2005).

[178] http://webbook.nist.gov/chemistry/.